Characterization of Highly Cross-linked Polymers

Characterization of Highly Cross-linked Polymers

S. S. Labana, EDITOR
Ford Motor Company

R. A. Dickie, EDITOR
Ford Motor Company

Based on a symposium sponsored by
the Division of Organic Coatings
and Plastics Chemistry
at the 185th Meeting
of the American Chemical Society,
Seattle, Washington,
March 20–25, 1983

ACS Symposium Series

M. Joan Comstock, *Series Editor*

Advisory Board

FOREWORD

The ACS SYMPOSIUM SERIES was founded in 1974 to provide
a medium for publishing symposia quickly in book form. The
format of the Series parallels that of the continuing ADVANCES
IN CHEMISTRY SERIES except that in order to save time the
papers are not typeset but are reproduced as they are sub-
mitted by the authors in camera-ready form. Papers are re-
viewed under the supervision of the Editors with the assistance
of the Series Advisory Board and are selected to maintain the
integrity of the symposia; however, verbatim reproductions of
previously published papers are not accepted. Both reviews
and reports of research are acceptable since symposia may
embrace both types of presentation.

PREFACE

Cross-linked polymers have long been an important class of materials and are used in a diverse assortment of applications including organic coatings, fiber-reinforced plastics, elastomers, and adhesives. Characterization of these materials has always been difficult, especially for the more highly cross-linked materials, because of their infusibility, insolubility, and general intractability. Considerable progress has been made in recent years in developing theoretical approaches to the description of the molecular structure of cross-linked polymers; several chapters describe the recent progress in this important area. Light scattering and rheological characterization techniques have been applied to cross-linking systems in the pre-gel state. Macroscopic mechanical characterization of cross-linked polymers has been the subject of many investigations; fracture behavior, relationships between molecular structure, morphology, and mechanical properties, and the dependence of properties on thermal history are discussed by several authors. Not all network formation occurs through formation of chemical bonds; in one chapter in this volume, neutron scattering results suggest the formation of correlation networks in certain polymer blends.

Characterization of the chemical structure of highly cross-linked polymers, and of the chemical changes that accompany degradation processes, relies on spectroscopic methods. Solid-state nuclear magnetic resonance techniques have the potential to allow a more detailed characterization than before possible of the chemical environment and structure of chemical cross-links in elastomers and thermoset epoxies. Degradation processes in cross-linked systems have been studied by using infrared spectroscopy, solid-state NMR, and electron spin resonance.

It is a pleasure to acknowledge the support of the Ford Motor Company. We also wish to thank A. Oslanci and M. Dvonch for their secretarial assistance. Finally, sincere thanks to the authors who have made this volume possible through their hard work and cooperation.

S. S. LABANA
R. A. DICKIE
Ford Motor Company
Dearborn, Michigan

November 3, 1983

Formation and Properties of Polymer Networks
Experimental and Theoretical Studies

J. L STANFORD, R. F. T. STEPTO, and R. H. STILL

Department of Polymer Science and Technology, The University of Manchester Institute of
Science and Technology, Manchester, M6O 1QD, England

Experimental results on reactions forming tri- and
tetrafunctional polyurethane and trifunctional poly-
ester networks are discussed with particular consider-
ation of intramolecular reaction and its effect on
shear modulus of the networks formed at complete
reaction.   The amount of pre-gel intramolecular
reaction is shown to be significant for non-linear
polymerisations, even for reactions in bulk. Gel-
points are delayed by an amount which depends on the
dilution of a reaction system and the functionalities
and chain structures of the reactants. Shear moduli
are generally markedly lower than those expected for
the perfect networks corresponding to the various
reaction systems, and are shown empirically to be
closely related to amounts of pre-gel intramolecular
reaction. Deviations from Gaussian stress-strain
behaviour are reported which relate to the low
molar-mass of chains between junction points.
Finally, a rate theory of random polymerisation is
described which enables the moduli of networks to
be predicted from the molar mass, functionality,
chain structure and initial dilution of the reactants
used for network formation.

This paper presents a survey of published and more recent work on
correlations between network properties and reactant structures
and reaction conditions, and extends the work presented in recent
publications (1,2,3). The reaction systems used have been poly-
oxypropylene (POP) triols or tetrols and mixtures of diols and
triols of various molar masses reacting with diisocyanates (to
give polyurethanes) or diacid chlorides (to give polyesters).
Systems have been chosen so that like groups had equal reactivit-
ies and reactions have been carried out in bulk and at various
dilutions in inert solvents using equimolar amounts of the
different reactive groups. Experimentally, emphasis has been
placed on the extent to which pre-gel intramolecular reaction

and the consequent delay in the gel point beyond the ideal,
Flory-Stockmayer gel point (4,5) defines the physical properties
of the networks formed at complete reaction. Intramolecular
reaction can introduce elastically ineffective loops into a
rubbery network. In general, loops produce the opposite effects
on physical properties to those expected from entanglements.
Theoretical approaches are outlined which attempt to account for
intramolecular reaction in terms of reactant structure (function-
ality, molar mass, and chain structure) and reaction conditions
(concentrations of reactants). The approaches allow the
prediction of gel points accounting for pre-gel intramolecular
reaction. Additionally, account of pre-gel and post-gel intra-
molecular reaction allows the prediction of shear modulus at
complete reaction.

Pre-Gel Intramolecular Reaction

Previous studies(6) have shown how the number fraction of ring
structures formed during irreversible linear random polymerisa-
tions leading to polyurethanes may be measured. The work has been
extended(7,8) to non-linear polyurethane formation using hexa-
methylene diisocyanate(HDI) and POP triols. For non-linear
polymerisations, it is found that the number of ring structures
per molecule(N_r) is always significant, even in bulk reactions.
For example, Figure 1 shows N_r versus extent of reaction(p), for
linear and non-linear polyurethane-forming bulk reactions with
approximately equimolar concentrations of reactive groups(2,6,7).
The much larger values of N_r in the non-linear compared with the
linear polymerisation are due to the larger number of opportunities
per molecule for intramolecular reaction in the former type of
polymerisation. However, the other factors influencing intra-
molecular reaction in the two systems, particularly the number of
bonds(ν) in the chain forming the smallest ring structure predict
more intramolecular reaction in the linear system. A detailed
discussion of these factors has been given elsewhere(2). It
should be noted that it is not possible to reduce the number of
ring structures formed in such reaction systems as the amounts of
intermolecular reaction relative to intramolecular reaction are
at a maximum for reactions in bulk.
     The gel point of the non-linear system shown in Figure 1 was
at p = 0.765 compared with the value of 0.707 expected in the
absence of intramolecular reaction. Thus, although p at gel is
only about 8% higher than expected, $N_r \cong 0.3$ at p = 0.765,
showing that at gel about one molecule in three contained a ring
structure. Such ring structures or loops can have marked effects
on the properties of networks formed at complete reaction(1,2,9-
12). Developments in the theoretical aspects of the work,
allowing prediction of N_r, the gel point, and the shear moduli
of networks formed at complete reaction are presented in the last
section of the present paper.
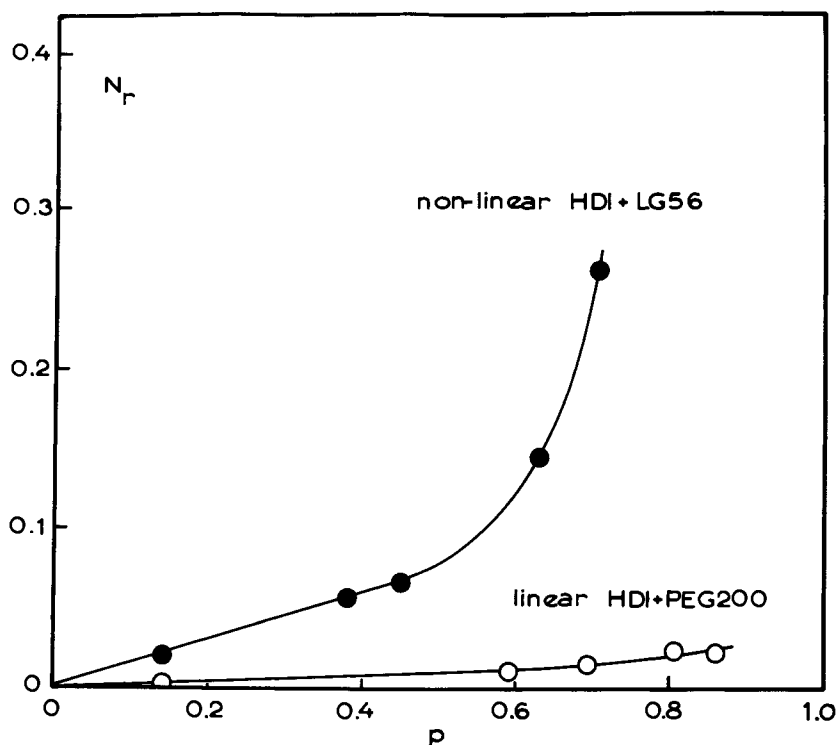
Figure 1. Number of ring structure per molecule (N_r) as a function of extent of reaction(p) for linear and non-linear polyurethane forming reactions in bulk with approximately equimolar concentrations of reactive groups.
$r = [NCO]_0/[OH]_0 \cong 1$) (6,7).

O – linear polymerisation, HDI + poly(ethylene glycol) (PEG200) at 70°C, $[NCO]_0 = 5.111$ mol kg^{-1}, $[OH]_0 = 5.188$ mol kg^{-1}; number-average of bonds in chain forming smallest ring structure (ν) = 25.2.
● – non-linear polymerisation, HDI + POP triol (LG56) at 70°C, $[NCO]_0 = 0.9073$ mol kg^{-1}, $[OH]_0 = 0.9173$ mol kg^{-1}; $\nu = 115$. Reproduced with permission, from Ref. 2. Copyright 1982, American Chemical Society.

Intramolecular Reaction and Gelation

An expression has been derived[4] for the extent of reaction at gelation in $RA_2 + RB_f$ random[13] or condensation polymerisation which accounts more completely than earlier expressions[14-16] for intramolecular reaction. It may be rearranged to give

$$\alpha_c(f-1) = (1 + \lambda'_{ab})^2 \qquad (1)$$

Here, $\alpha_c = p_a p_b$, where p_a and p_b are the extents of reaction of A and B groups at gel, respectively, and λ'_{ab} is a ring-forming parameter. When $\lambda'_{ab} = 0$, the classical Flory-Stockmayer condition for gelation is obtained. λ'_{ab} is predicted (4) to be proportional to the dilution of a reaction system, to increase with functionality, and to decrease with chain stiffness and molar mass of reactants. In detail,

$$\lambda'_{ab} = c_{int}/c_{ext} \qquad (2)$$

where $c_{int(ernal)}$ is the concentration of groups which can react intramolecularly with a given group on a molecule and $c_{ext(ernal)}$ is the concentration of groups which can react intermolecularly with the same group.

$$c_{int} = (f-2)Pab.\phi(1,3/2) \qquad (3)$$

with $\qquad\qquad Pab = (3/2\pi\nu b^2)^{3/2}/N \qquad (4)$

where ν is the number of bonds in the chain that can form the smallest ring, with b its effective bond length, defined such that its mean-square end-to-end distance equals νb^2, and N is the Avogadro constant. The possibility of forming rings of all sizes is accounted for by $\phi(1,3/2)$, with

$$\phi(1,3/2) = \sum_{i=1}^{\infty} 1^i i^{-3/2} = 2.612 \qquad (5)$$

Values of c_{ext} have to be chosen arbitrarily since λ'_{ab} is assumed to be constant for a given system. In practive, the two extreme experimental values, $c_{ext} = c_{ao} + c_{bo}$ and $c_{ext} = c_{ac} + c_{bc}$, representing the initial and gel-point concentrations, are used in the theoretical treatment described[4]. The dependence of λ'_{ab} on functionality is allowed for by the factor (f-2) in Equation 3. Similarly, chain stiffness and molar mass of reactants are allowed for by the factor $(\nu b^2)^{-3/2}$ in Equation 4 and the dependence of λ'_{ab} on dilution is represented by its proportionality to c_{ext}^{-1} in Equation 2.

Figure 2 illustrates results obtained from tri- and tetra-functional polyurethane-forming reaction systems, with λ'_{ab} plotted against $(c_{ao} + c_{bo})^{-1}$, the initial dilution of reactive groups. It is apparent that the plots are curved rather than
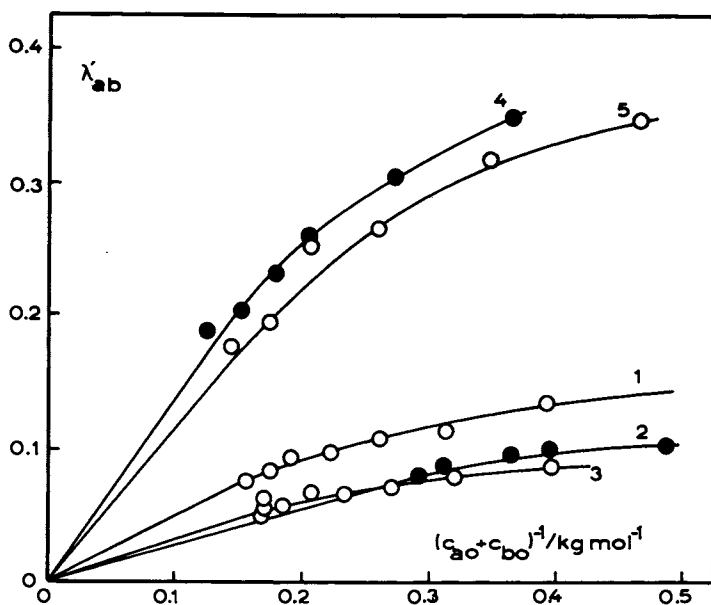
Figure 2. Ring forming parameter (λ'_{ab}) versus initial dilution of reactive groups ($(c_{ao}+c_{bo})^{-1}$). Experimental values of α_c were used to evaluate λ'_{ab} according to Eq. 1. Systems: 1 and 2, HDI+POP triols; 3, 4,4'-diphenyl methane diisocyanate(MDI)+POP triol; 4 and 5, HDI+POP tetrols. Reactions carried out at 80°C in bulk and in nitrobenzene solution. System 1, HDI+LHT240, ν=33; system 2, HDI+LHT112, ν=61; system 3, MDI+LHT240, ν=30; system 4, HDI+OPPE-NHI, ν=29; system 5, HDI+OPPE-NH2, ν=33.(LHT240 and LHT112-oxypropylated 1,2,6 hexane triols; OPPE-NHI and OPPE-NH2 -oxypropylated pentaerythritols.)
Reproduced, with permission,from Ref. 1. Copyright 1982, Plenum Publishing Corporation.

linear as predicted by Equation2. Detailed discussions of the
results shown in Figure 1 and of similar results for polyester-
forming systems have been given elsewhere(1,2,4,5). In general,
polyester-forming systems are found to give more linear plots
than polyurethane-forming systems and, with regard to the choice
of c_{ext}, the use of $c_{ao} + c_{bo}$ gives more linear plots than $c_{ext} = c_{ac} + c_{bc}$. Thus, the functional dependence of λ'_{ab} on dilution
appears to be better described by theory if initial dilution
$((c_{ao} + c_{bo})^{-1})$ is used.

From Figure 2 it is clear that intramolecular reaction
increases with dilution and, as indicated in Figure 1, with
functionality. In addition, the points on the curves at the low-
est dilutions refer to bulk reaction mixtures, indicating again
(c.f. Figure 1) that intramolecular reaction always occurs. The
effects of chain stiffness can be seen by comparing systems 1 and
3, which have similar values of ν but different chain structures;
that of system 3 contains a stiffer, aromatic residue.

The initial slopes of the curves in Figure 2 and of the
corresponding plots with $(c_{ac} + c_{bc})$ as abscissa can be analysed
according to Equations 3 and 4, and values of b found. The values
obtained are given in Table I. The two values of b for each
system generally encompass the value expected from solution

Table I. Values of Effective Bond Length (b) of Chains Forming
the Smallest Ring Structures (of ν bonds).
(i) $c_{ext} = c_{ao} + c_{bo}$; (ii) $c_{ext} = c_{ac} + c_{bc}$. ν_{DI} is the
fraction of bonds due to the diisocyanate residue in
the chain of ν bonds,
Reproduced, with permission, from Ref.1. Copyright 1982,
Plenum Publishing Corp.

	System	f	ν	ν_{DI}/ν	b/nm(i)	b/nm(ii)
1.	HDI/LHT240	3	33	0.303	0.247	0.400
2.	HDI/LHT112	3	61	0.164	0.222	0.363
3.	MDI/LHT240	3	30	0.233	0.307	0.488
4.	HDI/OPPE-NH1	4	29	0.345	0.240	0.356
5.	HDI/OPPE-NH2	4	33	0.303	0.237	0.347

properties(1,2,4,5). Thus the effective average value of c_{ext} lies
somewhere between $(c_{ao} + c_{bo})$ and $(c_{bc} + c_{bc})$, and probably
nearer to $(c_{ac} + c_{bc})$. The generally smaller values of b for the
aliphatic tetrafunctional systems (4 and 5) compared with the
aliphatic trifunctional systems (1 and 2) probably indicate a
relative undercounting of opportunities for intramolecular
reaction for growing species from tetrafunctional compared with
trifunctional reactants.

Comparison of systems 1 and 2 and systems 4 and 5 show that smaller values of b are obtained for the larger values of ν or the smaller values of ν_{DI}/ν, indicating that the chains with the larger proportions of oxypropylene units are the more flexible. Hence although system 1 gives higher values of λ'_{ab} than system 2 because it has a smaller value of ν, the difference between the curves for the two systems in Figure 2 is reduced because b for system 2 is smaller. Similar considerations hold true for the relative values of λ'_{ab} for systems 4 and 5.

Other aspects of gelation studies which have been reported are the determination of effective functionalities([2]) and the use of diol-triol mixtures([3]) to investigate the effects of variation of average functionality. The former work used a triol which had been independently characterised with respect to functionality and showed the shortcomings of using gelation data alone to deduce the chemical functionalities of reactants. The latter work used mixtures of a diol and triol reacting with sebacoyl chloride at different initial dilutions in diglyme as solvent. The hydroxyl groups had equal reactivities and the reaction mixtures were equimolar in hydroxyl and acid chloride groups. At zero dilution, the equation of Stockmayer ([5],[17]), $\alpha_c^{-1} = (f_w - 1)$, where f_w is the weight-average functionality of the polyol mixture, is obeyed. The results are illustrated in Figure 3, where α_c^{-1} is plotted versus initial dilution. The intercepts in α_c^{-1} at zero dilution are equal to the values of (f_w-1) calculated from the amounts of diol and triol in the reaction mixtures, and the decreases in α_c^{-1} with initial dilution are due to intramolecular reaction.

Network Properties

Correlations between Gel Point and Shear Modulus. The reaction

systems in Figure 2 were used to form networks at complete reaction([1],[2],[10],[11]). Sol fractions were removed and shear moduli were determined in the dry and equilibrium-swollen states at given temperatures using uniaxial compression or a torsion pendulum at 1Hz. The procedures used have been described in detail elsewhere([11],[12]). The shear moduli(G) obtained were interpreted according to Gaussian theory([18]-[20]) to give values of M_c, the effective molar mass between junction points, consistent with the affine behaviour expected at the small strains used ([20]).

Equation 6 was used with ρ

$$G = ART\rho\phi_2^{1/3}(V_u/V_F)^{2/3}/M_c \qquad (6)$$

the density of the dry network, ϕ_2 the volume fraction of solvent present in a swollen network, V_u the volume of the dry, unstrained network, and V_F the volume at formation. A has the value (1-2/f) for networks showing phantom behaviour and 1 for networks showing affine behaviour ([19],[20]).
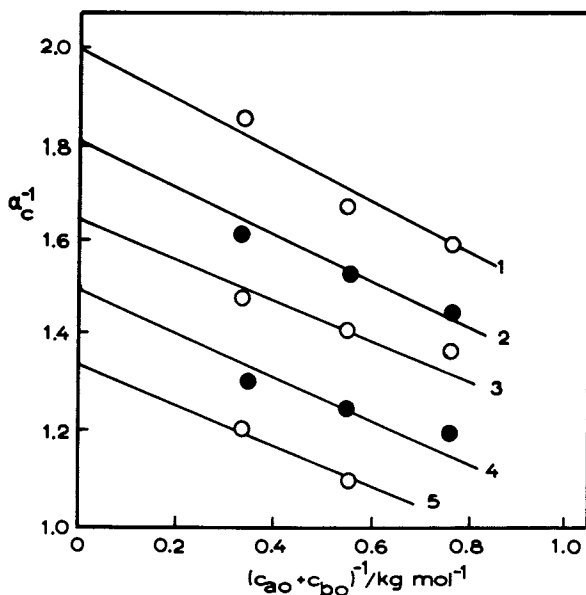
Figure 3. α_c^{-1} versus initial dilution of reactive groups $((c_{ao}+c_{bo})^{-1})$ for mixtures of diol(PPG1025) and triol(LHT 112) reacting with sebacoyl chloride at 60°C in diglyme. $r=[COC\ell]_o/[OH]_o \cong 1$.
PPG1025 – POP diol; LHT112 – POP triol (see caption Figure 2). Curves 1, f_w = 2.99; 2, f_w = 2.82; 3, f_w = 2.65; 4, f_w = 2.50; 5, f_w = 2.35.
Reproduced, with permission, from Ref. 3. Copyright 1982, Society of Polymer Science, Japan.

The results are shown in Figure 4, where M_c/M_c^0 is plotted
versus $p_{r,c}$. The molar mass between junction points of the
perfect network(M_c^0) is calculable from the molar mass and
structure of the reactants ([1,2]) and M_c was evaluated from the
measured modulus using Equation 6 with A=1. $p_{r,c}$ is the extent
of intramolecular reaction at gelation ([1,2]), given by the
expression

$$p_{r,c} = \alpha_c^{\frac{1}{2}} = (f-1)^{-\frac{1}{2}} \tag{7}$$

$p_{r,c} = 0$ corresponds to the ideal(Flory-Stockmayer) gel-point,
and $M_c/M_c^0 = 1$ to the perfect, affine network. In all cases in
Figure 4, M_c/M_c^0 exceeds 1 and tends to 1 as $p_{r,c} \rightarrow 0$. Thus,
only in the limit of a perfect gelling system is a perfect network
achieved, for which affine behaviour is predicted. Intercepts
equal to 3 and 2 on the M_c/M_c^0 axis would be required for perfect,
phantom networks of functionalities 3 and 4, respectively. The
pre-gel intramolecular reaction, which causes α_c to exceed $1/(f-1)$
in value, also produces some elastically ineffective loops which
have marked effects on the moduli of the dry networks. In fact,
M_c/M_c^0 is equal to the proportional reduction in modulus compared
with that expected for the perfect, dry network. Thus, $M_c^0/M_c =$
10 correpsonds to a 10-fold reduction. Any effects due to
entanglements are in all cases overshadowed by the reductions in
moduli due to loops.
   The poirts at the lowest values of $p_{r,c}$ for the various
systems are those for bulk reactions and even for these signi-
ficant reductions in moduli are apparent. In addition, such
reductions can be produced by relatively small values of $p_{r,c}$.
Thus, system 1 shows a 5-fold reduction in modulus for an excess
extent of reaction at gelation of only 0.05, and system 5 a
3-fold reduction for $p_{r,c} = 0.10$.
   The relative positions of the lines for the various systems
can be related to M_c^0(or ν), f, and the chain structures of the
reactants([1,2,9-12]). The slopes of the lines show that the re-
duction in modulus with pre-gel intramolecular reaction is larger
for trifunctional compared with tetrafunctional networks (c.f.
systems 1 and 2 with 4 and 5), although higher values of $p_{r,c}$
obtain for tetrafunctional reaction systems (c.f. Figure 2).
In addition, for a given functionality, the reduction is larger
for smaller values of M_c^0 (c.f. systems 1 with 2 and 4 with 5);
that is, for a given amount of intramolecular reaction (or value
of $p_{r,c}$) systems with smaller loops have larger proportions of
those loops elastically ineffective. The networks for system 3,
based of MDI, give values of M_c/M_c^0 near unity, corresponding to
relatively high values of their rubbery moduli. The reasons for
this phenomenon are not completely understood but are obviously
related to the stiffer, aromatic chain structure between junction
points in these networks.
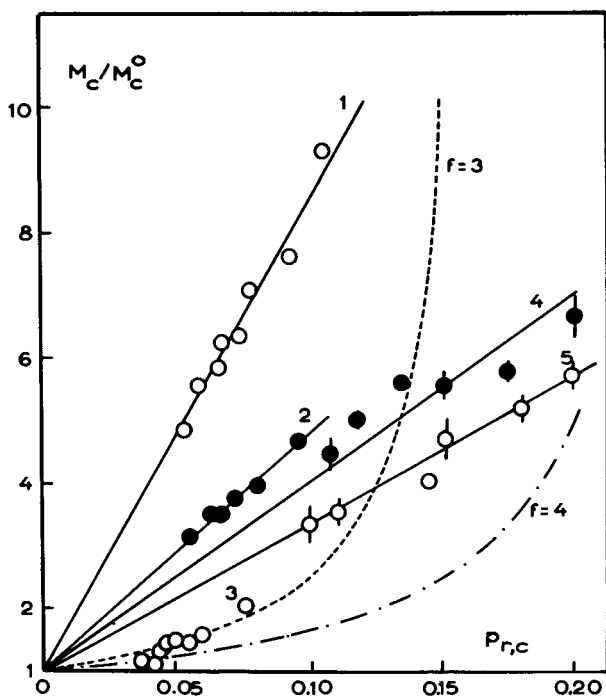
Figure 4. Molar mass between elastically effective
junction points (M_c) relative to that for the perfect
network(M_c^0) versus extent of intramolecular reaction at
gelation($p_{r,c}$). Reaction systems as for Figure 2.
———— lines through experimental points for systems 1,2,4,5;
——— and -.-.- theoretical curves for tri- and tetrafunc-
tional networks (see text, last section).
System 1, HDI+LHT240, M_c^0=0.635 kg mol^{-1}, ν=33; system 2,
HDI+LHT112, M_c^0=1.168 kg mol^{-1}, ν=61; system 3, MDI+LHT240,
M_c^0=0.705 kg mol^{-1}, ν=30; system 4, HDI+OPPE-NH1, M_c^0=0.500
kg mol^{-1}, ν=29; system 5, HDI+OPPE-NH2,M_c^0=0.586 kg mol^{-1},
ν=33.
Reproduced, with permission, from Ref. 2. Copyright 1982,
American Chemical Society.

Deviations from Gaussian Behaviour. The method of analysis of
experimental data used to obtain the values of M_c in Figure 4
involves approximations(2,10,12). However, the resulting uncert-
anties in M_c are much less than the changes in M_c produced by
intramolecular reaction. The magnitude of the uncertainties is
indicated by the error bars on the points for systems 4 and 5 in
Figure 4, for which systems a detailed analysis of the uncertain-
ties was carried out (12).

The stress-strain plots for uniaxial compression showed
deviations from Gaussian behaviour which decreased as M_c
increased. The deviations were not of the Mooney-Rivlin type, as
is shown in Figure 5, where $\sigma/(\Lambda-\Lambda^{-2})$ is plotted versus Λ^{-1} for
swollen networks derived from system 5. σ is the nominal stress
and Λ the deformation ratio. The symbol 5-69 denotes the network
formed at complete reaction by system 5 in the presence of 69%
w/w solvent, and, similarly 5-17 denotes that formed in the
presence of 17% w/w solvent. The slope for network 5-69, having
$M_c/M_c{}^0 = 5.6$ or $M_c = 3.28$kg mol^{-1}, is essentially zero, corres-
ponding to Gaussian behaviour, whereas, network 5-17 shows marked
deviations from Gaussian behaviour and has a non-linear Mooney-
Rivlin plot. The modulus of network 5-17 was higher than that
of 5-69 in the swollen and dry states, yet extrapolation of the
curve for 5-17 to $\Lambda^{-1} = 1$ gives apparently zero intercept.
The values of M_c used in Figure 4 for network 5-17 and other net-
works derived from systems 4 and 5 were obtained from moduli
evaluated from linear least-squares lines through the origins of
the respective Gaussian stress-strain plots (σ versus $\Lambda-\Lambda^{-2}$).
For swollen network 5-17 this gave a value of $M_c/M_c{}^0 = 3.5$ or
$M_c = 2.05$kg mol^{-1}.

In general, the measurements on systems 4 and 5 and on POP
triol-based polyester networks show that the deviations from
Gaussian behaviour decrease rapidly as M_c increases and are
approximately independent of whether the networks are in the
swollen or dry state(2,11,12). The deviations most probably have
their origin in the non-Gaussian nature of the distribution of
end-to-end vectors of chains between junction points. Changes in
the form of the distribution are expected at the relatively low
values of M_c of the networks studied, with a Gaussian form of
distribution being obtained as M_c increases. The deviations are
of significance in indicating shortcomings in present theories in
describing properties of networks with relatively short chains
between junction points, in terms of the distributions of end-to-
end vectors and the detailed chemical structures of such chains.
However, it can be seen from Figure 4 that the uncertainties
introduced in the derived values of modulus and M_c are of
secondary importance compared with the changes in modulus intro-
duced by loop formation. Indeed, the error bars in Figure 4 for
systems 4 and 5 result for the combined effects of the deviations
from Gaussian behaviour and measurements on dry and swollen
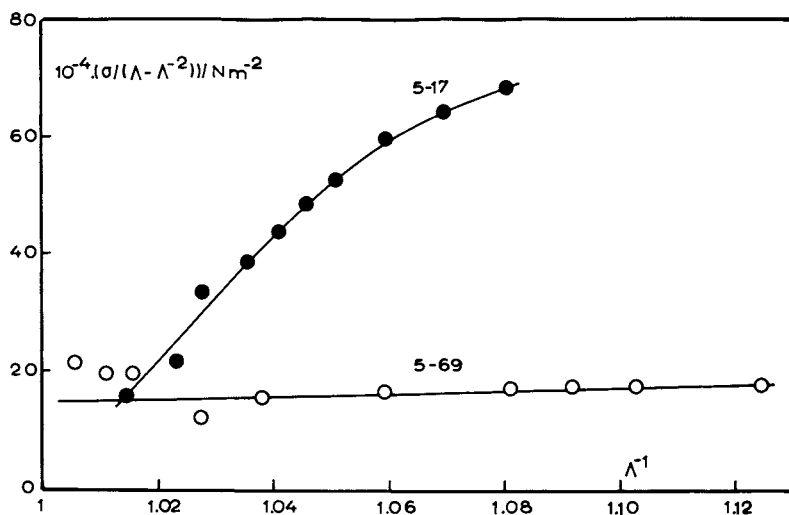samples.

Figure 5. Mooney-Rivlin plots of stress-strain data(<u>10</u>) for two tetrol-based polyurethane networks from system 5 of Figures 2 and 4, prepared at various dilutions in nitrobenzene as solvent. Networks swollen in nitrobenzene at 40°C
Reaction conditions: 5-69, 69% solvent; 5-17, 17% solvent.

Correlations Between Gel Point and Tg. The variation of Tg with α_c has been studied ($\underline{1},\underline{2},\underline{9},\underline{11}$), in particular for networks from system 3, where T_g increased from 301K,for a POP/MDI linear polymer with repeat-unit molar mass equal to $M_c^{\ O}$,to 312K for the limiting perfect network with $M_c = M_c^{\ O}$. Thus, a relatively small increase in Tg is produced by the restriction of chain movement due to junction points. A larger change between linear polymer and perfect network would be expected for networks with smaller values of $M_c^{\ O}$.

Theoretical Correlations between Gel Point and Shear Modulus

Pre-gel Loops. The theoretical curves in Figure 4 were obtained by calculating the shear modulus, assuming that only the smallest loops formed pre-gel are elastically ineffective($\underline{1},\underline{2},\underline{12}$). The equations used were

$$M_c/M_c^{\ O} = 1/(1-6p_{r,c}); \quad f = 3 \qquad (8)$$

and

$$M_c/M_c^{\ O} = 1/(1-4p_{r,c}); \quad f = 4 \qquad (9)$$

and the loops considered are illustrated in Figure 6. The model is an oversimplified one, as it neglects elastically ineffective loops of larger size and loops produced post-gel. However, the curves illustrate the smaller effects of loops on tetrafunctional compared with trifunctional networks. For f = 3, each smallest loop reduces the number of elastically effective junction points by 2, whereas for f = 4, only 1 junction point is lost.

Rate Theory: Pre-gel and Post-gel Loops. In order to account for the effects of pre-gel and post-gel intramolecular reaction on modulus, it is necessary to use a theory which describes the continuous growth of intramolecular reaction throughout an irreversible polymerisation. The rate theory($\underline{21}$-$\underline{24}$) is being further developed to this end. The theory already allows prediction of N_r and α_c given only the initial dilution of reactive groups, and reactant molar mass, chain structure and functionality, and has been applied to the interpretation of experimental values of N_r in linear($\underline{21}$) and non-linear reaction systems($\underline{22}$) and to the correlation of experimental values of α_c($\underline{22},\underline{23}$). In addition, correlations between α_c and M_c/M_c^O have been achieved for an RA₃ self-polymerisation($\underline{24}$) and a résumé of the results obtained are presented here.
     The rate-theory description of random polymerisations considers subsets of states of the monomer units involved in a polymerisation and the reaction routes by which they interconvert through intermolecular and intramolecular reaction. Unlike cascade theory($\underline{25}$) it allows analytical expressions for ring fractions, gel point, sol fraction, gel fraction and numbers of loops to be derived(5,24). It has also been found to provide a
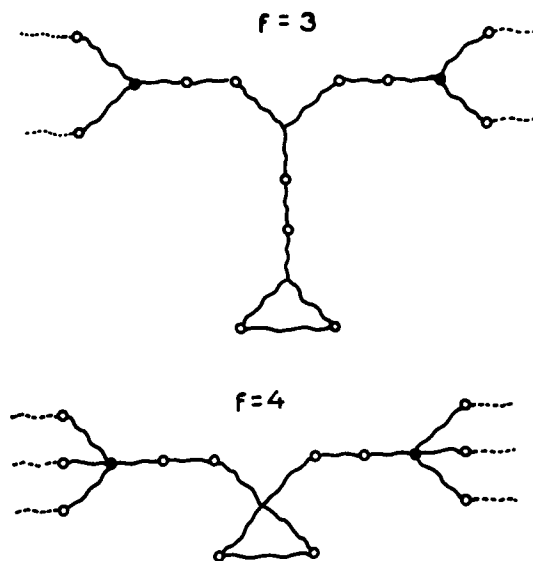
Figure 6. Ring structures of the smallest size in networks
formed in RA_2 + RB_3 and RA_2 + RB_4 polymerisations.
● - elastically effective junction points; O - pairs of
reacted groups (-AB-).
Reproduced, with permission, from Ref. 1. Copyright, 1982.
Plenum Publishing Corporation.

more consistent prediction of N_r and α_c in $RA_2 + RB_3$ polymerisations([22]).

For an RA_3 polymerisation, the smallest subset of states, including ring states, and their interconversion reactions are given in table II. Expressions for the rates of reaction of the various routes by which the states interconvert may be derived from general rules([5],[21]) using the extent of reaction of A groups, p, as independent variable. Integration of these expressions gives the unit (or weight) fraction of the states as a function of p. States with continuing chains contribute to network growth and can be used to define an expression for the gel point, and for the gel fraction in the reaction system after gel. In the absence of intramolecular reaction, only state 4 is left at complete reaction (p=1) and this defines the perfect network ($M_c = M_c{}^o$). With intramolecular reaction present, states 4 and 6 are left at complete reaction with a corresponding reduction in elastically effective junction points, giving $M_c > M_c{}^o$.

The presence of states 4 and 6 in a network at complete reaction is presented schematically in Figure 7. It can be seen that over the complete reaction system the number of junction points lost is $N_a \cdot P_6$, where N_a is the number of monomer units initially and P_6 is the fraction of units in state 6. Hence at complete reaction, the number of elastically effective function points in $N_a(P_4 - P_6)$, where $P_4 + P_6 = 1$. Thus,

$$M_c/M_c{}^o = 1/(1-2P_6) \qquad (10)$$

The analytical expression for P_6 is

$$P_6 = p(-p^2\lambda + (2\lambda - 4\lambda^2/3)p - (8\lambda^3/9)\ell n(1 - 3p/(2\lambda + 3))) + 3\lambda p^2/2$$

$$+ 3\lambda^2 p/2 + (3\lambda^2/2 + 3\lambda^3/4)\ell n(1 - 2p/(\lambda + 2)) \qquad (11)$$

Here, λ is a ring-forming parameter given by the equation (c.f. Equations 2 to 4)

$$\lambda = P_{ab}/c_{ao} \qquad (12)$$

with P_{ab} defined by Equation 4 and c_{ao} the intial concentration of A groups. Unlike λ'_{ab} of Equation 2, λ is a uniquely defined parameter; in the definition of λ'_{ab}, the denominator, c_{ext}, had to be chosen arbitrarily.

A corresponding equation to Equation 11 has been derived to define the extent of reaction at gelation([24]). It enables $p_{r,c}$ (see Equation 7) to be evaluated as a function of λ and allows prediction of the correlation between gel point and reduction in shear modulus (viz. $M_c/M_c{}^o$). The correlation is shown as curve 1 in Figure 8, which may be compared with the experimental curves in Figure 4 for $RA_2 + RB_f$ polymerisations.

Table II. Smallest Subset of States of Monomer Units in an RA₃
           Polymerisation.
           A- denotes a continuing chain of undefined length.

State	Reaction Route	Reaction
1.	1,2	
	1,5	
2.	2,3	
	2,6	
3.	3,4	
4.		
5.	5,6	
6.		

Figure 7. Rate theory – occurrence of states 4 and 6 in a
network at complete reaction from an RA$_3$ polymerisation.

State 4:   –AA $\Big\langle$ $\begin{matrix} AA- \\ AA- \end{matrix}$;   State 6: $\Big(\begin{matrix} A \\ A \end{matrix}\Big\rangle$ –AA–
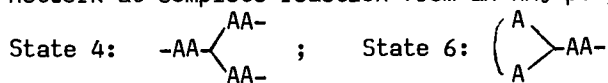
Figure 8. Predicted correlations(24)between reduction in
shear modulus at complete reaction(M_c/M_c^0) and extent of
intramolecular reaction at gelation($p_{r,c}$) for an RA_3
polymerisation.
Curve 1: From rate theory, accounting for pre-gel and post-
gel intramolecular reaction (Equation 10).
Curve 2: Accounting for pre-gel intramolecular reaction
only (Equation 13).

If only pre-gel intramolecular reaction is considered, then
the number of smallest loops in an RA_3 polymerisation is $3N_a p_{r,c}/2$.
The number of junction pints lost at complete reaction is
twice this number (see Figure 7) and

$$M_c/M_c^o = 1/(1-3p_{r,c}). \tag{13}$$

This equation corresponds to Equation 8 for an $RA_2 + RB_3$ polymer-
isation. The resulting relationship between M_c/M_c^o and $p_{r,c}$ is
shown by curve 2 in Figure 8, which may be compared with the
calculated curves in Figure 4.

In a real network of functionality four or less, the smallest
loops apparently lead to elastically ineffective junction points.
In addition, larger loops can also contribute to such defects.
The relative positions of the curves in Figure 8 show that, on
the basis of the smallest loops, post-gel intramolecular reaction
cannot be neglected, with approximately the same number of loops
occurring post-gel as pre-gel. The importance of both post-gel
and pre-gel intramolecular reaction is also apparent from Figure
4 for $RA_2 + RB_3$ systems, where, apart from the data for the aro-
matic system 3, the calculated curves generally lie well below
the experimental curves and have different shapes therefrom.
To allow direct comparison with such experimental data,
developments of the rate theory to evaluate M_c/M_c^o for $RA_2 + RB_3$
systems are presently in progress.

Literature Cited

1. Stanford, J.L.; Stepto, R.F.T.; Still, R.H., in "Reaction
    Injection Moulding and Fast Polymerisation Reactions";
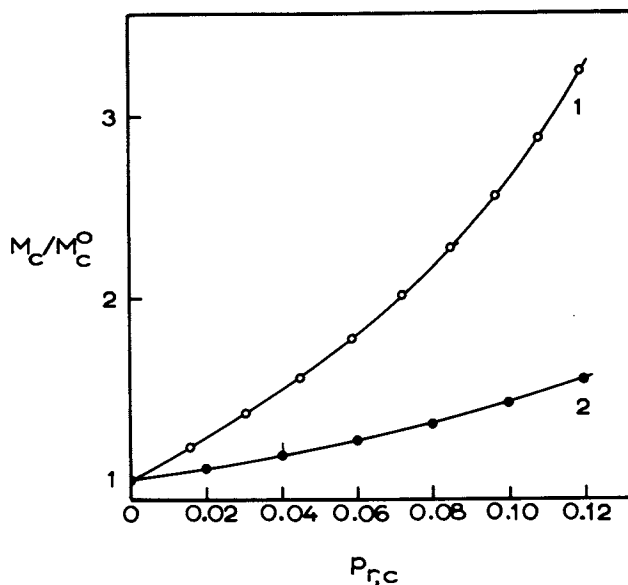   Kresta, J.E., Ed.; Plenum Publishing Corp: New York, 1982;
    p.31.
2. Stanford, J.L.; Stepto, R.F.T., in "Elastomers and Rubber
    Elasticity"; Mark, J.E.; Lal, J., Eds.; ACS SYMPOSIUM SERIES
    No. 193, American Chemical Society: Washington D.C., 1982;
    Chap. 20.
3. Ahmed, Z.; Stepto, R.F.T. Polymer J. 1982, 14, 767.
4. Ahmad, Z.; Stepto, R.F.T. Colloid and Polymer Sci. 1980, 258,
    663.
5. Stepto, R.F.T., in "Developments in Polymerisation - 3";
    Haward, R.N., Ed.; Applied Science Publishers Ltd.: London,
    1982; Chap. 3.
6. Stepto, R.F.T.; Waywell, D.R. Makromol. Chem. 1972, 152, 247,
    263.
7. Stanford, J.L.; Stepto, R.F.T. Brit. Polymer J. 1977, 9, 124.
8. Ahmad, Z. Ph.D. Thesis, University of Manchester, England,
    1978.
9. Stepto, R.F.T. Polymer 1979, 20, 1324.
10. Hunt, N.G.K.; Stepto, R.F.T.; Still, R.H. Proc. 26th IUPAC
    Int. Symp. on Macromolecules, Mainz, 1979, p.697.

11. Cawse, J.L. Ph.D. Thesis, University of Manchester, England, 1979.
12. Fasina, A.B.; Stepto, R.F.T. Makromol.Chem., 1981, 182, 2479.
13. Stanford, J.L.; Stepto, R.F.T. J. Chem. Soc. Faraday Trans.I 1975, 71, 1292.
14. Frisch, H.L. 128th Meeting Amer. Chem. Soc., Polymer Div., Minneapolis, 1955.
15. Kilb, R.W. J. Physic. Chem. 1958, 62, 969.
16. Stepto, R.F.T. Faraday Disc. Chem. Soc. 1974,57, 69.
17. Stockmayer, W.H. J. Polymer Sci. 1952, 9, 69; 1953, 11, 424
18. Dusek, K.; Prins, W. Adv. Polymer Sci. 1969, 6, 1.
19. Flory, P.J. Polymer 1979, 20, 1317.
20. Mark, J.E. Pure and Applied Chem. 1981, 53, 1495.
21. Stanford, J.L.; Stepto R.F.T.; Waywell, D.R. J. Chem. Soc. Faraday Trans.I. 1975, 71,1308.
22. Askitopoulos, V. M.Sc. Thesis, University of Manchester, England, 1981.
23. Cawse, J.L.; Stanford, J.L.; Stepto, R.F.T. Proc. 26th IUPAC Int. Symp. on Macrmolecules, Mainz, 1979, p.393.
24. Lloyd, A.C. M.Sc. Dissertation, University of Manchester, England, 1981.
25. Gordon, M.; Temple, W.B. Makromol. Chem. 1972, 160, 263.

Computer Simulation of End-linked Elastomers
Sol–Gel Distributions at High Extents of Reaction

YU-KWAN LEUNG and B. E. EICHINGER

Department of Chemistry, University of Washington, Seattle, WA 98195

The end-linking of poly(dimethylsiloxane) with tri- and tetrafunctional cross-linkers in the bulk has been simulated on the computer. The algorithm places the molecules at random in an image container and then joins their ends together at junctions. The spanning forest for the constructed graph is then found, and the sol and gel components are identified. The results that are reported here include, amongst other things, the distribution of cyclic species in the sol and the proportion of defects in the gel.

In the traditional gelation theory formulated by Flory (1) and Stockmayer (2), it is assumed that like functional groups are equally reactive and all reactions occur intermolecularly before the gel point. Subsequently, beyond gelation, finite species formed in the sol portion are limited to acyclic trees. This is not correct because intramolecular reaction leading to the formation of ring structures in a random polycondensation must occur. The effect of cyclization has been treated by various approaches, e.g. Jacobson–Stockmayer ring-chain factors (3), cascade theory (4), and rate theory (5). Since the probability of ring structures increases with the extent of reaction, the sol must eventually contain significant amounts of cyclics. Neglect of intramolecular reactions, especially in the post-gel region, can yield distorted distributions of sol species and inaccurate gelation conditions. Since many of the present studies on cyclization are directed to the pre-gel stage of the reaction, little is known about the molecular constituents of the sol species and the gel structures in the later stages of the reaction. The importance of intramolecular reactions in random polymerization was extensively discussed by Stepto in a recent review article (6).

The complexity of the post-gel problem renders
theoretical treatment rather difficult, but computer
simulation offers an attractive means to obtain some
information on the distributions of interest. A random
stepwise polyreaction was simulated by Falk and Thomas (7) to
examine the polymer size distributions with and without
consideration of ring formation. Their system was composed
of monomeric units RA_f , which were represented by an array
of random numbers, and during the reaction process details of
connectivity were not recorded. Recently, a Monte Carlo
simulation of network formation has been reported by Mikeš
and Dušek (8), who assumed that the sol molecules in the
post-gel period were acyclic. In our model, the spatial
arrangement of reactive groups is taken into account and
molecules of different shapes are sorted and counted.
Simulations were done (9) for A_2 + B_f systems (10), allowing
ring formation in all species. Beyond the gel point, the
largest particle obtained is identified as the gel. The
distribution of other finite species and network
imperfections are analyzed and discussed.

ALGORITHM

A number N_p of primary molecules or prepolymers (A_2) having n
bonds were distributed randomly in a cubical box whose length
is L, where

$$L = \left[\frac{n M_o N_p}{\rho N_a} \right]^{1/3} \qquad [1]$$

M_o is the molecular weight of one bond unit, ρ is the density
of the polymer and N_a is Avogadro's number. End-to-end
distances of the primary molecules were generated as random
three-dimensional vectors with a Gaussian distribution
characterized by a one-dimensional variance, σ^2

$$\sigma^2 = C_x n l^2 /3 \qquad [2]$$

where l is the length of one bond and C_x is the
characteristic ratio (11). The N_c molecules of f-functional
cross-linkers were also randomly distributed in the reaction
cube, with the number of cross-linking agents determined from

$$N_c = 2r N_p /f \qquad [3]$$

where r is the stoichiometric ratio, defined as the ratio of
the number of B functional groups to the number of A
functional groups.
    The growth of polymeric molecules was accomplished by
joining the ends of the prepolymers with available B
functional groups in the nearby cross-linkers. Junctions
were formed by starting with the nearest neighbor and

proceeded in the order of increasing r_{AB}, the distance
between A and B functional groups. Reactive groups were not
allowed to form a bond if their distances r_{AB} were greater
than a set distance parameter. Hence, the distance parameter
controls the extent of reaction in the polymerization.

A vertex is defined as a condensed point of a graph,
which may be a free end, joint or cross-link; its degree is
the number of prepolymers attached to it. As each -AB- bond
was formed, the degree of the cross-linker involved increased
by one (maximum allowable number is f) and the end was
labelled 'reacted'. The indices of ends to which the
connections were made through the shared cross-linker, called
the connecting index, were recorded. The process of net-
formation was closely monitored by keeping track of the
degrees and the connecting indices of the visited ends.
Finally, the connected components were sorted out from the
large random graphs by using the spanning-tree program SPANFO
written by Nijenhuis and Wilf (12).

Schematic diagrams illustrating representative
structures are depicted in Figure 1. Beyond the gel point,
only one large particle was observed, which is consistent
with results obtained from other methods (8,13). The
remaining molecules are finite species whose molecular sizes
seldom exceed 20 prepolymer units. The smallest ring that
can be formed is the one-chain loop. Dangling ends of the
molecules can be identified as those vertices whose degree
equals one. The structures of sol molecules could be
recognized by referring to the set of the degrees assigned to
its vertices and the number of one-chain loops formed (10).

EFFECT OF FINITENESS

Computation were made for trifunctional and tetrafunctional
end-linked poly(dimethylsiloxane) systems (14,15). Values of
the parameters for PDMS are: M_0=37 g/mol, $\overline{C}_x$=6.3, l=1.64 Å
and ρ=0.97 g/cm^3 (11). Edge effects were investigated by
performing calculations on systems of different sizes. Table
1 shows the results for a series of simulation with f=4, n=50
and N_p=5000, 7500, 10000, 12500, 15000. The number of
configurations for each N_p were chosen such that the total
sample consisted of ca. 80000 functional groups. The values
of the sol fractions w_s and the cycle rank per chain ξ',
averaging over different N_p, were 0.0886 and 0.303
respectively, and the average extent of reaction of A
functional groups, P_A, was 0.806. Individual w_s and ξ'
showed no trend that could be attributed to an edge effect
except for the case of N_p=5000. Values for N_x and N', the
mole fractions of x-mer and that of the bow-tie trimer (see
figure 1) respectively, are also included in Table 1. Given
these results, it was concluded that 4 different

configurations of 10000 A_2 molecules each would constitute an
adequate representation of thermodynamically large system;
all subsequent results were obtained with simulations of this
size. For systems of this size, a comparison of the
concentrations of free ends in the core and in the rim of the
reaction box indicated that edge effects result in an
overestimation of the concentration of free ends by no more
than ca. 4%.

Table I. The Effect of Reaction Box Sizes for A_2 + B_4 System[a]

N_p	L,Å	P_A	w_s	N_1	N_2	N_3	N^{*}[b]	$\xi \cdot$[c]
5000	251	0.803	0.095	0.879	0.037	0.037	0.026	0.313
7500	288	0.807	0.086	0.891	0.032	0.039	0.025	0.309
10000	316	0.807	0.087	0.870	0.033	0.043	0.032	0.292
12500	341	0.810	0.086	0.880	0.034	0.045	0.034	0.308
15000	362	0.803	0.089	0.888	0.038	0.034	0.026	0.294

[a] MW=1850 and r=1.0
[b] mole fraction of bow-tie trimer
[c] cycle rank per chain of the interior gel

SOL FRACTIONS

Accurate prediction of the dependence of sol fraction on the
extent of reaction requires information on the proportion of
ring structures formed by intramolecular reactions. The
weight fractions w_s of soluble material that were generated
for a variety of runs for trifunctional networks are
presented in Table 2. For comparison, sol fractions w_s',
calculated by means of a recursive method (16) allowing only
treelike sol molecules are entered in column 5 of Table 2. It
can be seen that for low molecular weight prepolymers, the
inclusion of cyclics boosts the sol fraction by 2 to 3 % for
P_A over 0.80.
     Sol fractions are plotted against the extent of reaction
for the case of an A_2 + B_4 copolymerization in Figure 2. The
broken curves represent results obtained from our simulation
program whereas the result of the treelike model (16) is
indicated by the solid curve. It is noted that deviations
between the two models increase as chain length decreases and
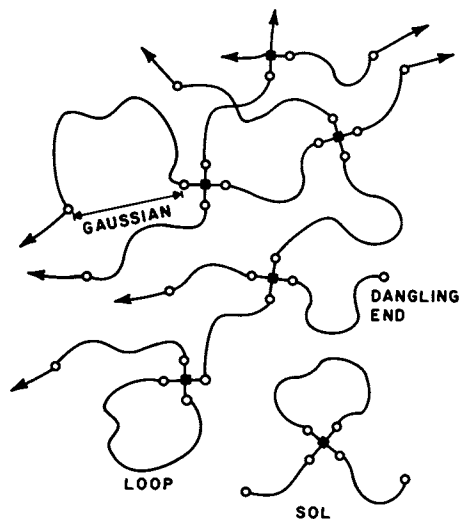as the extent of reaction increases.

Figure 1. Schematic diagram illustrating various structures in the post-gel stage of the reaction. The sol molecule drawn is a bow-tie trimer.
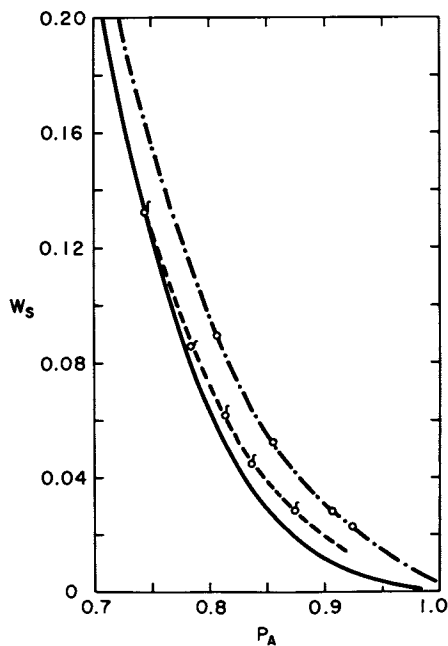

Figure 2. Variation of sol fraction with the extent of reaction for an $A_2 + B_4$ copolymerization: MW=1850 (circles) and 45000 (apples). Solid curve corresponds to results of the treelike model[16].

Table II. Sol Fractions for $A_2 + B_3$ System

MW	r	P_A	w_s	w_s' [a]
1850	1.0	0.809	0.172	0.152
		0.864	0.083	0.054
		0.897	0.051	0.022
		0.920	0.037	0.013
4700	1.0	0.883	0.051	0.036
		0.910	0.032	0.018
18500	1.0	0.851	0.069	0.070
		0.877	0.047	0.045
		0.897	0.033	0.024

[a] Ref. 16

CONSTITUENTS OF THE SOL

Figure 3 shows the histogram of the weight fraction of x-mers versus x for a trifunctional cross-linker at P_A=0.897. The prepolymer chosen has 50 Si-O bonds. The shaded bars represent weight fractions of molecular cyclics whereas the open bars indicate those of the treelike structures. For example, there are two types of dimer: the linear and the cyclic, where the latter has the shape of a tadpole. Our results show that the cyclics outnumber the linear by a ratio of 8:1. This is because the tadpole containing only one reactive group is a stable structure which has less chance to be absorbed by the gigantic gel particle. On the other hand, the branched trimer is predominant in the class of trimer. This can be understood to imply that the probability of double edge formation, which requires that the two chain vectors involved be located in the same volume element, is very small.

In Figure 4, the mole fractions of selected cyclic graphs, N_g, are plotted against P_A for different molecular weights of the prepolymer. The results for MW=1850, 4700, 18500 and 32900 are given by the *circles, triangles, squares* and *apples* respectively. As expected, the population of cyclics increases with higher degrees of conversion and shorter chain lengths.

Typical molecular weight distributions for the tetrafunctional system are depicted in Figure 5. In contrast to the monotonic w_x function predicted by the acyclic model (1), our findings show that the weight fractions have a maximum at the trimer. The high proportion of cyclic trimer,

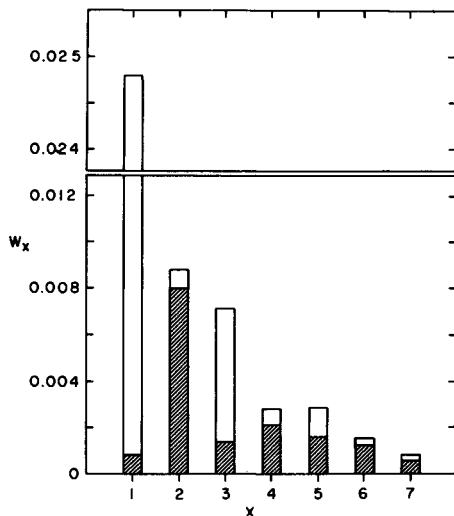Figure 3. Size distribution of the sol for the trifunctional system with n=50 and P_A=0.897. The shaded bars and the open bars represent weight fractions of cyclic and acyclic molecules respectively.
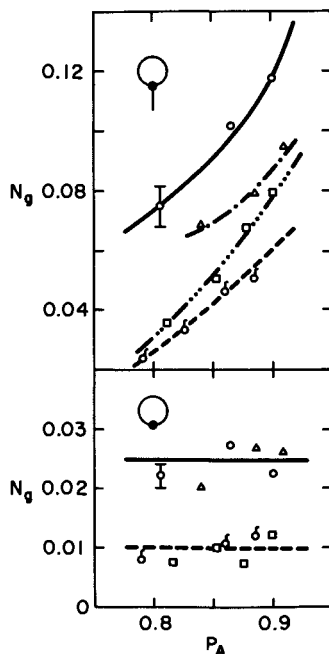

Figure 4. Dependence of the mole fraction of cyclics in the sol upon the extent of reaction for different molecular weights: MW=1850 (circles), 4700 (triangles), 18500 (squares) and 32900 (apples).

a 'bow-tie' graph consisting of one loop and two chains attached to a single junction, results from the favorable conversion of cyclic dimer (tadpole) to cyclic trimer due to the availability of an unreacted B functional group attached to the dimer. The population of tadpole trimer, resulting from the attachment of a third chain to the tail of the 'tadpole' dimer, is small because its formation requires another cross-linker, which is scarce at high conversion. It is evident that in the post-gel stage of the reaction, loop formation has a great influence on the pattern of molecular size distributions.

We have not considered the difference between the sol that might be extracted from a real network and that which is permanently incarcerated by virtue of its concatenation with the network. For more elaborate calculations, chain trajectories would be required to distinguish between molecules of these two types. For low molecular weights, e.g. n≈50, the proportion of incarcerated sol molecules should be small since the loops that are formed are too small to be wrapped around by another chain.

NETWORK IMPERFECTIONS

For trifunctional networks, three types of dangling ends were identified by the program. They are the dangling loop (see Figure 6), 'I' end and 'Y' end (see Figure 7). Symbols used in Figure 6 and 7 are the same as that of Figure 4. The population of dangling ends, η, is expressed in terms of the number of end configurations per number of prepolymers incorporated in the gel.

The populations of the 'I' and 'Y' free ends are independent of molecular weight, as illustrated in Figure 7. On the other hand, it can be seen in Figure 6 that the occurrence of one-chain loops in the network agrees with the trend shown by the sol cyclics as described in the previous section. The observed increase in one-chain loop probabilities with shorter chain lengths is consistent with the Gaussian statistics assumed by the molecules. Network imperfections do not vanish at complete conversion because of the loops. It is estimated by extrapolation that at 100% conversion, ca. 3% of the primary chains react to form loops for n=50.

The cycle rank of a network is defined as the number of cuts required to reduce the network to a tree (17). It is a structural factor characteristic of the perfection of a network (18); for a perfect network, the cycle rank per chain ξ' is given by $\xi'=1-2/f$. The ξ' values for various networks are listed in Table 3. The gels produced at very high extents of reaction still exhibit various kinds of structural imperfections: for example, the cycle rank of the

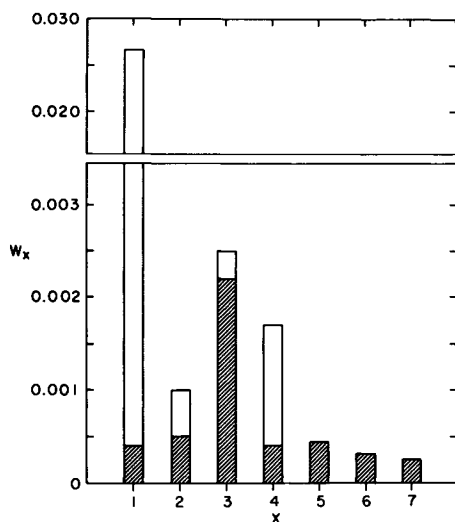**Figure 5. Histogram of the weight fractions of x-mer versus x for the tetrafunctional system with n=50 and P_A=0.886 (symbols same as in Figure 3).**
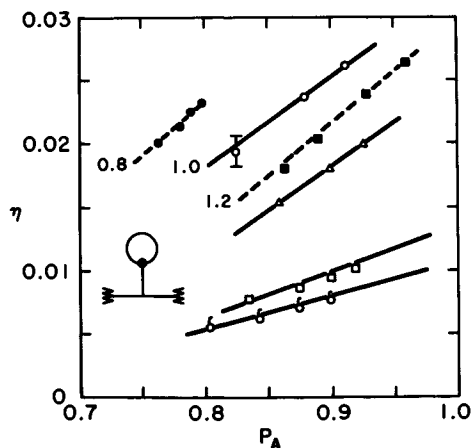

Figure 6. Plots of dangling end population versus the extent of reaction (symbols same as in Figure 4). Broken lines represent non-stoichiometric systems with r values indicated.

tetrafunctional network formed at complete conversion is
estimated to be 0.48, which is about 4% below the value 0.50
for the perfect network.

Table III. Cycle Rank per Chain ξ' for Various Networks

f	P_A				
	0.740	0.825	0.875	0.915	1.0^*
3	----	0.113	0.182	0.223	1/3
4	0.160	0.300	0.365	0.410	1/2

* Theoretical values for perfect networks

DEPEDENCE OF LOOP PROBABILITY ON CHAIN LENGTH

The weight fraction η_o of one-chain loops in the
polymerization system is defined as the percentage of primary
molecules whose ends are connected directly to each other.
The log-log plots of η_o vs. rms end-to-end distance $<r^2>_o^{1/2}$
of the primary chain at different functionalities and
conversions yield parellel straight lines. The average
least-squares slope of these lines is found to be -0.76,
which is taken to be -3/4 for subsequent calculations. The
standard deviation of the slope is 0.04. The relationship
between η_o and rms end-to-end distance is cast in Figure 8 as
a representation of the discovered relation

$$\eta_o = k(f-1)<r^2>_o^{-3/8} \; . \qquad [4]$$

The factor k is a function of the degree of conversion and
the concentration of functional groups. Our preliminary
study indicates that k is proportional to the extent of
reaction (19).

SUMMARY

Application of combinatorial algorithms to random stepwise
polymerization provides a basis for the understanding of the
effect of ring formation on network structures and sol
compositions. A substantial portion of the sol is cyclic.
Comparison with experimental data, such as ring fraction
measurements (20) or sol fraction analysis by GPC or HPLC,
could be useful to verify the findings obtained in these
computer simulation. The program can be easily adapted to
other polycondensation reactions, and to cover the entire
range of the polymerization process.

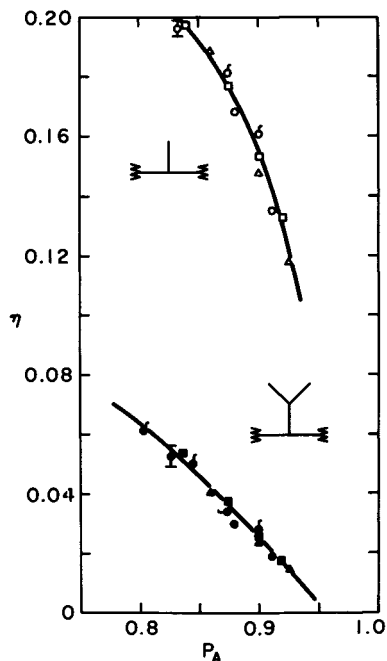**Figure 7.** Plots of η versus the extent of reaction for the 'I' and 'Y' free ends (symbols same as in Figure 4).
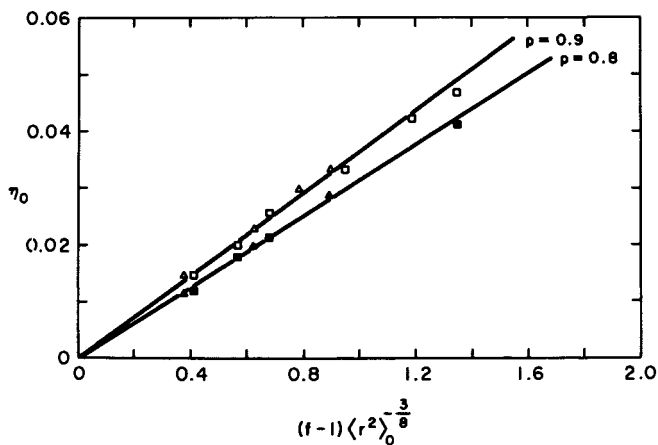

Figure 8. Plots of the weight fraction η_0 of one-chain loops versus $(f-1)\langle r^2 \rangle_0^{-3/8}$. The filled triangles and squares represent systems with f=3 and 4 respectively for P_A=0.8 whereas the open symbols represent similar quantities for P_A=0.9.

Literature Cited

(1) P. J. Flory, *Principles of Polymer Chemistry*,
     Cornell University Press, Ithaca, New York, 1953,
     Chpt. IX.
(2) W. H. Stockmayer, *J. Chem. Phys.*, 12, 125 (1944).
(3) H. Jacobson and W. H. Stockmayer, *J. Chem. Phys.*,
     18, 1600 (1950).
(4) M. Gordon and W. B. Temple, *Makromolek. Chem.*,
     160, 263 (1972).
(5) J. L. Stanford and R. F. T. Stepto,
     J. Chem. Soc. Faraday I, 71, 1292 (1975);
     J. L. Stanford, R. F. T. Stepto and D. R. Waywell,
     J. Chem. Soc. Faraday I, 71, 1308 (1975).
(6) R. F. T. Stepto, in *Developments in Polymerization-
     3*, Edited by R. N. Haward, Applied Science, Essex,
     England, Chpt. 3.
(7) Michael Falk and Ruth E. Thomas, *Can. J. Chem.*,
     52, 3285 (1974).
(8) Josef Mikeš and Karel Dušek, *Macromolecules*,
     15, 93 (1982).
(9) B. E. Eichinger, *J. Chem. Phys.*, 75, 1964 (1981);
     B. E. Eichinger and J. E. Martin, *J. Chem. Phys.*,
     69, 4595 (1978).
(10) Y. K. Leung and B. E. Eichinger, *Preprint, Div. of
     Polym. Mat.*, 48, 000, (1983).
(11) P. J. Flory, *Statistical Mechanics of Chain
     Molecules*, Interscience, New York, 1969.
(12) A. Nijenhuis and H. S. Wilf, *Combinatorial
     Algorithms*, Academic Press, New York, 1975,
     Chpt. 14.
(13) E. Donoghue, *J. Chem. Phys.*, 77, 4234 (1982);
     Edward Donoghue, *Macromolecules*, 15, 1634 (1982).
(14) J. E. Mark, R. R. Rahalkar and J. L. Sullivan,
     J. Chem. Phys., 70, 1794 (1979); J. E. Mark and
     J. L. Sullivan, *J. Chem. Phys.*, 66, 1006 (1977).
(15) M. Gottlieb, C. W. Macosko, G. S. Benjamin,
     K. O. Meyers and E. W. Merrill, *Macromolecules*,
     14, 1039 (1981).
(16) D. R. Miller and C. W. Macosko, *Macromolecules*,
     9, 206 (1976).
(17) F. Harary, *Graph Theory*, Addison-Wesley, Reading,
     Mass., 1969.
(18) P. J. Flory, *Proc. R. Soc. London, Ser. A*,
     351, 351 (1976).
(19) Yu-Kwan Leung and B. E. Eichinger, in
     preparation.
(20) J. L. Stanford and R. F. T. Stepto, *Br. Poly. J.*,
     9, 124 (1977).

Rheological Changes During the Copolymerization of Vinyl and Divinyl Monomers

D. T. LANDIN and C. W. MACOSKO

Department of Chemical Engineering and Materials Science, University of Minnesota, Minneapolis, MN 55455

Methyl methacrylate has been polymerized with small amounts of ethylene glycol dimethacrylate (0.5, 1.0, and 2.0 volume %) via a radical chain addition mechanism. Conversion, viscosity, and gel point data are presented. Branching theory based on the recursive nature of the branching process is developed to calculate M_w, the weight average molecular weight of the polymer, and $M_{L,w}$, the weight average molecular weight of the longest linear chain through a branched polymer molecule, taking into account the possibility of cyclization. It is found that the viscosity rise during the reaction correlates well to the parameter $cM_{L,w}$, where c is the concentration of polymer.

In recent years, Macosko and coworkers have carried out experimental studies on rheological property changes during network polymerization. Specifically they have measured viscosity change before the gel point of urethane (1) and silicone (2) systems, measured M_w on quenched systems (2,3), and have studied modulus, swelling, sol fraction, and stress strain behavior of silicone networks (4-7). These studies were motivated in part by the growing use of reactive polymer processing and more specifically by the development of reaction injection molding (RIM). Such studies provide the fundamental knowledge necessary to understand network formation and properties on the molecular level which in turn assist in the selection of optimum parameters for the processing operation.

Much less work has been done on relating rheological changes to structural changes during radical chain growth polymerization. Yet radical chain systems are widely used in reinforced plastics reaction molding. These systems are well suited for this use. The reactants have a low viscosity which allows good fiber wetting and packing, are low cost, and can be made to react very rapidly.

Some work has been done on relating rheological changes during the polymerization to conversion and time for chemical systems used industrially (8). Useful relationships based on empirical models have been obtained.

However, as in the stepwise network polymerization, it would be valuable to determine relationships between the molecular structure and rheological properties. The Flory-Stockmayer theory for the structural buildup in a network forming radical chain growth polymerization (9,10) predicts a conversion for gelation which is much less than that found experimentally (11). Analysis of experimental results has determined the cause of this deviation to be the formation of intramolecular crosslinks, i.e. cyclization (12).

Some attempts have been made to incorporate cyclization into branching theory (13,14). The difficulty here is that the nature of the cyclization is not well understood. A simple treatment of the problem might miss some of the physics of the phenomenon and a detailed treatment can be overburdened with the numerous cyclic possibilities leaving itself unusable in its complexity. In this paper, we incorporate a fairly simple treatment of cyclization into the branching theory we will use.

Once an adequate theory has been developed, structural parameters such as M_w and $M_{L,w}$, the weight average molecular weight of the longest linear chain through a branched molecule, can be predicted as a function of conversion or time during the course of the reaction. The next step in determining structure-property relationships is to correlate the experimental rheological properties to suitable structural parameters. It has been found that the viscosity in a network forming step polymerization correlates well to the parameter gM_w where g is the ratio of radii of gyration of branched to linear and also to the theoretical parameter $M_{L,w}$, the weight average molecular weight of the longest linear chain through a branched molecule (2). For a radical polymerization the same parameters should be useful but due to the nature of the reaction, polymer concentration, c, must also be included.

Of course, we would eventually like to be able to relate properties to structure directly by using a suitable dynamic theory of polymers. Reptation theory (15) is one which may be of great value for this purpose in the future.

Below we report a simple way to include cyclization in branching theory and some initial results for viscosity and conversion measurements on a nonlinear radical polymerization. We find a useful correlation between viscosity and $cM_{L,w}$.

Experimental

The chemical system studied was that of the network forming copolymerization of methyl methacrylate (Aldrich) with small amounts of ethylene glycol dimethacrylate (Monomer Polymer Laboratories). Four different ratios of EGDMA to MMA were investigated: 1) MMA

alone, 2) MMA with 0.5 vol. % EGDMA, 3) with 1.0 vol. %, and 4)
with 2.0 vol. % EGDMA.

The inhibitor in the MMA monomer was removed by two separate
washings using a 10% NaOH in water solution. The washed monomer
was stored over molecular sieves at 5-10°C until used. Ethylene
glycol dimethacrylate was not washed. The MMA and EGDMA were com-
bined in the desired proportions and 0.3 weight percent azobisiso-
butyronitrile (Kodak) was added as initiator. The reaction mix-
ture was divided into several 20 ml glass vials. Each vial was de-
gassed for two minutes by vacuum in combination with a sonic bath.
Then the vials were bubbled with nitrogen, sealed, and placed in a
water bath set at 70°C. At specified times, 2 vials were removed
from the bath and the reaction was quenched by quickly stirring in
0.03 gm of diphenylpicrylhydrazyl (Aldrich) and cooling the reac-
tion mixture. The crystals appeared to dissolve in less than one
second.

Conversion versus time was determined gravimetrically using
one vial from each pair. The polymer was precipitated in metha-
nol, vacuum dried, and weighed. The second vial was used to
obtain viscosity. A Deer Rheometer (16) cone and plate geometry
with a 65 mm diameter 0.0698 rad cone was used. A Rheometrics
System Four (17) in the fluids model (50 mm, 0.04 rad) was used in
later work.

Theory

Relations between conversion and molecular parameters in nonlinear
radical reactions have been developed by Macosko and Miller (18)
using the recursive nature of the branching process and elementary
laws of probability. One of the assumptions underlying this
theory is that of no intramolecular reaction, i.e. no cyclization.
As discussed previously, this is not valid for vinyl-divinyl co-
polymerization. A revision of this recursive theory to include
the effects of cyclization is necessary.

Using the same initial procedure as in (18), the vinyl-divinyl
copolymerization is thought of as:

$$A_4 + A_2 \longrightarrow \text{polymer}$$
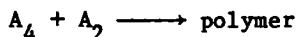
where A_4 is divinyl and A_2 is vinyl. A quantity q is defined as
the probability that an initiated radical chain will add one more
monomer unit and p is the conversion of vinyl groups. For a radi-
cal addition reaction, the value of q is normally in the range
0.99 to 0.999. The branched polymer can be pictured as
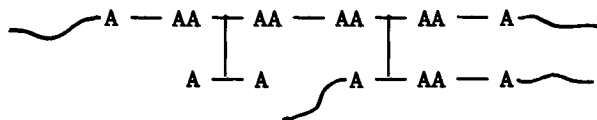
To begin the procedure, an A group on the polymer chain is selected at random and the expected weight attached to this A group looking out is sought. The expected weight looking out will be related to the expected weight looking in from the next A group. This expected weight looking in will depend on whether the A group belongs to an A_4 or A_2 unit and finally will be related to the expected weight looking out from the next A group. Here then is a recursion which can be simply written as

$$E(W_A^{out}) \longrightarrow E(W_A^{in}) \underset{E(W_{A_4}^{in})}{\overset{E(W_{A_2}^{in})}{<}} E(W_A^{out})$$
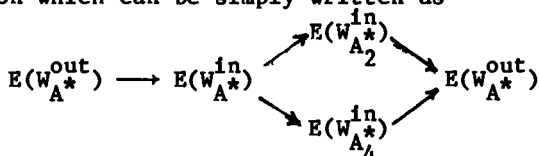
where $E(W_{A*}^{in \ or \ out})$ is the expected weight attached to an A unit which is part of a polymer chain.

Starting with $E(W_{A*}^{out})$, this will be equal to $E(W_{A*}^{in})$ multiplied by the probability that the A unit is not a chain end or

$$E(W_{A*}^{out}) = qE(W_{A*}^{in}) \tag{1}$$

$E(W_{A*}^{in})$ can be split into two parts:

$$E(W_{A*}^{in}) = (1-a_4)E(W_{A_2*}^{in}) + a_4 E(W_{A_4*}^{in}) \tag{2}$$

where a_4 is the proportion of vinyl groups which are on divinyl units. $E(W_{A_2*}^{in})$ will be equal to the weight of the monomer unit, M_{A_2}, plus $E(W_{A*}^{out})$ or

$$E(W_{A*}^{in}) = M_{A_2} + E(W_{A*}^{out}) \tag{3}$$

In order to evaluate $E(W_{A_4*}^{in})$, the possibility of cyclization must be considered. $E(W_{A_4*}^{in})$ can be written as:

$$E(W_{A_4*}^{in}) = E(W_{A_4*}^{in}|\text{no cyclization})P(\text{no cyclization})$$
$$+ E(W_{A_4*}^{in}|\text{cyclization})P(\text{cyclization}) \tag{4}$$

These can then be written as

$$E(W_{A_4*}^{in}|\text{no cyclization}) = M_{A_4} + (1 + 2p)E(W_{A*}^{out}) \tag{5}$$

$$E(W_{\substack{in \\ A_* \\ A_4}}|\text{cyclization}) = M_{A_4} + E(W_{A*}^{out}) \tag{6}$$

If s is defined as the probability that an A_4 unit does not cycle then substituting Equations 5 and 6 back into 4

$$E(W_{\substack{in \\ A_* \\ A_4}}) = M_{A_4} + (1 + 2ps)E(W_{A*}^{out}) \tag{7}$$

Using Equations 2, 3 and 7, Equation 1 can be written in terms of $E(W_{A*}^{out})$ or

$$E(W_{A*}^{out}) = \frac{q\left[(1 - a_4)M_{A_2} + a_4 M_{A_4}\right]}{1 - q\left[1 + 2a_4 ps\right]} \tag{8}$$

The weight average molecular weight, M_w, of the polymer is

$$M_w = W_{A_4}M_{A_4} + (1 - W_{A_4})M_{A_2} + 2(1 + W_{A_4}p)E(W_{A*}^{out}) \tag{9}$$

where W_{A_4} is the weight fraction of polymeric species consisting of divinyl units. The effect of cyclization on the molecular weight can be seen in Figure 1.

Since the expected weight goes to infinity at the gel point, Equation 8 can be used to predict gel point conversion, P_{gel}. At the gel point,

$$P_{gel} = \frac{1 - q}{2a_4 qs} \tag{10}$$

$\underline{M_{L,w}}$

This recursive approach can also be used to calculate the weight average of the longest linear chain through a branched molecule, $M_{L,w}$. $M_{L,w}$ will be indicative of the effective length of the molecule. This is an important quantity for properties which depend on contact between polymer coils. To calculate $M_{L,w}$ an A group on the polymer chain is picked at random and we look out of it in all directions seeking the longest chain. The length of the longest chain looking out from one end of a randomly chosen A is designated L_A^{out} and the length of the longest chain looking in L_A^{in}. If the A group has been initiated or reacted it is said to be activated and is represented by A^*. In Equation 11 we see that

$$--- A \xrightarrow[\substack{(1) \\ out}]{\substack{in \\ (2)}} A ---AA---AA---A \tag{11}$$
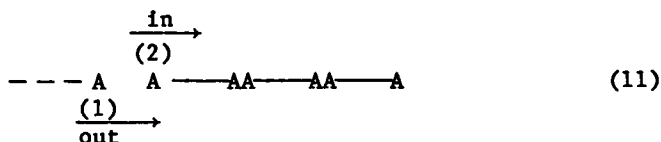
L_{A*}^{out} for A designated (1) will be equal to three as will L_{A*}^{in} for the A designated (2). An activated A may terminate with probability 1-q so the probability that L_{A*}^{out} is greater than a certain length ℓ is (where ℓ is an integer number of monomer units, either A_2 or A_4)

$$P(L_{A*}^{out} > \ell) = qP(L_{A*}^{in} > \ell) \quad . \tag{12}$$

L_{A*}^{in} will be equal to the weighted probabilities of $L_{A_2*}^{in}$ and $L_{A_4*}^{in} < \ell$ or

$$P(L_{A*}^{in} < \ell) = (1 - a_4)P(L_{A_2*}^{in} < \ell) + a_4 P(L_{A_4*}^{in} < \ell) \tag{13}$$

If an A_4 does not cycle (which has probability s), a randomly chosen A on an A_4^* will have three possibilities for the longest chain when looking in as seen in Equation 14.

$$
\begin{array}{c}
\xrightarrow{\text{in}} \\
A^* \rule{2cm}{0.4pt} A^* \rule{1cm}{0.4pt} \\
\big| \\
A \rule{2cm}{0.4pt} A
\end{array}
\tag{14}
$$

Therefore,

$$P(L_{A_4*}^{in} < \ell) = P(L_{A*}^{out} < \ell-1)\left[P(L_A^{out} < \ell-1)\right]^2$$

$$= P(L_{A*}^{out} < \ell-1)\left\{pP(L_{A*}^{out} < \ell-1)^2 + (1-p)P(L_A^{out} < \ell-1)^2\right\}$$

$$= 0 \qquad \qquad \text{if } \ell = 0 \tag{15}$$

$$= (1-q)\left\{p(1-q)^2 + (1-p)\right\} \qquad \text{if } \ell = 1$$

$$= pP(L_{A*}^{out} < \ell-1)^3 + (1-p)P(L_{A*}^{out} < \ell-1) \qquad \text{if } \ell > 1$$

If an A_4 does cycle (probability 1-s), a randomly chosen A on an A_4^* will have only one possibility for the longest chain when looking in as seen in Equation 16.

$$
\left.
\begin{array}{c}
\xrightarrow{\text{in}} \\
A^* \rule{1.5cm}{0.4pt} A \\
\big| \\
{}^*A \rule{1.5cm}{0.4pt} A
\end{array}
\right)
\tag{16}
$$

Then,

$$P(L_{A_4^*}^{in} < \ell) \quad \begin{array}{ll} = 0 & \text{if } \ell = 0 \\ = P(L_A^{out} < \ell-1) & \text{if } \ell > 1 \end{array} \qquad (17)$$

Combining Equations 15 and 17 multiplied by their respective probabilities gives for $P(L_{A_4^*}^{in} < \ell)$ of any A on an A_4^* as

$$P(L_{A_4^*}^{in} < \ell) = P(L_{A^*}^{out} < \ell-1)\{1-sp[1 - P(L_{A^*}^{out})^2]\} \qquad (18)$$

As in the case of a cyclized A_4, a randomly chosen A on an A_2 will have only one possibility for the longest chain when looking in so

$$P(L_{A_2^*}^{in} < \ell) = 0 \quad \begin{array}{ll} & \text{if } \ell = 0 \\ = P(L_{A^*}^{out} < \ell-1) & \text{if } \ell > 1 \end{array} \qquad (19)$$

Substituting these results back into Equation 12 gives

$$P(L_{A^*}^{out}) < \ell) = 1 - q+q\{P(L_{A^*}^{out} < \ell-1)[1 - a_4 sp(1 - P(L_{A^*}^{out} < \ell-1)^2]\} \qquad (20)$$

Starting with $P(L_{A^*}^{out} < 0) = 1 - q$, Equation 20 can be used recursively to calculate $P(L_{A^*}^{out} < \ell)$ for $\ell = 1,2,3,\ldots$. We know from probability that

$$P(L_{A^*}^{out} > \ell) = 1 - P(L_{A^*}^{out} < \ell) \qquad (21)$$

with this, the expected length of the longest linear chain can be calculated with the relation (19)

$$E(L_{A^*}^{out}) = \sum_{\ell=0}^{\infty} P(L_{A^*}^{out} > \ell) \qquad (22)$$

Then the weight average molecular weight of the longest linear chain will be

$$M_{L,w} = 2E(L_{A^*}^{out})M_A \qquad (23)$$

Figure 2 shows $M_{L,w}$ and M_w as a function of conversion for a polymerization with no cyclization (s = 1). As expected, $M_{L,w}$ and M_w have the same value in the limit of zero conversion and go to infinity at the gel point with $M_{L,w}$ less than M_w between these two points.
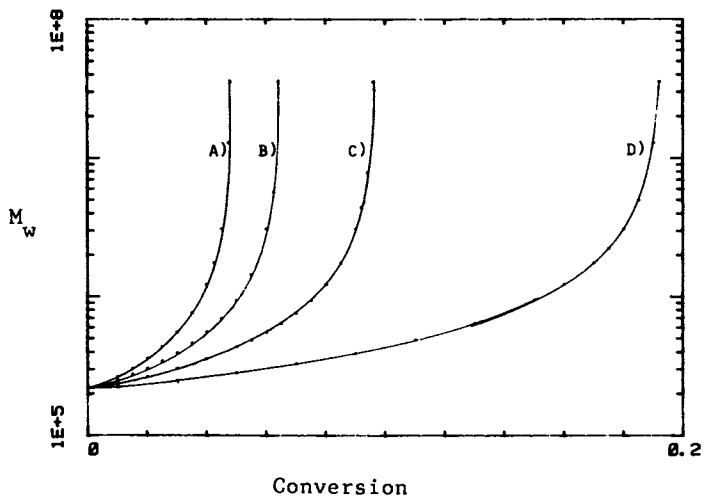
Figure 1. M_w vs. conversion for 0.5% divinyl, q = 0.999, A) s = 1, B) s = 0.75, C) s = 0.50, and D) s = 0.25.
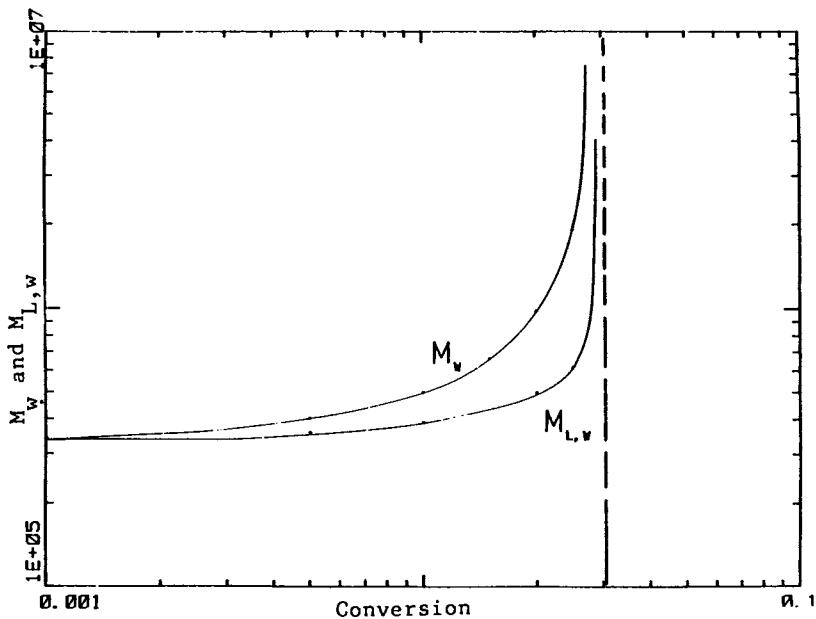

Figure 2. M_w and $M_{L,w}$ vs. conversion for 0.5% divinyl, q = 0.999, s = 1.

Results and Discussion

The experimental conversion and viscosity are shown in Table I. Gel point conversions were determined by plotting $\eta^{-1/2}$ vs. conversion and taking as the critical conversion that value where the line crossed the conversion axis.

Using the critical conversion and Equation 10, values for the parameter s have been calculated and are listed in Table II. This value of s is a cumulative average value over the entire conversion interval from zero to gelation. At the very beginning of the reaction, the polymer chains are infinitely diluted by monomer which causes the probability of a radical on one chain attacking a pendant vinyl on another to approach zero. Therefore, in the limit of zero conversion, the instantaneous value of s will be zero. As the reaction progresses, the polymer concentration increases and with it the probability of intermolecular contact and reaction. The instantaneous value of the parameter s will therefore rise and continue to rise up to the gel point qualitatively as shown in Figure 3.

As shown in Table II, the cumulative value of s decreases with increasing divinyl content which indicates an increasing tendency to form cycles. It is interesting to note that if the average value of s is considered as the ratio of the rate of propagation to the rate of propagation plus the rate of cyclization, the rate of cyclization is found to be linearly dependent on divinyl concentration in the limited divinyl range investigated (0.5-2.0%) as shown in Figure 4.

Using the average value of s, M_w and $M_{L,w}$ of the polymerizing samples can be calculated at any conversion. Once these structural parameters are known, we can attempt to correlate viscosity to structure. One way to treat the viscosity rise of a linear polymerization is to correlate it to the segment contact parameter cM_w where c is the concentration of polymer or since concentration is approximately proportional to conversion, the contact parameter can be rewritten as pM_w where p is the conversion.

A plot of viscosity vs. the contact parameter pM_w is shown in Figure 5. As would be expected, branched polymer has a lower viscosity than linear polymer of equal M_w. The parameter pM_w does not provide a good correlation for the viscosity rise during a branching polymerization. The parameter $pM_{L,w}$, however, does provide a good correlation for the viscosity rise as shown in Figure 6. The data for the three different systems fall onto one curve.

The usefulness of this correlation is that $pM_{L,w}$ is determined theoretically using well documented kinetic data and does not have to be found experimentally. Then, polymerization conditions can be changed, i.e. temperature, initiator concentration, etc., and yet with a few simple calculations, $pM_{L,w}$ can be calculated and the viscosity rise predicted.

The curve in Figure 6 shows the expected break point in slope believed to be due to the onset of entanglement. For undiluted

Table I. Experimental Conversion
and Viscosity

% DIVINYL	TIME(MIN)	CONVERSION	VISCOSITY(cP)
0.0	7.5	0.039	6.6
0.0	15.0	0.089	23.0
0.0	22.5	0.151	250.0
0.0	30.0	0.212	3200.0
0.5	5.0	0.025	4.8
0.5	10.0	0.058	11.0
0.5	15.0	0.090	43.0
0.5	20.0	0.135	620.0
1.0	5.0	0.023	4.5
1.0	10.0	0.058	12.0
1.0	15.0	0.096	180.0
2.0	4.0	0.026	3.4
2.0	7.0	0.047	7.0
2.0	9.0	0.064	16.5
2.0	11.0	0.074	59.0

Table II. Values for Parameter S

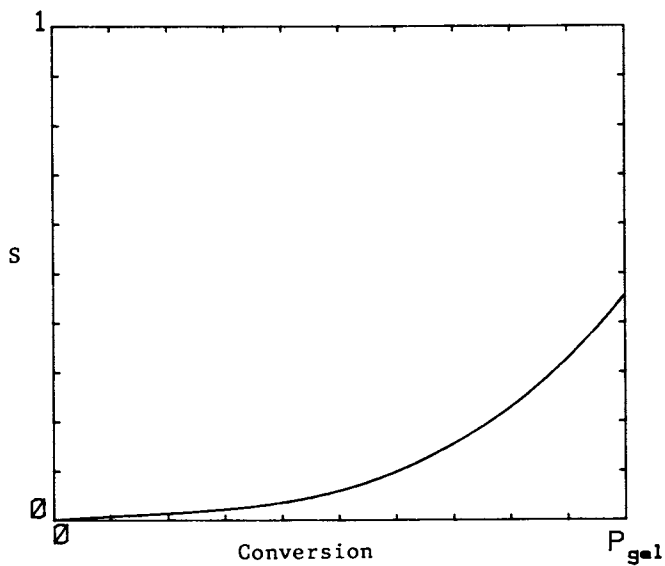| % DIVINYL	P_{GEL}	S
0.5	0.139	0.349
1.0	0.110	0.220
2.0	0.091	0.135

Figure 3. Qualitative trend of parameter s up to the gel point.
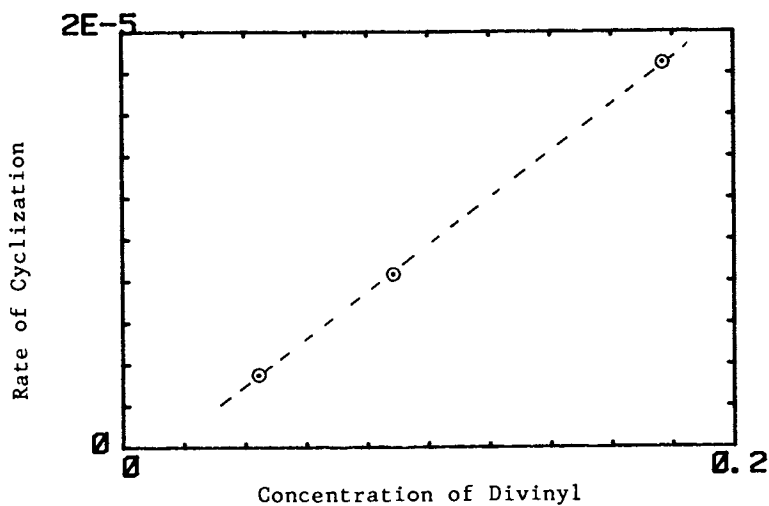

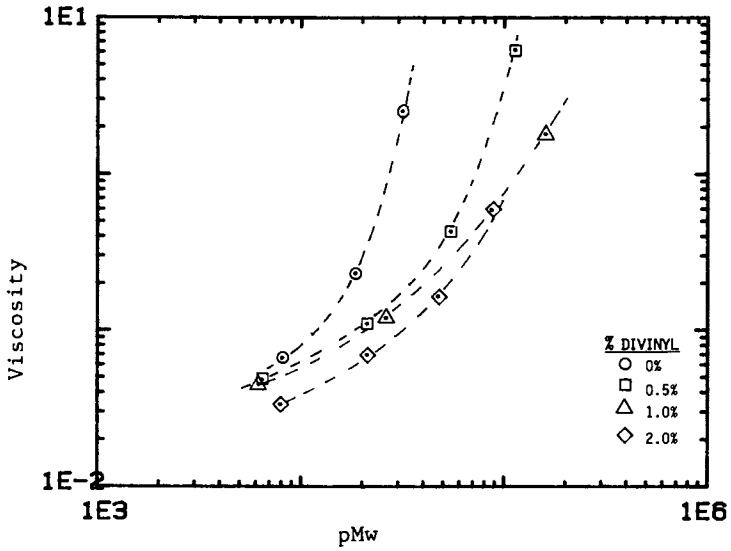**Figure 4.** Cumulative rate of cyclization vs. initial concentration of EGDMA.
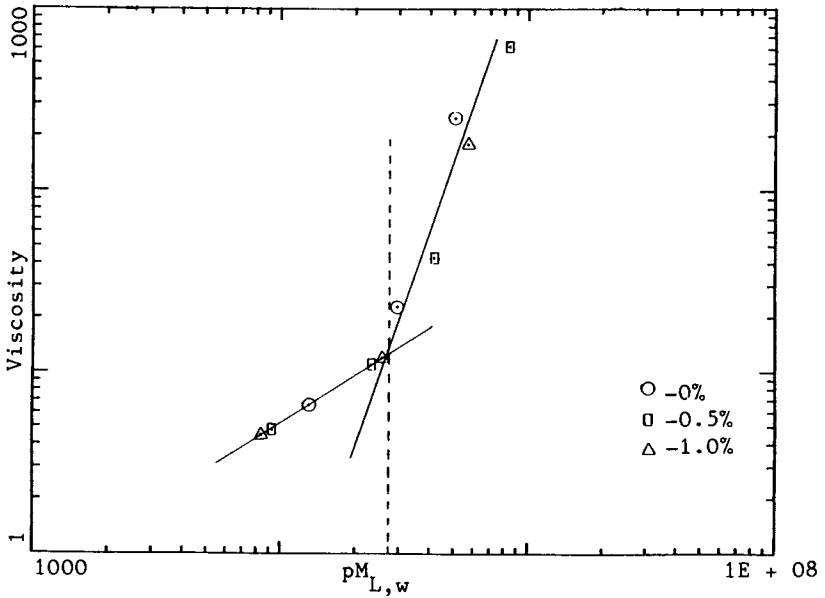
Figure 5.   Viscosity vs. pM_w.

Figure 6.   Viscosity vs. $pM_{L,w}$.

MMA, the critical M_c for this to occur is 2.75×10^4 (21). Then the critical cM for MMA in solution will be

$$(cM)_{soln.} = \rho M_c \qquad (24)$$

where ρ is density. The numerical value for $(cM)_{soln.}$ is 3.3×10^4. Using conversion the critical value for $(\rho M)_{soln.}$ becomes 2.75×10^4 which agrees quite well with what is seen in Figure 6.

This theoretical prediction of the viscosity rise still depends on knowing an experimental parameter s, the cumulative probability of forming crosslinks up to the gel point, for the particular reaction conditions. Of course, it is desirable to be able to predict this theoretically. To do this, we will need a better understanding of both crosslinking and cyclization. Due to the nature of the radical addition polymerization, crosslinking is concentration dependent. So as the concentration is continuously changing during the reaction, the amount of crosslinking also changes. Cyclization is probably not burdened with this concentration dependence but due to the difficulty of actually detecting these cycles, they are still just assumed phenomenon.

Acknowledgments

Literature Cited

1. Lipshitz, S. D.; Macosko, C. W. Polym. Eng. Sci. 1976, 16, 803.
2. Valles, E. M.; Macosko, C. W. Macromolecules 1979, 12, 521.
3. Hickey, W. J.; Macosko, C. W. ACS Polymer Preprints 1981, 22, No. 2, 579; Hickey, W. J. M.S. Thesis, University of Minnesota 1980.
4. Valles, E. M.; Macosko, C. W. Macromolecules 1979, 12.
5. Macosko, C. W.; Benjamin, G. S. Pure Appl. Chem. 1981, 53, 1505.
6. Gottlieb, M; Macosko, C. W.; Lepsch, T. C. Polym. Phys. Ed. 1981, 19, 1603-1067; reprinted in Rubber Chem. & Techn. 1982, 55, 1108.
7. Gottlieb, M; Macosko, C. W.; Benjamin, G. S., Meyers, K. A.; Merrill, E. W. Macromolecules 1981, 14, 1039; portions in Polymer Preprints 1981, 22, No. 2, 155.
8. Gonzalez, V. M. Ph.D. Thesis, University of Minnesota 1983.
9. Flory, P. J. "Principles of Polymer Chemistry"; Cornell University Press, Ithaca 1953.
10. Stockmayer, W. H. J. Chem. Phys. 1943, 11, 45.
11. Walling, C. J. Am. Chem. Soc. 1945, 67, 441.

12. Dusek, K.; Galina, H.; Mikes, J. Polymer Bulletin 1980, 3, 19.
13. Gordon, M.; Roe, R.-J. J. Polymer Sci. 1956, 21, 75.
14. Dusek, K.; Ilavsky, M. J. Polymer Sci., 1975, Symposium No. 53, 57.
15. de Gennes, P. G. J. Chem. Phys. 1971, 55, 572.
16. Deer Rheometers, Rheometer Marketing Limited, Leeds LS122EJ, England.
17. Starita, J. M. in "Rheology" Vol. 2, Astarita, G.; Marucci, G.; Nicolais, L., Eds.; Plenum, New York, 1980, p. 229. Rheometrics Inc., Union NJ.
18. Macosko, C. W.; Miller, D. R. Macromolecules 1976, 9, 199.
19. Miller, D. R.; Valles, E. M.; Macosko, C. W. Polym. Eng. and Sci. 1979, 19, 272.
20. Gordon, M.; Ward, T. C.; Whitney, R. S., "Polymer Networks"; Chompf, A. J.; Newman, S., Eds.; Plenum Press, 1971.
21. Ferry, J. D., "Viscoelastic Properties of Polymers"; 2nd ed., Wiley, New York, 1970.

Elastomeric Poly(dimethylsiloxane) Networks with Numerous Short-Chain Segments

J. E. MARK

Department of Chemistry and Polymer Research Center, The University of Cincinnati, Cincinnati, OH 45221

J. G. CURRO

Physical Properties of Polymers Division, Sandia National Laboratories, Albuquerque, NM 87185

End-linking techniques may be used to prepare (unfilled) elastomeric networks of poly-dimethylsiloxane) (PDMS) $[Si(CH_3)_2O-]$ which contain a large mol fraction of unusually short chains along with chains of the lengths usually associated with rubberlike materials. Such bimodal networks frequently have very attractive mechanical properties, in particular high extensibility at relatively high average degrees of cross-linking, and thus are unusually tough elastomers. Measurements of stress-strain isotherms over a wide range in temperature and degree of swelling, stress-temperature coefficients, and birefringence-temperature coefficients indicate the improvements in properties to be intramolecular, specifically non-Gaussian effects related to limited chain extensibility. These effects are explored using a theory of rubberlike elasticity based on network distribution functions generated from the rotational isomeric state model for PDMS chains.

Elastomeric networks of known structure may be prepared by the end-linking of functionally terminated chain molecules ([1-6]) rather than by the usual random procedure ([7-8]) of linking chains through repeat units with arbitrary locations within the chain structures. These highly specific chemical reactions can thus be used to provide networks of any desired molecular weight M_c between cross-links, by simply end-linking such chains having number-average molecular weights M_n equal to M_c.

A network obtained in this manner, of course, has a network chain length <u>distribution</u> which is also the same as that of the polymer from which it was prepared. The technique thus permits the preparation of elastomeric materials having distributions which are multimodal (e.g. bimodal) as well as the usual unimodal type (<u>7,8</u>).

Recently, particular interest has focused on bimodal poly(dimethylsiloxane) (PDMS) networks (<u>9-17</u>) containing large mol fractions of very short chains as well as chains of the usual lengths required for rubberlike elasticity (<u>7,8,18</u>). Typical values of M_n are a few hundred g mol^{-1} and 18,000 g mol^{-1}, respectively. The interest is due to the fact that these elastomers, in the unfilled state, frequently have excellent mechanical properties. Their relatively high values of both the maximum extensibility and ultimate strength combine to yield large values of the energy required for rupture; i.e., such bimodal networks are unusually "tough" elastomers. The most interesting aspect of this toughening effect from the fundamental point of view is the very large increase in modulus which can occur at high extensions (<u>9-17</u>). A variety of studies (<u>16</u>) demonstrated that this non-Gaussian effect shown by the bimodal PDMS networks could properly be attributed to limited chain extensibility. The results included stress-strain isotherms over a wide range in temperature, stress-temperature coefficients, and birefringence-temperature coefficients. The molecular origin of the non-Gaussian effect having been established, it becomes important to develop a molecular theory for its elucidation.

Non-Gaussian theories of rubberlike elasticity currently available (<u>8,19,20</u>) generally have the disadvantage of containing parameters which can be determined only by comparisons between theory and experiment. The approach taken in the present investigation avoids this shortcoming by utilizing the wealth of information which rotational isomeric state theory provides on the spatial configurations of chain molecules (<u>21</u>), including most of those used in elastomeric networks. Specifically, Monte Carlo calculations (<u>22-24</u>) based on the rotational isomeric state approximation (<u>21</u>) are used to simulate spatial configurations, and thus distribution functions for the end-to-end separation r of the network chains. These distribution functions may be used in place of the Gaussian function to give a molecular theory of rubberlike elasticity which is unique to the particular polymer of interest, and applicable to the regions of very large deformation, where the bimodal networks exhibit their highly unusual properties.

Short-Chain Unimodal PDMS Networks

Information on the conformational preferences of the PDMS chain

was obtained from previous experimental and theoretical investigations (21,25). The Monte Carlo method was used in conjunction with this information to generate large numbers of typical spatial configurations, at $110°C$ (23), for chains having a specified number n of skeletal bonds (18,22-24). The configurations were grouped according to their values of the end-to-end separation r, and the results curve-fitted using a cubic-spline least-squares technique (26). The distribution function thus obtained was then used in the standard "three-chain" model approach (8) to rubberlike elasticity, in order to estimate the entropy of deformation in the affine limit, and from that the nominal stress $f^* \equiv f/A^*$ (where A^* is the undeformed cross-sectional area). The resulting values of f^* were normalized by νkT, where ν is the number density of network chains, k is the Boltzmann constant, and T is the absolute temperature.

Figure 1 presents the results for the illustrative cases n = 20 and 40 skeletal bonds, as a function of the elongation $\alpha = L/L_i$, where L and L_i are the stretched and unstretched sample lengths, respectively. An alternative representation of the same results is in terms of the reduced stress or modulus defined by (27,28)

$$\left[f^*\right] \equiv f/\left[A^*(\alpha - \alpha^{-2})\right] \qquad (1)$$

These results are typically plotted against reciprocal elongation, as suggested by the semiempirical equation of Mooney and Rivlin (8,28-30)

$$\left[f^*\right] = 2C_1 + 2C_2\alpha^{-1} \qquad (2)$$

in which $2C_1$ and $2C_2$ are constants independent of α. Such a plot of these theoretical results is shown in Figure 2. The curves in this figure are quite similar to experimentally obtained results on PDMS networks, as is illustrated by some of the curves in Figure 3(12). The curves in these figures show upturns in the stress and modulus as the elongation increases. The upturns are due to the rapidly diminishing number of configurations consistent with the required large values of r, and thus, correspondingly large decreases in the entropy of the network chains, and increases in f^* and $\left[f^*\right]$.

Bimodal PDMS Networks

The long and short chains in the bimodal PDMS networks were assumed to have values of n of 20 and 250, respectively (9-16). The long chains were modeled as Gaussian chains, whereas the distribution function for the short chains was determined from Monte Carlo calculations as already described. The entropy of the bimodal network was then taken to be the sum of
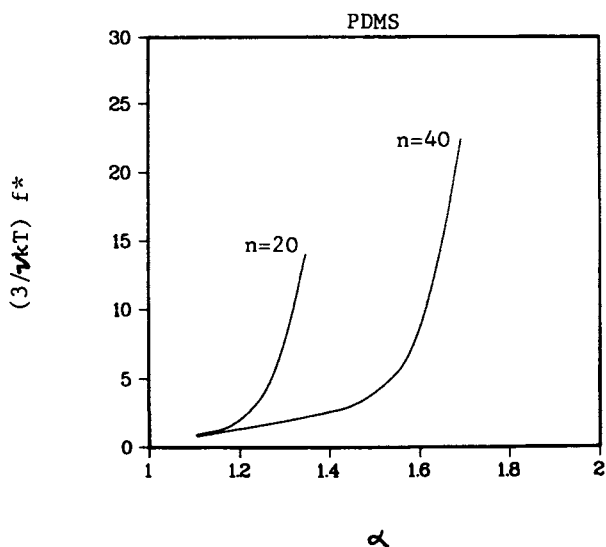
Figure 1. Theoretical curves of stress against strain for unimodal PDMS networks consisting of chains with 20 and 40 skeletal bonds, respectively.
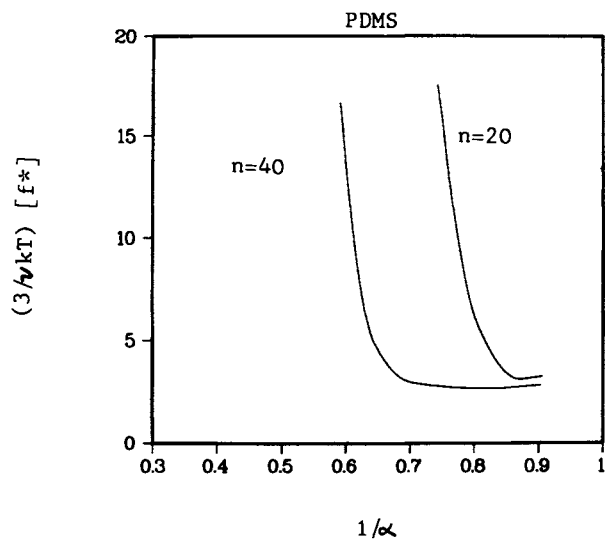
Figure 2. The results of Figure 1 represented as suggested by the semi-empirical Mooney-Rivlin relationship (8,28-30) which usually gives a modulus [f*] decreasing linearly with decreasing α^{-1} (28).
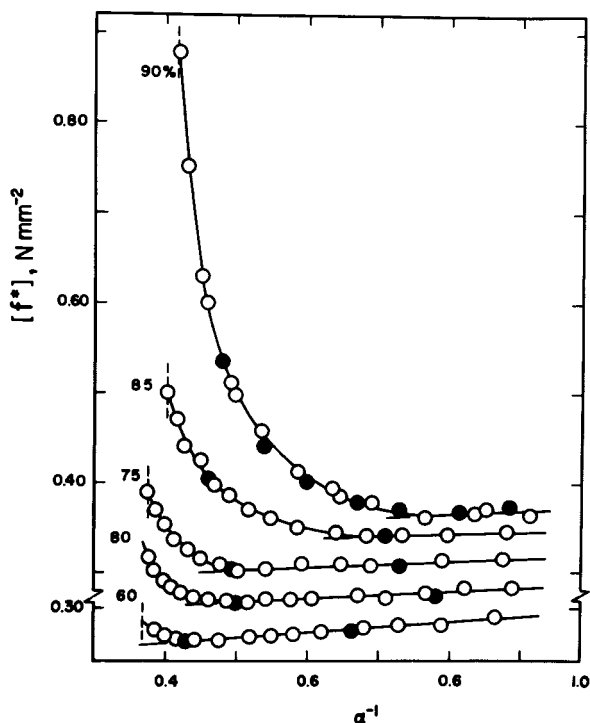
Figure 3. Some typical stress-strain isotherms experimentally obtained on bimodal PDMS networks consisting of very short and relatively long chains having molecular weights of 220 and 18,500 g mol^{-1}, respectively (12). The mol % of short chains is used to label each isotherm, and the filled circles locate results obtained out of sequence to test for reversibility.

contributions from ν_L long chains and ν_S short chains per unit volume,

$$\Delta S = \Delta S_L + \Delta S_S \tag{3}$$

In order to couple the local deformation to the macroscopic deformation we make the preliminary but crude assumption that the average deformation is affine. This implies that

$$\alpha = X_L\alpha_L + X_S\alpha_S \tag{4}$$

where X_L and X_S are the mol fractions of long and short chains, respectively. The deformation is then partitioned non-affinely between the long and short chains in order to maximize the entropy of the network.

Some typical results are presented in Figure 4. It can be seen that the theoretical curves show increased steepness at high elongation as the fraction of short chains is increased, in agreement with experimental observations (12,14). The position of the upturn, however, does not appreciably change with composition as it does in the experimental curves. This difference is almost certainly due to the affine (average) deformation assumption made in the present theory. It may be possible to refine the theory to take approximate account of the nonaffineness of the elastic deformation, which becomes particularly important in the region of very high elongations (31-33).

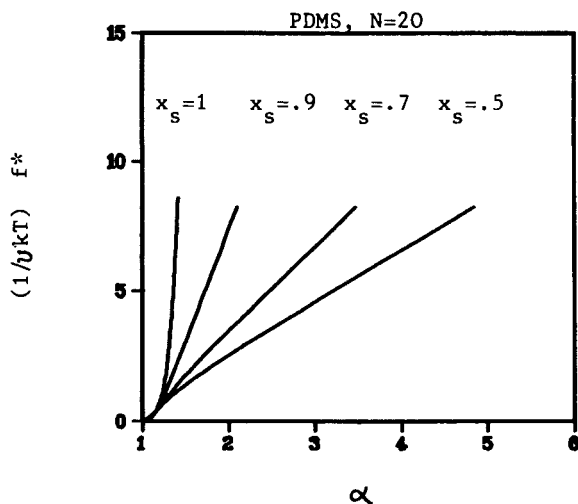Figure 4. Theoretical curves of stress against strain for bimodal PDMS networks consisting of long PDMS chains (n = 250 skeletal bonds), and very short chains (n = 20) present to the extent of the values of the volume fraction X_s specified for each curve.

Acknowledgments

Literature Cited

1.   J. E. Mark and J. L. Sullivan, J. Chem. Phys., **66**, 1006 (1977).
2.   J. E. Mark, Makromol. Chem., **Suppl. 2**, 87 (1979).
3.   J. E. Mark and M. A. Llorente, J. Am. Chem. Soc., **102**, 632 (1980).
4.   A. L. Andrady, M. A. Llorente, M. A. Sharaf, R. R. Rahalkar, J. E. Mark, J. L. Sullivan, C. U. Yu, and J. R. Falender, J. Appl. Polym. Sci., **26**, 1829 (1981).
5.   J. E. Mark, Pure Appl. Chem., **53**, 1495 (1981).
6.   J. E. Mark, Rubber Chem. Technol., **54**, 809 (1981).
7.   P. J. Flory, "Principles of Polymer Chemistry", Cornell University Press, Ithaca, N.Y., 1953, ch. XI.
8.   L. R. G. Treloar, "The Physics of Rubber Elasticity", 3rd Ed., Clarendon Press, Oxford, 1975.
9.   A. L. Andrady, M. A. Llorente, and J. E. Mark, J. Chem. Phys., **72**, 2282 (1980).
10.   A. L. Andrady, M. A. Llorente, and J. E. Mark, J. Chem. Phys., **73**, 1439 (1980).
11.   J. E. Mark and A. L. Andrady, Rubber Chem. Technol., **54**, 366 (1981).
12.   M. A. Llorente, A. L. Andrady, and J. E. Mark, J. Polym. Sci., Polym. Phys. Ed., **19**, 621 (1981).
13.   M. A. Llorente, A. L. Andrady, and J. E. Mark, Colloid and Polym. Sci., **259**, 1056 (1981).
14.   J. E. Mark, Adv. Polym. Sci., **44**, 1 (1982).
15.   J. E. Mark, in "Elastomers and Rubber Elasticity", ed. by J. E. Mark and J. Lal, American Chemical Society, Washington, D.C., 1982.
16.   Z.-M. Zhang and J. E. Mark, J. Polym. Sci., Polym. Phys. Ed., **20**, 473 (1982).
17.   S.-J. Pan and J. E. Mark, Polym. Bulletin, **7**, 553 (1982).
18.   J. E. Mark, J. Chem. Educ., **58**, 898 (1981).
19.   K. J. Smith, Jr., J. Polym. Sci., A-2, **9**, 2119 (1971).
20.   J. Kovac and C. C. Crabb, Macromolecules, **15**, 537 (1982).
21.   P. J. Flory, "Statistical Mechanics of Chain Molecules", Interscience, New York, 1969.

22. D. Y. Yoon and P. J. Flory, <u>J. Chem. Phys.</u>, **61**, 5366 (1974).
23. P. J. Flory and V. W. C. Chang, <u>Macromolecules</u>, **9**, 33 (1976).
24. J. C. Conrad and P. J. Flory, <u>Macromolecules</u>, **9**, 41 (1976).
25. P. J. Flory, V. Crescenzi, and J. E. Mark, <u>J. Am. Chem. Soc.</u>, **86**, 146 (1964).
26. C. H. Reinsch, <u>Numerishe Mathematik</u>, **10**, 177 (1967).
27. J. E. Mark and P. J. Flory, <u>J. Appl. Phys.</u>, **37**, 4635 (1966).
28. J. E. Mark, <u>Rubber Chem. Technol.</u>, **48**, 495 (1975).
29. M. Mooney, <u>J. Appl. Phys.</u>, **19**, 434 (1948).
30. R. S. Rivlin, <u>Phil. Trans. R. Soc. London</u>, <u>Ser. A</u>, **241**, 379 (1948).
31. G. Ronca and G. Allegra, <u>J. Chem. Phys.</u>, **63**, 4990 (1975).
32. P. J. Flory, <u>Proc. R. Soc. London</u>, <u>Ser. A</u>, **351**, 351 (1976).
33. P. J. Flory and B. Erman, <u>Macromolecules</u>, **15**, 800 (1982).

Light Scattering of Randomly Cross-linked Polystyrene

KANJI KAJIWARA[1] and WALTHER BURCHARD

Institute of Macromolecular Chemistry, University of Freiburg Stefan-Meier-Str. 31, 7800 Freiburg i.Br., Federal Republic of Germany

The dynamic and static light scattering behavior of crosslinked polystyrene chains has been studied in a good and a theta solvent. Two series of samples, based on two different primary chain lengths, have been prepared by γ-irridiation. The mean square radius of gyration as function of the molecular weight of the different samples were found to fall on a common line, and the same behavior was obtained for the diffusion coefficient. The ratio ρ of the geometric to the hydrodynamic radii increases slightly with the molecular weight, i.e. with increasing extent of crosslinking, but it then decreases sharply when the gelpoint is approached. The independence of ρ of the primary chain length and also the virtual constancy of this parameter in a wide range of molecular weights is in agreement with theory. The sharp decrease near the gelpoint is unexpected and indicates either a certain heterogeneity in the crosslinking density or a hydrodynamic behavior which up to date cannot be described by the Kirkwood-Oseen approach for the hydrodynamic interaction.

Recent development in photon correlation spectroscopy has provided a new way of characterizing a polymer molecule in solution in terms of its hydrodynamic radius. The hydrodynamic radius R_h is defined via the Stokes-Einstein relationship

$$R_h = k_B T / (6\pi \eta_o D) \tag{1}$$

with D and η_o being the translational diffusion coefficient and the solvent viscosity respectively. We rely on Kirkwood (1) for the calculation of the hydrodynamic radius of models for polymer molecules. Then a dimensionless quantity ρ can be defined as a ratio of two radii, i.e. the radius of gyration $\langle s^2 \rangle^{1/2}$ and the

[1] Current address: Institute for Chemical Research, Kyoto University, Uji, Kyoto, 611 Japan.

hydrodynamic radius R_h

$$\rho = \langle s^2 \rangle^{1/2} / R_h \tag{2}$$

For polydisperse systems this parameter is defined by the z-avera-ges $\langle s^2 \rangle_z^{1/2}$ and $(1/R_h)_z$.

Here ρ can be calculated for various model polymers, and it depends on molecular structure as well as molecular weight dis-tribution (2). Thus ρ provides a useful information concerning molecular structure and polydispersity, when the structure is known. For example, polydispersity causes an increase and bran-ching a decrease of ρ. Excluded volume increases this value. Fur-ther examples are discussed in detail in (2). Here we mention in particular the special case of the f-functional random polyconden-sates where according to theory the decrease of ρ is exactly ba-lanced by the increase as the result of the very pronounced poly-dispersity; the ρ-parameter remains constant in the whole pre-gel region up to the gelpoint.

The translational diffusion coefficient D is obtained from the first cumulant Γ of the electric field time correlation func-tion $g_1(t)$, which is directly measured by photon correlation technique

$$D = \lim_{q \to 0} \Gamma / q^2 \tag{3}$$

where

$$g_1(t) = \frac{\left| \langle E^*(t) E(0) \rangle \right|}{\langle E^*(0) E(0) \rangle} = e^{-\Gamma t - \Gamma_2 t^2 / 2 - \ldots} \tag{4}$$

The first cumulant Γ is generally calculated by assuming the hydrodynamic interaction as described by Oseen (3) where no know-ledge of the space-time correlation function is needed (4-6). The purpose of the present contribution is an experimental test of theoretical relationships which are based on the Flory-Stockmayer (FS) branching theory (7) of the solution properties from ran-domly crosslinked monodisperse primary chains. Most of the theo-retical work and part of the experimental work has been published previously (8-13). We, therefore, bring here only a short outline of the theory and confine ourselves mainly to the discussion of the dynamic properties.

Theoretical Background

According to Kirkwood (1) the translational diffusion coefficient D of an x-mer is given as

$$D/k_B T = (x\zeta_o)^{-1} + (6\pi\eta_o x^2)^{-1} \sum_{i,j} R_{ij}^{-1} \tag{5}$$

where ζ_o is the friction coefficient of a monomer unit. The sum of the configurational average of the reciprocal distance between the i-th and j-th units extends over all pairs of units in a molecule. The hydrodynamic radius is defined for the non-draining case as

$$R_h^{-1} = (6\pi\eta_o/k_BT)/D = x^{-2} \sum_{i,j} R_{ij}^{-1} \qquad (6)$$

The observable quantity, D or R_h is subject to various types of ensemble averages, and the z-average translational diffusion coefficient (or the z-average of the reciprocal effective hydrodynamic radius) is measured by dynamic light scattering.

Branched polystyrene used in the present study is produced by random crosslinking of linear polystyrene of narrow molecular-weight distribution. The application of Good's stochastic theory of cascade processes ([8]) yields the 'structure factor' $S^*(q^2) = DP_wP_z(q^2)$ of randomly crosslinked Gaussian chains ([9,10])

$$S^*(q^2) = \frac{(1+\alpha\phi)f_w(\phi)}{1 - (f_w(\phi)-1)\alpha\phi} = \frac{(1+\alpha)S_p^*(q^2)}{1 - \alpha(S_p^*(q^2)-1)} \qquad (7)$$

where

$$f_w(\phi) = \frac{1+\phi}{1-\phi} - \frac{2\phi}{(1-\phi)^2 y} = DP_{wp}P_{zp}(q^2) = S_p^*(q^2) \qquad (8)$$

In these equations α denotes the extent of crosslinking, i.e. the fraction of repeating units bearing a crosslink, and $y = DP_{wp}$ is the weight average degree of polymerization of the primary chains, i.e. the chains before crosslinking. DP_w is the weight-average degree of polymerization of the total, crosslinked polymer, and $P_z(q^2)$ and $P_{zp}(q^2)$ are the particle scattering factors of the crosslinked and of the primary chains respectively. The variable q gives the magnitude of the scattering vector $\underline{q}$ as

$$q = (4\pi/\lambda)\sin(\theta/2) \qquad (9)$$

and the variable ϕ is defined as

$$\phi = \exp(-q^2 b^2/6) \qquad (10)$$

with b^2 denoting the mean square distance between two adjacent repeating units. Then the weight-average degree of polymerization is given by

$$DP_w = S^*(0) = y(1+\alpha)/(1 - \alpha(y-1)) \qquad (11)$$

and the particle scattering factor

$$P_z(q^2) = S^*(q^2)/S^*(0) = \frac{(1+\alpha\phi(f_w(\phi))}{DP_w(1 - (f_w(\phi)-1)\alpha\phi)} \tag{12}$$

Equation (11) is the well known Stockmayer formula for the DP_w of randomly crosslinked chains (11). It will be noticed that the equation (12) for the structure factor $S^*(q^2)$ can be obtained from equation (11) simply by replacing the weight-average degree of polymerization of the primary chain y by its 'structure factor' $S_p^*(q^2) = yP_{zp}(q^2)$.

The z-average radius of gyration follows from equation (12) by expanding $P_z(q^2)$ in terms of q^2 which yields for the branched molecule

$$\langle S^2 \rangle_z = -3(\partial S^*(q^2)/\partial q^2)_{q^2 \to 0} /S^*(0)$$

$$\cong \langle S^2 \rangle_{zp}(DP_w/DP_{wp}) \tag{13}$$

The z-average translational diffusion coefficient and the first cumulant can be found by integration (8,12)

$$D_z = (2A/\pi^{1/2}) \int_0^\infty S^*(q^2)dq/S(0) \tag{14}$$

and

$$\Gamma/q^2 = \frac{2A}{\pi^{1/2}S^*(q^2)} \int_0^\infty S^*(q^2+\beta^2)d\beta \tag{15}$$

$$-0.1q^2 \int_0^\infty \beta^{-2}(S^*(0.72q^2)-S^*(0.72q^2+\beta^2))d\beta$$

with

$$A = k_BT/(6\pi^{3/2}\eta_o) \tag{16}$$

Numerical integration of equation (14) yield to a good approximation the simple relationships (12)

$$bD_z = 3.685(k_BT/6\pi\eta_o)DP_w^{-1/2} \tag{17a}$$

for monodisperse primary chains and

$$bD_z = 3.464(k_BT/6\pi\eta_o)DP_w^{-1/2} \tag{17b}$$

for primary chains which obey the most probable distribution, i.e.

$M_{wp}/M_{np} = 2$. Combination of the equations (1),(13) and (17) yields, independent of the extent of crosslinking, ρ parameters of

$$\rho = 1.5045 \quad \text{for monodisperse chains}$$
$$\rho = 1.7321 \quad \text{for polydisperse chains} \tag{18}$$

where with polydisperse we always mean here primary chains which obey the most probable distribution. The invariability of ρ is again the result of the balance between the effect of branching, which causes a decrease in ρ, and the effect of polydispersity of the crosslinked system, which causes an increase. In fact, for monodisperse fractions of the crosslinked chains a decrease from $\rho = 1.5045$ for the monodisperse primary chain down to a value of $\rho = 1.1318$ is obtained in the limit of high degrees of crosslinking (12). Further details are given in Ref.12. The results of the numerical integration of equation(15) for the first cumulant will be discussed below.

The results of the theory for the crosslinked system in the unperturbed state may be summarized as follows

(i)   Particle scattering factor, radius of gyration and hydro-dynamic radius do not explicitly depend on the length of the primary chains.
(ii)   The exponent ν in the molecular weight dependence of the radius of gyration is the same as for the hydrodynamic radius, and is in the theta solvent $\nu = 1/2$.
(iii) The parameter $\rho = \langle s^2 \rangle_z^{1/2}/R_{hz}$ is independent of the molecular weight M_w in the whole pre-gel region and is the same as for the linear primary chains. ρ depends, however, on polydispersity of the primary chains.

Experimental

Crosslinked polystyrenes were prepared by Co^{60} γ-ray irradiation in vacuo on commercial polystyrene of very narrow molecular weight distribution for various periods, where chain scission during irradiation was negligible (13). Two series were prepared with primary chains of $M_w = 188\ 000$ (S200) and $M_w = 400\ 000$ (S400). The number- and weight-average molecular weights (M_n and M_w) were determined with the conventional techniques of high speed membrane osmometry (Hewlett Packard High Speed Membrane Osmometer) and static light scattering (Fica 4200 Photogoniometer). The z-average mean square radii of gyration were estimated by static light scattering from cyclohexane and toluene solutions of crosslinked polystyrene at 34.5 and 20.0 °C respectively with vertically polarized blue light ($\lambda_o = 435.8$ nm) and scattering angles from 20 to 150° as described previously (13)

Dynamic light scattering measurements were performed with a Malvern photon correlation system equipped with a krypton ion laser KR 165-11 from Spectra Physics (λ_0=647.1 nm). The intensity time correlation function (TCF) was recorded by a Malvern auto-correlator. The electric field TCF $g_1(t)$ normalized to the base line of the intensity TCF, and its first cumulant $\Gamma = -\partial\ln g_1(t)/\partial t$ at time t=0 were calculated as usual [14] by an on-line computer where 80 channels of a total of 96 channels were used for the recording of the TCF, and the last 12 channels, shifted by 164 sample times, were used for the detection of the base line.

The translational diffusion coefficient was determined from the extrapolation of $\Gamma/q^2 = D_{app}(q)$ against $q^2 - 0$, using a least-square method. Measurements were made at 4 to 5 different concentrations and extrapolated to zero concentration. An example of the dynamic light scattering measurements is shown in Figure 1. The usual precautions were taken to prepare solutions for these measurements. The sample characteristics are summarized in Table I. The molecular weight distribution widens considerably when the gelpoint is approached.

Results and Discussion

(a) The ρ-value. $R_h \equiv \langle 1/R_h \rangle^{-1}$ was found at low extents of cross-linking being approximately proportional to $M_w^{1/2}$ in cyclohexane when $\alpha/\alpha_c < 0.8$, though its proportional constant is slightly larger than that estimated for linear polystyrene [15] (see Figure 2). $\langle S^2 \rangle_z^{1/2}$ is in the same region proportional to $M_w^{0.56}$. At larger extents of crosslinking both the geometric and the hydrodynamic radii show deviations to higher values. Thus the ρ value increases slightly with branching from 1.27 observed for linear polystyrene in cyclohexane at 34.5 °C, and then decreases sharply to 0.8 near the gelpoint (when α/α_c exceeds 0.9), as shown in Figure 3. (α_c is the critical extent of crosslinking at which gelation occurs). This type of transition of ρ values with branching was also observed in the system of polyvinyl acetate (PVAc) / methanol where the ρ value drops as low as 0.55 from 1.8 with gel-formation in the latex particle (microgel) [16]. Here the ρ value is attributed to the effect of the dangling chains of microgels where a much softer decay in the segment density results in a larger hydrodynamic radius than for a hard sphere with its well defined surface. The drop of the ρ value in the system of crosslinked polystyrene in this region ($\alpha/\alpha_c > 0.9$) is better modelled by a soft sphere proposed for PVAc Microgels [17] with a better defined surface. Such behavior may indicate a certain inhomogeneity in the crosslinking density, i.e. crosslinkes may be clustered together, or the Kirkwood-Oseen approximation [2,3] is no longer capable to describe satisfactorily the hydrodynamic interaction in a highly crosslinked molecule. The broad distribution of sphere sizes in the system of crosslinked polystyrene increases apparent-
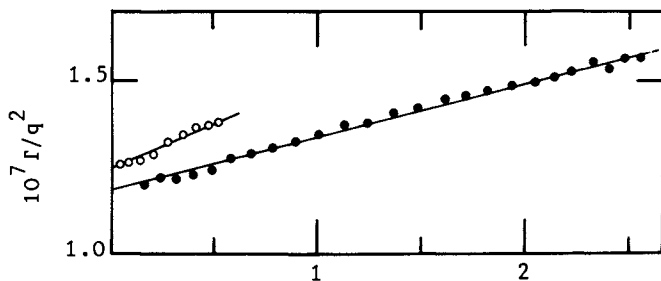
Figure 1 : Plot of $D_{app} = \Gamma/q^2$ against $q^2\langle S^2\rangle_z$ for the sample S200R4 in toluene (●) and cyclohexane (○) for the concentrations of 8.77×10^{-4} g/ml and 2.51×10^{-4} g/ml respectively. See also equation (20).
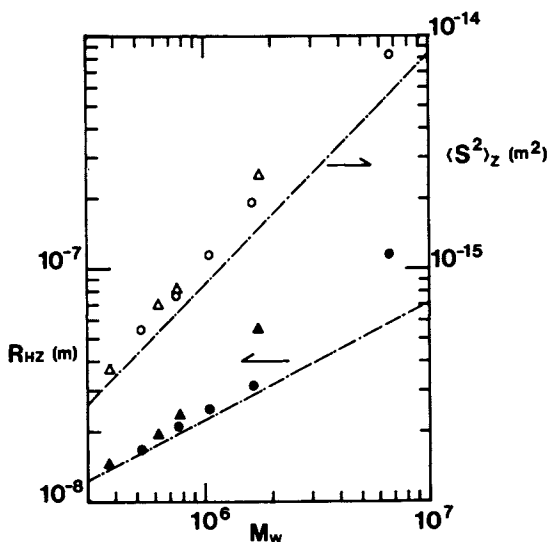

Figure 2 . Molecular weight dependence of the hydrodynamic radius R_{hz} (●,▲) and the radius of gyration $\langle S^2\rangle_z^{1/2}$ (○,△) for the two series of crosslinked, monodisperse chains in cyclohexane at 34.5°C. The circles and triangles refer to primary chains of $M_{wp} = 188\ 000$ and $M_{wp} = 400\ 000$ respectively.

Table I .   Molecular weights M_n and M_w, mean square radii of gyration $\langle s^2 \rangle_z$ translational diffusion coefficients D_z and hydrodynamic radii R_h of two series of crosslinked polystyrene in cyclohexane (cyclohex) at 34.5 °C and toluene at 20 °C. The molecular weights of the two linear primary chains are M_w = 188 000 for S200 and M_w = 400 000 for S400.

S200	R1	R2	R3	R4	R5
M_n	2.18×10^5	2.36×10^5	2.65×10^5	--	3.06×10^5
M_w	3.06×10^5	3.73×10^5	6.18×10^5	7.70×10^5	1.88×10^6
$\langle s^2 \rangle_z$ (cm²)	--	3.73×10^{-12}	6.92×10^{-12}	8.01×10^{-12}	2.45×10^{-11}
D_z (cm²/s)	--	2.08×10^{-7}	1.55×10^{-7}	1.26×10^{-7}	5.45×10^{-8}
R_h (cm)	--	1.43×10^{-6}	1.93×10^{-6}	2.38×10^{-6}	5.46×10^{-6}
$\langle s^2 \rangle_z$ (cm²)	7.99×10^{-12}	1.02×10^{-11}	2.08×10^{-11}	3.24×10^{-11}	1.24×10^{-11}
D_z (cm²/s)	2.13×10^{-7}	1.94×10^{-7}	1.35×10^{-7}	1.16×10^{-7}	4.52×10^{-8}
R_h (cm)	1.71×10^{-6}	1.87×10^{-6}	2.70×10^{-6}	3.14×10^{-6}	8.05×10^{-6}

cyclohex. at 34.5°C

toluene at 20°C

S400	R1	R2	R3	R4	R5	
M_n	--	5.14×10^5	5.47×10^5	--	6.93×10^5	
M_w	5.26×10^5	7.65×10^5	1.03×10^6	1.65×10^6	6.61×10^6	
$\langle s^2 \rangle_z$ (cm^2)	5.25×10^{-12}	7.75×10^{-12}	$1.16 \times 10^{-??}$	1.93×10^{-11}	8.35×10^{-11}	cyclohex. at 34.5°C
D_z (cm^2/s)	1.80×10^{-7}	1.42×10^{-7}	1.20×10^{-7}	9.58×10^{-8}	2.65×10^{-8}	
R_h (cm)	1.65×10^{-6}	2.10×10^{-6}	2.48×10^{-6}	3.13×10^{-6}	1.13×10^{-5}	
$\langle s^2 \rangle_z$ (cm^2)	1.25×10^{-11}	2.04×10^{-11}	2.84×10^{-11}	5.29×10^{-11}	1.83×10^{-10}	toluene at 20°C
D_z (cm^2/s)	1.76×10^{-7}	1.45×10^{-7}	1.05×10^{-7}	7.22×10^{-8}	2.45×10^{-8}	
R_h (cm)	2.07×10^{-6}	2.51×10^{-6}	3.46×10^{-6}	5.03×10^{-6}	1.48×10^{-6}	

ly increases the value of ρ to O.8. A list of the ρ parameters for different models is given in Table II.

The reduced first cumulant Γ/q^2 exhibits for the higher M_w a convexed curve in the good solvent when plotted against q^2 whereas the Γ/q^2 versus q^2 curve in the theta solvent is well approximated by a linear line. A convexed curve was predicted for the soft sphere model (17) and was found for PVAc microgels (16). The molecular weight dependence of R_{hz} and $\langle s^2 \rangle_z^{1/2}$ of the corresponding crosslinked polystyrene samples in the good solvent toluene are shown in Figure 4. The behavior is similar to that in cyclohexane, but the points of measurement from the two series no longer seem to form a common curve. The ρ parameters are about 20 to 45% larger than in the theta solvent, a behavior that is found also for linear polystyrene and which was predicted by theory (8,18,19). It should be mentioned, however, that the absolute values of ρ found by experiment are about 14% lower than predicted from theory when the Kirkwood -Oseen approach for the hydrodynamic interaction (1,3) is taken.

(b) Angular Dependence of Γ/q^2. Equation (14) reduces for small q to

$$D_{app}/D = 1 + (1/3)\langle s^2 \rangle_z q^2$$
$$+(4/5)q^2 \int_0^\infty ds^*(\beta^2)/d\beta^2 \; d\beta / \int_0^\infty ds^*(\beta^2) \, d\beta \qquad (19)$$
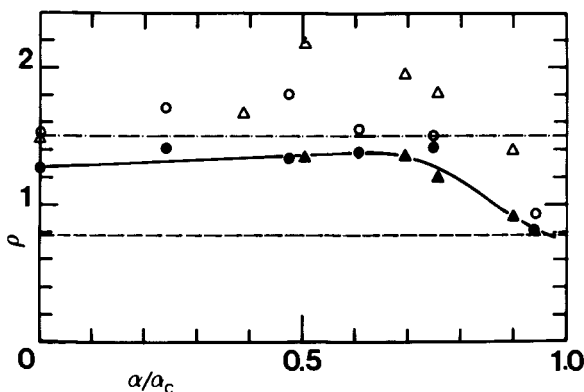

Figure 3. Dependence of the parameter $\rho = \langle s^2 \rangle_z^{1/2}/R_{hz}$ on the reduced extent of crosslinking α/α_c for randomly crosslinked polystyrene chains of two different primary chains in a theta solvent (●,▲) and in toluene (○,△). Meaning of the symbols as in Figure 2. α_c corresponds to the critical γ-ray dose where gelation occured, i.e. where $M_w \to \infty$.

Table II. ρ-values for various types of polymers with Gaussian subchains

	ρ (theoretical)		ρ (observed)	
Linear Polymers				
a.) monodisperse	1.504	(2)	1.27	(15)
b.) polydisperse 1	1.732	(2)		
Crosslinked Monodisperse primary chains				
a.) whole ensemble	1.504		see Text	
b.) monodisperse fractions (No of crosslinks = 1)	1.375	(12)		
c.) monodisperse fractions (No of crosslinks = ∞)	1.130	(12)		
f-functional Polycondensates				
a.) whole ensemble (independent of f)	1.732	(2)	1.48^2	
b.) monodisperse fractions (independent of f)	1.127			
f-Ray Star-Shaped Polymers				
a.) regular star (f=3)	1.401	(2)		
b.) regular star (f=∞)	1.079	(2)		
c.) polydisperse star (f = 3) 1	1.591	(2)		
d.) polydisperse star (f = ∞) 1	1.225	(2)		
Regularly Branched Polymers (Soft Sphere)				
a.) No of shells = 1	1.401	(17)		
b.) No of shells = 18	0.977	(17)	0.55	(16)
Hard Sphere	0.775	(2)	0.77	(14)

1 'polydisperse' denotes the most probable distribution of chain length

2 in the good solvent toluene
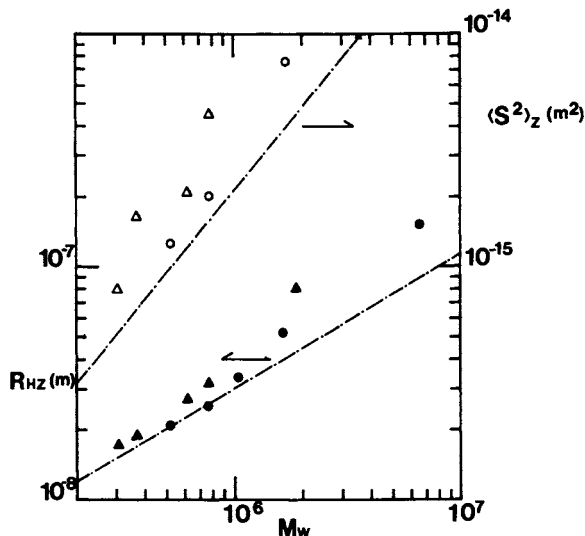
Figure 4.   The same plot as in Figure 2 but for the good solvent toluene at 20.0°C.

and in most cases this apparent diffusion coefficient is written in terms of $\langle S^2 \rangle_z$ as   (2,8)

$$D_{app}/D = 1 + C\langle S^2 \rangle_z q^2 \tag{20}$$

where C is a dimensionless quantity that has been calculated for several polymers. A few examples are given below (2)

Table III . Theoretical values for the coefficient C in equation (20) for several models

Model	C	Ref.
monodisperse linear chain	0.1733	(2)
polydisperse linear chain	0.2000	(2)
crosslinked monodisperse primary chains	0.1733	(12)
crosslinked polydisperse primary chains	0.2000	(12)
regular star shaped chains f ⟶ ∞	0.0979	(2)
polydisperse star shaped chains f ⟶ ∞	0.1333	(2)
hard sphere	0.000	

where with 'polydisperse' we here mean primary chains with
$M_{wp}/M_{np} = 2$. Thus C increases with polydispersity and decreases
with branching. As for the ρ parameter we obtain again a full
balance of the effect of polydispersity and of branching for the
randomly crosslinked system.

In practice the first cumulant is determined from the slope
of the $-\ln g_1(t)$ versus t curve at $t = t_o$ where t_o is the delay
time of the first channel of the autocorrelator. This apparent
first cumulant is, however, smaller than the true one which is de-
fined by $-d\ln g_1(t)/dt$ at the delay time $t_o = 0$ ((20). The C
parameter of the apparent first cumulant depends often on the
time t_o and should be extrapolated towards $t_o = 0$. In general
$C(t_o)$ is smaller than C. The observed parameter C was in fact
found considerably lower than predicted by theory under the re-
commended optimum condition where the overall time correlation
function should have decayed to e^{-2} at the last channel of the
autocorrelator (21). Figure 5 shows the slopes of D_{app}/D versus
q^2 i.e. $C\langle S^2\rangle_z$ as function of $\langle S^2\rangle_z$, where the solid line indi-
cates the theoretical prediction $6.17733 \langle S^2\rangle_z$. We notice
that the theoretical line is approached only for the largest mole-
cular weights, and this may be the result of the fact that we did
not extrapolate the C values to zero delay time.

The C values from the two series of crosslinked primary
chains form in Figure 5 a common line. When, however, the same
values are plotted against the extent of crosslinking i.e. against
α/α_c a clear and non-predicted dependence on the primary chain
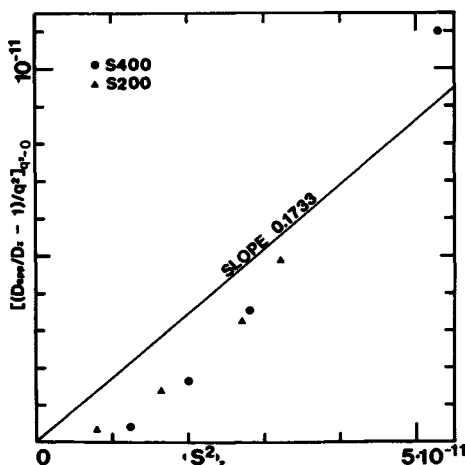length appears. (Figure 6)

Figure 5. Plot of the reduced first cumulant$(D_{app}/D -1)/q^2$
against $\langle S^2\rangle_z$. The straight line corresponds to $C = 0.1733x$
$\langle S^2\rangle_z$ which is the predicted value for randomly crosslinked
monodisperse primary chains. See Table III and equation (20).
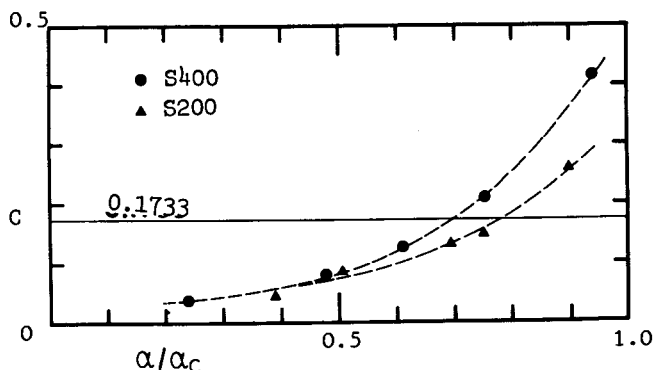The symbols have the same meaning as in Figure 2.

Figure 6 . Plot of the measured coefficients C against the reduced extent of crosslinking α/α_c. Symbols as in Figure 5.

In Conclusion we can state that the general properties of randomly crosslinked chains are found in qualitative good agreement with the prediction of the cascade branching theory. Near the gelpoint, however, deviations, mainly in the hydrodynamic behavior, occurs, which may be an indication for a heterogeneous crosslinking but which also may be interpreted as a failure of the Kirkwood-Oseen approach of describing the hydrodynamic interaction between segments in a higly crosslinked system.

Acknowledgments

Literature Cited

1.   Kirkwood, J.G. J. Polymer Sci. 1954 , 12, 1-14
2.   Burchard, W.; Schmidt, M. ;Stockmayer, W. H. Macromolecules 1980, 13, 1265-1272
3.   Oseen, C. W. "Hydrodynamik";Akademische Verlagsgesellschaft: Leipzig 1927
4.   Fixman, M. J.Chem. Phys. 1965, 42, 3831-3837
5.   Bixon, M. J. Chem. Phys. 1973, 58, 1459-1466
6.   Akcasu, A. Z.;Gurol, H. J. Polymer Sci. Physcs Ed. 1976, 14 1-10

7.   Flory, P. J. "Principles of Polymer Chemistry"; Cornell University Press: Ithaca 1953
8.   Burchard, W. Adv. Polymer Sci. 1983, 48, 1-124
9.   Kajiwara, K.; Ribeiro, C. A. M. Macromolecules 1974, 7, 121-128
10. Kajiwara, K.; Gordon, M. J. Chem. Phys. 1973, 59, 3626-3632
11. Stockmayer, W. H. J. Chem. Phys. 1944, 12, 125- 131
12. Kajiwara, K.; Burchard, W. Polymer 1981, 22,1621-1628
13. Gordon, M.; Kajiwara, K.; Charlesby, A. Europ. Polymer J. 1975, 11, 385-396
14. Bantle, S.; Schmidt, M.; Burchard, W. Macromolecules 1982,15 1604-1609
15. Schmidt, M.; Burchard, W. Macromolecules 1981,14, 210-211
16. Schmidt, M.; Nerger, D.; Burchard, W. Polymer 1979, 20, 582-588
17. Burchard, W.; Kajiwara, K.; Nerger, D. J. Polymer Sci. 1982 20, 157-171
18. Benmouna, M.; Akcasu, A. Z. Macromolecules 1978, 11, 1187-1192
19. Huber, K. Diploma Thesis 1982 , University of Freiburg
20. Stockmayer, W. H.; Burchard, W. J. Chem. Phys.1979, 70,3138

RECEIVED August 29, 1983

Correlation Networks in Polymeric Materials Determined by Small-Angle Neutron Scattering

L. H. SPERLING, A. M. FERNANDEZ, and G. D. WIGNALL[1]

Materials Research Center No. 32, Lehigh University, Bethlehem, PA 18015

Two nonclassical methods of aggregation as detected
by small-angle neutron scattering, SANS, are examined.
In one case, deuteropolyethylene separates from poly-
ethylene on slow cooling from the melt, because of
a six degree difference in their melting tempera-
tures. In the second case, polystyrene crosslinked
with divinyl benzene was examined. The network had
a delta fraction of deuterated polystyrene inserted
at various points in the reaction via a substitution
method. Both cases of aggregation were shown to fit
the Schelten correlation network concept, where no
real center of mass motion takes place. For the
polystyrene-DVB network case, the SANS experiments
make it possible to distinguish networks formed
during the polymerization from those vulcanized
after polymerization is complete.

Polymer networks may be brought about by actual chemical cross-
links between the polymer chains, or through a variety of physical
mechanisms which serve to attach the chains to each other, either
permanently or temporarily. As an example of the physical attach-
ment of chains, Schelten and coworkers (1-3) found that, on
blending hydrogenated polyethylene (H-PE) and deuterated polyethy-
lene (D-PE) in the melt, unusually high molecular weights were
observed by small-angle-neutron scattering, SANS, when samples
were slowly cooled from the melt. Normal molecular weights were
observed when the samples were rapidly cooled from the melt. One
of the major purposes for this entire series of experiments (1-3)
was to study the chain-folding-reentry problem in lamella crys-
tallized from the bulk.
   It was pointed out by Stehling, Ergas, and Mandelkern (4)
that H-PE and D-PE had melting temperatures of about 135°C and

[1]Current address: Oak Ridge National Laboratory, P.O. Box X, Oak Ridge, TN 37830.

129°C respectively, about six degrees apart. It was first thought
that on slow cooling, the difference in melting point caused a
significant aggregation of the deuterated chains in the crystal-
line material resulting in the high molecular weights recorded.
Commonly, molecular weights were found in the range of ten to one
thousand times the primary chain molecular weights. When the
samples were quenched, normal molecular weights were observed.
It was then reasoned that when the blend of the two polymers was
quenched, insufficient time was available to permit a separation
and the material remained homogeneously dispersed even in the
crystalline state.

     More recently, Schelten, et al. (5,6) developed a theory of
the phenomenon called "correlation networks" to describe the so-
called aggregation of D-PE in H-PE. As opposed to an aggregate
consisting of regions which are enriched in tagged molecules
formed by the motion of the centers of gravity of the individual
molecules, a correlation network is formed by individual segments
of different chains touching each other in above statistical
average numbers of contacts.

     More recently, Fernandez, et al. (7) found that the concept
of the correlation network best explained their data on chemically
crosslinked polystyrenes containing a delta fraction of deuterated
polystyrene. In this last study (7) as well as in Schelten's
work, very high molecular weights were found by SANS, correspond-
ing to a state of aggregation ranging from two to about forty
molecules.

     The purpose of this paper will be to describe the works of
Schelten et al. and Fernandez et al. and illustrate how the
concept of the correlation network can provide a physical model
for similar results in two very diverse materials.

Theory

The principles of neutron scattering theory as applied to the
solution of polymer problems have been described in a number of
papers and review articles (8-23). The coherent intensity in a
SANS experiment is given by the scattering cross-section $d\Sigma/d\Omega$,
which is the probability that a neutron will be scattered into
a solid angle, Ω, for unit volume of the sample. The quantity
$d\Sigma/d\Omega$ expresses the neutron scattering power of a sample and is
the counterpart of the Rayleigh ratio, $R(\theta)$, used in light-
scattering.

     For homopolymer blends consisting of deuterated (labeled)
polymer molecules randomly dispersed or dissolved in a protonated
polymer matrix, small-angle neutron scattering in the Guinier
region arises from the contrast between the labeled (deuterated)
and the protonated species. The scattering cross-section can
be expressed

$$[\frac{d\Sigma}{d\Omega}(K)]^{-1} = \frac{1}{C_N M_w} [S(k)]^{-1} \qquad (1)$$

The quantity M_w represents the weight-average molecular weight of the deuterated polymer, and C_N is a calibration constant given by

$$C_N = \frac{(a_H - a_D)^2 N_A \rho (1-X)X}{m_D^2} \qquad (2)$$

where a_H and a_D are the scattering lengths of normal (hydrogenated) and deuterated (labeled) monomer structural units. The quantity ρ is the density of the polymer, X is the mole fraction of labeled chains, m_D is the mass of the deuterated monomer structural unit and N_A is the Avogadro's number.

The quantity $S(k)$ is the single chain form factor [identical with the $P(\theta)$ function used in light scattering], which describes the conformation of an individual labeled chain. This molecular structure factor becomes independent of particle shape as the angle of scatter θ approaches zero, and under these limiting conditions (Guinier region, $K^2 R_g^2 < 1$) becomes a measure of the radius of gyration, R_g.

After rearranging, equation (1) becomes:

$$[\frac{d\Sigma}{d\Omega}(k)]^{-1} = \frac{1}{C_N M_w} (1 + \frac{K^2 R_g^2}{3}) \qquad (3)$$

The quantity K equals $4\pi \lambda^{-1} \sin(\theta/2)$, where λ is the neutron wave length and θ is the angle of scatter. Thus, the Z-average mean square radius of gyration, R_g^2, and the polymer molecular weight, M_w, may be obtained from the slope and intercept respectively of a Zimm plot of $[d\Sigma/d\Omega]^{-1}$ vs. K^2. The values of M_w and R_g were evaluated after appropriate subtraction of the scattering from an unlabeled polymer matrix (blank) from the samples containing different fractions of labeled molecules.

In the above derivation it was assumed that the labeled molecules are fully deuterated. Thus, considering the structural units of the hydrogenated and deuterated polystyrene as C_8H_8 and C_8D_8, respectively, $a_H = 2.328 \times 10^{-12}$ cm, and $a_D = 10.656 \times 10^{-12}$ cm. Thus, the difference in scattering lengths between hydrogenated and deuterated monomer repeat units (mers), $(a_H - a_D)$ is 8.328×10^{-12} cm. Equation (3) is applicable to miscible homopolymer blends in which the molecular size distribution of the labeled and unlabeled polymer molecules are identical. If the size distributions are different, the SANS scattered intensity contains information of both species; therefore, corrections to the measured values of R_g and M_w are needed. These corrections

have been developed by Boué et al. (17), and previously used by
other authors (14,18).

In the Guinier range, the scattering cross-section under
conditions of mismatch in molecular sizes is given by (17):

$$[\frac{d\Sigma}{d\Omega}(K)]^{-1} = \frac{1}{C'_N} \{\frac{(1-X)}{N_{wD}} + \frac{X}{N_{wH}} + \frac{K^2a^2}{18} [\frac{N_{ZD}(1-X)}{N_{wD}} + \frac{XN_{ZH}}{N_{wH}}] \} \qquad (4)$$

where

$$C'_N \approx \frac{(a_D-a_H)^2 \rho N_a X (1-X)}{m_D} \qquad (5)$$

The weight average, N_w, and the Z-average, N_Z, degree of polymer-
ization of the labeled (D) and unlabeled (H) polymer chains, are
related by:

$$N_{wH} = N_{wD} (1 + \Delta w) \qquad (6)$$

$$N_{ZH} = N_{ZD} (1 + \Delta Z) \qquad (7)$$

Substituting N_H in terms of N_D, $N_Z a^2/6$ by R_g^2, and $m_D N_{wD}$ by M_w,
equation (4) becomes:

$$[\frac{d\Sigma}{d\Omega}(K)]^{-1} = \frac{1}{C_N M_w} \{[1 - \frac{X\Delta w}{1+\Delta w}] + \frac{K^2 R_g^2}{3} [1 + \frac{X(\Delta Z-\Delta w)}{1+\Delta w}] \qquad (8)$$

The correction terms in the square brackets depend on the mis-
match in the size distribution. The curve of $[d\Sigma/d\Omega(K)]^{-1}$ vs. K^2,
yields apparent values of M_w and R_g^2. The corrected values may be
obtained:

$$M_w = M_{w\,app} \qquad [1 = \frac{X\Delta w}{1+\Delta w}] \qquad (9)$$

$$R_g^2 = R_{g\,app}^2 [1 + \frac{X\Delta Z}{1+(1-X)M_w}]^{-1} \qquad (10)$$

It should be pointed out that when the molecular sizes of the two
species are equal, $\Delta w = \Delta Z = 0$, and equation (8) reduces to (3),
as expected.

Experimental

The method of synthesis of the delta fraction of deuterated poly-
styrene (D-PS) in polystyrene will be briefly reviewed (7). In

the following, hydrogenated and deuterated styrene, H–S and D–S, respectively, stand for the ordinary monomer and the monomer with deuterium atoms in place of hydrogen atoms. The monomers have not been hydrogenated in the sense of being saturated or reduced.

    Figure 1 illustrates two different methods of synthesis. In the first method, hydrogenated styrene (H–S) monomer, divinyl benzene (DVB), (1 mole %) and benzoin, 0.4% by weight, were subjected to free radical polymerization via UV light exposure. The synthesis was permitted to continue until about sixty to seventy per cent (60% to 70%) conversion. At that point, the remaining styrene and DVB were removed by evaporation and replaced by an exactly equal amount of deuterated styrene (D–S) and fresh DVB and initiator. The polymerization was then permitted to continue for another several per cent. Delta fraction sizes of 5 to 20% were obtained. After the delta fraction had been synthesized in place, the remaining D–S and DVB were again removed by evaporation, and replaced by an exactly equal amount of H–S, DVB and new initiator. Then the reaction was permitted to continue to completion via UV exposure.

    In a second synthetic method (7), D–PS was formed from a mixture of D–S and DVB by permitting the reaction to proceed to about ten (10%) per cent. The resultant still soluble polymer was then precipitated and recovered. Two per cent (2%) by weight of this deuterated polymer was then dissolved in H–S, DVB, and benzoin. This solution was then permitted to polymerize until the entire mixture was fully reacted. As before, free-radical chemistry was employed in the polymerization via UV initiation. It must be stressed that free-radical polymerization was used, and not an anionic polymerization. The latter, of course, has been used widely in the synthesis of polymers for SANS experiments. The two methods result in quite different polymers, the free-radical synthesis yielding a broader molecular weight distribution than the anionic method.

Correlation Networks

As mentioned above, a long-standing problem in polymer science has been the supermolecular organization of polymeric crystals. After Keller (24) discovered the presence of single crystals of polyethylene in 1957, people became interested in the concept of chain-folding. Several models evolved. These included the switchboard model, which suggests that re-entry of polymer molecules into a particular lamella is random. Another model suggested that regular folding and re-entry was more probable. While infrared studies (25) were used to characterize the crystal re-entry problem, basically this remained an incompletely solved problem until the advent of small-angle neutron scattering. (It must be remarked that after ten years of small-angle neutron scattering research, the problem is still unresolved although we know much more about it.)

One of the main conclusions from these experiments (8,9,24) was that when the blend of hydrogenated and deuterated polyethylene was cooled slowly from the melt, SANS experiments showed molecular weights many times the size of the molecular weight of the primary chains. In contrast, the expected molecular weights were obtained when the polymers were quenched from the melt.

Schelten et al. (5,6) showed that the radius of gyration, R_g, depended on the apparent state of aggregation, N,

$$(R_g)_{agg} = (R_g)_{single} N^{1/2} \tag{11}$$

where

$$M_{agg} = NM_{single} \tag{12}$$

and M_{agg} is the aggregate molecular weight determined by SANS and M_{single} is the primary chain molecular weight, as determined by GPC or intrinsic viscosity.

Equation (11) can be expressed directly in terms of the aggregated molecular weight, M_{agg},

$$(R_g)_{agg} = K'M_{agg}^{1/2} \tag{13}$$

For all polymers studied in the bulk amorphous state, the radius of gyration was found to go as the molecular weight to the 1/2 power, substantially the same as was found in Flory-theta solvents. Equations (11) and (13) express a circumstance where individual chains are connected together to form a much longer super chain. Schelten and coworkers (5,6) pointed out that relatively few deuterated intermolecular contacts above that expected statistically are required to produce substantially higher molecular weights than would be expected for the individual primary chains.

To illustrate the effect of slow-cooling and quenching from the melt on the apparent molecular weight and size of the chain, some of the data of Schelten, et al. (4) are reproduced in Table I. It is seen that the aggregated molecular weights can be as high as several hundred times the primary molecular weight.

Schelten and coworkers expressed the one-half power molecular weight dependence of the radius of gyration for the aggregates, equations (11) and (13), in terms of a new type of network which they called a "correlation network". As opposed to a regular aggregation or phase separation, a correlation network merely requires that the chains of one of the components has a greater probability of touching other members of the same component above that of the other components. In touching each other statistically on an above average frequency, the SANS instrument "sees" a larger molecule.

Table I. D-Polyethylene in H-Polyethylene: SANS Results for
          Different Thermal Histories

Sample No.	c(gm/gm)	H-PE $M_w \times 10^{-3}$	D-PE $M_w \times 10^{-3}$	Quenched		Slow Cooled	
				N	R_g (Å)	N	R_g (Å)
PE31	0.31	217	510	0.99	399	15.5	1130
PE35	0.053	41.5	54	1.00	131	140	913
PE37	0.051	15.7	17	1.80	100	721	2000

In order to test their hypothesis of a correlation network being formed, Schelten et al. (6) prepared several H-PE and D-PE blended samples and gamma-irradiated them in the melt and also in the quenched crystalline state. Of course, gamma irradiation causes actual chemical crosslinking. Schelten and coworkers theorized that if aggregates were built up by the correlation mechanism, they should occur or disappear on cooling and heating respectively, irrespective of the extent of gamma irradiation.

On the other hand, if real aggregates in the sense of phase separation were forming, then center-of-mass motion would be taking place which would be hindered by the presence of real chemical crosslinks.

The major finding of this paper (6) was that the degree of "aggregation" was not affected at all by the extent of irradiation or by its absence. Thus Schelten concluded that the chain's center of mass could not be moving very far during the formation of the correlation networks.

The Delta Deuterated Fraction Method

More recently, Fernandez and coworkers (7) prepared networks of polystyrene with DVB, inserting a delta-fraction of deuterated material as described in the experimental section. The original objective of this experiment was to provide a study of polystyrene conformation in network form before going on to preparing inter-penetrating polymer networks out of this material. This was the principal reason that the H-S or D-S was replaced during the synthesis in quantities exactly equal to that removed so that the network structure already formed would not be disturbed, and the original unperturbed dimensions would be retained. As it was, the major method of synthesis employed, that of inserting a delta-fraction of 5% to 20% of D-PS somewhere after 60% of polymerization of H-PS, resulted in a state of aggregation which was

detected in two independent runs at Oak Ridge using the 30-meter
SANS instrument.

Results

The extent of conversion of the polystyrene network was examined
as a function of time, see Figure 2. [In this experiment, linear
polystyrene was employed rather than decrosslinked polystyrene
(26).]
     The major point of interest in the polymerization curve,
Figure 2, is the onset of the Trommsdorff effect, sometimes called
autoacceleration. As is well known, the molecular weight in-
creases rapidly after the onset of the Trommsdorff effect.
     Molecular weights were determined as a function of conversion
by gel-permeation chromatography, GPC. This data is illustrated
in Table II. Of particular interest in Table II are the weight-
average molecular weights and the dispersion, which is weight-
average molecular weight divided by number-average molecular

Table II. Molecular Weights as function of Conversion by
Gel Permeation Chromatography, GPC.

Extent of Conversion %	$M_n \, 10^{-4}$ gms/mol	$M_w \, 10^{-4}$ gms/mole	D (M_w/M_n)
9.51	3.9	6.1	1.57
20.6	3.9	6.4	1.67
39.0	4.0	6.5	1.63
60.0	4.1	6.5	1.61
70.8	4.3	7.4	1.71
74.6	4.5	7.8	1.74
90.7	5.5	10.0	1.85
96.9	5.3	19.0	3.53
99.1	5.7	23.0	4.02
99.3	6.6	35.0	5.24

weight. It will be noted that the weight average molecular weight
is in the range of 60,000 to 100,000 up to 90% conversion. Above
about 90% conversion, molecular weight increases very rapidly.
The dispersion likewise remains nearly constant in the range of
about 1.6 up to about 90% conversion. The value of 1.6 for M_w/M_n
means that two major polymerization mechanisms: chain transfer
and termination by disproportionation together must occur in very
limited amounts. This was estimated algebraically as being more
than 25% to 40% of the total. The major termination mechanism

The Deuterated Delta Fraction Synthesis

Yielded Aggregate MW:
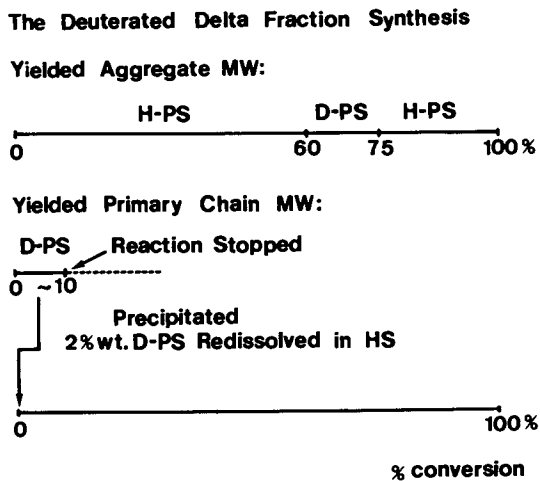
Figure 1.   The deuterated delta fraction synthesis.
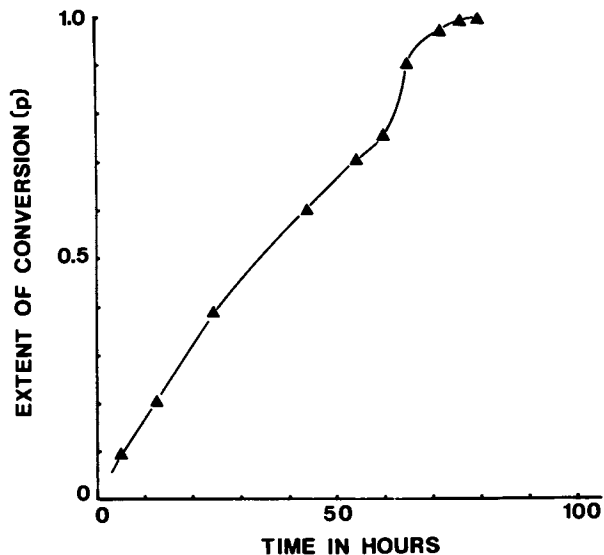
Figure 2.   Rate of polymerization of linear polystyrene.

for polystyrene free radical polymerization is known to be
termination by combination, which yields a weight to number
average molecular weight of 1.50. The other two mechanisms of
course, yield molecular weight dispersions in the range of 2.0.
This latter will be of great significance in evolving a model to
describe the final results.

The molecular weight as a function of conversion is further
illustrated in Figure 3. Not only are the number- and weight-
average molecular weights shown but also the instantaneous mole-
cular weight, which is obtained from the slope of the weight-
average curve. The instantaneous molecular weight is the molecu-
lar weight of polymer actually being formed at that particular
instant of time. This is particularly important because when
the delta-fractions were prepared the molecular weight at inser-
tion is required.

Incidentally, it should be remarked that even though linear
polymers were employed in the determination of the molecular
weights in Table II as well as the data in Figure 3, it is known
from prior experiments that the molecular weights of the primary
chains are the same as they are if they were part of an actual
chemical network. Sperling et al. (26) for example, prepared
polystyrene networks crosslinked with acrylic acid anhydride which
is easily hydrolyzed with ammonia water to produce the linear
polymer. In a series of experiments, Sperling, et al. (26)
determined that the molecular weights of a polystyrene acrylic
acid anhydride network after hydrolysis had a weight-average
molecular weight of about 350,000 grams/mole. This compares to
the value obtained by Fernandez et al. who found weight-average
molecular weights of just over 300,000 gms/mole in a similar
linear polymer synthesis, Table II.

The results from small-angle neutron scattering are summar-
ized in Figures 4 and 5. In Figure 4, a normal molecular weight
of 70,000 grams/mole and an R_g value of 121 Å was obtained. In
Figure 5, a molecular weight of about 15 times that of the primary
chains is shown with the corresponding increase in R_g values.

In all, a total of seven samples were examined as illustrated
in Table III. Sample 1 was prepared by adding the 2% of preformed
D-PS mix containing the DVB and benzoin. Samples 2 through 7
were prepared by the deuterated delta-fraction technique, and all
showed molecular weights very much higher than expected. These
molecular weights range from about one to nearly forty times the
molecular weights expected from the GPC measurements performed, as
described above.

The state of aggregation of these materials, samples 2 thru 7,
is shown in Table IV, in order of increasing state of aggregation.
It will be observed that the state of aggregation appears to
increase as the size of the delta-fraction decreases. An extrapo-
lation to zero delta-fraction size was performed, data not shown,
and approximately an aggregation state of forty was deduced. (f
course, for very large delta-fraction sizes, the sample develops
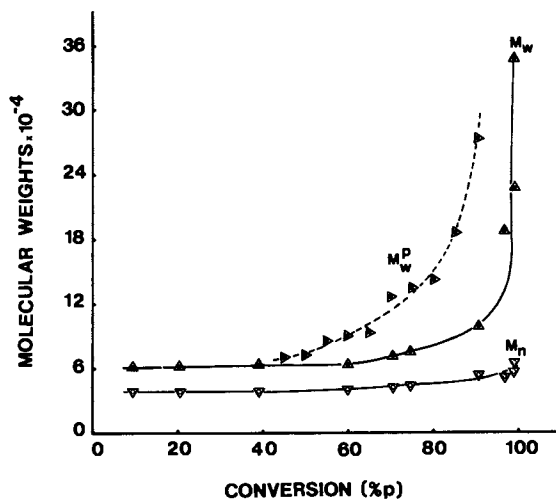
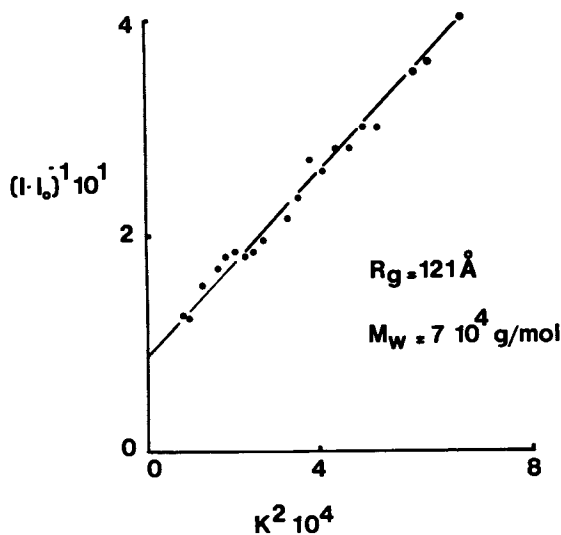Figure 3.   Cumulative and instantaneous molecular weights of polystyrene.

Figure 4.   SANS molecular weight and R_g values from a non-aggregated synthesis, Sample 1. See Figure 1 lower portion for schematic of synthesis.
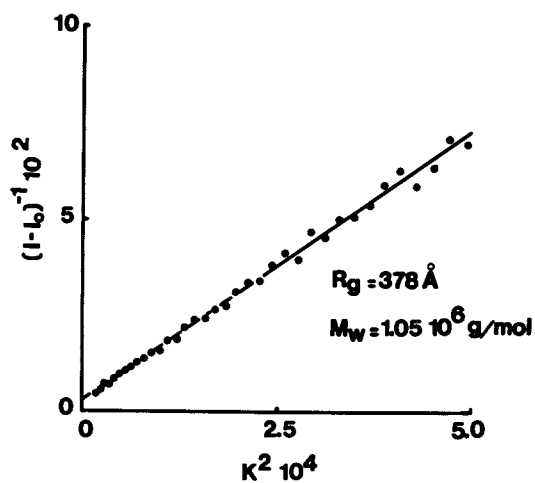
Figure 5. SANS molecular weight and R_g values of Sample 5 showing higher than expected M_w and R_g. See upper portion of Figure 1 for synthesis description.

Table III.   Corrections of M_w(SANS) and R_g^2(SANS) for Mismatch in
            Average Degrees of Polymerization between the Delta
            Fraction and the Hydrogenated Matrix.

Sample No.	Δw [a]	Correction [b] factor for R_g^z	Correction [c] factor for M_w	R_g^z (Å) Corrected	$M_w \times 10^{-5}$ Corrected
1	4.40	1.02	0.98	120	0.69
2	-0.53	0.82	1.22	387	9.76
3	-0.84	0.78	1.28	459	30.0
4	-0.68	0.82	1.21	388	14.3
5	-0.56	0.85	1.18	366	10.0
6	-0.64	0.85	1.17	410	12.3
7	-0.53	0.86	1.16	423	9.28

[a] $\Delta z \cong w = \dfrac{M_{wH}}{M_{wD}} - 1$; $M_{wH} = 3.5 \times 10^5$ gms/mole; $M_{wD} = M_w$(SANS)

[b] $1 + \dfrac{x \Delta z}{1+1(1-x)\Delta w}$

[c] $1 - \dfrac{x \Delta w}{1+\Delta w}$

Table IV.   State of Aggregation as a Function of Delta Fraction
            Size

Sample No.	Delta Fraction Size, %	$M_w 10^{-5}$ SANS [a]	$M_w^P 10^{-5}$ GPC [b]	N Aggregation Number	N Mismatch Corrected
2	20.1	8.0	17.0	(1) [c]	(1)
5	13.9	8.5	2.78	3	4
7	13.9	8.0	0.82	10	11
4	10.2	11.8	0.98	12	15
6	10.0	10.5	0.78	13	16
3	5.38	23.5	0.88	27	34

[a] M_w (SANS uncorrected for degree of polymerization mismatches.

[b] Instantaneous molecular weight (figure 3).

[c] This sample was affected by the Trommsdorff effect, and its molecular weight is known with less certainty than the other samples.

a certain degree of continuity, and one would not expect the theory to hold.

The molecular weights shown in the two preceding tables, it must be remarked, were corrected for the differences in weight-average molecular weight between the deuterated fraction and the overall material, as illustrated in the theoretical section. As is seen from Table III, the corrections of the weight-average molecular weight are of the order of 5% or 10% in most cases.

Table V shows a calculation of the corresponding weight-average radii of gyration calculated from the z-average radii of gyration. More importantly, Table V also shows that the molecular weights obtained vary as equations (11) and (13) with respect to their radii of gyration.

Table V. Comparison of weight-average radii of gyration, R_g^w, from Molecular Size Mismatch Corrected M_w.

Sample No.	R_g^w From M_w(a)	$R_g^{agg} = R_g^{sing} \times N^b$ (c) $[R_g^{sing}$ From (a)$]$
1	72(b)	72
2	272	272
3	476	420
4	328	279
5	275	144
6	305	288
7	265	239

(a) $R_g^w = 0.275 M_w^{0.5}$, data from Table III.

(b) All values in Ångstroms.

(c) From the relation $R_g^{agg} = R_g^{sing} N^b$ (using values of R_g^{sing} (R_g, single chain) equal to 72Å, the corrected values of N, and a value of b=0.50).

Equation (11) can be generalized to read:

$$R_g^{agg} = R_g^{sing} N^b \tag{14}$$

where b is a constant to be determined by experiment. By plotting log R_g vs. log N, data not shown, it was determined that the exponent b was equal to 0.50 within experimental error, see Table V.

Discussion

Several models could be imagined which could explain the above
polystyrene data. Four possibilities are illustrated in Figure
6. First of all, one very long chain actually having a molecular
weight of one to two million might be imagined. However, the GPC
values which yielded molecular weights of 60,000 to 70,000 gm/mole
belie this model, and hence it was discarded.
    Chain transfer might be considered also. Then one would have
several long chains which are placed end on end. In a network
synthesis, they would be held more or less in place. These super
chains would have the correct relationship between the radius of
gyration and the molecular weight. However, it is known that the
extent of chain transfer permitted by the molecular weight distri-
bution is far too small to explain the results by this mechanism.
    A third mechanism is due to Bobalek et al. (37) and Labana
et al. (28), who postulated that there are series of small gels
which are formed during the early part of a network polymerization.
It is well verified experimentally that in the early stage of
polymerization of a network, one has a collection of microgels,
linear polymer, and monomer. Of course, by free radical polymeri-
zation, there is very little living or growing polymer at any
point in time, while by condensation polymerization aligiomeric
species may dominate at a certain period of time. The presence
of small gels dispersed in monomer suggests regions of relatively
high and low monomer concentration in a partly polymerized network.
If the deuterated monomer is added in the delta fraction manner,
the deuterated polymer will tend to form spherical shaped regions
which would have a super molecular weight dependence of the radius
of gyration of one-third. However, the molecular weight depen-
dence of the radius of gyration is 0.50, rather than one-third.
Therefore, this mechanism was also set aside.
    As explained above, Schelten et al. (5,6) have developed a
correlation network which predicts the 0.5 power behavior of the
exponent b. In fact, an exact quantitative agreement with the
Schelten correlation network was obtained.
    The mechanism of correlation network formation is described
in Figure 7. The correlation network of D-PE is formed on cooling
from the melt through the formation of an above-average number
of contacts, statistically, between deuterated chains. This
arises as follows. In a formation of a D-PS delta-fraction, the
chains have an above-statistical average probability of being
connected to each other, because chains recently formed have a
larger than average number of pendant vinyl groups. Of course as
time passes, these vinyl groups are reacted to form part of the
network. Thus, chains polymerized within a short time of each
other have a greater than average probability of being reacted
with each other, and hence this is picked up by small-angle
neutron scattering to give an apparent increase in molecular
weight. It must be emphasized that the aggregation noted in the

One long chain (but
GPC shows M~7 10^4)

Several short chains by
chain transfer (but chain
transfer = 25-40%)

Shelten's correlation
network $R_g \sim M^{0.5}$

Bobalek - Labana gel
(but $R_g \sim M^{1/3}$)
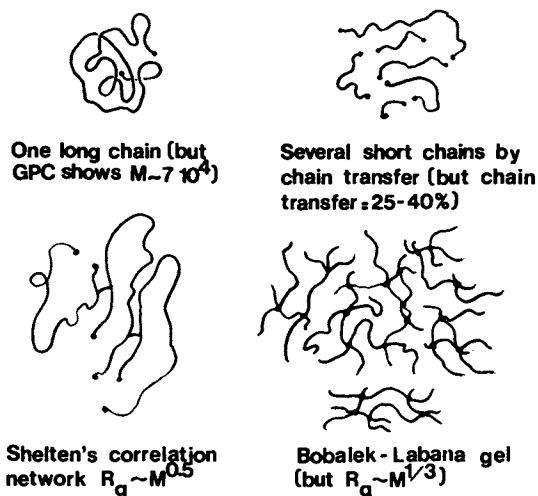
Figure 6.   Models for polymerization aggregation.

Correlation Networks: $(R_g)_{agg} \sim M_{agg}^{0.5}$

$\xrightarrow{\text{cooling}}$

Melt   Crystalline

Formation of Systematic Points of Contact

$\xrightarrow[\text{C=C}]{\text{polymerization}}$

Free Radical Synthesis   Crosslinked Network

Crosslinks Can Form Systematic Point of Contact
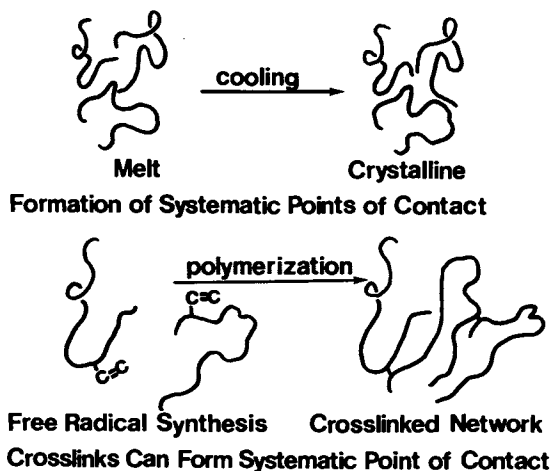
Figure 7.   Correlation networks for semi-crystalline polymers
            and for delta fraction chemical networks.

present system is highly unusual. Previously, blends of atactic
H-PS and D-PS have been examined by SANS techniques (13,29), and
these studies report the expected single chain molecular weights.
Thus, the phenomenon is caused by the delta fraction sample prepa-
ration technique, rather than being a general phenomenon.

Conclusions

The term correlation network describes various polymer systems
where the chains have a greater than average probability of being
in contact with each other. In the case of crystallizing blends
of D-PE and H-PE a correlation network is caused by the slightly
different crystallizing temperatures of D-PE and H-PE. Extensive
center of mass motion of the deuterated chains towards each other
is not required.
        In the case of the PS-DVB networks, aggregates of from about
1 to 34 D-PS molecules were formed with radii of gyration ranging
upwards to 350 to 400Å. The Schelten correlation network model
seems to fit the present data better than other models at this
time.
        It should be noted that these chains are actually chemically
crosslinked to each other. The higher than statistical probabil-
ity of chemically connecting two chains that are reacted at nearly
the same point in time during the polymerization leads to a very
high molecular weight by SANS instrumentation. In this system,
likewise, it is not necessary for the centers of mass of the
chains to have moved. Thus, it is concluded that the system is
not aggregated in any real sense of the term, except that there is
a preference for chains that are polymerized in the same time
period to be chemically attached to each other. Since deuterated
chains were formed in the delta-fraction method, this led to the
apparent increase in the molecular weight. Most importantly the
present experiment provides a new method of evaluating the proba-
bility of two chains being linked during a network polymerization.
This experiment also distinguishes between a network formed by
vulcanization, i.e., crosslinking after polymerization, and cross-
linking during polymerization.
        To test the ideas in this paper further, PS delta fraction
polymerizations should be conducted with the crosslinker systema-
tically omitted from the various parts of the polymerization shown
in Figure 1.

Acknowledgments

Literature Cited

1. Schelten, J.; Wignall, G. D.; Ballard, D. G. H. Polymer.
    1974, 15, 682.
2. Schelten, J.; Wignall, G. D.; Ballard, D.G.H.; Schmatz, W.
    Colloid Polymer Sci. 1974, 252, 749.
3. Wignall, G. D.; Ballard, D. G. H.; Schelten, J. J. Appl.
    Phys. 1976, (B)12, 75.
4. Stehling, F. S.; Ergos, E.; Mandelkern, L. Macromolecules.
    1971, 4, 672.
5. Schelten, J.; Wignall, G. D.; Ballard, D. G. H.; Longman,
    G. W. Polymer. 1977, 18, 1111.
6. Schelten, J.; Zinken, A.; Ballard, D. G. H. Colloid Polym.
    Sci. 1981, 259, 260.
7. Fernandez, A. M.; Widmaier, J. M.; Sperling, L. H.;
    Wignall, G. D. submitted, Polymer. 1983.
8. Sperling, L. H.; submitted, Poly. Eng. Sci. 1983.
8a. Maconnachie, A.; Richards, R. W. Polymer, 1978, 19, 739.
9. Higgins, J.S.; Stein, R. S. J. Appl. Cryst. 1978, 11, 346.
10. Schmitt, B. J. Angew. Chem. Int. Ed. Eng. 1979, 18, 273.
11. Kirste, R. G. Kruse, W. A.; Schelten, J. J. Makromol. Chem.
    162, 299.
12. Ballard, D.G.H.; Wignall, G.D.; Schelten, J. Europ. Polym. J.
    1983, 9, 965.
13. Wignall, G. D.; Ballard, D. G. H.; Schelten, J. Eur. Polym.
    J. 1974, 10, 861.
14. Benoit, H.; Decker, D.; Duplessix, R.; Picot, C.; Rempp, P.;
    Cotton, J. P.; Farnoux, B.; Jannick, G.; Ober, R. J. Polym.
    Sci., Polym. Phys. Ed. 1976, 14, 2119.
15. Clough, S.; Maconnachie, A.; Allen, G. Macromolecules. 1980,
    13, 774
16. Hinkley, J. A.; Han, C.C.; Mozer, B.; Yu, H. Macromolecules.
    1978, 11, 836.
17. Ullman, R. in "Elastomers and Rubber Elasticity"; Mark, J.E.;
    Lal, J., Eds.; ACS SYMPSOIUM SERIES No. 193, American Chemi-
    cal Society: Washington, DC, 1982.
18. Ullman, R. Macromolecules. 1982, 15, 1395.
19. Ullman, R. Macromolecules. 1982, 15, 582.
20. Wignall, G. D.; Child, H. R.; Samuels, R.J. Polymer. 1982,
    23, 957.
21. Koehler, W. C.; Hendricks, R. W.; Child, H.R.; King, S. P.;
    Lin, J.S.; Wignall, G.D. Proceedings of NATO Advanced Study
    Institute on Scattering Techniques Applied to Supramolecular
    and Nonequilibrium Systems. 1981, p. 75.
22. Boue, F.; Nierlich, M.; Leiber, L. Polymer. 1982, 23, 29.
23. Crist, B.; Graessley, W. W.; Wignall, G. D. Polymer. 1982
    23, 1561.
24. Keller, A.; Phil. Mag. 1957, 2, 1171.
25. Tatsumi, M.; Krimm, J. J. Polym. Sci. 1968, A-2,6, 995.

26. Sperling, L. H.; Ferguson, K. B.; Manson, J. A.; Corwin, E. M.; Siegfried, D. L. Macromolecules. 1976, 9, 743.
27. Bobalek, E. G.; Moore, E. R.; Levy, J. S.; Lee, C. C. J. Appl. Polym. Sci. 1964, 8, 625.
28. Labana, S. S.; Newman, S.; Chompff, A. J., in "Polymer Networks: Structure and Mechanical Properties"; Chompff, A. J.; Newman, S., Eds; Plenum. 1971.
29. Cotton, J.P.; Decker, D.; Benoit, H.; Farnoux, B.; Higgins, J.A.; Jannink, G.; Ober, R.; Picot, C.; desCloizeaux, J. Macromolecules. 1974, 7, 863.

Carboxyl-Terminated Butadiene–Acrylonitrile-Modified Epoxy Resin and Its Graphite Fiber-Reinforced Composite

Morphology and Dynamic Mechanical Properties

SU-DON HONG[1], SHIRLEY Y. CHUNG, GEORGE NEILSON, and ROBERT F. FEDORS

Applied Mechanics Division, Jet Propulsion Laboratory, California Institute of Technology, Pasadena, CA 91109

Measurements of dynamic mechanical properties, optical and scanning electron microscopy and small-angle X-ray scattering were carried out to characterize the state of cure, possible phase separation and morphology of both HX-205 and F-185 neat resins and their graphite fiber reinforced composites. HX-205 is a diglycidyl ether bisphenol A (DGEBA) based epoxy resin and F-185 is a rubber-modified epoxy resin containing 86.5 weight % HX-205, 8.1 weight % Hycar 1300 x 9 (a liquid carboxyl-terminated polybutadiene-acrylonitrile, CTBNX) and 5.4 weight % Hycar 1472 (a solid copolymer of butadiene-acrylonitrile having acrylic acid pendant group). The neat resins and the composites were prepared using identical curing cycles. The neat resins as well as the matrix materials in the composites appear to have the same state of cure as characterized by dynamic mechanical properties. The F-185 resin contains CTBN-rich domains with sizes ranging from 50 Å (and possibly smaller) to 20 μm and larger. The F-185 neat resin and the F-185 matrix in the composite both display ductile fracture behavior compared to a brittle fracture of HX-205 neat resin and its composite, indicating a toughening effect of the CTBN inclusions. The morphology of the CTBN domains in the F-185 matrix appear to differ from that in the F-185 neat resin. There are a greater fraction of smaller CTBN domains in the F-185

[1] To whom correspondence should be directed.

matrix than in the F-185 neat resin.
Because CTBN domains in the size range of the order
of several hundred angstroms are less effective in
improving fracture toughness (6,8), the fact that
there are a greater fraction of smaller CTBN
particles in the composite matrix may partially
explain the reported observations that some of the
composites made with the CTBN-modified DGEBA epoxy
resin did not show significant improvement in
fracture toughness. This study indicates that,
when using multiphase resins to make composites,
the neat resin and the matrix of the composite may
not have similar morphology even when prepared
under the same curing program.

It has been shown that the fracture toughness of the matrix resin
itself in a fiber-reinforced composite has a significant effect
on the fracture toughness, particularly the interlaminar fracture
toughness, of the composite. For instance, the critical strain
energy release rate, G_{IC}, of the three matrix resins, i) tetra-
glycidyl diaminodiphenyl methane (TGDDM) cured with diaminodi-
phenyl sulfone (DDS), ii) diglycidyl ether bisphenol A (DGEBA)
cured with dicyandiamide and iii) poly (bisphenol-A-diphenyl-
sulfone) is 0.076 KJ/m^2(1,2), 0.27 KJ/m^2 (1,2) and 3.2 KJ/m^2 (2),
respectively; the G_{IC} for interlaminar fracture for the
corresponding graphite cloth-reinforced composite is 0.36 KJ/m^2
(1), 0.6 KJ/m^2 (1) and 2.2 KJ/m^2 (2), respectively. Much work
has been carried out in an effort to toughen the epoxy resin by
various modifications such as the incorporation of a rubber
component, mainly carboxyl-terminated butadiene acrylonitrile
(CTBN) polymers (2-10). It was reported that the incorporation
of a CTBN elastomer in diglycidyl ether bisphenol A resin
produced more than a 10-fold increase in the fracture toughness
(2-10) of the resin matrix itself. The fracture toughness of
fiber-reinforced composites containing such modified resins,
however, has not always been reported to be increased. For
example, for interlaminar fracture energy of composites
containing a CTBN-modified DGEBA matrix, McKenna, Mendell, and
McGarry (11) reported no measurable effect of CTBN for a glass
cloth composite (12), while Scott and Phillips (12) reported a
two-fold increase for a non-woven graphite fiber composite and
Bascom, Bitner, Moulton and Siebert (1) reported a nearly 8-fold
increase for a graphite composite. It was thought that these
diverse results were at least in part due to the fact that the
CTBN-modified DGEBA matrix had differing rubber particle sizes as
well as size distributions which influenced the shape of the
crack-tip deformation zone (1) and hence the fracture toughness
of the material.

The enhanced toughness of the CTBN–modified DGEBA epoxy was the result of the presence of discrete CTBN–rich regions, which precipitated from the resin mixture during polymerization. These regions consist of relatively soft particles of sizes ranging from several hundred angstroms to 10 μm and larger (2–9), depending on the type of carboxyl-terminated rubber used. The toughness was significantly affected by the particle size. For resins containing small particles of sizes less than about 0.5 μm, the samples failed by shear band formation and were only slightly tougher than the unmodified resin (6,8). When the resins contained particles of sizes 1 μm or larger, the samples deformed by a combination of, i) a dilatational deformation of the rubber inclusion at the crack tip (7,8,11), ii) the elongation of the rubber particles (10) and iii) localized shear deformation of the epoxy matrix (6,10). These deformation mechanisms lead to the development of a large plastic zone at the crack tip. The plastic zone diameters of CTBN–modified DGEBA containing large CTBN particles are typically of the order of 20–40 μm compared with about 1 μm for the unmodified epoxies (1). The large plastic zone at the crack tip contributes to the large increase in fracture toughness. It also was reported that a bimodal distribution of CTBN particle sizes contributes to a greater fracture toughness than does a unimodal distribution (8).

The particle sizes and size distribution of the rubber inclusions in a CTBN–modified epoxy can be affected by both the curing conditions and the chemistry and composition of the starting resin mixture. It is known that the phase separation behavior of CTBN–modified epoxy, which has a direct influence on the sizes and size distribution of the inclusion, is affected by 1) reactivity and selectivity of the functional groups of rubber and hardener (6,8,9,13), ii) the solubility parameter of rubber which is related to the acrylonitrile content in the rubber (4,14), iii) initial molecular weight of the rubber (4,6), iv) concentration of rubber and hardener (4,9,13,14) and v) addition of a modifier such as bisphenol A (8). The curing temperature also influences the phase separation because of the temperature dependence of miscibility of the CTBN–epoxy misture (14) and of the temperature dependence of copolymeriza-tion of the resin mixture. Block copolymerization of the CTBN component will favor formation of CTBN particles.

When the graphite fibers are impregnated with the resin to fabricate the composite, the morphology of the CTBN inclusions may also be further influenced by the presence of graphite fiber. Depending on the fiber manufacturing process and surface treat-ment, the surfaces of graphite fibers may have reactive chemical groups (15,16) which will influence the cure kinetics of the resin and, consequently, possibly change the morphology of CTBN inclusion.

In this paper, we report the results of a morphological characterization of a DGEBA-based epoxy resin, a CTBN-modified DGEBA resin and their corresponding graphite fiber-reinforced composites.

Experimental

Materials. The compositions of the unmodified base epoxy resin, trade name Hexcel 205 (HX-205), and the CTBN-modified epoxy resin, trade name F-185, are summarized in Table I. The chemical structure of CTBNX is as follows:

$$HOOC \left[(CH_2-CH = CH-CH_2)_x - (CH_2-CH)_y - (CH_2 - CH)_z \right]_m COOH$$
$$\underset{CN}{|} \qquad \underset{COOH}{|}$$
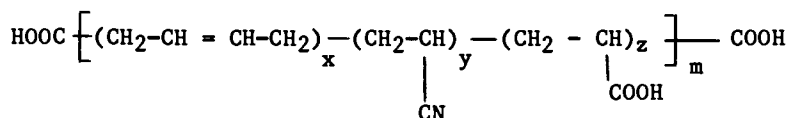
where x, y, z and m depend on the molecular weight and the acrylonitrile content. Hycar CTBNX 1300 x 9 (B. F. Goodrich Chemical Company) is a terpolymer which has a nominal molecular weight of 3500, and Hycar 1472 is a higher molecular weight (260,000) terpolymer of butadiene, acrylonitrile and acrylic acid having carboxyl pendant groups randomly distributed along the polymer backbone. Hycar 1300 x 9 has an acrylonitrile content of 18% and, for Hycar 1472, the acrylonitrile content is 26% (17).

Table I. Compositions of HX-205 and F-185 Resins

HX-205		F-185	
Component	Approx. Wt. %	Component	Approx. Wt. %
EPOXIDES			
(Diglycidyl Ether of Bisphenol A) (Epoxidized Novolac, Epox. Eq. Wt 165)	73	HX-205	86.5
DIPHENOLS			
(Bisphenol-A) (Tetrabromobisphenol-A)	20	Hycar 1300 x 13	8.1
CATALYST			
(Dicyandiamide)	7	Hycar 1472	5.4

Two fiber–reinforced composites, designated GD–31 and GD–48, made from Celion 6000 graphite fiber were also used for the testing. Both composites are 6-ply laminates (thickness approximately 0.045 inch) with unidirectional fiber layup. The matrix corresponding to GD–31 is F–185 and that for GD–48 is HX–205. The resin content in both composites is about 37% by weight. The porosity of the composites was characterized by ultrasonic C-scans. The test specimens of no measurable porosity were used. The resin specimens and the composite laminates were cured in a hydraulic press at 250°F and 75 psi for one hour, and subsequently postcured at the same temperature in the absence of pressure for another two hours. Additional curing for up to 16 hours in the case of HX–205 and F–185 resins showed no measurable changes in dynamic mechanical properties.

Microscopy. The polarized optical micrographs of thin films of HX–205 and F–185 neat resins were obtained using a Zeiss ultraphot microscope equipped with a polarizer and an analyzer. Thin films, approximately 100 microns thick, were prepared by thin-sectioning the resin sheet with a razor blade at room temperature. The domains were observable because of light scattering as a result of refractive index mismatch between the rubber domain and the epoxy matrix, as well as to stress-induced birefringence produced by the thermal stress imposed on the domains.

An ISI model 60Å scanning electron microscope was used to examine the morphology of the fracture surfaces. Both the neat resins and the composite laminates were notched at room temperature with a razor blade. The samples were then immersed in liquid nitrogen and fractured in air immediately after removal from liquid nitrogen. The neat resins were fractured by bending the samples with pliers and the laminates were fractured along the fiber by opening up the notched cracks with pliers.

Small–Angle X–Ray Scattering. The small-angle X-ray scattering (SAXS) measurments were carried out on a conventional Kratky instrument (made by Anten Paar) having a sample to detector-slit distance of 208 mm. Entrance slits of 0.030 and 0.060 mm were used. Nickel-filtered $CuK\alpha$ radiation was employed, which was measured with a scintillation counter in conjunction with a pulse-height analyzer. A microcomputer was employed for automatic stepwise collection and analysis of the scattering data. The scattering curves shown in this paper are the experimental curves after correction for parasitic scattering. Also no correction was made for differences in SAXS intensities between samples due to differences in X-ray transmission, since all samples were about the same thickness (0.6 mm), the measured transmission (I/I_0) values for samples F–185, HX–205, GD–31 and GD–48 were 0.56, 0.46, 0.66 and 0.63, respectively.

Dynamic Mechanical Properties. A Servohydraulic Instron Model
1322 was utilized to measure both the storage and loss modulus as
a function of temperature. A sine wave deformation mode at a
frequency of 3.5 Hz and a static strain of 0.3% with a superposed
dynamic strain of $\pm$ 0.1% was employed in the test. A lock-in
amplifier, EG&G Model 5422, was used to measure the storage and
loss modulus. A command signal from a digital function generator
to control the cyclic motion of the ramp of the Instron was used
as the reference signal to the lock-in amplifier. The dynamic
strain was first measured by balancing the phase difference
between the signal for strain and the reference signal using the
phase adjustment of the lock-in amplifier. Subsequently the in-
phase force component and the out-of-phase force component from
which the storage and loss moduli as well as the tan δ were
calculated, were directly measured. The composite specimens used
for testing were 16-ply and 6-ply unidirectional laminates cut so
that the fiber orientation was perpendicular to the stretching
direction. The dynamic mechanical properties so measured
represent primarily the response of the matrix.

Results and Discussion

Figures 1 and 2 show the storage modulus E^1 and tan δ for HX-205
and F-185 neat resins as a function of temperature. E^1 for
HX-205 decreases gradually with an increase in temperature and
does not show any transition indicative of secondary molecular
relaxation until the temperature reaches the glass transition
temperature, which is approximately 60°C. E^1 for F-185, on the
other hand, shows a transition starting at about -50°C
accompanied by an increase in tan δ. The tan δ continues to
increase until the temperature reaches the glass transition
temperature at which point the tan δ increases drastically.
Figure 3 shows the comparison of the tan δ vs temperature plots
for HX-205 and F-185. F-185 shows an enhanced tan δ at
temperatures above -50°C, and when the temperature reaches 25°C,
the tan δ for F-185 starts to increase drastically even though
HX-205 and F-185 appear to have the same glass transition
temperature. The glass transition temperature for Hycar 1300 x 9
is -49°C and is approximately -24°C for Hycar 1472 as reported by
the manufacturer (18). F-185 does not show the separate
transition peaks corresponding individually to Hycar 1300 x 9 and
Hycar 1472 in the tan δ vs temperature plot as would be expected
in a completely phase-separated system. It appears that Hycar
1300 x 9 and Hycar 1472 do not form a pure rubber phase, but
rather the rubber phase is blended with the epoxy resin to form
CTBN-rich domains. The appearance of extensive blending of epoxy
resin with CTBN is probably due to the high acrylonitrile content
of Hycar 1300 x 9 and Hycar 1472. Wang (14), Sultan and McGarry
(19), and Manzione, Gillham and McPherson (20) have reported that
CTBN copolymer with a higher acrylonitrile content tends to mix
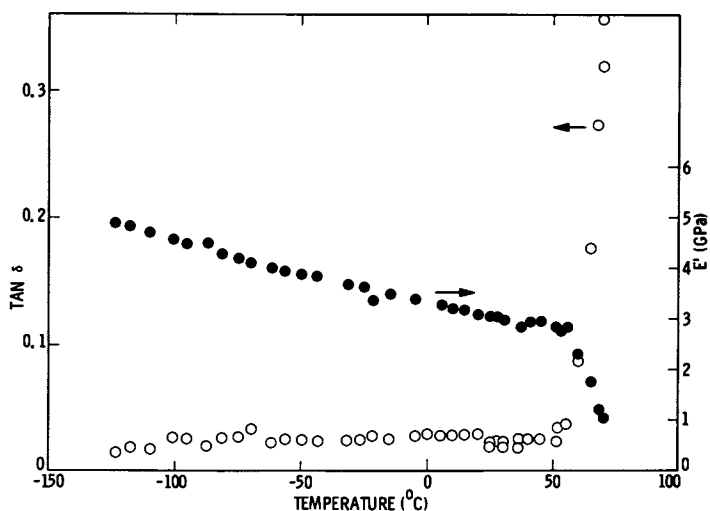
Figure 1. The storage modulus E^1 and tan δ for HX-205 neat resin measured at 3.5 Hz.
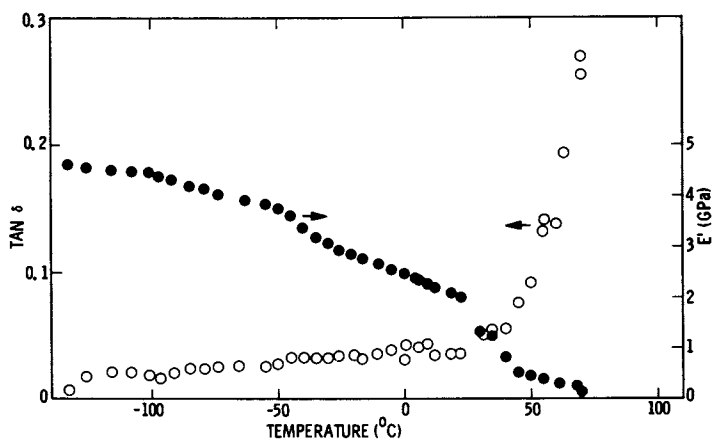
Figure 2. The storage modulus E^1 and tan δ for F-185 neat resin measured at 3.5 Hz.

more readily before cure with epoxy because of closer matching of
solubility parameters.

The plots of storage modulus and tan δ as a function of
temperature for the composites GD-48 and GD-31, shown in Figures
4-6, are very similar to the corresponding plots for the HX-205
and F-185 neat resins. Thus the dynamic mechanical properties
characterization indicates that the HX-205 material both as neat
resin and the matrix in GD-48 composite as well as F-185 neat
resin and matrix in GD-31 composite have similar states of cure.
For both F-185 neat resin and matrix extensive mixing of CTBN
rubber and epoxy resin occurs.

Figure 7 shows the polarized optical micrographs for HX-205
and F-185 resins. The F-185 resin has a large number of
inclusions of sizes greater than 40 μm. These inclusions which
are shown as the white regions are probably the rubber-rich
regions. In addition, there are many smaller domains which
probably represent both rubber-rich domains as well as
inhomogeneous regions in the epoxy-rich phase. These inhomoge-
neous regions in the epoxy phase are also present in the HX-205
neat resin.

Figure 8 shows the SEM micrographs of fracture surfaces of
both HX-205 and F-185 neat resins. The fracture surface of
HX-205 is very smooth, indicative of typical brittle fracture
behavior. On the other hand, F-185 has a very rough fracture
surface, indicating that the resin was highly strained before
fracture occurred. There are also some craters which appear to
represent the separation of spheroidal rubber domains from the
matrix.

SEM micrographs of interlaminar fracture surfaces of both the
HX-205/graphite fiber composite (GD-48) and the F-185/graphite
fiber composite (GD-31) are shown in Figure 9. The GD-48
laminate gave a relatively clean fracture with no sign of the
resin being strained before fracture occurred. On the other
hand, the GD-31 laminate exhibited a very rough fracture surface
with indications that some regions of the matrix were highly
strained before fracture. Figure 10 shows additional SEM micro-
graphs of the fracture surfaces of GD-31. This figure shows more
clearly the domains resembling the separation of rubber particles
from the matrix. In the GD-31 laminate, furthermore, there are
indications that the fracture may have propagated from one ply to
the adjacent plies as shown in Figure 11. The branching of
cracks from one ply to the adjacent ones has been reported (1).

The characteristics of fracture surfaces of F-185 neat resin
and those of F-185 matrix in the composites are similar to those
reported in the literature (1). The fact that the fracture
surfaces of F-185 neat resin and F-185 matrix in the composites
show typical ductile fracture behavior, while the unmodified
HX-205 shows brittle fracture behavior, seems to indicate the
toughening effect of F-185 as a result of incorporation of CTBN
rubber. The fracture energies of these materials are being
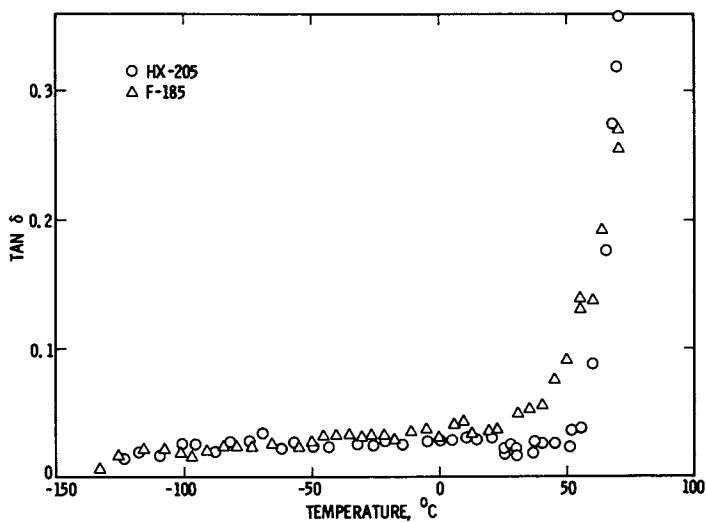
Figure 3. Comparison of tan δ for HX-205 and F-185 neat resins replotted from data in Figures 1 and 2.
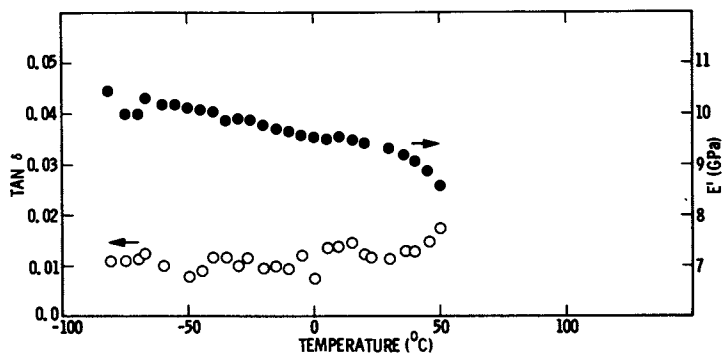
Figure 4. The storage modulus E^1 and tan δ for composite GD-48 measured at 3.5 Hz. The matrix is HX-205.
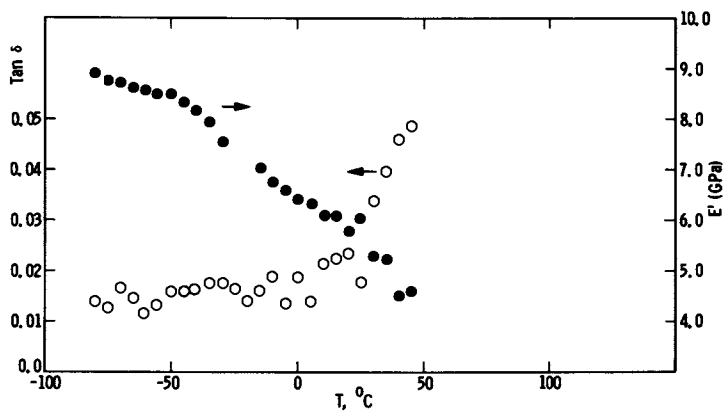
Figure 5.   The storage modulus E^1 and tan δ for composite
             GD-31 measured at 3.5 Hz.   The matrix is F-185.
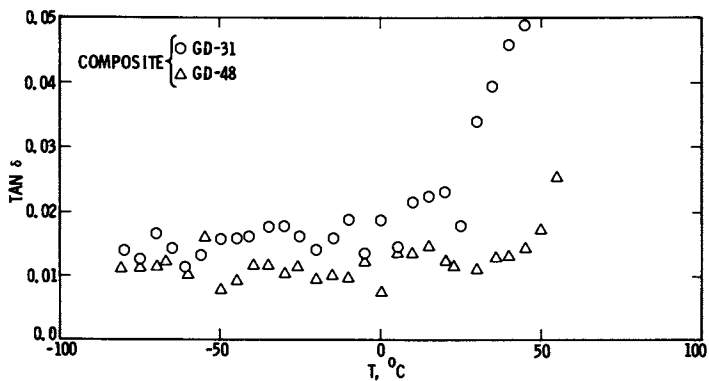
Figure 6.   Comparison of tan δ for composite GD-48 and
             GD-31 replotted from data in Figures 4 and 5.

HX–205   100 μm   F–185
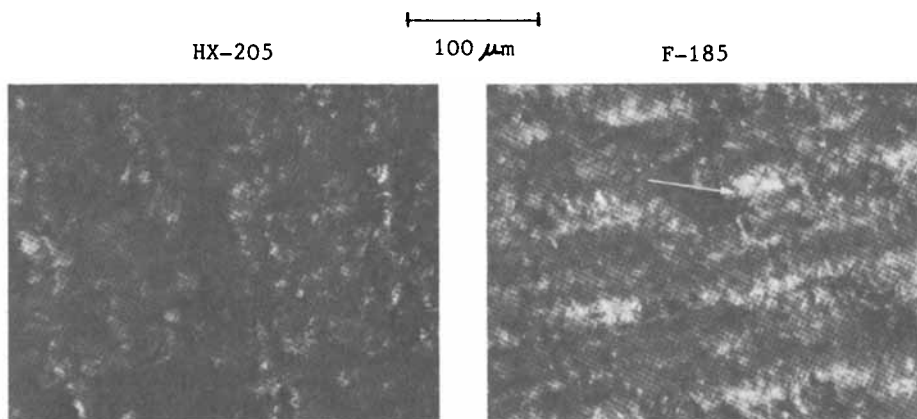
Figure 7. Polarized optical micrographs obtained from thin films of HX-205 and F-185 neat resins. The magnification is 224. The size of the largest domains is about 45 μm.

HX–205   F–185
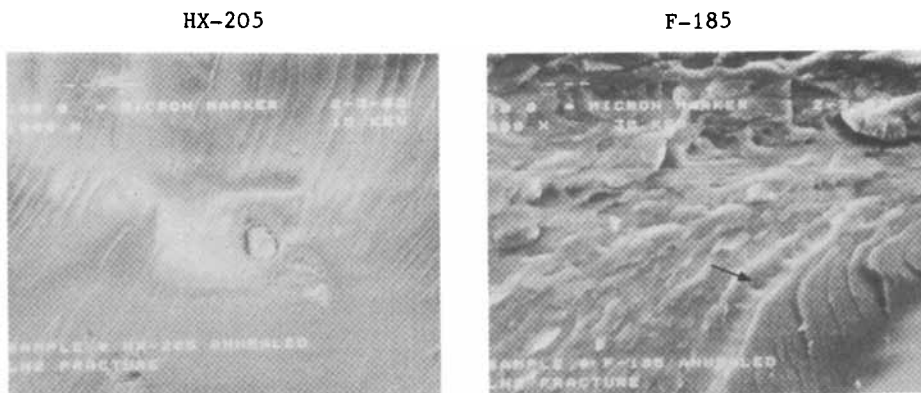
Figure 8. SEM micrographs of fracture surfaces of HX-205 and F-185 neat resins. The marker shown on the micrographs is 10 μm. The specimens were cooled in liquid nitrogen and then fractured in air immediately after removing from the liquid nitrogen.

HX-205/Graphite Fiber Composite   F-185/Graphite Fiber Composite
             (GD-48)   (GD-31)

Figure 9. SEM micrographs of the interlaminar fracture
            surfaces of the composites GD-48, whose matrix
            is HX-205, and GD-31, whose matrix is F-185.
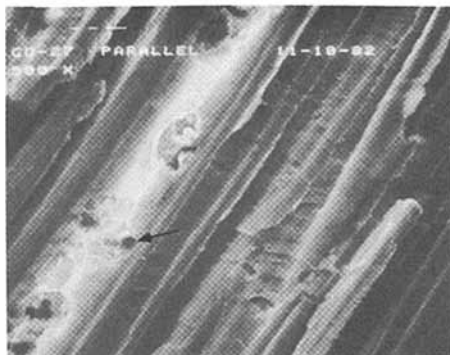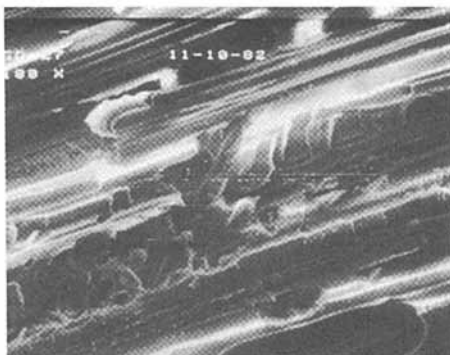
Figure 10. SEM micrographs of the interlaminar fracture
            surfaces of GD-31 composite. The domains
            resembling the separation of CTBN particles are
            clearly shown in the micrograph. The marker
            indicates 10 μm.
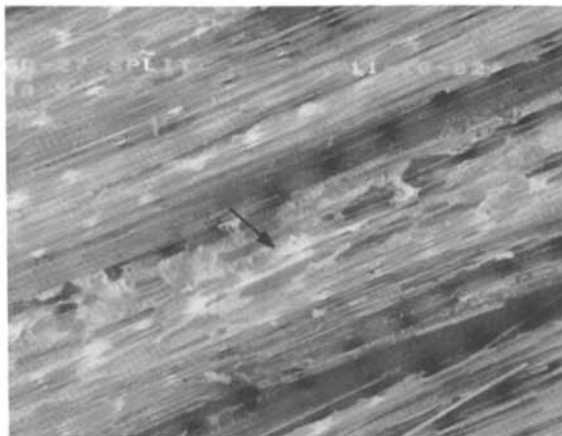
Figure 11. SEM micrograph of the interlaminar fracture
surface of GD-31 composite at lower
magnification. The cracks are shown to branch
from one ply to adjacent plies.

measured and will be reported in the future to correlate with the
morphology characterization. The details of the fracture
surfaces of F-185 neat resin and those of F-185 matrix in the
composites do not appear alike. However, the fine difference in
the fractographic appearances of F-185 neat resin and F-185
matrix in the composites can be due to morphological difference
of the CTBN-rich domains as well as other factors such as slight
differences in fracturing conditions and the presence of fiber,
etc. In order to determine whether or not the morphology of the
CTBN-rich domains in the neat resin and in the composite matrix
is smaller, small-angle X-ray scattering characterization was
carried out.

Results of small-angle X-ray scattering on both HX-205 and
F-185 neat resins as well as their corresponding composite are
shown in Figure 12. In the scattering angle range 0.7×10^{-3} to
40×10^{-3} radians, the F-185 neat resin has a higher scattering
intensity, by a factor of about 10 in the lower angle region,
than does the HX-205 neat resin. This indicates that, in
addition to the larger domains observed by optical microscopy and
SEM, there are smaller rubber-rich domains having sizes of the
order of 100Å to several thousand angstroms present in the
CTBN-toughened neat resin. A comparison of the scattering
profiles for both the F-185 neat resin and the GD-31 composite
indicates that both have nearly identical scattering intensity in
the region of scattering angle lower than 4×10^{-3} radians.
Considering the fact that the amount of F-185 material in the
GD-31 is only about half of that in the F-185 neat resin in terms
of volume, the scattering intensity per unit volume from the
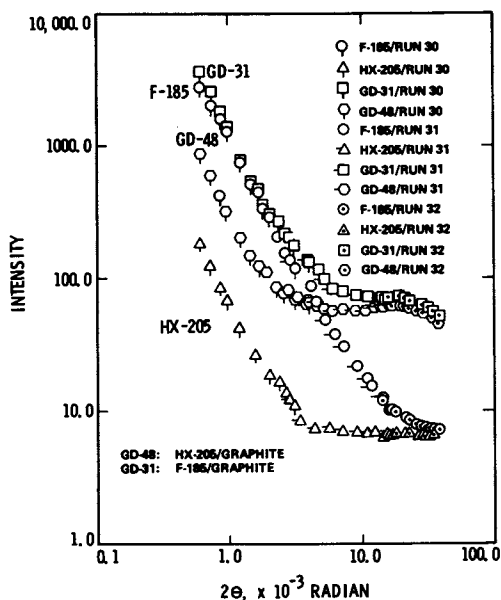
Figure 12. The scattering intensity of X-ray as a function
of scattering angle for HX-205 and F-185 neat
resins for the composites GD-48 and GD-31. The
run number indicates measurements carried out
at different scattering angle range.

F-185 in the composite is much higher than that from the F-185
neat resin. In order to analyze the contribution to scattering
intensity from the CTBN component, a theory recently developed by
Wu (21) will be utilized. The theory shows that in the high
angle region where the Porod law is applicable, the angle-
dependent scattering intensity for a multiphase system can be
expressed as follows:

$$I(h) \simeq I_e(h) \frac{2\pi}{h^4} \sum (\rho_i - \rho_j)^2 S_{ij} \qquad (1)$$

where $h = \frac{4\pi}{\lambda} \sin \theta$, θ is the scattering angle and λ the wave-
length. I_e is the scattered intensity of a single electron. ρ_i
is the electron density of phase i and S_{ij} is the total inter-
face area between phases i and j within the scattering volume.
To obtain the contribution to the scattering intensity from the
CTBN component one may subtract the scattering intensity due to
the epoxy phase from the scattering intensity of F-185. There-
fore for the neat resin one obtains

$$I_{FH} (h) = I_{F-185} - \nu\, I_{HX-205}$$

$$= I_e (h)\, \frac{2\pi}{h^4} \sum_i \left[(\rho_{e_i} - \rho_R)^2\, S_{e_i R} \right] \qquad (2)$$

where e_i represents the epoxy phase and R represents the CTBN phase. $\nu = 0.43$ is the volume fraction of epoxy resin in F-185. For the composite, one obtains

$$I^1 (h) = I_{GD-31}(h) - I_{GD-48}(h) + \nu^1\, I_{HX-205}$$

$$= I_e (h)\, \frac{2\pi}{h^4} \sum_j \left[(\rho_{e_j} - \rho_R)^2\, S_{e_j R} \right] \qquad (3)$$

where ν^1 which is taken equal to 0.08 takes into account the fact that there is a smaller amount of HX-205 resin in the GD-31 composite than in the GD-48 composite. The use of equation (3) is based on the assumption that the graphite fibers in the composite form a macroscopic domain, which seems reasonable since the diameter of the fiber is of the order of 10 μ; consequently equation (3) contains no contribution to the scattering intensity from the presence of fiber.

Figure 13 shows the plots of I_{FH} (h), which represents the neat resin, and I^1(h), which represents the corresponding composite. It is clear that the scattering intensity at a given scattering angle for the F-185 in the composite is much higher than that for the F-185 neat resin. Since the scattering intensity was measured in the scattering range where the scattering is produced mainly by domains ranging in size from approximately 50 Å to 1500 Å, the results indicate that there are more smaller CTBN domains in the F-185 matrix of the composite than in the F-185 neat resin. Since CTBN particles of several hundred angstroms are not very effective in improving the fracture toughness (6), the F-185 matrix of the composite will be characterized by a lower fracture toughness.

In conclusion, the HX-205 and F-185 neat resins and the corresponding composites (GD-48 using HX-205 as matrix and GD-31 using F-185 as matrix) appear to have the same state of cure as characterized by dynamic mechanical properties. It appears that the CTBN-rich domains in F-185 neat resin and F-185 matrix in the composite are extensively mixed with DGEBA epoxy resin. The F-185 resin has CTBN-rich domains with sizes ranging from 50 Å or smaller to 40 μm and larger. The F-185 material both as neat resin and matrix show a ductile fracture behavior, indicating a toughening effect due to incorporation of CTBN rubber. The morphology of the CTBN domains in the F-185 matrix, as determined by small-angle X-ray scattering, appears to be different from that in the neat resin. There is a larger fraction of smaller
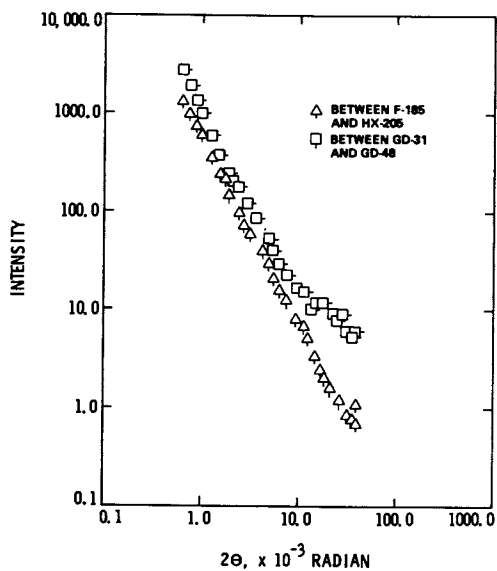
Figure 13. The scattering intensity difference as a function of scattering angle between F-185 and HX-205 neat resins, and between GD-31 and GD-48 composites.

sizes of CTBN domains existing in the F-185 matrix as compared to the corresponding F-185 neat resin. Because CTBN domains in the size range of the order of several hundred angstroms are less effective in increasing fracture toughness (6,8), this fact may partially explain the reported observation that some composites made with the CTBN-modified DGEBA epoxy resin did not show significant improvement in fracture toughness. It is emphasized that the neat resin as well as the corresponding matrix prepared from the identical resin material may not have similar morphology even when prepared using the same curing program.

Acknowledgments

Literature Cited

1. W. D. Bascom, J. L. Bitner, R. J. Moulton and A. R. Siebert, Composites, January 1980, 9.
2. W. D. Bascom, R. J. Moulton, E. H. Rowe and A. R. Siebert, Org. Coat. Plast., Preprint, 1978, 39, 164.
3. F. J. McGarry, Proc. Roy. Soc. London, 1970, A319, p. 59.
4. E. H. Rowe, A. R. Siebert and R. S. Drake, Mod. Plast., 1970, 417, 110.
5. J. N. Sultan, R. C. Laible and F. J. McGarry, Appl. Polymer Symp., 1971, 16, 127.
6. J. N. Sultan and F. J. McGarry, Polym. Eng. Sci., 1973, 13, 29.
7. W. D. Bascom, R. L. Cottington, R. L. Jones and P. Peyser, J. Appl. Polymer Sci., 1975, 19, 2545.
8. C. K. Riew, E. H. Rowe, and A. R. Siebert, ACS ADVANCES IN CHEMISTRY, 1976, SERIES No. 154, p. 326.
9. C. B. Bucknall and T. Yoshii, Brit. Polym. J., 1978, 10, 53.
10. W. D. Bascom and D. L. Hunston, Plastic and Rubber Institute, London, Preprints, 1978, 1, p. 22.
11. G. B. McKenna, J. F. Mendell and F. J. McGarry, Soc. Plastic Industry, Ann. Tech. Conf., 1974, Section 13-C.
12. J. M. Scott and D. C. Phillips, J. Mat. Sci., 1975, 10, 551.
13. A. C. Meeks, Polymer, 1974, 15, 675.
14. T. T. Wang and H. M. Zupko, J. Appl. Polym. Sci., 1981, 26, 2391.
15. F. Hopfgarten, Fiber Sci. Technol., 1978, 11, 67.
16. G. E. Hammer and L. T. Drzal, Applications of Surface Science, 1980, 4, 340.
17. R. Drake and A. Siebert, SAMPE Quarterly, July 1975, 6, No. 4.

18. A. Siehert, Private communication.
19. J. N. Sultan and F. J. McGarry, Research Report R68-8,
     School of Engineering, Massachusetts Institute of Technology
     (1968).
20. L. T. Manzione, J. K. Gillham and C. A. McPherson, ACS Pre-
     prints, Div. Org. Coat. Plast. Chem., 1979, 41, 364.
21. W. L. Wu, Polymer, 1982, 23, 1907.

Mechanical Behavior of Some Epoxies with Epoxidized Natural Oils as Reactive Diluents

SHAHID QURESHI[1], J. A. MANSON, J. C. MICHEL, R. W. HERTZBERG, and L. H. SPERLING

Materials Research Center No. 32, Lehigh University, Bethlehem, PA 18015

Several epoxidized botanical oils (linseed, crambe, and lunaria oils) were used as reactive diluents for typical bisphenol-A-based and cycloaliphatic prepolymers using nadic methyl anhydride as curing agent; such use of the latter two oils has not been described before. The effects of oil type and content on viscoelastic, stress-strain and fatigue crack propagation response were examined. A wide range of behavior was obtained, depending on the base epoxy, concentration of diluent, and the oxirane content. For example with 25% epoxidized crambe and lunaria oils, significant improvements in resistance to fatigue crack propagation were achieved without significant sacrifice in tensile or impact strength and Young's modulus, and with only a slight decrease in T_g in the case of a cycloaliphatic base resin.

In recent years, interest in monomers based on renewable resources has increased (1-4). Some of this interest has been related to concern over the long-term future of petrochemicals, while some such monomers, e.g., sebacic acid and drying oils, have long been valuable per se. Reflecting both of these factors, a program was begun several years ago in this laboratory to investigate the use of several triglyceride botanical oils (especially castor, crambe, lesquerella, linseed, vernonia, and lunaria oils) as the precursors of elastomer networks which were then combined with polystyrene to yield elastomer/plastic interpenetrating polymer networks (5-10). In the case of oils containing no hydroxy or epoxy functional groups functionality for crosslinking was provided by epoxidation of the carbon-carbon double bonds in the triglyceride oils.

[1]Current address: Union Carbide Corporation, P.O. Box 670, Bound Brook, NJ 08805.

In view of the functionality thus created, it is interesting
to consider possible applications for the epoxidized oils men-
tioned as epoxy monomers per se. Indeed, some epoxidized oils
are commonly used as reactive diluents for other epoxy prepolymers
in order to reduce cost or improve processability (10,11);
examples claimed in reference 11 include epoxidized linseed,
butylated linseed, soybean, and tall oils. However, although
some fundamental studies of the effects of monofunctional reactive
diluents on the viscoelastic and other properties of epoxy resins
have been published (see, for example, reference 12), little or
no analogous information on the effects of multifunctional reac-
tive diluents appears to exist. At the same time, some reactive
additives such as polyols (13), poly(ether esters) (14) and
carboxy-terminated elastomers (15) have been used to provide an
elastomeric toughening phase for epoxies.

Thus it was decided to examine the viscoelastic response and
ultimate mechanical behavior of several systems based on a typical
cycloaliphatic and a bisphenol-A-type epoxy prepolymer, using a
variety of epoxidized botanical oils as reactive diluents. This
paper describes the first results of this investigation, in which
epoxidized linseed, lunaria, and crambe oils were selected as
diluents.

Experimental

Materials

Prepolymers, Curing Agent, and Catalysts. Prepolymers ERL-4221
(cycloaliphatic type, Union Carbide Corporation) and D.E.R.331
(bisphenol-A type, Dow Chemical Company) were selected. The
nominal structures are as follows:
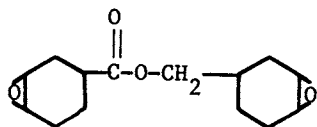
ERL-4221 (13)
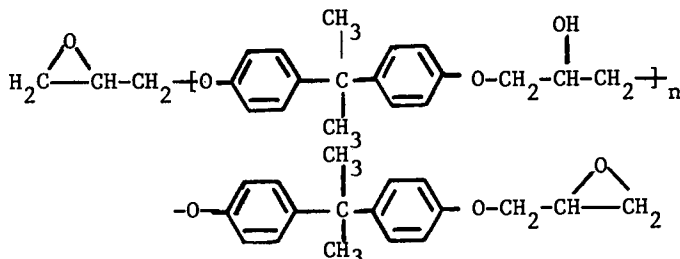
D.E.R.331; n∿0.15 (16)

Nadic methyl anhydride (NMA) (Allied Chemical) was used as the curing agent, while benzyl dimethylamine (BDMA) (Fisher Scientific Co.) and a quaternary ammonium salt, Arquad 18-50 (QA) (Armack Chemical Co.) were used as catalysts.

Purified crambe and lunaria oils were supplied by the U.S. Department of Agriculture; epoxidized linseed oil was obtained from the Swift Specialty Products Division, Eschem, Inc. The structures of the principal triglycerides present are:

crambe:
$$CH_2-O-\overset{\overset{\displaystyle O}{\|}}{C}-(CH_2)_{11}-CH=CH-(CH_2)_7-CH_3$$
$$CH-O-\overset{\overset{\displaystyle O}{\|}}{C}-(CH_2)_{11}-CH=CH-(CH_2)_7-CH_3$$
$$CH_2-O-\overset{\overset{\displaystyle O}{\|}}{C}-(CH_2)_{11}-CH=CH-(CH_2)_7-CH_3$$

linseed:
$$CH_2-O-\overset{\overset{\displaystyle O}{\|}}{C}-(CH_2)_7-CH=CH-CH_2-CH=CH-CH_2=CH=CH-CH_2-CH_3$$
$$CH-O-\overset{\overset{\displaystyle O}{\|}}{C}-(CH_2)_7-CH=CH-CH_2-CH=CH-CH_2-CH=CH-CH_2-CH_3$$
$$CH_2-O-\overset{\overset{\displaystyle O}{\|}}{C}-(CH_2)_7-CH=CH-CH_2-CH=CH-CH_2-CH=CH-CH_2-CH_3$$

lunaria:
$$CH_2-O-\overset{\overset{\displaystyle O}{\|}}{C}-(CH_2)_{13}-CH=CH-(CH_2)_7-CH_3$$
$$CH-O-\overset{\overset{\displaystyle O}{\|}}{C}-(CH_2)_{13}-CH=CH-(CH_2)_7-CH_3$$
$$CH_2-O-\overset{\overset{\displaystyle O}{\|}}{C}-(CH_2)_{13}-CH=CH-(CH_2)_7-CH_3$$
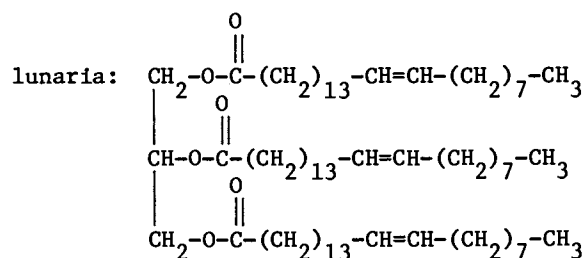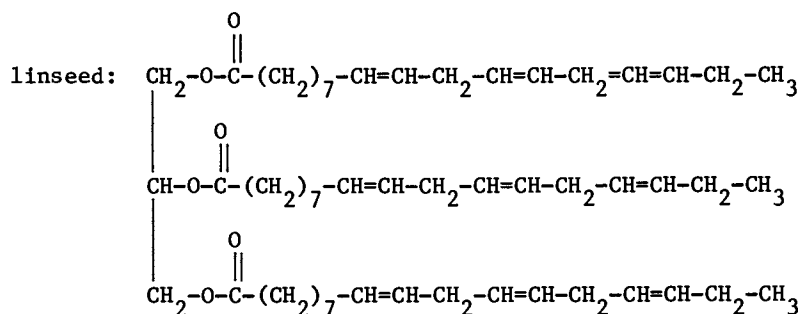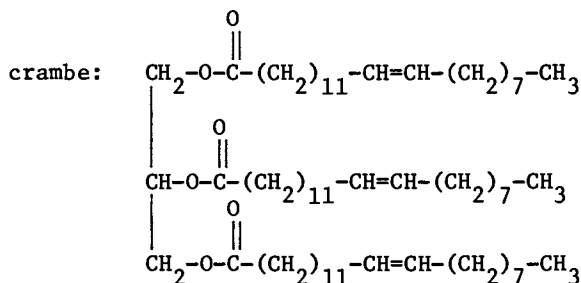
It may be noted that in addition to containing about 49 percent of the linolenic fatty acid as the triglyceride shown above, linseed oil also contains significant quantities of linoleic (9,12-octadecadienoic) and oleic (9-octadecenoic) acids – about 17 and 24 percent, respectively.

Iodine and acid values obtained by standard titration methods
(17,18) are given in Table I, along with approximate values of
epoxy equivalent weights and oxirane and double bond contents,
for the epoxidized crambe and lunaria oils, and for a typical
epoxidized commercial linseed oil.

Epoxidation

Epoxidation of botanical oils was carried out using hydrogen
peroxide, acetic acid, and an ion-exchange (cationic) catalyst,
in this case Dowex 50W-X-8, which yields a rapid establishment
of equilibrium. The epoxidation reaction is shown below:

$$CH_3-\overset{\overset{\text{O}}{\|}}{C}-OH+H_2O_2 \rightarrow CH_3-\overset{\overset{\text{O}}{\|}}{C}-O-OH+H_2O \tag{1}$$

$$CH_3-\overset{\overset{\text{O}}{\|}}{C}-O-OH+-CH=CH- \rightarrow -\overset{\overset{\text{O}}{/\backslash}}{CH-CH}-+CH_3-\overset{\overset{\text{O}}{\|}}{C}-OH \tag{2}$$
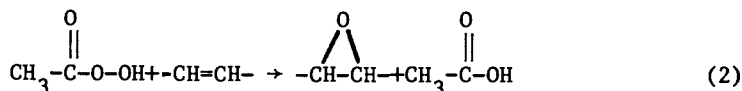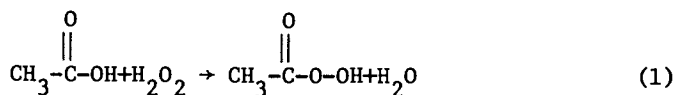
Following immersion in glacial acetic acid and slow agitation for
3-4 hrs, the ion-exchange resin was filtered from the acetic acid,
washed thoroughly with acetone, and air-dried. The subsequent
procedure is as follows for the case of crambe oil having 3.5
double bonds per molecule [as determined by the iodometric analy-
sis (17)]. Sixty g of dried resin and 70 g of glacial acetic
acid were charged to a two-liter three-necked flask equipped for
mechanical agitation. The flask was immersed in a water bath
equipped with automatic heating and cooling, and 400 g of oil and
171 g of toluene were then added. The contents were agitated at
a moderate rate and the bath temperature was set at 60°C. After
the system attained equilibrium, 170 ml of 50% hydrogen peroxide
were added dropwise over a period of 3-4 hours. The addition had
to be slow in order to maintain control of the temperature.
After stirring for 5-7 hours, the resin was filtered out and the
oil and aqueous phases were separated by gravity. The oil phase
was washed several times with hot water and 0.1 N aqueous Na_2CO_3.
The toluene and water were removed from the neutralized oil layer
using a rotary evaporator, and the epoxidized oil was filtered.
    As shown in Table I, oxirane contents of 5.5 and 4.0% were
obtained for the epoxidized crambe (ECrO) and lunaria (ELuO) oils,
respectively. The epoxidized linseed oil was used as received,
and had an oxirane content of 9.5%; epoxidation of linseed oil by
the method above was also possible.

Polymerization

The liquid epoxy mixture, i.e. 100 g of the D.E.R.331 or ERL-4221

Table I. Epoxidation of Botanical Oils

Oil	Iodine Value[a]	Iodine Value[b]	Acid Value[c]	% Ox.	Epoxy Equiv. Wt.(approx.)	Av. functionality, moles epoxy / mole of oil	% Epoxidation	% Conversion of double bond
Linseed	173	3.0	0.21	9.5	179	5.5	84-92	98
Crambe	87	4.2	2.29	5.5	288	3.4	90-93	95.2
Lunaria	76	1.8	0.92	4.0	397	2.7	∿ -91	97.6

[a] A measure of the ethylenic unsaturation of botanical oils.

[b] After epoxidation.

[c] A measure of oxirane content.

prepolymers with the desired amount of epoxidized oil, was mixed
at 120°C with 100 g NMA along with 1 g of catalyst, degassed,
and poured between glass plates (10 x 10 x 6 to 12 mm), using
0.7-mm Mylar sheets for mold release purposes. Specimens were
then cured for 2 hr at 120°C and 4 hr at 140°C, and demolded.
The mixture proportions were such that the components of the neat
ERL-4221 system were present in nearly stoichiometric quantities,
while the neat D.E.R.331 system had the hardener in excess.
The maximum cure temperature was limited to 140°C to ensure mini-
mum homopolymerization of the epoxidized oils. Gel times were
determined in separate experiments at 120°C by noting the time
required for gelation to prevent stirring.

Characterization

Plots of shear modulus vs temperature were made using a Gehman
torsional tester (ASTM D 1053-61); dynamic mechanical spectra
(DMS) were obtained at 110 Hz using an Autovibron DDV IIIC. With
this instrument, values obtained for T_g have generally been
reproducible to within ±2°C. Stress-strain behavior was deter-
mined using an Instron tester (ASTM D 638-68; rate, 0.085 mm/s),
and notched Izod impact tests were made (ASTM D 256-73). Tests
of fatigue crack propagation (FCP) rates were conducted at 10 Hz
(min/max load = 0.1) using notched specimens, a sinusoidal wave
form, and standard procedures (19). FCP rates were plotted in
terms of the crack growth rate per cycle (da/dN), as a function
of the stress intensity factor range, ΔK, following the Paris
equation (20) [da/dN = $A\Delta K^n$]. Here ΔK is given by K = $Y\Delta\sigma\sqrt{a}$,
where Y is a geometrical factor, Δσ the range in applied stress
and a the crack length.

Results and Discussion

Polymerization

Gel times are given in Table II. It may be seen that the diluents
retarded gelation somewhat in all cases, though the effects were
smallest in the ERL-4221/AQ and D.E.R.331/AQ systems. Also, the
gel times were much less with the AQ than with the BDMA catalyst
(22-30 min. compared to 85-125 min.) Subsequent studies were
restricted to the use of the AQ catalyst.

Viscoelastic Response

T_g Behavior. As shown in Figures 1 and 2 all the D.E.R.331/ECrO
systems exhibited single glass-to-rubber transitions; the resins
were also quite clear in appearance. Thus it was concluded that
in these systems the epoxidized oil acted as a relatively miscible
internal plasticizer. At the same time, the increasing breadth
of the transition with increasing ECrO content suggests the onset
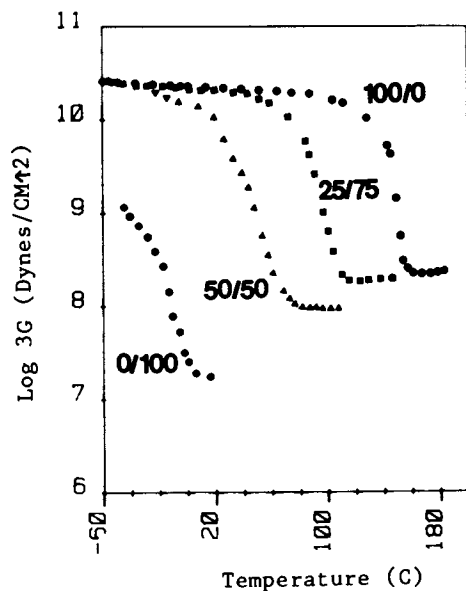
Figure 1. Modulus-temperature plots for DER 331/crambe systems (E 3G).
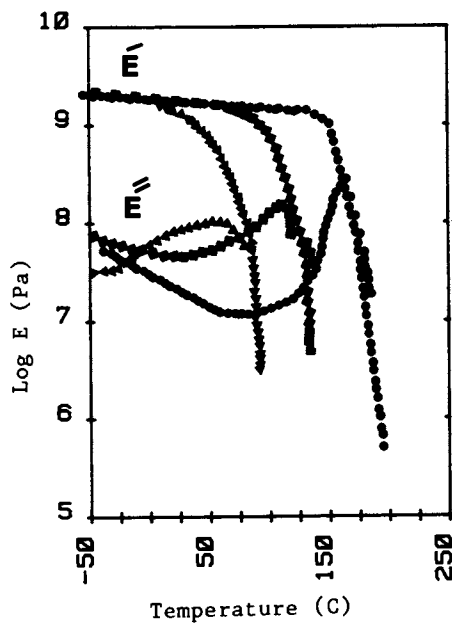
Figure 2. Dynamic mechanical behavior (at 110Hz) of DER 331/crambe systems: ●, 0/100; ■, 25/75; ▲, 50/50.

Table II.   Gel Times at 120°C for Epoxide-epoxidized Oil Systems
            Cured with Nadic Methyl Anhydride

Composition	Gel time,[a] min	Gel time,[b] min	Composition	Gel time,[b] min
100/0 ERL-4221 Control	85	22	100/0 D.E.R.331 Control	23
75/25 Epoxy/Linseed	105	22	75/25 Epoxy/Lunaria	25
75/25 Epoxy/Lunaria	---	23	75/25 Epoxy/Crambe	24
75/25 Epoxy/Crambe	---	25	50/50 Epoxy/Crambe	27
50/50 Epoxy/Crambe	---	30		
50/50 Epoxy/Linseed	125	--		

[a] Catalyst: benzyl dimethylamine.
[b] Catalyst: Arquad quarternary ammonium salt.

of some small-scale heterogeneity, even though no opacity was
evident to the eye. Generally similar behavior was seen with the
D.E.R.331/ELuO system (Figure 3), but in this case some opacity
was seen.
        The glass transition temperatures themselves were, of course,
lowered by the presence of the epoxidized oil (Table III). With the
D.E.R.331/ECrO system, the T_g's followed equation (1) very well:

$$T_g = W_A T_{gA} + W_B T_{gB} \qquad (1)$$

Where W is the weight fraction, and the subscripts A and B refer
to the oil and epoxy prepolymer components.
        Experimental points fell 10 to 15°C above the calculated
curve for Equation (2) (commonly used for predicting T_g's in
polymer blends or copolymers), while Equation (3) predicted much
lower values than those observed:

$$T_g = V_A T_{gA} + V_B T_{gB} \qquad (2)$$

$$\frac{1}{T_g} = \frac{W_A}{T_{gA}} + \frac{W_B}{T_{gB}} \qquad (3)$$
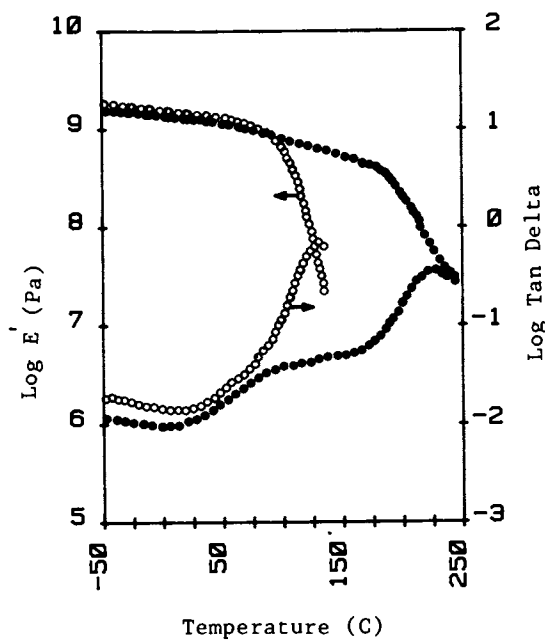
Figure 3. Effect of type of epoxy on dynamic mechanical response at 110 Hz: •, 75/25 ERL 4221/lunaria; o, DER 331/lunaria.

TABLE III. Glass Transitions for Base Epoxy/Diluent Systems.

Composition	T_g,°C[a]	Composition	T_g,°C[a]
100/0 D.E.R.331 Control	152(163)	100/0 ERL-4221 Control	206(225)
75/25 Crambe	96(108)	75/25 Crambe	188(198)
75/25 Lunaria	--(115)	75/25 Lunaria	---(206)
50/50 Crambe	50(57)	75/25 Linseed	195(206)
0/100 Crambe	-50(-37)[b]	50/50 Crambe	---(190)
0/100 Lunaria	--(-30)[b]	50/50 Linseed	---(190)
		0/100 Linseed	---(20)

[a]First value by Gehman tester; second by DMS.   [b]Estimated.

With the one D.E.R.331/ELuO system studied, the T_g was about 7°C higher than for the corresponding ECrO-based resin. Quite different behavior was noted with the cycloaliphatic system based on ERL-4221 (Figures 3-5). The transition regions were much broader with both the control and diluted systems; in addition secondary loss peaks were observed below the major ones. The secondary peaks shift upwards with increasing concentration of the base epoxy, while the major peaks shift downwards. While this behavior is typical of many semi-miscible systems, the control resin also showed a secondary peak. Furthermore, although a repeated DMS test on one specimen (75/25 ERL-4221 ELO) resulted in an increase in T_g from 196 to 236°C, the shapes of the curves were essentially unchanged. The most likely explanation is the development of significant small-scale heterogeneity, even though the samples were transparent to the eye. Clearly further study is required to interpret the spectra. (Studies of morphology are in progress by SEM; so far, evidence of some phase separation has been confirmed in the 75/25 D.E.R.331/Lunaria system.)

Such a conclusion is supported by the fact that the T_g's of all the ERL-4221 systems are much higher than predicted by any of the rules of mixtures (Equations 1 to 3). Indeed even with 50% of diluent, the T_g of the resin was reduced relatively little in comparison with that of the neat resin. This certainly suggests the likelihood of a phase-separated oil-based component. One might well expect a sigmoidal curve of T_g vs concentration of epoxy prepolymer if the epoxy resin constitutes the continuous phase; a phase inversion would then be expected at some value of epoxy resin content.

Dynamic Response. Values of the storage modulus, E', at room temperature in ERL-4221 systems decreased slightly as the proportion of diluent was increased, from 1.9 GPa (control) to 1.8, 1.6, and 1.5 GPa for 75/25 systems based on ELO, ECrO, and ELuO, respectively. With 50/50 ELO and ECrO systems, E' decreased slightly more, to 1.6 and 1.4 MPa, respectively. This slight
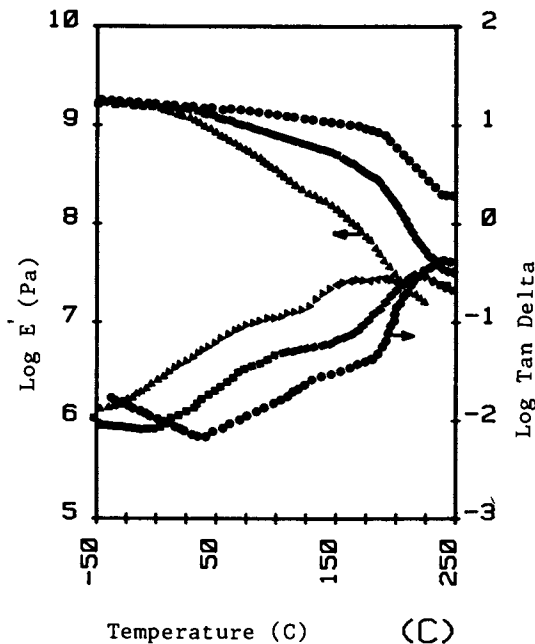
Figure 4. Dynamic mechanical behavior (at 110Hz) of ERL 4221/crambe systems: ●, 100/0; ■, 75/25; ▲, 50/50.
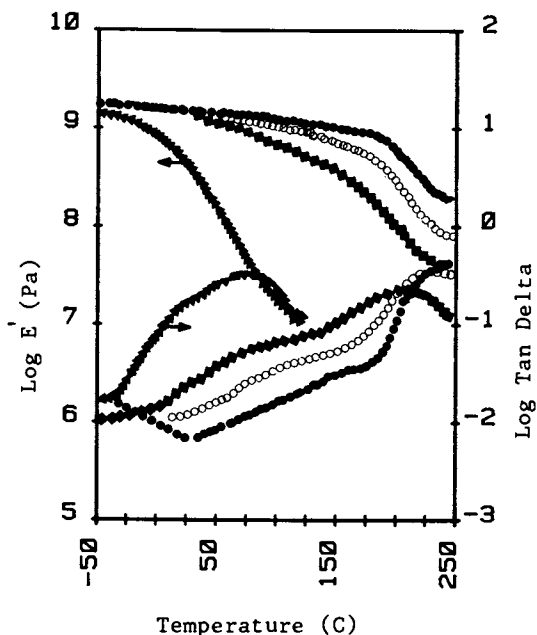
Figure 5. Dynamic mechanical behavior (at 110 Hz) of ERL 4221/linseed systems: ●, 100/0; o, 75/25; ■, 50/50; ▲, 0/100.

decrease may reflect a somewhat less effective chain packing in the diluent systems. (See Table IV.)

Table IV. Viscoelastic Data from DMS for ERL-4221/Epoxidized Oil Networks

Composition	tan δ(max) at 25°C	E' at 25°C (GPa)	E' at 250°C (GPa)	$M_c = \frac{3d}{E'}RT$ [a]
100/0 ERL-4221 Control	0.01	1.9	2.2	0
75/25 Linseed	0.013	1.8	0.9	150
75/25 Crambe	0.014	1.6	0.4	360
75/25 Lunaria	0.012	1.5	0.4	360
50/50 Linseed	0.024	1.6	0.5	290
50/50 Crambe	0.05	1.4	0.08	1700

[a] E' arbitrarily taken at 250°C

Much larger changes were seen in the value of E' at 250°C; this value may be taken as a relative inverse measure of cross-link density. Indeed (again with ERL-4221 systems), E' (250) decreased from 0.22 GPa for the control to 930, 380 and 380 MPa for 75/25 systems based on ELO, ECrO, and ELuO, respectively, and to 470 and 80 MPa for 50/50 systems based on ELO and ECrO, respectively. Thus the diluents reduced the crosslink density 2 to 3-fold at a 25% concentration, and 5-fold or more at 50% concentration. The reduction depends on the oil concerned; ECrO and ELuO have greater effects than ELO. This is not surprising, for the ELO used had the highest oxirane content, and the shortest chain length between possible crosslink sites, corresponding to a minimum of 20 atoms. In contrast, the chain lengths between possible crosslink sites in the crambe and lunaria oils are not very different, corresponding to 28 and 32 atoms, respectively.

Ultimate Mechanical Behavior

Stress-strain Response. As shown in Table V, the incorporation of the reactive diluent to a level of 25% resulted in a slight decrease in Young's modulus, an increase in % elongation at break, and little or no effect on tensile strength. However, the plasticizing effect of the diluent becomes quite marked at a diluent concentration of 50%. At this concentration, the crambe

diluent has a greater effect than ELO, perhaps because the crambe component contributes greater mobility (lower crosslink density— see above).

Because of the higher elongations at break (ϵ_B), the overall energy to fracture (area under the stress-strain curve) tended to be increased somewhat by all the diluents (at 25% concentration) except ELO; again this probably reflects the higher crosslink density associated with the latter.

In all cases, impact strengths were essentially unchanged by the presence of the diluent, at least at all concentrations studied. Thus at the high strain rate characteristic of the impact test, any differences in the low-strain-rate stress-strain response associated with different systems are overwhelmed.

Table V. Stress-strain and Impact Behavior of Base Epoxy/Diluent Systems

Composition	TS, MPa	ϵ_b, %	E, MPa	IS, J/m
100/0 ERL-4221 (Control)	54	9	830	11
75/25 Linseed	48	7	820	12
75/25 Lunaria	53	10	760	13
75/25 Crambe	53	12	760	12
50/50 Linseed	32	10	520	10
50/50 Crambe	24	17	330	13
100/0 D.E.R.331 (Control)	57	8	900	12
75/25 Lunaria	58	12	870	13
75/25 Crambe	57	12	800	12
50/50 Crambe	24	30	300	11

Fatigue Response. As shown in Figure 6, significant differences in FCP response were observed. With 75/25 ERL-4221/diluent systems, the incorporation of ECrO and ELuO resulted in a lowering of FCP rates at a constant ΔK by a factor of up to 3. At the same time, the maximum value of ΔK possible, ΔK_{max}, (a measure of static fracture toughness) was increased by up to ~25%. On the other hand, ELO conferred no benefit, again probably because of the higher crosslink density and consequently lower capacity for dissipating energy. With 75/25 DER 331/diluent systems (Fig.7), the FCP curves diverge, so that as ΔK increases, the ECrO and ELuO systems become relatively more and more resistant to FCP, both in terms of lower FCP rates and ΔK_{max}. With 50/50 D.E.R.331/ ECrO, on the other hand, FCP rates are increased at a constant ΔK, though ΔK_{max} is increased and the FCP rate at ΔK_{max} approaches that of the ELuO system.

Thus, while the incorporation of diluents has little effect on impact strength at a 25% concentration, both ECrO and ELuO yield significant improvements in FCP behavior. Such a distinction between the relative effects of composition on impact (high

Figure 6. Fatigue crack prop-
agation response of systems
based on ERL 4221 epoxy: ●,
0/100; dark star, 25/75,
crambe; white star, 25/75,
lunaria; ☐ , 25/75, linseed;
0, 50/50, linseed; and star
in circle, 50/50, crambe.
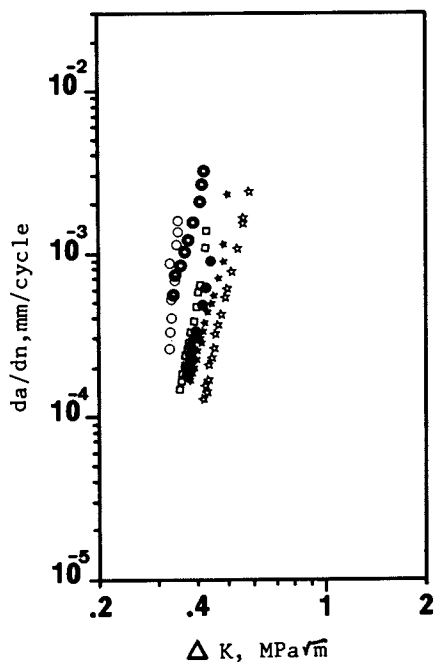
Figure 7. Fatigue crack prop-
agation response of systems
based on DER 331 epoxy: ●,
0/100; dark star, 25/75,
crambe; white star, 25/75,
lunaria; and star in circle,
50/50, crambe.
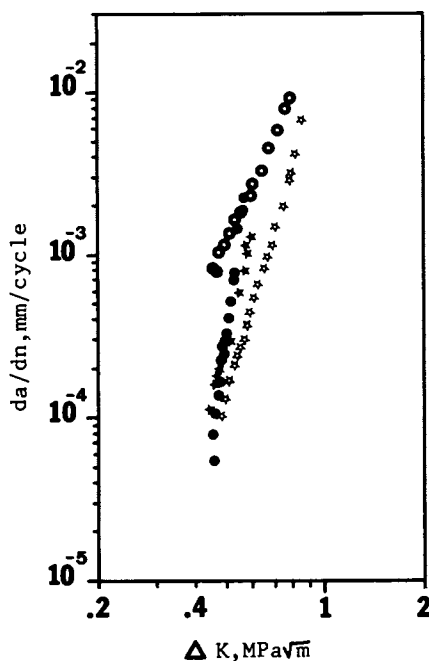
strain rate) and fatigue (low strain rate) has been noted before (19). At higher levels, the associated decrease in modulus probably is responsible for the decreased fatigue resistance observed.

One other interesting observation may be made. Whereas in some cases, the resins did not unmold from the Mylar sheet, the FCP rate (not shown) was decreased by several orders of magnitude. Evidently such lamination can dissipate very large amounts of energy that would otherwise be available to drive the crack.

Conclusions

It may be concluded that epoxidized crambe and lunaria oils can be used as reactive diluents for typical bisphenol-A-type and cycloaliphatic epoxies. A wide range of viscoelastic behavior may be obtained, depending on the base epoxy, concentration of diluent, and the oxirane content. For example, with 25% epoxidized crambe and lunaria oils, significant improvements in resistance to fatigue crack propagation can be achieved without much sacrifice in tensile or impact strength and Young's modulus, and with only a slight decrease in T_g in the case of a cycloaliphatic base resin.

Acknowledgments

Literature Cited

1. Princen, L. H. J. Coatings Tech. 1977, 49(12), 88.
2. "Renewable Resources for Industrial Materials," National Research Council, National Academy of Sciences, Washington, DC, 1976.
3. Pierce, L.E.; Brown, G.R., eds., "Future Sources of Organic Raw Materials," Pergamon Press, New York, 1980.
4. Carraher, C.; Sperling, L. H. "Use of Regenerable Raw Materials for Coatings and Plastics," Plenum Press, New York, 1982.
5. Yenwo, G.M.; Manson, J.A.; Pulido, J.; Sperling, L.H.; Conde, A.; Devia, N. J. Appl. Polym. Sci. 1977, 21, 1531.
6. Devia, N.; Manson, J.A.; Sperling, L. H.; Conde, A. Polym. Eng. Sci. 1978, 18, 200.

7. Fernandez, A.M.; Murphy, C.J.; DeCrosta, M.T.; Manson, J.A.;
    Sperling, L. H., in "Use of Regenerable Raw Materials for
    Coatings and Plastics"; Carraher, C.; Sperling, L. H., Eds.;
    Plenum Press: New York, 1982.
8. Sperling, L. H.; Manson, J.A.; Qureshi, S.; Fernandez, A.M.
    Ind. Eng. Chem. Prod. Res. Dev., 1981, 20, 113.
9. Qureshi, S.; Manson, J.A.; Sperling, L.H.; Murphy, C.J.;
    in "Use of Regenerable Raw Materials for Coatings and
    Plastics"; Carraher, C.; Sperling, L. H., Eds.; Plenum Press:
    New York, 1982.
10. Brydson, J.A. "Plastics Materials"; 3rd ed. Newnes-
    Butterworth: London, 1975.
11. U.S. Patent 4,040,994, August 9, 1977.
12. Whiting, D.A.; Kline, D.E. J. Appl. Polym. Sci., 1974, 18,
    1043.
13. Anon.; "Cycloaliphatic Epoxide Systems"; Union Carbide
    Corporation, 1978.
14. Samejina, H.; Fukuzawa, T.; Toda, H.; Saga, M. Ind. Eng.
    Chem. Prod. Res. Dev., 1983, 22,10.
15. Drake, R. Org. Coat. Appl. Polym. Sci. Proc., 1983, 48, 490.
16. Anon.; "Dow Liquid Epoxy Resins", The Dow Chemical Company,
    1976.
17. ASTM D1959 (Wiji's method).
18. ASTM D1639.
19. Sperling, L. H.; Devia, N.; Manson, J.A.; Conde, A. ACS
    Symp. Ser., 1980, 121, 163.
20. Qureshi, S; Manson, J.A.; Hertzberg, R.W.; Sperling, L.H.
    Org. Coatings Appl. Polym. Sci. Proc. 1983, 48, 576.

Volume Recovery in Aerospace Epoxy Resins

Effects on Time-Dependent Properties of Carbon Fiber-Reinforced Epoxy Composites

ERIC S. W. KONG

Department of Materials Science and Engineering, Joint Institute for Surface and Microstructure Research, Stanford University/NASA-Ames Research Center, Stanford, CA 94305

Matrix-dominated physical and mechanical properties of a carbon-fiber-reinforced epoxy composite and a neat epoxy resin have been found to be affected by sub-T_g annealing in an inert dark atmosphere. Postcured specimens of Thornel 300 carbon-fiber/Fiberite 934 epoxy as well as Fiberite 934 epoxy resin were quenched from above T_g and annealed at 140°C, 110°C or 80°C, for times up to 10^5 minutes. No weight loss was observed during annealing at these temperatures. Significant variations were found in density, modulus, hardness, damping, moisture absorption ability, and thermal expansivity. Moisture-epoxy interactions were also studied. The kinetics of aging as well as the molecular aggregation during this densification process were monitored by differential scanning calorimetry, dynamic mechanical analysis, tensile testing, and solid state nuclear magnetic resonance spectroscopy.

Time-dependent variations have been observed in mechanical and physical properties of polymeric network epoxies and also carbon-fiber-reinforced composites with epoxy-matrices. These property variations are the result of differences in specimen preparation conditions and/or thermal histories which the materials have experienced ([1-7]). In general, with slower cooling rates from above the glass temperature, T_g, and/or increasing the sub-T_g annealing time, the density increases, while impact strength ([8]), fracture energy ([8]), ultimate elongation ([9]), mechanical damping ([5]), creep rates ([10]), and stress-relaxation rates ([5]) decrease.
    Of particular concern in the processing and wide-ranging application of structural epoxies is the loss of ductility of such materials on sub-T_g annealing, i.e., thermal aging at temperatures below the glass transition of epoxy resin. This sub-T_g annealing process, more commonly known as "physical aging" ([10]), is confirmed to be thermoreversible ([5]). That is, with a brief

anneal at temperatures in excess of the resin T_g, the thermal history of an aged epoxy can be erased. A subsequent quench from above T_g would render a "rejuvenated" epoxy. In other words, the polymer embrittles during sub-T_g annealing. But with an aging history erasure above T_g, the ductile behavior can be restored (5,10).

If epoxies are to be strong candidates as structural matrices for composite materials, it is of primary importance that an understanding of the nature of this volume recovery process as well as an assessment of the magnitude of its effects be achieved. To date, there is a general consensus that the property changes in glassy polymers on sub-T_g annealing are the result of relaxation phenomena associated with the non-equilibrium nature of the glassy state (11,12). However, a basic understanding of the changes at the molecular level is still lacking. Fortunately, substantial progress has been made in the past few years in characterizing the glassy state from the molecular point of view by powerful techniques such as proton-decoupled cross-polarized magic-angle-spinning (CP/MAS) nuclear magnetic resonance (NMR) spectroscopy (13). Combining such techniques with other conventional instrumental tools, which measure excess thermodynamic properties, it is now possible to ascertain the changes in properties that can be attributed to relaxations of excess thermodynamic state functions such as enthalpy and volume. This paper addresses the pertinent relations between excess thermodynamic properties and the time-dependent behavior of epoxy glasses. Also, an attempt is made to describe the molecular nature of this relaxation process.

Moisture is a well-known plasticizer for macromolecules (14). Specifically, water penetrates into an epoxy network and can lower the glass temperature of the resin (15). In this report, moisture has for the first time been utilized as a probe to characterize densification process during epoxy aging. Also, using the same rationale, heavy water diffused into the epoxy resin is used to study the interactions of moisture with the aging polymer by hydrogen-2 (deuterium) NMR spectroscopy.

Experimental

The epoxy used in this study was Fiberite 934 resin supplied by Fiberite Corporation, Winona, Minnesota, U.S.A. The chemical formulation of this resin is shown in Figure 1. The chemical constituents are 63.2% by weight of tetraglycidyl- 4,4'-diaminodiphenyl methane (TGDDM tetrafunctional epoxy), 11.2% of diglycidyl ortho-phthalate (DGOP difunctional epoxy), 25.3% of the crosslinking agent 4,4'-diaminodiphenyl sulfone (DDS crosslinker), and 0.4% of the boron trifluoride/ethylamine catalyst complex (16,17). The neat epoxy resin was prepared by casting. The as-received B-stage material was subjected to degasification at 85°C inside a vacuum oven. The softened resin was then transferred into a preheated silicon-rubber mold. The curing schedule was 121°C
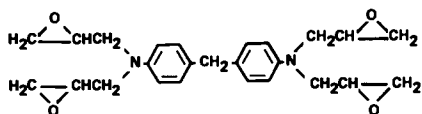
TETRAGLYCIDYL 4,4' DIAMINODIPHENYL METHANE (63.2%)
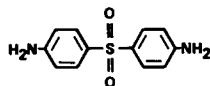
4,4' DIAMINODIPHENYL SULFONE (25.3%)
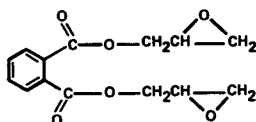
DIGLYCIDYL ORTHOPHTHALATE (11.2%)
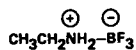
BORON TRIFLUORIDE/ETHYLAMINE COMPLEX (0.4%)

Figure 1. Chemical constituents of Fiberite 934 epoxy resin.

for 2 hours, 177°C for 2.5 hours, followed by a slow cooling at
ca. 0.5°C per minute to room temperature (23°C).

Thornel 300 carbon-fiber-reinforced Fiberite 934 epoxy lamin-
ates (ca. 60% fiber and 40% resin by volume) were fabricated from
prepreg tapes manufactured by Fiberite Corporation. The details
of this fabrication process have been disclosed elsewhere (4,5).

With the exception of five specimens (which were to be tested
in the as-fabricated condition), all specimens were postcured for
16 hours at 250°C, followed by a slow cooling to room temperature
at a rate of 0.5°C per minute. Testing was then performed on the
five as-postcured specimens. The other postcured specimens were
heated to 260°C for 20 minutes and then immediately air-quenched
to room temperature. Five of these quenched specimens were immed-
iately tested, others were sub-T_g annealed in darkness at either
80, 110 or 140°C (in nitrogen) for time increments of 10, 10^2, 10^3
10^4 and up to 10^5 min. The specimens were aged in darkness in
order to avoid any chemical aging due to uv irradiation. Time
zero was taken as the time when a mercury thermometer placed adja-
cent to the specimens reached the sub-T_g annealing temperature.
At each decade of aging time, five specimens were removed from the
environmental chamber and stored at room temperature prior to
testing.

In order to demonstrate the "thermoreversibility" of physical
aging, the following requenching procedure was carried out. Spe-
cifically, some 10^4 min.-aged specimens were heated to above T_g
for 20 minutes (260°C), followed by air quenching to room tempera-
ture. Five of these requenched specimens were tested immediately,
while the rest were subjected to "reaging" in darkness at either
80, 110 or 140°C in nitrogen for time increments of 10, 10^2, 10^3,
10^4 and up to 10^5 minutes. At least five specimens were tested
for each decade of aging time.

Time-dependent stress-strain behavior of the neat resins was
studied using an Instron 1122 tensile tester. Dog-bone-shaped
epoxy specimens were prepared in accordance to ASTM: D1708-66.
Strain rate used was 5 x 10^{-5} sec^{-1}.

Dynamic mechanical analysis was performed on 8-ply Thornel
300/Fiberite 934 composites that were symmetrically reinforced in
configuration of $(\pm45°)_{2s}$. A dynamic mechanical thermal analyzer
interfaced with a Hewlett Packard 85 computer was kindly supplied
by Professor R. E. Wetton of Polymer Laboratories, Loughorough
University, Loughborough, United Kingdom. This instrument util-
ized a sinusoidal bending mode of mechanical deformation on a
double cantilever beam (18). Both mechanical dispersions and
dynamic storage modulus were measured in nitrogen from −100°C to
300°C at 1 Hz and 5°C per minute heating rate.

Differential scanning calorimetry was used to measure both
the extent of cure as well as the progress of enthalpy recovery in
the neat epoxy resin. A Perkin Elmer DSC-2 differential scanning
calorimeter equipped with a scanning-auto-zero unit for baseline
optimization was utilized to measure the heat capacity of the

polymeric network glasses. Each disc-like, 0.8mm thick specimen of diameter 5mm was measured from 50 to 280°C in nitrogen at a heating rate of 10°C/min. Each specimen was scanned two times (160°C cooling rate from 280 to 50°C after the first scan). The enthalpy recovery measurements were made by superimposing the first and the second scans for each specimen using a data-analysis method suggested by M. G. Wyzgoski (19).

Density measurements were made at 23°C on spherical neat resins of 5mm diameter using the flotation method in accordance to ASTM: D-1505. The density gradient column (model DC1) was supplied by Techne Incorporated, Princeton, New Jersey. Calcium nitrate solution column was set up which could measure density that ranges from 1.210 to 1.290.

Hardness measurements were made on 500Å gold-decorated epoxy square plates (2.5cm. by 2.5cm., 2mm thick) using a Leitz miniload micro-hardness tester, supplied by Ernst Leitz Company, Midland, Ontario, Canada. A load of 200gm was applied to the specimen. Experiments were done in accordance to ASTM D-785 and ASTM D-1706 test procedures.

Thermal mechanical analysis was performed on 2.5mm thick neat epoxy discs of 6mm diameter using a Perkin Elmer TMS-2 analyzer. The expansion mode was utilized in order to study the thermal expansion behavior of the network epoxies. Each specimen was measured from 50°C to 260°C at 5°C per minute heating rate in helium atmosphere. Similar to the DSC experiment described earlier, each specimen was scanned twice from 50°C to 260°C. After the first scan, a cooling rate of 160°C per minute was utilized to quench the system from 260°C to 50°C. The first and second scans were then superimposed at the high-temperature "rubbery" domain in order to measure the volume recovery during sub-T_g annealing. Thermal expansivity was measured at the linear expansion regions below and above the epoxy glass temperature.

Moisture sorption kinetics by neat epoxies were measured using gravimetric analysis using a Mettler balance which was accurate to ±0.05mg. This technique was described in detail elsewhere (20). Another method was used to monitor the sorption kinetics of heavy water diffusing into neat epoxies. This technique involved the use of solid state hydrogen-2 NMR spectroscopy. By the use of the normalized free induction decay (FID) NMR signal one can readily determine the amount of heavy water sorbed by the epoxy specimen. Cylindrical-shaped 20mm-long epoxy specimens of 5mm diameter were immersed in heavy water at 23°C for 2 months and 40°C for 1 month before the NMR experiment. The hydrogen-2 NMR experiment involved locating the non-spinning heavy-water-saturated solid polymer in a magnetic field of 5 Tesla while pulsing the material with a radio frequency of 30.7 MHz. This technique was used to study moisture-epoxy interactions at the molecular level (14).

In order to study the molecular aggregation during the volume relaxation of network epoxies, CP/MAS carbon-13 (natural abundance)

NMR was utilized. The Hartman-Hahn cross-polarization technique
(21) was used with a cross-contact time of 1 msec for transfer of
proton polarization to carbon nuclei. The proton-decoupling was
achieved at the radio frequency of 56.4 MHz. Carbon-13 14.2 MHz
spectra were measured in a 1.4 Tesla magnetic field. Room tempera-
ture (23°C) experiments were performed at 54.7° MAS at 1 KHz. The
brittle, aged epoxies posed some experimental difficulties in
using higher spinning rates (e.g., 4 KHz) at which the spectrum
would have a higher resolution. The probe was constructed using a
double-tuned/single-coil circuitry. The spinner was constructed
using an Andrew-type rotor driven by compressed air.
      A Bruker WM-500 NMR Spectrometer was used to study the carbon-
13 resonances for epoxy components (TGDDM and DDS) dissolved in
deuterated chloroform (CDCL₃). TGDDM or DDS components were dis-
solved in solvent-containing 10mm NMR tube. 125 MHz carbon-13 NMR
spectra were measured at 23°C using a superconducting magnetic
field of 11.7 Tesla.

Results and Discussion

In previous communications (4,7,9,22), we reported the importance
of physical aging processes in affecting time-dependent changes in
mechanical properties of TGDDM-DDS network epoxies and their
carbon-fiber-reinforced composites. Recently, by means of a trans-
port experiment, we have demonstrated the time-dependent "free
volume collapse" in neat, fully-crosslinked TGDDM-DDS epoxies by
water diffusion experiments (6,23). In addition, the mechanical
damping and stress relaxation rates of such epoxies were observed
to decrease, while tensile modulus of the carbon-fiber-reinforced
epoxies was suggested to increase by our stress-relaxation studies
(22).
      In this paper, results from various instrumental techniques
will be discussed and critically reviewed. Thermal analysis per-
formed by differential scanning calorimetry (DSC) of as-cast epoxy
indicated the material was not fully crosslinked — an exotherm
with a maximum peak temperature at 263°C was detected during the
first scan from room temperature to 300°C, using a heating rate of
20°C per minute. Because it is obvious that continued "chemical
aging" such as an increase in crosslink density can change the
physical and mechanical properties of an epoxy, it was important
to this study that all possibilities of continuous chemical aging
be eliminated to permit a full evaluation of the effect of the
physical aging phenomenon on mechanical behavior. The Fiberite 934
epoxies and their composites were given a postcuring treatment
of 16 hours at 250°C in nitrogen. After postcuring, DSC confirmed
that the epoxy matrix was in a fully-cured state with a regular
step-function increase in heat capacity at a Tg range of 180°C to
270°C. This result was also confirmed using dynamic mechanical
analysis and Fourier transform infrared spectroscopy (24).

Stress-Strain Analysis

Tensile tests were performed on neat epoxy resins in the follow-
ing conditions: as-cast, as-postcured, as-quenched, and aged at
decade increments from 10 to 10^4 minutes at 140°C in nitrogen
while stored in darkness. A summary of the observed resin stress-
strain behavior is shown in Figure 2. As can be seen, the epoxy
polymer was found to be extremely sensitive to thermal history.
The as-cast specimens exhibited the highest value of ultimate-
tensile-strength (UTS) and by far the greatest values of strain-
to-break (ε_B) and toughness. Toughness here is defined as the
area under the stress-strain curve, which is different from the
dynamic toughness values obtained from impact tests. As reported
earlier in the carbon/epoxy composites investigations (4,23), the
postcuring treatment resulted in a significant reduction in these
mechanical properties. This effect is undoubtedly due to the
crosslinking reactions in the thermoset.
      Oddly enough, the postcured specimens given an air-quench
from above Tg exhibited a loss in strength, ductility and tough-
ness significantly greater than that of the as-postcured specimens
(Figure 2). This observation was unexpected, based on the free-
volume concept. A rapid quench will result in a larger deviation
from the equilibrium glassy state; thus, a relatively large amount
of free volume will be frozen into the epoxy. Because more free
volume can be interpreted to mean higher chain mobility and
shorter molecular relaxation time, an increase in free volume was
anticipated to result in an increase in epoxy tensile properties
instead of a severe decrease.
      Quenched specimens given a brief thermal annealing at 140°C
for 10 minutes were found to exhibit toughness similar to that
observed for as-postcured specimens (Table 1). Even though the
strength for 10 minutes annealed specimens was not totally
restored compared to the as-postcured specimens, the ductility
was much improved. One explanation for these observations is the
presence of residual thermal stresses, which can develop in the
bulk material as the result of rapid thermal changes. The skin
and the core of the bulk epoxy would experience different cooling
rates during the air-quench, and rapid cooling of the specimen
would not permit the time-dependent relaxation of these stresses.
The fact that a brief thermal annealing results in restoration of
epoxy tensile properties suggests that the residual thermal
stresses have been removed and have not caused irreversible damage
in specimen.
      Thermal annealing at 140°C in an inert dark atmosphere result-
ed in decreases in strength, ductility, and toughness, as seen in
Figure 2 and Table 1. These changes are attributed to physical
aging processes occurring in the glassy polymer. As an additional
check to assure that compositional changes were not occurring in
the polymer with thermal exposure, specimen weights were followed.
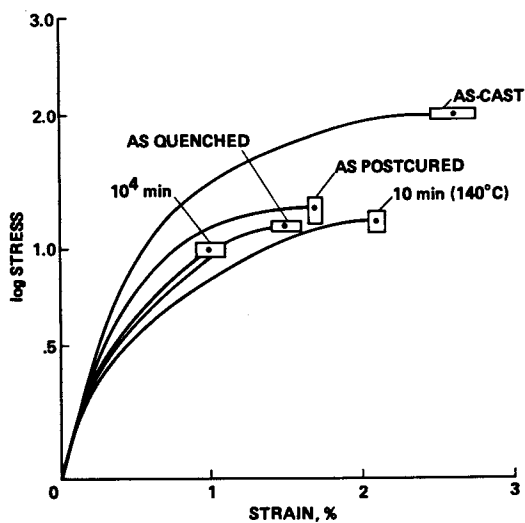
Figure 2. Stress–strain behavior of Fiberite 934 neat resins as a function of thermal history.

Table I. Mechanical properties of Fiberite 934 epoxy as a function of thermal history and sub-T_g annealing time.

THERMAL HISTORY	AS-CAST	POSTCURING 16 hr 523K (250°C)	ANNEALING 533K (20 min) +QUENCHING 296K (23°C)	SUB-Tg ANNEALING			
				10 min 413K (140°C) N₂ atm	10^2 min 413K (140°C) N₂ atm	10^3 min 413K (140°C) N₂ atm	10^4 min 413K (140°C) N₂ atm
UTS, MPa	102.20 ± 1.16	17.71 ± 1.14	13.76 ± 1.13	14.73 ± 1.11	13.30 ± 1.11	11.66 ± 1.19	9.50 ± 1.01
ϵ_B, %	2.6 ± 0.82	1.7 ± 0.90	1.5 ± 0.90	2.1 ± 0.58	1.6 ± 0.55	1.2 ± 0.55	1.0 ± 0.50
TOUGHNESS J/cm³	2.69	0.30	0.21	0.31	0.10	0.07	0.06
E, MPa	13000	12381	11063	11817	8965	8666	10399
σ_y, MPa	7.59	4.47	3.55	2.66	2.37	2.00	1.80

No resolvable weight change was observed in any of the aged specimens.

The effects of physical aging at 140°C on UTS and ε_B of Fiberite 934 epoxies are shown in Figures 3 and 4, respectively. The effects of thermal history on the ductility of network epoxies are summarized in Figure 5. The decreases in UTS and ε_B appear to be linear as a function of logarithmic aging time (see Figures 3 and 4). Toughness and yield strength (σ_y) also decreased with time (Table 1). The modulus (E) varied somewhat erratically, but was roughly constant.

Dynamic Mechanical Analysis

Dynamic mechanical analysis of polymeric materials, including epoxies (25-43), is an established tool in measuring the mechanical dispersion peaks as well as other parameters such as the dynamic storage modulus of the macromolecules. Wetton has reported some effects by sub-T_g annealing on the modulus and damping peaks a low-T_g epoxies (44). In this investigation of high-performance/high-T_g epoxy-matrix composites, we have observed a decrease in damping and an increase in dynamic storage modulus of the composite as a function of physical aging time (5). Figure 6 shows a specific example of a 140°C/10^2 min.-aged carbon/epoxy composite having a glass transition maximum peak temperature near 242°C. The onset of the T_g is near 175°C. This composite, which is $\pm 45^\circ$ carbon-fiber-reinforced, shows a dynamic storage modulus of the epoxy matrix in the glassy-state of ca. 15 GPa. At the onset of the glass-to-rubber transition (see Figure 6), the modulus drops gradually from 15 GPa (175°C) to about 3 GPa (300°C) as the rubbery plateau is reached.

With physical aging at 140°C in nitrogen/dark atmosphere, the dynamic storage modulus is very sensitive to aging time. The modulus increased from 13 GPa (10 min.-aged) to 18 GPa for samples aged up to 10^5 min. at 140°C (see Figure 7). These results agree with observations made in the stress relaxation experiments reported earlier (5) in which the epoxy tensile modulus increased with sub-T_g annealing.

The mechanical dispersion peaks in low-T_g epoxies such as Epon 828 resin have been the subject of numerous studies (26,28-31,35-38,42). The α peak can undoubtedly be attributed to the large-scale cooperative segmental motion of the macromolecules. The β relaxation near -55°C, however, has been the subject of much controversy (29,36). One postulated origin of the dispersion peak is the "crankshaft mechanism" (29,42,45) at the junction point of the network epoxies (Figure 8). The "crankshaft motion" for linear macromolecules was first proposed (46-49) as the molecular origin for secondary relaxations which involved restricted motion of the main chain requiring at least 5 and as many as 7 bonds (50). This kind of crankshaft rotation needs an energy of activation of
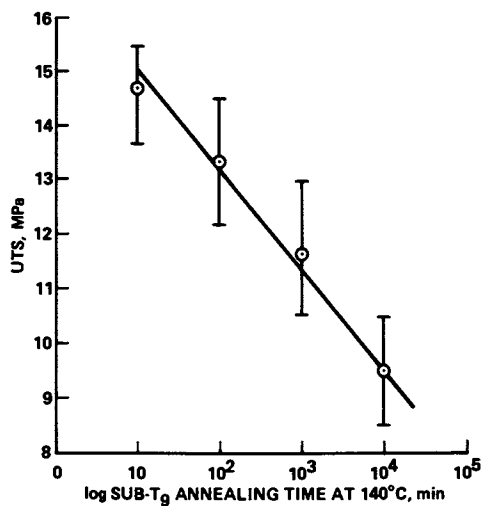
Figure 3. Ultimate tensile strength of fully-cross-linked Fiberite 934 epoxy as a function of log sub-T_g aging at 140 °C.
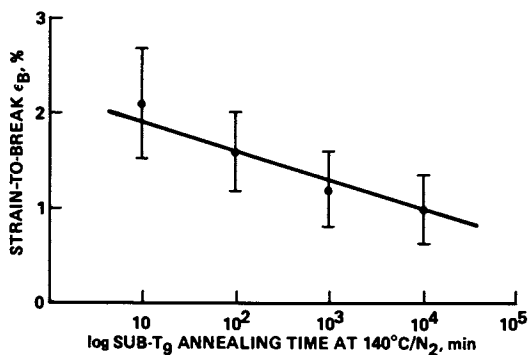
Figure 4. Ductility of Fiberite 934 epoxy as a function of log sub-T_g aging at 140 °C.
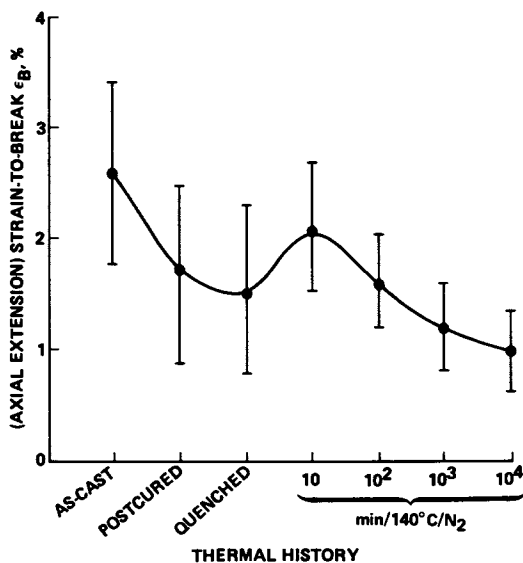
Figure 5. Ductility of Fiberite 934 epoxy as a function of thermal history.
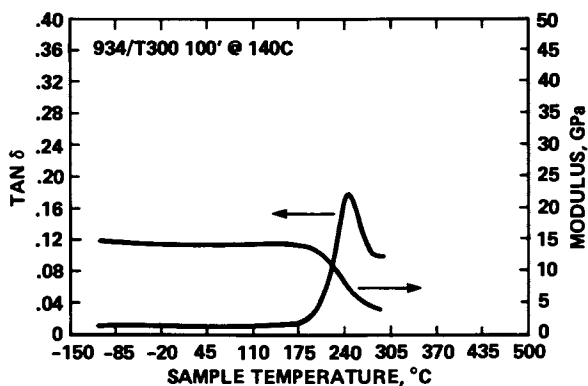
Figure 6. Dynamic mechanical analysis of 10^2 min.—aged $(\overset{+}{-} 45^{\circ})_{2S}$ Thornel 300/Fiberite 934 composite showing the loss tangent and the dynamic storage modulus.
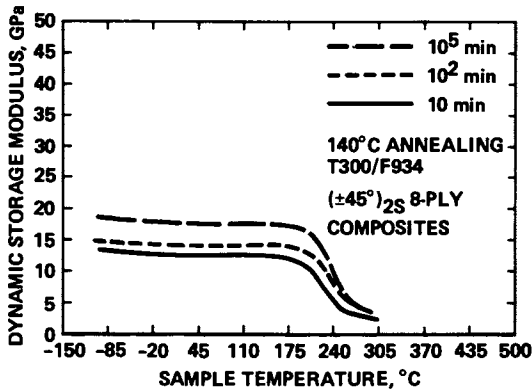
Figure 7. The influence of physical aging time on the dynamic storage modulus of Thornel 300/Fiberite 934 composites.
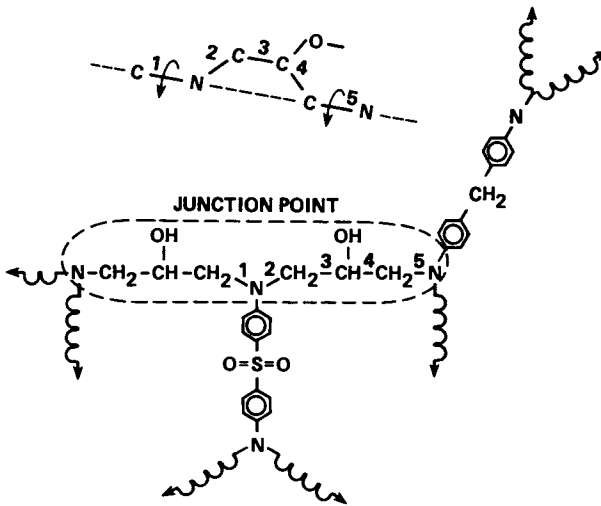
Figure 8. Proposed "crankshaft motion" at the junction point of a cross-linked TGDDM–DDS epoxy.

the order of 11 to 15 Kcal/mol and most likely requires creation
of free volume in order that the crankshaft may rotate (50).

Figure 9 shows the effects of thermal history on the mechani-
cal dispersion peaks in Fiberite 934 epoxy composites. The as-
fabricated materials show by far the largest damping (T_β spans
from -100°C to ca. 20°C for this epoxy system). Postcuring com-
pletes the crosslinking and results in a significantly lower-
damping composite.

Physical aging affects significantly the mechanical damping
in both the α and β relaxation peaks. Figure 10 shows the decrease
in the β loss peak as a function of aging time at 140°C in nitro-
gen. This gradual decrease in damping can be explained by a
relaxation model in which the epoxy network loses mobility and
free volume during its asymptotic approach towards the equilibrium
glassy state; as a result, the ability to dissipate energy is
reduced. This is a significant observation in view of the fact
that the area under the secondary mechanical dispersion peak is
often correlated with the impact resistance of the polymer (51).
Upon requenching from above T_g and re-aging such material, the
thermoreversible nature of physical aging can be demonstratively
shown. The effect of 140°C aging on the β-transition in the epoxy
matrix of requenched specimens is shown in Figure 11.

With sub-T_g annealing at 140°C the maximum peak temperature
of T_g tended to shift to higher temperatures. For example, the
value was 242.0°C for 10 min.-aged samples. In the two aging/
reaging experiments, T_g shifted to 253.0°C for both 10^5 min.-aged
and reaged samples. T_β, however, appeared to be less sensitive
to physical aging time and the β maximum peak temperature stayed
at about -55°C.

Differential Scanning Calorimetry

DSC was utilized to study both the state of the cure (extent of
crosslinking) as well as the kinetics of enthalpy relaxation in
network epoxies (5,12,52,53). DSC results confirmed a fully-
crosslinked epoxy network having no exotherm at temperatures up to
280°C.

In an earlier communication (5), we reported enthalpy relaxa-
tion studies at 140°C aging. In this paper, both 110°C and 80°C
sub-T_g annealing data are presented for neat-epoxy aging. Figure
12 shows the DSC scans of fully-cured epoxy samples that were
quenched from above T_g and then subjected to aging at 110°C. The
full line is the first scan, and the dotted line represents a
second scan taken immediately after cooling from the initial scan.
The following observations were made:
1. The enthalpy relaxation peak appears near the onset of the
   transition from the glassy state to the rubbery state. This
   peak appears after only 10 min. of aging at 110°C.
2. During sub-T_g annealing, the relaxation peak shifts to higher
   temperature and grows in magnitude.
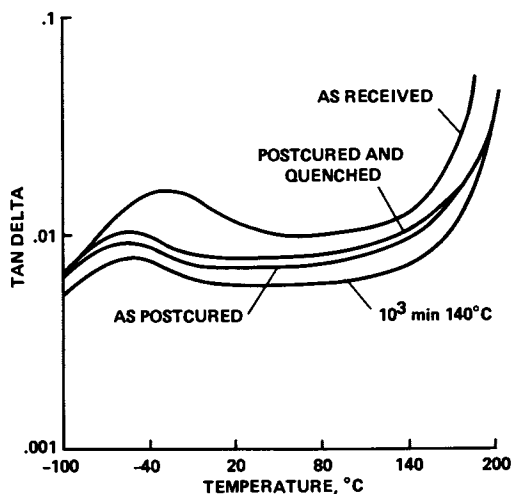
Figure 9. Secondary mechanical dispersion peaks of Thornel 300/ Fiberite 934 composites as influenced by their specimen thermal history.
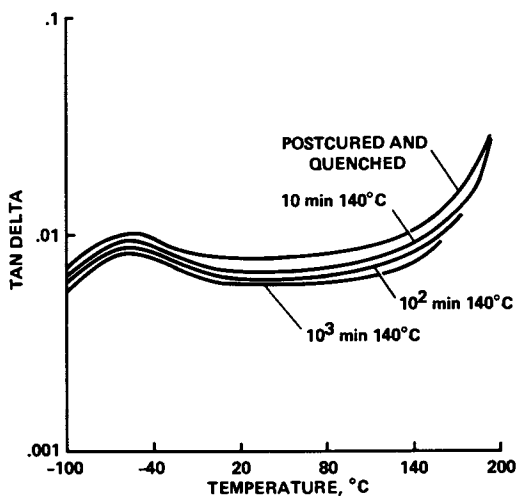
Figure 10. The influence of physical aging time on the secondary loss peaks of Thornel 300/ Fiberite 934 composites.
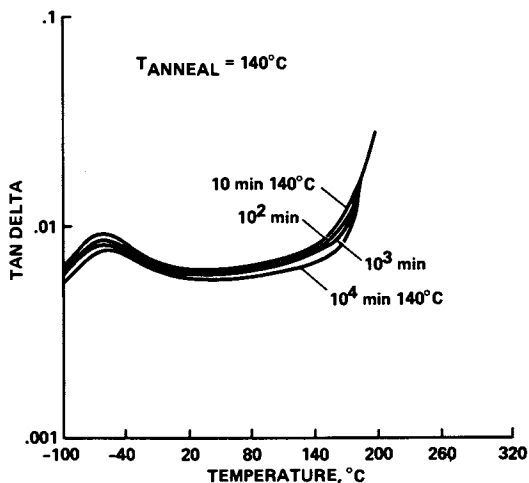
Figure 11. The influence of requenching followed by reaging on the secondary loss peaks of Thornel 300/Fiberite 934 composites.
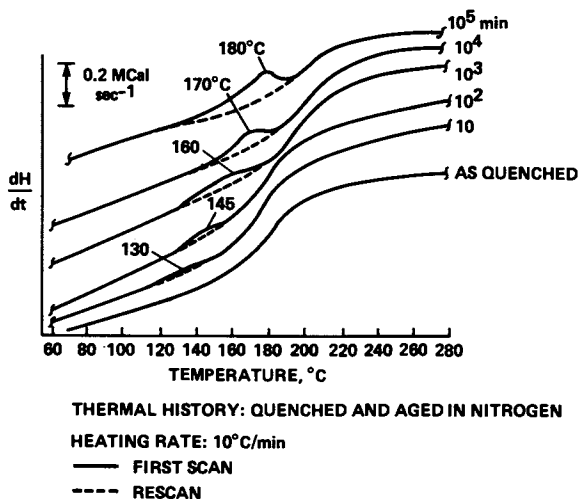
Figure 12. The influence of 110 °C physical aging on the endo-thermic enthalpy relaxation peak of neat Fiberite 934 epoxies.

3. This recovery phenomenon is thermoreversible. Upon re-aging
    material that is cooled from above T_g, the relaxation peak
    will reappear and grow with annealing time (see Figure 13).
        Compared to the 140°C enthalpy relaxation data reported
earlier (5), the 110°C aging kinetics are definitely slower. A
series of 80°C sub-T_g annealing experiments were also performed
using similar postcured-and-quenched specimens. "Aging peaks"
were again observed for 80°C annealing even though this time the
magnitude of the relaxation peak was much smaller compared to
110°C aging data. In 80°C aging, the peak temperature shifted
from the 100°C (10 min.) to 125°C (10^5 min.). In the case of
110°C aging, that peak temperature shifted from 130°C to 180°C
(10 min. to 10^5 min. aging). In an earlier report, we noticed a
shift from 160°C (10 min.-aged) to 210°C (10^5 min.-aged) for 140°C
sub-T_g annealing (5).
        As mentioned earlier, the relaxation enthalpy was measured by
superimposing the first and second DSC scans for each specimen.
Figure 14 shows the relaxation-enthalpy loss versus logarithmic
sub-T_g annealing time at 140°, 110° and 80°C. There is clearly a
linear relationship between the enthalpy relaxation process and
the logarithmic aging time.
        Figure 14 demonstrates that aging kinetics slow down as the
temperature increment ($T_g - T_a$), increases, i.e., the recovery
process is a thermally-stimulated phenomenon which requires seg-
mental mobility of the polymer in its glassy state. The lower the
sub-T_g annealing temperature, T_a, the slower is the aging kinetics.
Since there exists a linear relationship between ΔH (decrease in
enthalpy) and aging time, we can determine the activation energy
of the enthalpy relaxation process assuming the Arrhenius equation
holds. Figure 15 shows the Arrhenius plot. From the slope, we
can estimate the activation energy to be 5.9 Kcal/mol. This acti-
vation energy is very close to the typical hydrogen bond dissocia-
tion energy for a majority of hydrogen-bonded systems (54-56). It
is suggested that during the resin contraction (densification)
process in volume relaxations, hydrogen bonds may be broken and
re-formed.
        The activation energy for epoxy polymer relaxation of 5.9
Kcal/mol. estimated from the Arrhenius anlaysis is a low value
compared to enthalpy relaxation in inorganic glasses such as the
B_2O_3 system as reported by Moynihan et al (57) (ΔH activation
energy values of the order of 90 Kcal/mol). This simply suggests
that the relaxation mechanisms in the epoxy polymer-network-
glasses (PNG) may proceed by different mechanisms than do struc-
tural relaxations in inorganic glasses. The low value estimated
may also suggest that relaxation mechanism at 140°C versus those
at 110°C and 80°C in this epoxy system may be different from each
other.
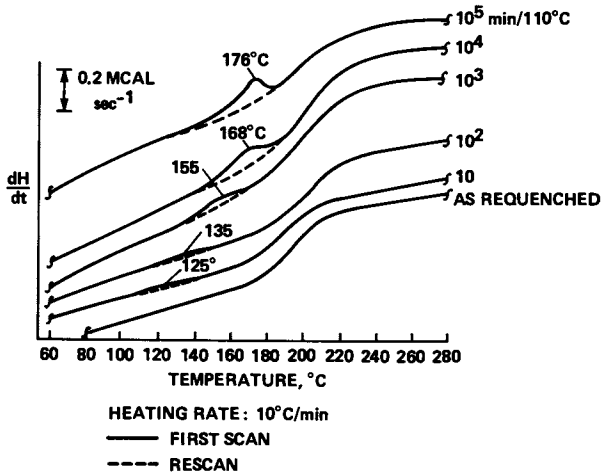
Figure 13. The effect of 110 ^{O}C reaging on the enthalpy relaxation peak of as-requenched Fiberite 934 epoxies.
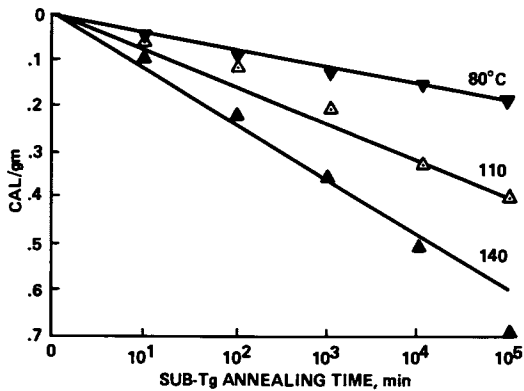
Figure 14. Enthalpy loss at 80 ^{O}C, 110 ^{O}C, and 140 ^{O}C aging as function log sub-T_g annealing time.

Density

The density of the cured epoxy was followed as a function of its
thermal history. Postcuring caused the largest decrease in
density, from 1.290 gm/cm^3 for as-cast epoxy to 1.230 gm/cm^3 for
as-postcured/slowly-cooled epoxy. The decrease in room tempera-
ture-density can be explained partially by escape of unreacted DDS
crosslinker (density = 1.380 gm/cm^3) during postcuring. Aherne et
al. (58) also observed a decrease in density with Epon 828 epoxy
postcuring, but argued from a free-volume explanation for the
observation. A priori, one would assume on the basis of crosslink-
density that a postcured system (presumably with a higher cross-
link density) would have a higher density. This may actually be
the case at the postcure temperature. At 23°C, however, Gillham
et al. (59) have indicated that the higher-crosslinked system may
be quenched further from the hypothetical equilibrium glassy state
resulting in a higher value of free volume, i.e., lower epoxy
density (59).
     With an air-quench, the density of the fully-crosslinked
epoxy drops from 1.230 to 1.215 gm/cm^3. With sub-T_g annealing, an
increase of 0.82% in the resin density was observed during the
140°C aging. This fits the "free volume collapse" model in which
the resin densifies. Figure 16 summarizes these observations.

Hardness

The hardness of a material is related to its resistance to scratch-
ing or denting. The hardness value for the cured epoxy is very
dependent on its thermal history and is also a time-dependent
parameter during physical aging. M-scale of the Rockwell hardness
index is reported. As-case epoxy has a low hardness value of
M70±3. With postcuring, the value increased to M97±3. This repre-
sents a 39% increase of hardness with postcuring. With an air-
quench, the epoxy hardness dropped slightly for about 4% to M93±3.
This is reasonable since the excess trapped free volume in the as-
quenched epoxy may well soften the system. With aging at 140°C,
the epoxy hardened from M93±3 to M110±3 for 10^4 min. aged material
(an 18% increase). With a requenching of 10 min.-aged epoxy, a
drop of 7% in the hardness is observed, probably due to a restora-
tion of free volume in the resin, as manifested in a softened
hardness index of M92.5±2.5. Hence, once again, is demonstrated
the thermo-reversibility of the physical aging process. Figure 17
summarizes the observations.

Thermal Mechanical Analysis

Thermal mechanical analysis (TMA) was utilized by Ophir (60) to
study the densification of Epon 828 epoxy. The glass transition
temperature can be easily characterized by a slope change as the
resin transits from the glassy state to the rubbery state (see
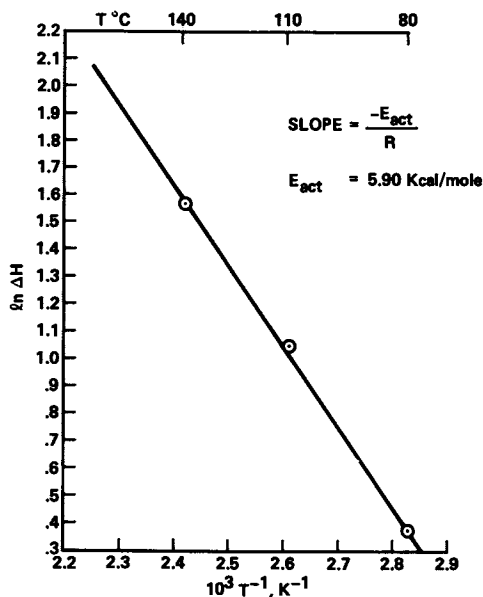
Figure 15. Arrhenius analysis of the enthalpy loss data of Figure 14.
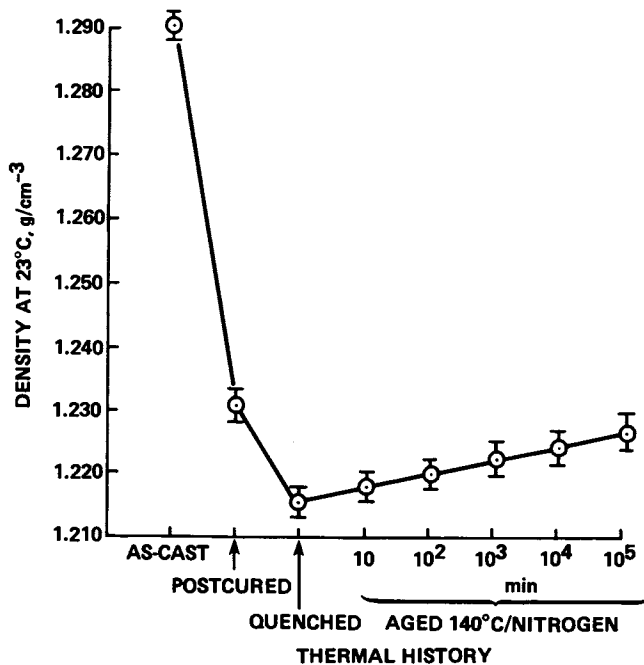
Figure 16. Density of neat Fiberite 934 epoxy as a function of thermal history.
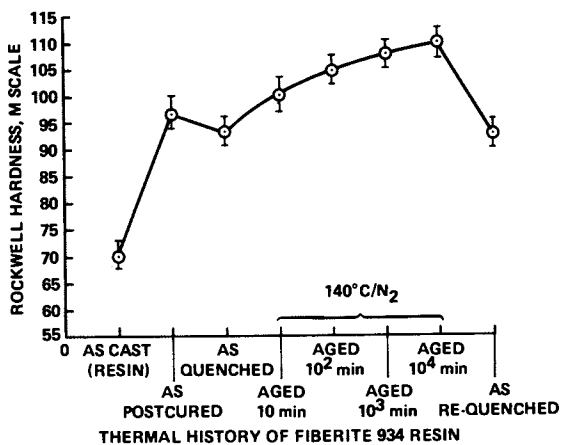
Figure 17. Hardness of neat Fiberite 934 epoxy as a function of thermal history.

Figure 18). Hence, in glassy material, it is typically represented by two thermal expansivity parameters, one below T_g (glassy thermal expansivity) and one above T_g (rubbery thermal expansivity).

Figure 18 shows the thermal expansion behavior of a fully-crosslinked epoxy as a function of aging time at $140^{\circ}C$ sub-T_g annealing. By superimposing the first scan (for aged material) and the second scan (for as-quenched material) at the high-temperature rubbery region, it is possible to monitor the development of aging in the resin, i.e., the progress of the densification process.

As shown in Figure 18, the aged glass typically has a lesser volume in the glassy state as compared to the as-quenched state. It is obvious from the data that the longer the aging time, the larger is the amount of volume lost due to sub-T_g annealing at $140^{\circ}C$. This observation also fits well into the "free-volume-collapse" model discussed earlier.

Figure 19 shows the thermal expansion behavior of requenched epoxies. Upon reaging, the densification process was again measurable. Data shown in Figure 19, therefore, supports the thermoreversible nature in physical aging.

By analyzing the linear portion of the thermal expansion curves below and above T_g, it is possible to calculate the expansivity of each specimen taking into account its individual thickness. Through such analysis, significant variations were observed in the thermal expansivity of the cured epoxy both below and above its T_g.

Figure 20 shows the expansivity variations as a function of thermal history. As-cast epoxy has a value of $5.43 \times 10^{-5} {}^{\circ}C^{-1}$ (below T_g). Expansivity below T_g decreased with postcuring to $5.20 \times 10^{-5} {}^{\circ}C^{-1}$, which is reasonable because postcuring resulted in a network which has higher crosslink-density and hence, lesser mobility. Quenching, which introduced a thermal shock and also residual thermal stresses, caused the epoxy to be less expansible below T_g ($4.98 \times 10^{-5} {}^{\circ}C^{-1}$) in spite of the increased free volume through quenching. In this experiment, similar to the results suggested by the stress-strain analysis, residual thermal stresses seem to override the importance of free volume considerations in affecting the glassy expansivity of the as-quenched resin.

With 10 minutes of sub-T_g anneal at $140^{\circ}C$, the thermal expansivity below T_g decreased to $4.78 \times 10^{-5} {}^{\circ}C^{-1}$. This parameter decreased throughout the $140^{\circ}C$ aging experiment. After 10^5 minutes of aging, the value decreased to $4.30 \times 10^{-5} {}^{\circ}C^{-1}$. The free volume decrease evidently dictates the thermal expansivity in the glassy state during sub-T_g annealing.

To erase resin history, aged samples were quenched from above T_g. With the requenching, glassy state expansivity was restored to high value of $5.22 \times 10^{-5} {}^{\circ}C^{-1}$, comparable to the as-postcured value. Requenching obviously has introduced a significantly
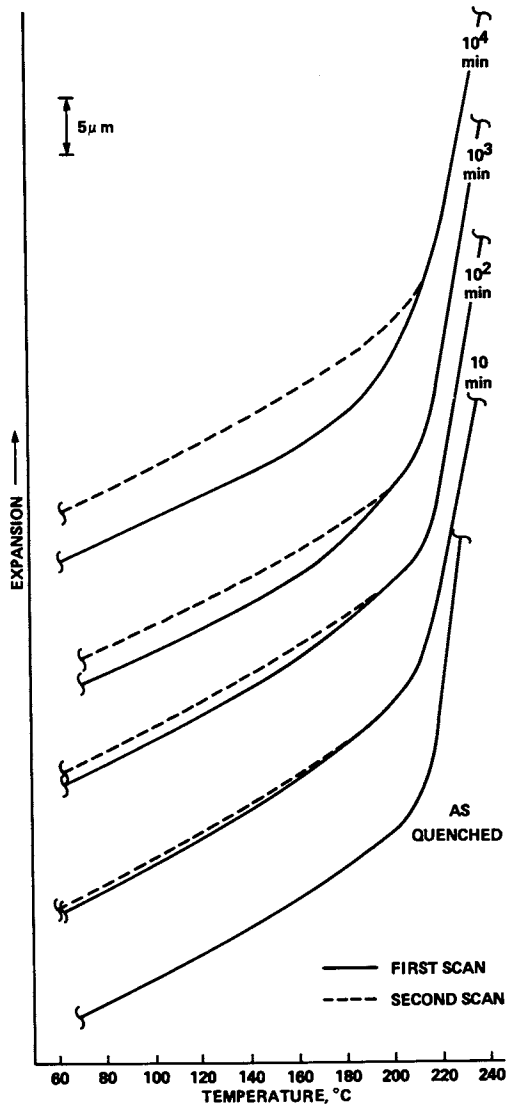
Figure 18. Thermal expansion behavior of neat Fiberite 934 epoxies as influenced by aging history at 140 °C.
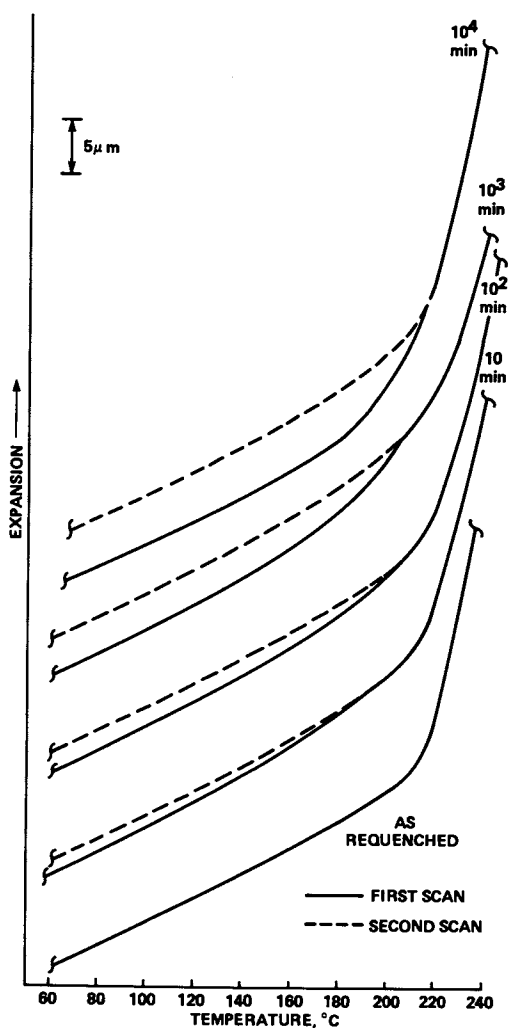
Figure 19. Thermal expansion behavior of neat Fiberite 934 epoxies as influenced by requenching (erasure of thermal history) and subsequent reaging at 140 °C.
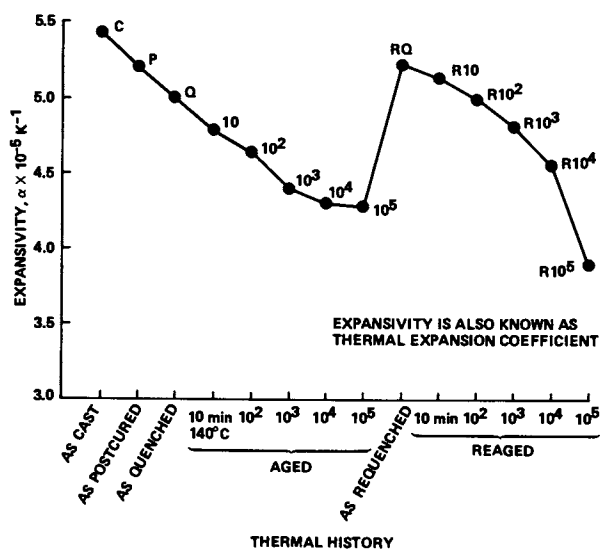
Figure 20. Glassy–state thermal expansivity (60–160 °C) of Fiberite 934 epoxies as a function of thermal history.

larger amount of free volume in the resin and thus made the resin more expansible (see Figure 20).

Reaging the resin at 140°C again caused a decrease in glassy-state expansivity but the decrease was larger than in the first round of aging. Evaluating the decrease for 10^4 minute data in the two series of aging indicated that the aging kinetics was probably similar.

Figure 21 shows the thermal expansivity of the epoxy above its T_g as a function of thermal history. Rubbery-state expansivity is generally an order of magnitude larger compared to the glassy-state expansivity (Table 2). As-cast epoxy has an expansivity above T_g of 3.22 x 10^{-4} °C^{-1}. With postcuring and quenching, this parameter tends to increase due to the interplay of free volume variations and factors involving residual thermal stresses (see Figure 21).

As is clearly indicated by the data in Figure 21, expansivity above T_g for epoxies tend to increase with aging at 140°C. This increase in expansivity in the rubbery-state probably can be traced to a "catching-up-process" for volume lost during physical aging. At temperatures above T_g, there is enough thermal energy for the system to reach equilibrium. Since volume was lost during physical aging, the high temperatures provide the thermal energy to recover for the "lost volume". The longer the glass is subjected to aging, the higher would be its tendency to recover the lost volume, hence, manifested in a larger value of thermal expansivity above T_g. An increase from 3.14 x 10^{-4} °C^{-1} to 5.11 x 10^4 °C^{-1} (62.7% increase) was observed.

With requenching and reaging, expansivity above T_g again increases with reaging time (96.6% increase), demonstrating once again the thermoreversibility of physical aging. Table 2 summarizes the results of the TMA investigations.

Moisture Sorption Kinetics

140°C aged epoxy glasses were subjected to 40°C/98% relative humidity moisture penetration. Figure 22 shows the results of this transport experiment. We observed both a decrease of initial sorption kinetics as well as a decrease of equilibrium sorption level as a function of aging time. This supports the idea that during sub-T_g annealing, the resin contracts and densifies, resulting in decreased free volume.

In another series of diffusion experiments, as-postcured epoxies were first immersed in 23°C heavy water for 2 months. Then the temperature of the epoxy/heavy water interacting system was increased to 40°C. The continuous influx of heavy water into the epoxy can be easily monitored by deuterium NMR spectroscopy. The free induction-decay signal as normalized by the specimen weight showed an increase as a function of sorption time (see Figure 23). For example, a 2 month room-temperature sorption results in an epoxy having 2.10% of moisture (determined by gravimetry). With
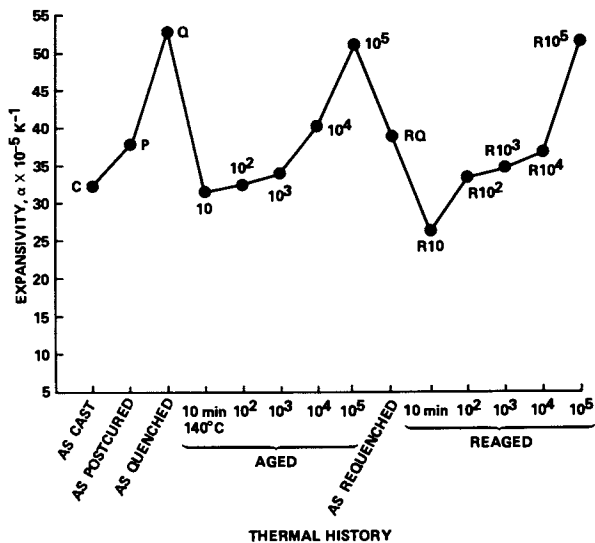
Figure 21. Rubbery-state thermal expansivity (200-240 °C) of Fiberite 934 epoxies as a function of thermal history.
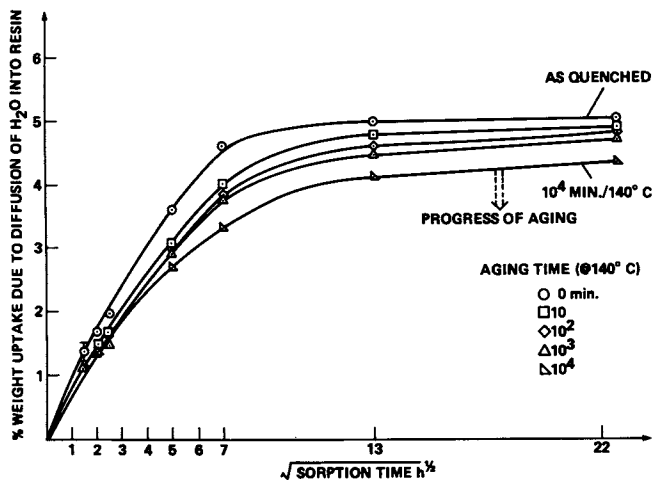
Figure 22. Moisture absorption behavior of fully-cross-linked Fiberite 934 epoxy as influenced by 140 °C sub-T_g aging.

Table II. Thermal expansivity of Fiberite 934 neat epoxies
as a function of thermal history.

THERMAL HISTORY		α(BELOW Tg) $\times$ 10^5 K^{-1} (ca. 60 – 160°C)	α(ABOVE Tg) $\times$ 10^5 K^{-1} (ca. 200 – 240°C)
AS-CAST		5.43	32.2
AS-POSTCURED		5.20	37.7
AS-QUENCHED		4.98	52.9
140°C AGED	10	4.78 DE-CREASE WITH AGING	31.4 IN-CREASE WITH AGING
	10^2	4.63	32.4
	10^3	4.40	33.9
	10^4	4.32	40.1
	10^5 min	4.30	51.1
AS-REQUENCHED		5.22	38.8
140°C REAGED	10	5.13 DE-CREASE WITH AGING	26.2 IN-CREASE WITH AGING
	10^2	5.00	33.3
	10^3	4.82	34.5
	10^4	4.56	36.6
	10^5 min	3.88	51.5

667 h of additional sorption at 40°C, 3.14% of moisture resided in
the epoxy. Correspondingly, the sorption kinetics for NMR FID
signal showed an increase from 275 (arbitrary units) for 2 months/
23°C diffusion to ca. 990 with additional 667 h of diffusion at
40°C (Figure 23). In general, the epoxy-water gravimetry experi-
ment and the epoxy-heavy water deuterium NMR agree well with each
other.

In addition to detecting the heavy water content, we also
utilized the deuterium NMR technique to study epoxy/moisture
interactions. Figure 24 shows the 4.65 ppm nuclear magnetic
resonance of freely-tumbling heavy water. Figure 25 shows the NMR
spectrum of deuterium as it resides inside an as-quenched epoxy
after immersion in heavy water for 2 months at 23°C and then 1
month at 40°C.

In Figure 25, we can clearly see the sharp component (with
little broadening) that is due to isotopically tumbling or less-
bound heavy water. The wide broadening of the deuterium resonance
could be due to deuterium oxide trapped by the hydrogen bonds of
epoxy resin. It is possible that the deuterium of heavy water may
exchange with the protons in the epoxy (61) so the broadening may
only reflect deuterons that have exchanged and now reside in the
epoxy network. Experiments using deuterated resin can clarify
this point.

In the TGDDM-DDS epoxies, hydrogen bonds may be formed among
the polar groups. Figure 26 summarizes such possible hydrogen
bonding possibles. To propose one example, hydroxyl groups may
hydrogen bond in the following fashion.
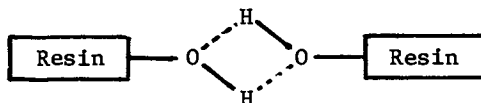
Similar to water, it is also known that heavy water is highly
associated by hydrogen bonding. It is very likely that the heavy
water hydrogen bonding system disrupts the epoxy hydrogen-bonding
system (Figure 27), thereby causing swelling in the moisture-
saturated-resin network (6,20,62). The epoxy-heavy-water inter-
acting model is proposed in Figure 28 in which some less-bound
moisture molecules would reside in voids (free volume) hence giving
rise to the sharp NMR component, whereas some moisture would be
trapped by the epoxy hydrogen bonds, resulting in the NMR broad
component. From the NMR broadening, it can be estimated that the
correlation time for heavy water among the epoxy hydrogen bonds is
in the order of 10^{-7} sec.

Earlier we reported that physical aging affects the "swelling
efficiency" and diffusivity of epoxy as moisture is transported
into the network (6). In conjunction with this earlier communica-
tion (6), we can now summarize the findings for interactions
between moisture and aging epoxies:
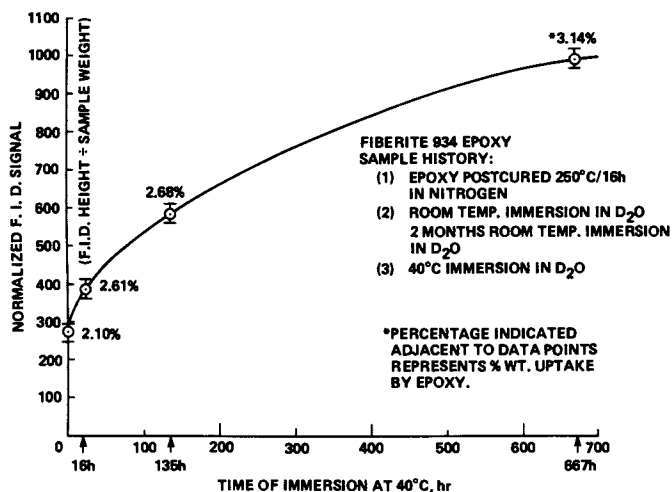
Figure 23. Heavy water absorption by Fiberite 934 epoxy as a function of immersion time at 40 °C as monitored by deuterium NMR spectroscopy.
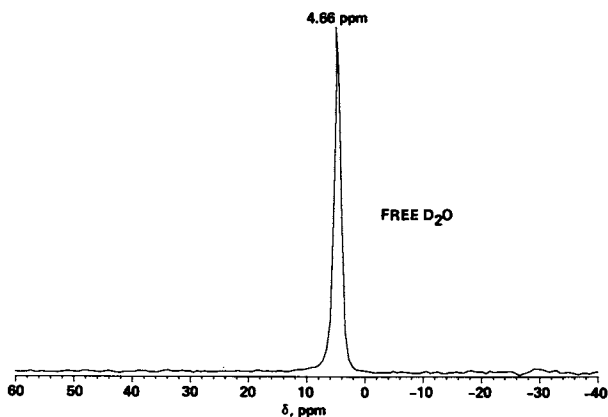
Figure 24. Deuterium NMR spectrum of isotropically-tumbling heavy water molecules.
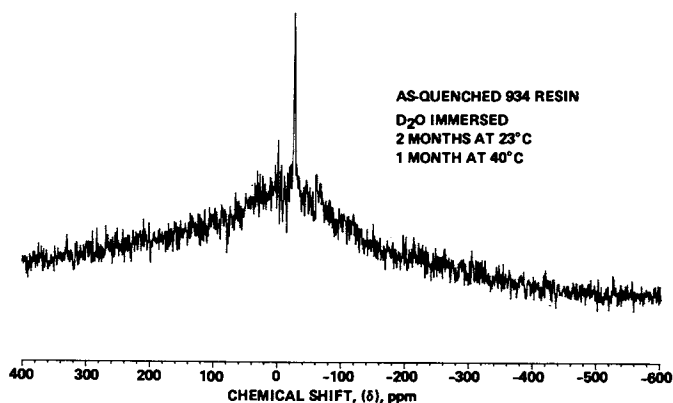
Figure 25. Deuterium NMR spectrum of heavy water absorbed by an as-quenched Fiberite 934 epoxy.
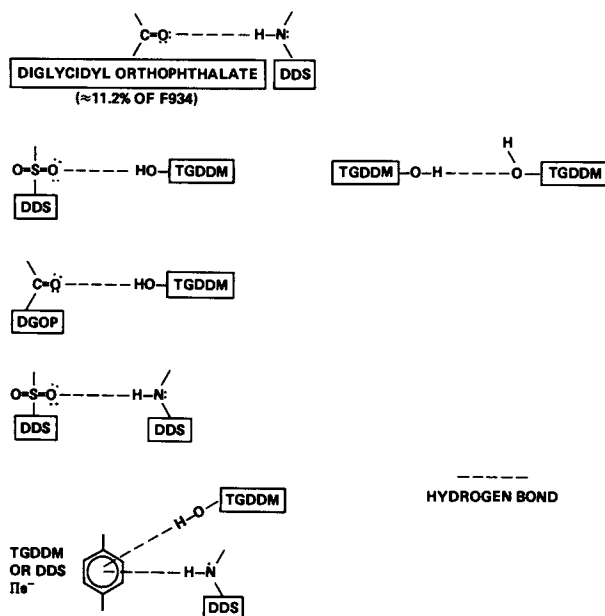
Figure 26. Various hydrogen bonding possibilities by polar groups in Fiberite 934 epoxy (N.B.: Diglycidyl orthophthalate is given the acronym DGOP).
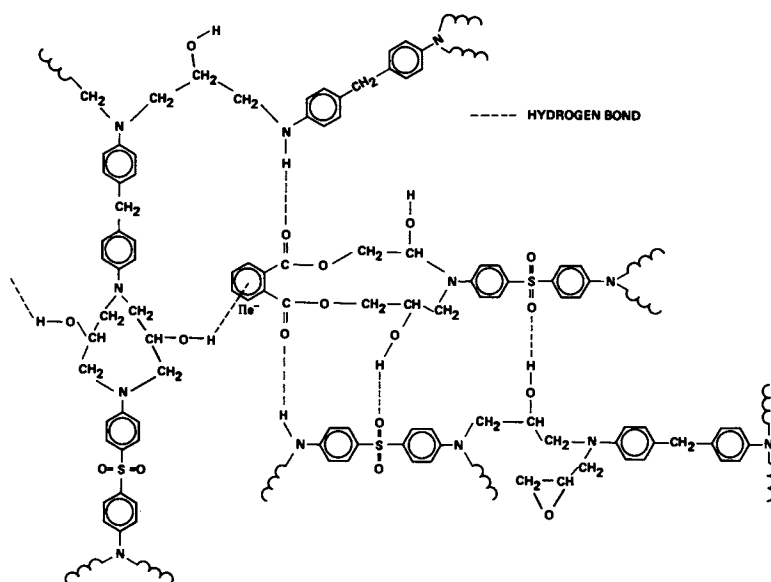
Figure 27. Hydrogen-bonded network of Fiberite 934 epoxy (N.B.: π electrons may also participate in hydrogen bonding).
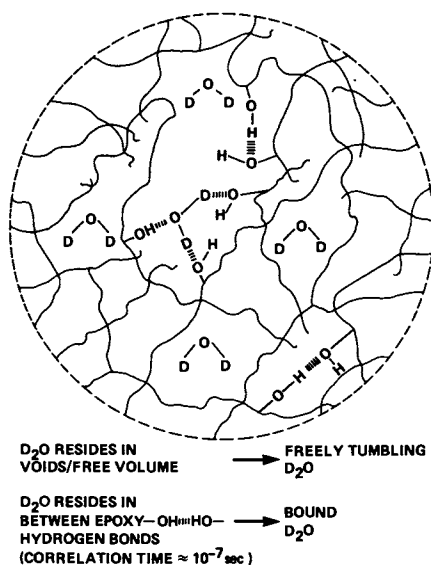
Figure 28. Proposed model for "heavy water-epoxy interactions" (N.B.: Heavy water may form aggregates in the voids or disrupt the epoxy hydrogen bonds).

1. As epoxies densify, the amount of moisture uptake
    decreases.
2. As epoxies densify, the "swelling efficiency" (6,10)
    of aged epoxy is increased.
3. Diffusivity (6) decreases with physical aging.
4. Moisture can either reside in the free volume or
    disrupts the epoxy hydrogen bonds.

Proton-Decoupled CP/MAS NMR and Solution C-13 NMR

For the first time, proton-decoupling, cross-polarization, and
magic angle spinning NMR techniques are applied to study the
Fiberite 934 TGDDM-DDS system. Figure 29 shows a carbon-13 spec-
trum of as-cast epoxy. In the spectrum, the aromatic carbons
(residing in downfield between 100 to 150 ppm) can clearly be
resolved from the aliphatics (20 to 80 ppm). By integration, the
population of aliphatic and aromatic carbons was shown to be
roughly the same (Figure 29).
      In order to study physical aging at the molecular level,
CP/MAS NMR was used to study the epoxy densification process.
Figure 30 shows the spectral difference between as-cast, 10 min.-
aged and 10^5 min.-aged epoxies. Postcuring and aging clearly has
resulted in many spectral changes (see Figure 30). Of greatest
interest was the observation that the sharp and highest aromatic
resonance at 127 ppm (as-cast epoxy) tended to shift downfield
with aging. With aging to 10^5 min., this resonance peak shifted
to ca. 131 ppm. We can interpret this downfield shift of aromatic
resonance to molecular aggregation of the phenyl rings in the
resin causing "ring-current effects" (63) during volume relaxation
in the epoxy resins.
      125 MHz carbon-13 spectra of TGDDM, DDS, and DGOP in deuter-
ated chloroform solutions are shown in Figures 31-33, respectively.
The spectra show sharp components of resonance peaks for the
aromatics between 110 and 150 ppm and for the aliphatics between
40 and 80 ppm. The large peak at 77 ppm is due to $CDCl_3$ carbon-13
resonance. In Figure 32, the doublets at 45 ppm and 50 ppm can be
attributed to conformational isomers arising from an "umbrella-
like" inversion at the pyramidal-bonded nitrogen atom.

Conclusions

For the first time, it is now possible to characterize the molecu-
lar aggregation during physical aging in network epoxies by spec-
troscopic technique. Other important findings are summarized:
as physical aging of the polymer network glass proceeds,
      - Damping decreases
      - Ultimate mechanical properties decrease
      - Stress relaxation rates (and creep rates) decrease
      - Moisture sorption decreases
      - Moisture diffusivity decreases

127 ppm

HARTMANN-HAHN CROSS POLARIZATION

P2 =   1.50 msec
D3 =   4.50 usec
D4 = 50.00 msec
D5 =   2.00 sec

180   160   140   120   100   80   60   40   20   0
                          ppm
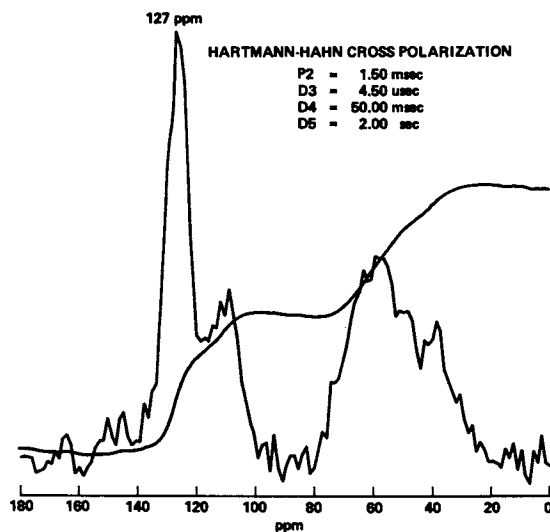
Figure 29. Proton-decoupled CP/MAS carbon-13 NMR spectrum of an as-cast Fiberite 934 epoxy showing also the integration of the aromatic (downfield) and aliphatic (upfield) carbons.
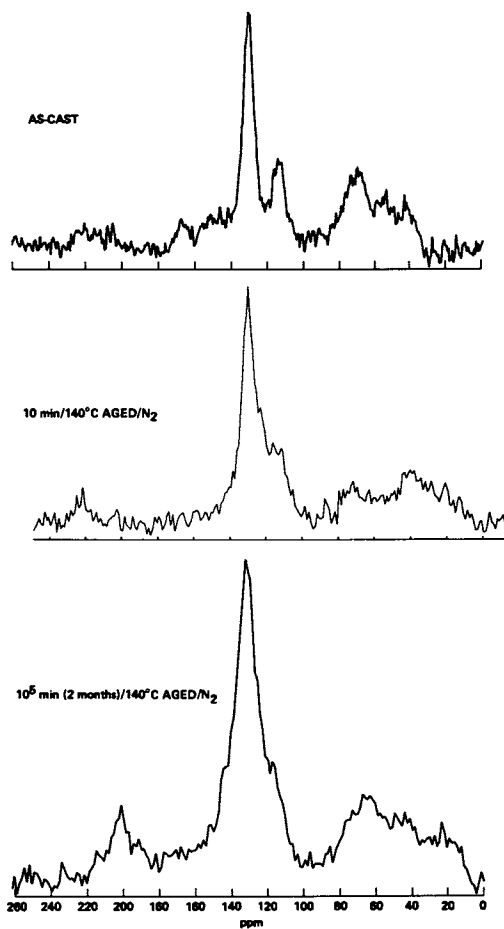
Figure 30. The effect of physical aging on the spectral changes in proton-decoupled CP/MAS carbon-13 NMR measurements.
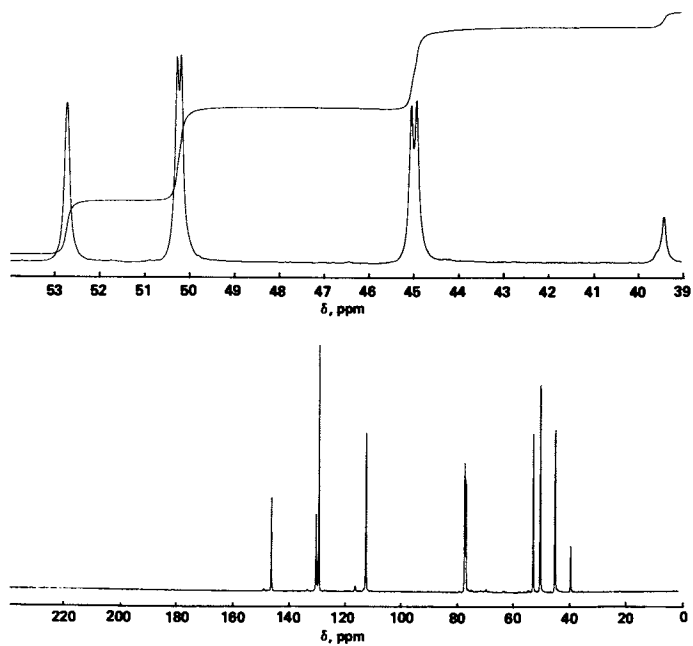
Figure 31. 125 MHz carbon–13 NMR spectrum of TGDDM in deuterated chloroform solution.
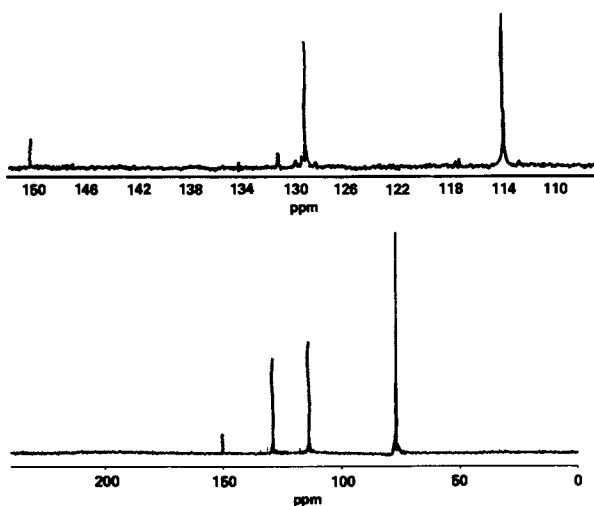
Figure 32. Proton-decoupled 125 MHz carbon-13 NMR spectrum of DDS cross-linking agent in deuterated chloroform solution.
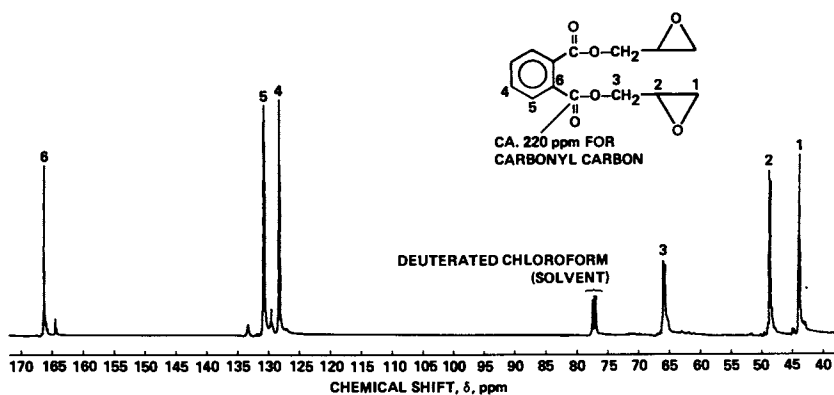
Figure 33. Proton-decoupled 125 MHz carbon-13 NMR spectrum of DGOP in deuterated chloroform solution. Downfield carbonyl carbon resonance not shown.

- Density increases
- Dynamic modulus increases
- Hardness increases
- Moisture-epoxy interaction increases (i.e., swelling increases)
- Glassy-state expansivity decreases; rubbery-state expansivity increases

Acknowledgments

Literature Cited

1. Ophir, Z. H.; Emerson, J. A.; Wilkes, G. L., J. Appl. Phys. 1978, 49, 5032.
2. Kaiser, J. Makromol. Chem., 1979, 180, 573.
3. Kong, E. S. W.; Wilkes, G. L.; McGrath, J. E.; Banthia, A. K.; Mohajer, Y.; Tant, M. R., Polym. Eng. Sci., 1981, 21, 943.
4. Kong, E. S. W., J. Appl. Phys., 1981, 52, 5921.
5. Kong, E. S. W., Composites Technol. Rev., 1982, 4, 97.
6. Kong, E. S. W.; Adamson, M. J., Polymer Commun., 1983, 24, 171
7. Kong, E. S. W.; Lee, S. M.; Nelson, H. G., Polym. Composites, 1982, 3, 29.
8. Chang, T. D.; Brittain, J. O., Polym. Engin. Sci., 1982, 22, 1228.
9. Kong, E. S. W., Contemporary Topics in Polymer Science, 1983, 4, ed. by J. Bailey and T. Tsuruta, Plenum Press, New York.
10. Struik, L. C. E., "Physical Aging in Amorphous Polymers and Other Materials"; Elsevier: Amsterdam, 1978; p. 16.
11. Kovacs, A. J., Fortschr. Hochpolym. Forsch., 1963, 3, 394.
12. Petrie, S. E. B., "Polymeric Materials: Relationships Between Structure and Mechanical Behavior"; ed. by E. Baer and S. V. Radcliffe, Amer. Soc. Metals, Metals Park, Ohio, 1975; p. 55.
13. Schaefer, J.; Stejskal, E. O., J. Amer. Chem. Soc., 1976, 98, 1031.
14. Rowland, S. P. (Ed.), "Water in Polymers"; Amer. Chem. Soc. Symp. Series 127; American Chemical Society; Washington, DC, 1980.
15. Moy, P.; Karasz, F. E., Polym. Eng. Sci., 1980, 20, 315.

16. May, C. A.; Fritzen, J. S.; Whearty, D. K., "Exploratory Development of Chemical Quality Assurance and Composition of Epoxy Formulations", Lockheed Missiles and Space Company, Air Force Technical Report: AFML-TR-76-112, 1976.

17. Hadad, D. K.; Fritzen, J. S.; May, C. A., "Exploratory Development of Chemical Quality Assurance and Composition of Epoxy Formulations", Lockheed Missiles and Space Company, Air Force Technical Report: AFML-TR-77-217, 1977.

18. Wetton, R. E.; Croucher, R. G.; Fursdon, J. W. M., Polym. Prepr., Amer. Chem. Soc., Div. Poly. Chem., 1981, 22 (1), 256.

19. Wyzgoski, M. G., J. Appl. Polym. Sci., 1980, 25, 1455.

20. Adamson, M. J., J. Mater. Sci., 1980, 15, 1736.

21. Fukushima, E.; Roeder, S. B. W., "Experimental Pulse NMR", Addison-Wesley: Reading, Massachusetts, 1981; p. 284.

22. Kong, E. S. W., "Epoxy Resins - II"; Bauer, R. W., A.C.S. Symp. Series, 22, American Chemical Society: Washington, DC 1983 Chapter 9, p. 171-191.

23. Kong, E. S. W., "Physical Aging in Graphite/Epoxy Composites" Science of Advanced Materials and Processing Series, S.A.M.P.E. National Meeting, 1983, 28, 838.

24. Kong, E. S. W., unpublished data.

25. Heijboer, J., Annals New York Acad. Sci., 1976, 279, 104.

26. Takahama, T.; Geil, P. H., J. Polym. Sci., Phys. Ed., 1982, 20, 1979.

27. Bailey, R. T.; North, A. M.; Pethrick, R. A., "Molecular Motion in High Polymers", Oxford University Press, Oxford, United Kingdom, 1981; p. 287.

28. Kaelble, D. H., J. Appl. Polym. Sci., 1965, 9, 213.

29. May, C. A.; Weir, F. E. Soc. Plast. Eng. Transactions, 1962, 7, 207.

30. Browning, C. E., Polym. Eng. Sci., 1978, 18, 16.

31. Murayama, T.; Bell, J. P., J. Polym. Sci., A-2, 1970, 8, 437.

32. Kalfoglou, N. K.; Williams, H. L., J. Appl. Polym. Sci., 1973, 17, 1377.

33. Cook, W. D.; Delatycki, O., J. Polym. Sci., Polym. Phys. Ed., 1975, 13, 1049.

34. Murayama, T., "Dynamic Mechanical Analysis of Polymeric Material", Elsevier: Amsterdam, 1978.

35. Wyzgoski, M. G., J. Appl. Polym. Sci., 1980, 25, 1443.

36. Willbourn, A. H., Transactions Faraday Soc., 1958.

37. Kenyon, A. S.; Nielsen, L. E., J. Macromol. Sci. Chem., 1969, A3, 275.

38. Chang, T. D.; Carr, S. H.; Brittain, J. O., Polym. Eng. Sci., 1982, 22, 1205.

39. Nielsen, L. E., Soc. Plast. Engin., 1960, 16, 525.

40. Read, B. E.; Dean, G. D., "The Determination of Dynamic Properties of Polymers and Composites", Adam Hilger: Bristol, United Kingdom, 1978.

41. von Kuzenko, M.; Browning, C. E., *Amer. Chem. Soc., Preprints Org. Coat. Plast. Chem.*, 1979, 40, 694.
42. Keenan, J.; Seferis, J. C.; Quinlivan, J. T., *J. Appl. Polym. Sci.*, 1979, 24, 2375.
43. Hata, N.; Yamaguchi, R.; Kumanotani, J., *J. Appl.*, 1973, 17, 2173.
44. Wetton, R. E., *Anal. Proc., Anal. Div. Royal Soc., Chem.*, 1981, October, 416.
45. Bank. L.; Ellis, B., *Polym. Bull.*, 1979, 1, 377.
46. Schatzki, T. F., *J. Polym. Sci.*, 1962, 57, 496.
47. Wunderlich, B., *J. Chem. Phys.*, 1962, 37, 2429.
48. Boyer, R. F., *Rubber Rev.*, 1963, 34, 1303.
49. Pogany, G. A., *Polymer*, 1970, 11, 66.
50. Roberts, G. E.; White, E. F. T., "The Physics of Glassy Polymers", ed. by R. N. Haward, Wiley: New York, 1973, p. 153.
51. Meier, D. J. (ed.), "Molecular Basis of Transitions and Relaxations", Midland Macromolecular Monographs, Volume 4, Gordon and Breach Science Publishers, 1978.
52. Wyzgoski, M. G., *Polym. Eng. Sci.*, 1976, 16, 265.
53. Matsuoka, S.; Bair, H. E., *J. Appl. Phys.*, 1977, 48, 4058.
54. Hoeve, C. A. J., "Water in Polymers", ed. by S. P. Rowland, Amer. Chem. Soc. Symp. Series No. 127, American Chemical Society: Washington, DC, 1980, p. 135.
55. Joesten, M. D.; Schaad, L. J., "Hydrogen Bonding", Dekker: New York, 1974.
56. Pimentel, G. C.; McClellan, A. L., "The Hydrogen Bond", Freeman: San Francisco, 1960.
57. Moynihan, C. T.; Macedo, P. B.; Montrose, C. J.; Gupta, P. K.; DeBolt, M. A.; Dill, J. F.; Dom, B. E.; Drake, P. W.; Easteal, A. J.; Elterman, P. B.; Moeller, R. P.; Sasabe, H.; Wilder, J. A., *Ann. New York Acad. Sci.*, 1976, 279, 15.
58. Aherne, J. P.; Enns, J. B.; Doyle, M. J.; Gillham, J. K., *Amer. Chem. Soc. Org. Coat. Appl. Polym. Sci. Proc.*, 1982, 46, 574.
59. Gillham, J. K., Private communications, 1983.
60. Ophir, Z., Ph.D. Thesis, Princeton University, Princeton, NJ, 1979.
61. Jelinski, L. W.; Dumais, J. J.; Stark, R. E.; Ellis, T. S.; Karasz, F. E., *Macromolecules*, 1983, in press.
62. Garcia-Fierro, J. L.; Aleman, J. V., *Macromolecules*, 1982, 15, 1145.
63. Levy, G. C.; Nelson, G. L., "Carbon-13 Nuclear Magnetic Resonance for Organic Chemists", Wiley: New York, 1972.

Structure and Fracture of Highly Cross-linked Networks

J. D. LEMAY, B. J. SWETLIN, and F. N. KELLEY

Institute of Polymer Science, The University of Akron, Akron, OH 44325

Amine cured epoxy networks were investigated to determine the effect of cross-link density on fracture toughness and other properties. Two series of networks were studied: the first having M_c (the average molecular weight of a network chain) controlled by the amine/epoxy reactant ratio; the second controlled by the average molecular weight of several homologous difunctional epoxy prepolymers. Expected topological variations of the first series were confirmed by T_g differences and soluble fractions. The second series was presumed to display only M_c variations.

    Cross-link densities were characterized above T_g by equilibrium modulus measurements employing rubber elasticity theory. The results indicate that this method yields surprisingly reasonable values. Glassy fracture energies of both network series showed an M_c dependence when ductile yielding of the crack tip preceded crack propagation. Studies on the second series suggest that glassy fracture energies are closely proportional to $M_c^{\frac{1}{2}}$.

Epoxy thermosets are typical densely cross-linked polymer materials. They are used in a wide variety of practical applications and thus have been studied extensively. However, the quantitative dependence of physical properties, such as strength, stiffness, and fracture toughness, on network microstructure are largely undetermined. This can be attributed, in part, to the lack of adequate techniques for characterizing densely cross-linked network structure. Several microstructure variables that have been studied with some success are (1) cross-link density, (2) specific volume or bulk density, and (3) nodular or inhomogeneous morphology.

This paper presents characterization studies performed on amine cured epoxy resins. Particular emphasis is placed on the characterization of the cross-link density, and on its influence on physical properties, especially the fracture toughness.

Cross-link Density

The effective cross-link density or the average molecular weight of a network chain, M_c, of typical epoxy thermosetting systems may be modified by a number of techniques. Most commonly it has been changed by varying the epoxy resin/curing agent functional group ratio (1-8). Unfortunately, this approach introduces variations in the network topology as well as in cross-linking. Elucidating the direct effect of M_c on physical properties is thus complicated by the presence of other microstructure variations such as dangling chain ends and a soluble fraction. Processing conditions also have been used to modify the cross-link density. They have a direct effect on the reaction kinetics which in turn determine the network structure. For example, several studies (4,6,9-13) have employed different cure and postcure schedules to modify M_c. As with the use of reactant stoichiometry, the use of processing conditions to control M_c may yield other changes in network micro-structure.

Seemingly, a preferred route to the control of M_c would involve the use of different molecular weight epoxy resins cured by simple end-linking chemistry with a stoichiometric quantity of curing agent. Such a series of networks would presumably display variations in only the cross-link density. Since the M_c should be directly related to the resin functionality and molecular weight, the accuracy of M_c characterization techniques could be studied. Obviously, the role that M_c might play in determining physical properties would be facilitated by the study of such networks. Some structure-property studies using such a series of networks have been reported by Manson et al. (8) who utilized networks prepared from Shell Epon resins and methylene dianiline (MDA). They reported considerable difficulty processing these networks.

The characterization of M_c for epoxy networks has been attempted by theoretical estimations from the reactant ratio and assumed reaction kinetics, estimations by an empirical dependence of M_c on T_g, swelling, and the application of simple rubber elasticity theory to experimental equilibrium modulus measurements. The latter technique appears to be the most promising. Bell (14) has derived expressions relating M_c to the amine/epoxy ratio using the assumption that the reaction proceeds by polymerization of the epoxy with primary amine followed by cross-linking reactions of epoxy with secondary amine. Nielson (15) has related the degree of cross-linking to the corresponding shift in T_g through the empirical equation, $M_c = 39,000 \ (T_g - T_{g_0})$, where T_g is the glass transition temperature of the cross-linked polymer and T_{g_0} is that of the uncross-linked polymer. It is emphasized that this equation

was obtained by averaging data for a variety of polymer networks and does not account for copolymer effects; it yields, at best, rough estimates of M_c. Reports of swelling measurements on epoxy networks are few (14,16) and the results are generally in poor agreement with other techniques. Significant deviations in M_c may be introduced by the choice of the swelling equation (17-19), the state of equilibrium, and the chosen value of the interaction parameter. The most commonly used characterization method is the measurement of the rubbery equilibrium modulus, generally at temperatures $T>T_g+40^oC$. A number of investigators (3,8,20-24) have obtained reasonable M_c values by applying the simple rubber elasticity theory to such modulus measurements. The theory relates the equilibrium shear modulus G_e to M_c through:

$$M_c = \phi\rho RT/G_e \tag{1}$$

where R is the gas constant, ρ the density at absolute temperature T and ϕ the front factor, the ratio of the mean square end-to-end distance of a network chain to that of a randomly coiled chain. Since testing is done well into the rubbery state, constant volume deformation assumptions should apply, therefore G_e can be substituted with $E_e/3$ where E_e is the equilibrium tensile modulus. A systematic study involving a series of networks of known M_c's would be extremely useful for determining the applicability and range of application of this approach to measuring the cross-link density. Furthermore, such a study would be of interest from a theoretical standpoint for testing some of the assumptions used in the simple rubber elasticity theory.

Fracture

Interest in the fracture behavior of densely cross-linked polymers is evidenced by a large body of original research (2,4,6,7,10, 25-29) and several reviews of the subject (30,31). Both the energy balance concepts of Griffith (32) and linear elastic fracture mechanics (LEFM) have been employed. It is not the objective of this work to extend these concepts, which can be found in a number of texts (33,34), but rather to derive from them a material property which can be related to network variations. The energy balance approach yields a critical potential energy release rate, G_c, which is related to the fracture energy per unit area of new surface γ by the relation $G_c=2\gamma$. In LEFM the fracture toughness K describes the stress field in the region of the crack tip which at the moment of crack propagation reaches a critical value, K_c. For mode I fracture (opening mode), the two fracture mechanics approaches are related by the expressions (27):

$$K_{IC}^2 = EG_{IC} \qquad \text{plane stress} \tag{2}$$

$$K_{IC}^2 = EG_{IC}/(1-\nu^2) \qquad \text{plane strain} \tag{3}$$

where E is Young's modulus and ν is Poisson's ratio.

Structure-Property Relationships

The generalized theory of fracture mechanics of Andrews (35)
predicts that the cohesive fracture energy per unit surface area
J is given by the energy required to break the bonds crossing the
fracture plane, J_o, multiplied by a loss function, θ.

$$J = J_o \theta(\varepsilon_o, T, \dot{c}) \tag{4}$$

Any factor contributing to the energy dissipating characteristics
of the material, e.g., as it may be affected by the applied strain
ε_o, temperature T, and crack velocity $\dot{c}$, is reflected in θ. In
the absence of energy loss, i.e., in a perfectly elastic material,
θ reduces to unity and J approaches J_o. Thus, J_o is a rate and
temperature independent lower limit, or threshold fracture energy.
Lake and Thomas (36) suggested that cross-linking affects J_o, thus
relating the material property J to a structural parameter, M_c.
Their derivation suggests that as network chain lengths are
increased two conditions exist: (1) the number of bonds capable
of supporting stress are increased; and (2) the number of chains
crossing the crack plane are decreased. The net effect is a
dependence of J_o on M_c given by:

$$J_o = kM_c^{\frac{1}{2}} \tag{5}$$

where k is a proportionality constant incorporating the polymer
density, flexibility, mass and length of the repeat unit and
dissociation energy of the weakest chain bond. Thus, under
elastic conditions, the cohesive fracture energy is proportional
to $M_c^{\frac{1}{2}}$. Under normal testing conditions of rubbery and glassy
polymers, however, loss conditions are presumed to prevail. The
magnitude and structure dependencies of θ, if any, may mask the
simple M_c dependence expressed by Equation 5.

Experimental

The epoxy networks studied were prepared from Shell Chemical Co.
Epon 828, 1001F, 1002F and 1004F epoxy resins and the curing
agents 4,4'-methylene dianiline (MDA) and 4,4'-diaminodiphenyl
sulfone (DDS). Chemical structures and relevant physical
properties are given in Table I. The epoxy resin prepolymer
equivalent weights were characterized via endgroup titration per
ASTM method D1652. Using the assumption that the resin molecules
were difunctional, the prepolymer number average molecular weight
M_n was estimated as twice the equivalent weight. The amine
curing agents were assumed to be tetrafunctional.
    Two network systems were prepared: (1) Epon 828/MDA net-
works, in which the reactant ratios were varied; and (2) stoichio-
metric Epon resin/DDS networks incorporating variations in the
prepolymer M_n. The more latent amine DDS was used for curing the

Table I. Experimental Materials

Epon Epoxy Resins

Amine Curing Agents

MDA (4,4'-methylene dianiline)

DDS (4,4'-diamino diphenyl sulfone)

Table I. Experimental Materials (continued)

Material	Supplier	$\overline{M}_n$ g/mole	$\overline{n}$	MP °C	$\rho^{23°C}$ g/cm³
Epon 828	Shell	380	0.14	< RT	1.2
Epon 1001F	Shell	996	2.31	∿ 70	1.2
Epon 1002F	Shell	1342	3.52	∿ 80	1.2
Epon 1004F	Shell	1720	4.85	∿100	1.2
MDA	Fisher	198.3	--	90-93	1.16
DDS	Aldrich	248.3	--	175-178	1.38

higher molecular weight resins because of the harsher processing
conditions required; gel times were long enough (1/2 to 1 hour)
to permit sufficient mixing and degassing operations. The
reactant ratio was designated by an A/E value, the mole ratio of
amine hydrogens to epoxy groups, given by:

$$\frac{A}{E} = 4 \; \frac{W_A \cdot EEW}{W_E \cdot M_A} \tag{6}$$

where W_A is the mass and M_A is the molecular weight of the amine,
and W_E is the mass and EEW is the equivalent weight of the Epon
resin. For system 1 three networks of A/E=0.65, 1.0, and 1.6 were
prepared. For system 2 all networks were prepared with A/E=1.0.
    System 1 networks were prepared by mixing molten MDA with
degassed Epon 828 at 60°C. The resulting mixture was again
degassed and poured into a 60°C preheated Teflon-coated steel
mold. The mixture was cured in a circulating air oven according
to the schedule in Table II. This procedure yielded void-free
sheets from which test samples were machined. A final postcure of
5 hrs. at 180°C under vacuum was applied to all samples prior to
testing.
    System 2 networks were prepared by heating and degassing the
Epon resins for 1-2 hrs. between a minimum temperature of 50°C
and a maximum temperature of 100°C above their respective melting
temperatures. Powdered DDS was added and stirred into the resin.
The mixture was degassed and poured into preheated molds: Teflon-
coated aluminum molds were used to prepare sheets, and Dow Corning

Table II.   Cure Schedules

Network System		Time at Temperature Sequence
Epon 828/MDA	Cure	0.75 hr @ 60°C + 0.5 hr @ 80°C + 2.5 hr @ 150°C
	Postcure	5 hr @ 180°C
Epon 828/DDS	Cure	2 hr @ 150°C + 3 hr @ 200°C
	Postcure	10 hr @ 200°C
Epon 1001F/DDS	Cure	2 hr @ 150°C + 3 hr @ 200°C
	Postcure	10 hr @ 200°C
Epon 1002F/DDS	Cure	0.5 hr @ 180°C + 4.5 hr @ 200°C
	Postcure	10 hr @ 200°C
Epon 1004F/DDS	Cure	5 hr @ 200°C
	Postcure	10 hr @ 200°C

Silastic J silicone molds were used to prepare tensile microdumbbells. The networks were cured under N_2 according to the schedules in Table II. After test samples were machined, a final postcure of 10 hrs. at 200°C under vacuum was applied. This postcure was found to give a network with a stable maximum T_g.

Structure Characterization. The molecular weight between cross-links M_c was characterized by measurement of the equilibrium rubbery tensile modulus E_e which was obtained from the slope of near-equilibrium stress-strain curves (Figures 1 and 2). The two quantities are related in simple rubber elasticity theory by Equation 1. For this work the front factor ϕ and density ρ were assumed to be unity. Dumbbell specimens with a gauge length of 4 cm and a cross-sectional area of 0.14 cm^2 were tested at $T=T_g$ + 40°C in an Instron Universal tester equipped with an environmental chamber continuously purged with N_2. The specimen was extended in small load-increments of 50 to 150g at a rate of 0.05 cm/min to a total strain of <20% or to breaking. After each increment, load and extension data were recorded when the load decayed to an apparent equilibrium value. Extensions were determined using a cathetometer to measure the displacement of bench marks in the sample gauge region. The condition of equilibrium was verified by the fact that identically measured recovery stress-strain curves fell exactly on the extension curves (Figure 2).

Soluble fractions of the Epon 828/MDA networks were determined by extration with methyl ethyl ketone for 160 hrs. (Table III). The extracts were determined by gel permeation chromatography to be primarily unreacted Epon 828 and some higher molecular weight material.

Table III. Network Properties

Network	A/E	T_g °C	Resin M_n g/mole	Network M_c g/mole	$\rho^{23°C}$ g/cm^3	Sol Fraction %
828/MDA	0.65	71	380	1500	1.197	12
828/MDA	1.00	159	380	300	1.190	< 1
828/MDA	1.60	114	380	750	1.192	1
828/DDS	1.00	212	380	360	1.232	
1001F/DDS	1.00	132	996	824	1.205	
1002F/DDS	1.00	120	1342	1088	1.200	
1004F/DDS	1.00	114	1720	1506	1.196	
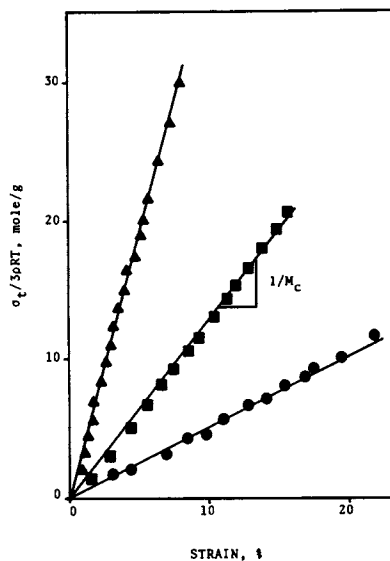
Figure 1. Epon 828/MDA near equilibrium tensile stress-strain curves at T=T$_g$ + 40°C: $\bullet$, A/E=0.65;$\blacktriangle$, A/E=1.00; $\blacksquare$, A/E=1.60.
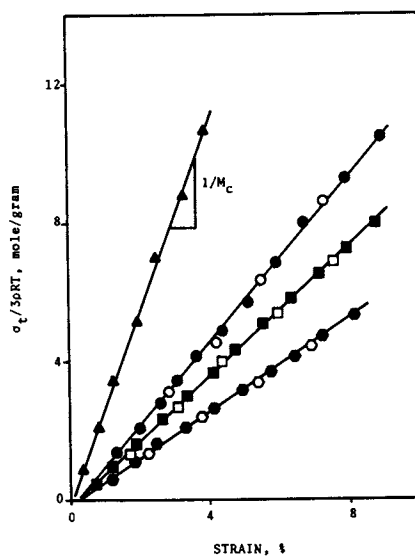
Figure 2. Stoichiometric Epon resin/DDS near equilibrium tensile stress-strain curves at T=T$_g$ + 40°C: $\blacktriangle$, Epon 828; $\bigcirc$, Epon 1001F;$\boxdot$, Epon 1002F; $\bigcirc$, Epon 1004F. Closed symbol, extension curve; open symbol, return curve.

Physical Testing. Glass transition temperatures were measured with a DuPont 990 thermal analyzer. Reported values of T_g for the Epon 828/MDA networks (Table III) were extrapolated to zero rate from measurements made at heating rates of 5, 10, and 20°C/min. Epon/DDS network T_g's were measured at 10°C/min. Bulk densities were measured at room temperature employing hydrostatic weighing techniques (37).

Below T_g (glassy) tensile testing was performed on a model 1131 Instron tester equipped with an environmental chamber. Molded microdumbbell specimens with a gauge length of 2.5 cm and a cross-sectional area of about 3 mm² were fitted with an extensometer to accurately measure strain. A cross-head rate of 0.05 cm/min (an initial strain rate of 3.4×10^{-4}/sec) was employed for all testing. The tensile data were analyzed assuming that the Poisson's ratio was 0.35.

Glassy fracture energies were measured using single edge notch (SEN) and double torsion (DT) specimens (Figure 3). Rubbery fracture measurements above T_g employed only the SEN specimen. All of the tests were performed at a cross-head rate of 0.05 cm/min. The fracture energy 2J determined from the SEN specimens was calculated from the relationship (35)

$$2J = 2\pi c W_{oc} \tag{7}$$

where c is the crack length and W_{oc} is the critical input strain energy derived from the area under the stress-strain curve extending to the point of initial crack growth. The SEN specimen dimensions were approximately 125 x 25 x 2 mm. A sharp, reproducible crack was inserted with a razor blade midway along the specimen edge using a special jig which maintained the specimen at a right angle to the blade. The sample and jig were heated well above T_g during insertion of the crack.

The fracture energy using the DT specimen was calculated from (38,39):

$$2J = G_{IC} = P_c^2 M^2 \frac{3(1+\nu)}{EWt^3 t_n} \tag{8}$$

where P_c is the critical load, E the tensile modulus, and ν is Poisson's ratio (assumed 0.35). The other geometric terms are defined in Figure 3. Typical specimen dimensions were 60 x 30 x 3 mm. The testing was performed on an Instron tester in the compression mode. Depending on the temperature fracture was either stick-slip or continuous (Figure 4). Thus three fracture energies were defined: initiation, arrest and continuous. For the Epon/MDA networks E was determined from dynamic modulus data; for the Epon/DDS networks E was obtained from tensile measurements.
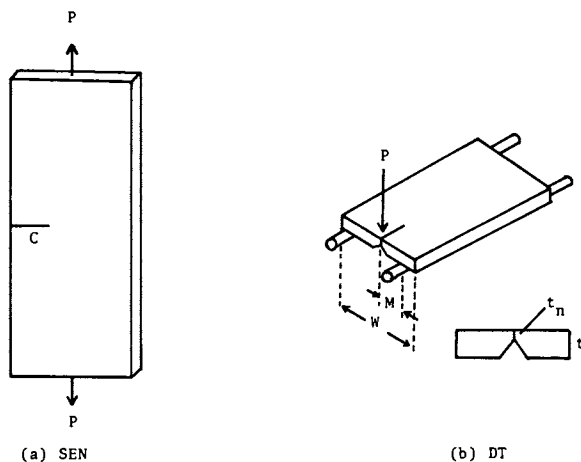
Figure 3. Fracture test specimens: (a) Single edge notch (SEN); (b) Double torsion (DT).
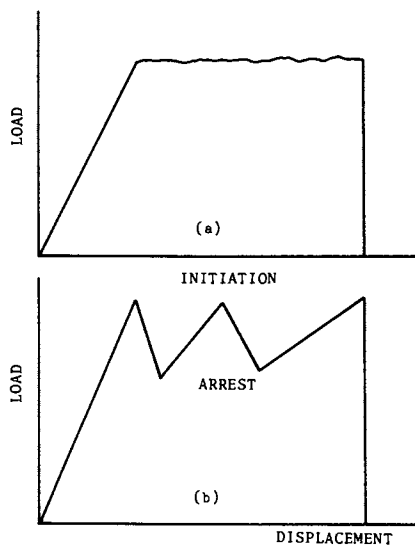
Figure 4. Typical schematic load-displacement traces for double torsion test specimen: (a) continuous (stable) crack growth; (b) discontinuous (unstable) crack growth showing initiation and arrest loads.

Results and Discussion

Network Characterization. The experimental network systems were
considered to be generated as a result of simple end-linking
chemistry on the basis of several studies. Experimental measure-
ments of T_g for all networks as a function of varying A/E ratios
in the range 0.6 < A/E < 1.6 yielded a maximum value at stoichio-
metry (A/E=1.0). This was consistent with similar measurements of
M_c as a function of A/E which also showed a minimum at stoichio-
metry. Both of these studies are represented by the Epon 828/MDA
network series data in Table III. Furthermore, the M_c vs. A/E
data displayed the functional form predicted by Bell (14) for
simple end-linking epoxy/amine networks. Finally, infrared
spectra of the networks did not reveal evidence of etherification,
the most likely competing cross-linking reaction. As the pre-
polymer molecular weight is increased, however, the reaction
becomes increasingly more difficult to detect by infrared
spectroscopy.

     For a network generated from stoichiometric quantities of a
difunctional polymer and a tetrafunctional cross-linker where
cross-linking occurs only at the chain ends the network chain
average molecular weight should approximate the prepolymer M_n.
The Epon/DDS series of stoichiometric networks is envisioned to be
such a system. Table III lists the prepolymer M_n and the experi-
mental M_c of each member of this series. The M_c's are observed to
order exactly as the M_n values, and have very similar magnitudes,
although consistently lower by 4 to 20%. These differences
possibly may be accounted for through the assumptions taken with
Equation 1, i.e., a density and front factor of unity and also
the assumption of epoxy resin difunctionality. However, the
results suggest that simple rubber elasticity theory is applicable
to these densely cross-linked networks in the rubbery state,
although such networks would apparently contradict some assump-
tions central to the theory (40), e.g., that Gaussian statistics
describe the network chain configurations and that internal
energy changes on extension are negligible. While the interpre-
tation of the meaning of the magnitudes of the M_c values from
equilibrium modulus measurements might be justifiably questioned,
the values are reasonable and correctly rank relative to one
another and, therefore, may serve as a means to correlate cross-
link density to physical properties.

     The soluble fraction was also used to characterize the Epon
828/MDA networks (Table III). The presence of a soluble fraction
in the off-stoichiometric networks is an indication of topological
variations introduced into these networks along with the intended
M_c variations. It will be shown that topology can greatly
influence the fracture behavior of these networks, thereby
complicating the effects of changes in M_c.

Fracture and M_c. Fracture energies as a function of temperature
for both network series are shown in Figures 5 and 6. They are
plotted against T_g-T_{test} to facilitate comparison between networks
by accounting for differences in T_g. A positive value of T_g-T_{test}
indicates testing in the glassy state; likewise negative values
indicate testing in the rubbery state. When double torsion
testing is employed, the plotted fracture energies are obtained
from the crack initiation values during discontinuous crack
growth.

Figures 5 and 6 show the rubbery fracture energies of the two
network series ($T_g-T_{test}<0$). The fracture energies increase with
M_c throughout the range of temperatures investigated. Apparently
the topology differences in the Epon 828/MDA networks do not
greatly affect the rubbery fracture. The glassy fracture energies
($T_g-T_{test}>0$) of these networks, however, do not order with M_c.
In fact, the highest M_c network (A/E=0.65) exhibits the lowest
glassy fracture energy. The other two networks (A/E=1.0, 1.6)
apparently do order with M_c. Evidently, the large soluble
fraction in the A/E=0.65 network plays a significant role in the
fracture behavior. Close investigation of the crack tip of SEN
specimens during testing showed this network was anomalous in
that it did not exhibit ductile yielding before failure as did the
other networks. The glassy fracture of the stoichiometric Epon/
DDS network series (Figure 6) showed, at least within 60°C of T_g,
that the initiation fracture energy is dependent on the cross-
link density. Thus for epoxy networks of similar topology
exhibiting only M_c variations, the glassy fracture apparently
increases with M_c at the same T_g-T_{test}.

The data, presented in another form, are shown in Figure 7
where log 2J is plotted against log M_c. The solid lines represent
the initiation fracture energy dependence on M_c, which is tempera-
ture dependent. The dashed line represents arrest and continuous
fracture energy dependence on M_c, which is apparently temperature
independent. The drawn lines of 1/2 slope fit the experimental
data quite well. Thus Figure 9 suggests the following approximate
relationship

$$2J = K(M_c)^{0.5} \qquad (9)$$

where K is a proportionality constant.

Why the glassy fracture energy should show any dependence on
M_c is not immediately clear. All motions and deformations that
occur in the glassy state are assumed to be short range, on the
order of one to several segments in magnitude. How a long range
structural variable such as M_c enters into the fracture process
is an interesting question. Figures 8 and 9 show the temperature
and M_c dependence of the tensile modulus and yield stress for the
Epon/DDS networks. As expected, there is no apparent M_c
dependence at any temperature except for the most densely cross-
linked Epon 828/DDS network. A number of factors other than M_c
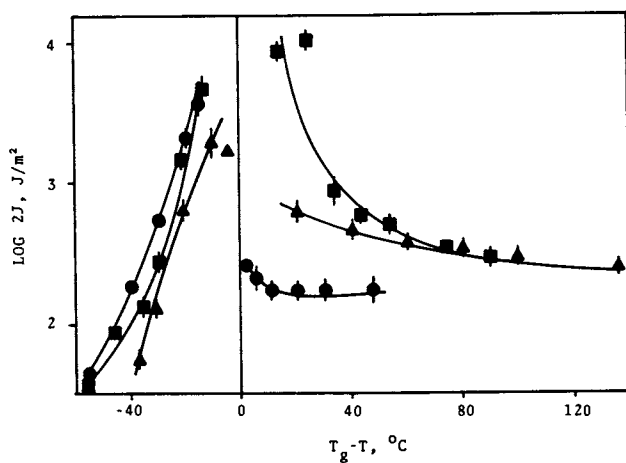
Figure 5.   Epon 828/MDA fracture behavior: ●, A/E=0.65;
▲, A/E=1.00; ■, A/E=1.60.
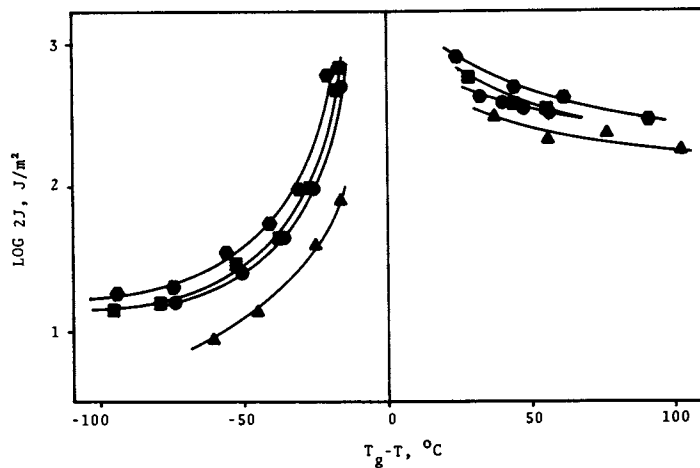
Figure 6. Stoichiometric Epon resin/DDS fracture
behavior: ▲, Epon 828; ●, Epon 1001F; ■, Epon 1002F;
⬢, Epon 1004F.
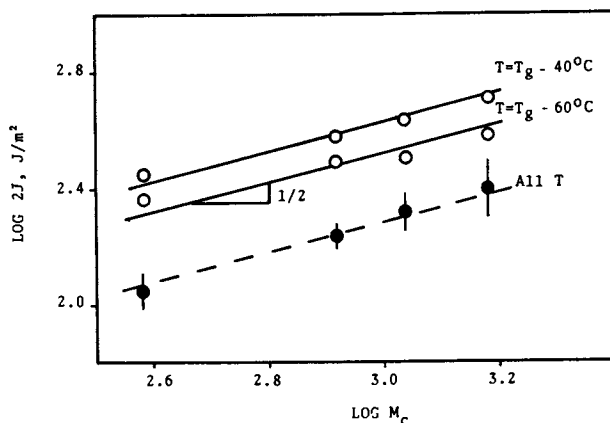
Figure 7.   Fracture energy as a function of M_C for stoichiometric Epon resin/DDS networks: ————, initiation fracture energies; ----, arrest and continuous fracture energies.   Lines with slope of 1/2 are drawn through the three data sets.
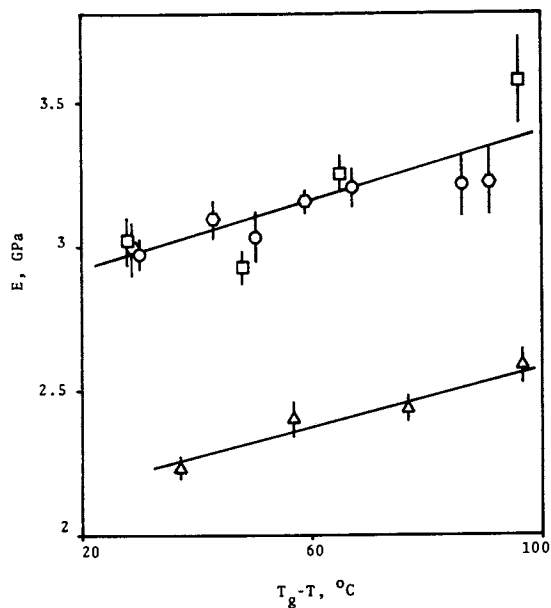
Figure 8.   Young's moduli of stoiochiometric Epon resin/DDS networks as a function of test temperature: △, Epon 828; ○, Epon 1001F; □, Epon 1002F; ◯, Epon 1004F.
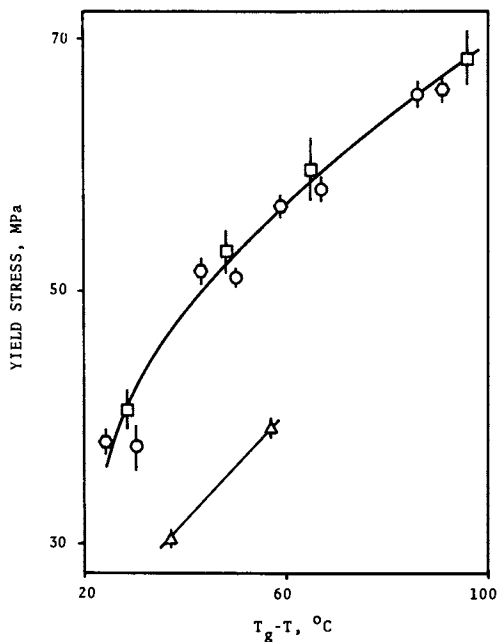
Figure 9. Tensile yield stresses of stoichiometric Epon resin/DDS networks as a function of test temperature: △, Epon 828; ○, Epon 1001F; □, Epon 1002F; ⬡, Epon 1004F.

may be responsible for this exception, e.g., a much higher and possibly inaccurate T_g, a higher bulk density, or involvement of cross-links in short range motions. The main point, however, is that only the fracture energy shows a definite M_c dependence. In addition, the M_c dependence is similar to that observed for some rubbery materials (41,42), and depends on M_c in very nearly the same way as the threshold fracture energy predictions of Lake and Thomas (36). Obviously the glassy state is not representative of threshold conditions. Why we observe the M_c dependence of fracture energy might be explained by a thermoplastic crazing theory introduced by Gent (43). He suggests that the dilational stress field induced in the region of the crack may reach sufficient magnitude to effectively increase the fractional free volume of a minute strip of material just ahead of the crack. If sufficient free volume is introduced, the effective T_g may be lowered to below the testing temperature making the material ahead of the crack tip "rubber-like". In thermoplastics this region may cavitate or craze, however in a densely cross-linked network crazing might be inhibited by the network structure. (References on crazing in epoxy networks are few and speculative (44).) If a crack propagated at a subcritical rate through this rubber-like region, then the fracture energy could conceivably show similar characteristics to rubbery fracture, i.e., a dependence on the cross-link density.

Conclusions

1. Based on studies of an homologous, endlinked, epoxy/amine network series, the simple theory of rubber elasticity has proved effective for determining reasonable cross-link densities from equilibrium modulus measurements in the rubbery state.
2. Controlling epoxy network cross-link density by varying the reactant ratio may result in changes in other structure variables as well, which may be observed by their effects on physical properties.
3. As testing temperatures approach T_g, the fracture energy of glassy epoxy networks is apparently dependent on the cross-link density when crack propagation is preceded by ductile yielding of the crack tip. An approximate proportionality of the fracture energy to M_c^2 (the average molecular weight of a network chain) has been observed for the homologous network series. A theory presuming devitrification of the crack tip is consistent with this observation.

Acknowledgments

Literature Cited

1. Bell, J. P. J. Appl. Poly. Sci. 1970, 14, 1901.
2. Gledhill, R. A.; Kinloch, A. J.; Yamini, S.; Young, R. J.
    Polymer 1978, 19, 574.
3. King, N. E.; Andrews, E. H. J. Mat. Sci. 1978, 13, 1291.
4. Yamini, S.; Young, R. J. J. Mat. Sci. 1979, 14, 1609.
5. Mijovic, J. S.; Koutsky, J. A. Polymer 1979, 20, 1905.
6. Yamini, S.; Young, R. J. J. Mat. Sci. 1980, 15, 1814.
7. Yamini, S.; Young, R. J. J. Mat. Sci. 1980, 15, 1823.
8. Manson, J. A.; Sperling, L. H.; Kim, S. L. "Influence of
    Crosslinking on the Mechanical Properties of High T_g
    Polymers"; AFML TR-77-109: A. F. Materials Laboratory,
    WPAFB, Ohio, 1977.
9. Chang, T. D.; Carr, S. H.; Brittain, J. O. Poly. Eng. Sci.
    1982, 22, 1205.
10. Chang, T. D.; Carr, S. H.; Brittain, J. O. Poly. Eng. Sci.
    1982, 22, 1213.
11. Chang, T. D.; Brittain, J. O. Poly. Eng. Sci. 1982, 22,
    1221.
12. Chang, T. D.; Brittain, J. O. Poly. Eng. Sci. 1982, 22,
    1228.
13. Thomson, K. W.; Broutman, L. J. J. Mat. Sci. 1982, 17,
    2700.
14. Bell, J. P. J. Poly. Sci.-A2 1970, 8, 417.
15. Nielson, L. E. J. Macromol. Sci. 1969, C3, 69.
16. Kelley, F. N.; Swetlin, B. J.; Trainor, D. in "IUPAC
    Macromolecules"; Benoit, H.; Rempp, P., Eds.; Pergamon
    Press: Oxford, 1982; p. 275.
17. Flory, P. J. "Principles of Polymer Chemistry"; Cornell
    Univ. Press: Ithaca, N. Y., 1953; p. 579.
18. Hermans, J. J. J. Poly. Sci. 1962, 59, 191.
19. James, H. M.; Guth, E. J. Chem. Phys. 1953, 21, 1039.
20. Katz, D.; Tobolsky, A. V. Polymer 1963, 4, 417.
21. Kaelble, D. H. J. Appl. Poly. Sci. 1965, 9, 1213.
22. Murayama, T.; Bell, J. P. J. Poly. Sci.-A2 1970, 8, 437.
23. Lunak, S.; Dusek, K. J. Poly. Sci.: Sym. No. 53 1975,
    p. 45.
24. Takahama, T.; Geil, P. H. J. Poly. Sci.: Poly. Letters
    1982, 20, 453.
25. Selby, K.; Miller, L. E. J. Mat. Sci. 1975, 10, 12.
26. Phillips, D. C.; Scott, J. M.; Jones, M. J. Mat. Sci.
    1978, 13, 311.
27. Gledhill, R. A.; Kinloch, A. J. Poly. Eng. Sci. 1979, 19,
    82.
28. Kinloch, A. J.; Williams, J. G. J. Mat. Sci. 1980, 15, 987.
29. Scott, J. M.; Wells, G. M.; Phillips, D. C. J. Mat. Sci.
    1980, 15, 1436.
30. Pritchard, G.; Rhoades, G. V. Nat. Sci. and Eng. 1976, 21, 1.

31. Morgan, R. J.; O'Neal, J. Poly. Eng. Sci. 1978, 18, 1081.
32. Griffith, A. A. Philos. Trans. R. Soc. London, Ser. A, 1921, 221, 163.
33. Andrews, E. H. "Fracture in Polymers"; American Elsevier: New York, 1968.
34. Jayatilaka, A. de S. "Fracture of Engineering Brittle Materials:; Applied Science Publishers Ltd.: London, 1978; Chap. 7.
35. Andrews, E. H. J. Mat. Sci. 1974, 9, 887.
36. Lake, G. J.; Thomas, A. G. Proc. Roy. Soc. Ser. A. 1967, 300, 108.
37. Bowman, H. A.; Schoonover, R. M. J. of Resch. of NBS 1967, 71C, 179.
38. Kies, J. A.; Clark, B. J. in "Fracture-1969"; Pratt, P. L., Ed.; Chapman Hall: London, 1969; p. 483.
39. Williams, D. P.; Evans, A. G. J. Testing and Evaluation 1973, 1, 264.
40. Treloar, L. R. G. "The Physics of Rubber Elasticity"; Clarendon Press: Oxford, 1975; Chap. 4.
41. Su, L. Ph.D. Dissertation, The University of Akron, Akron, Ohio, 1983.
42. Plazek, D. J. J. Poly. Sci.-A2 1966, 4, 745.
43. Gent, A. N. J. Mat. Sci. 1970, 5, 925.
44. Kinloch, A. J.; Williams, J. G. J. Mat. Sci. 1980, 15, 995.

Fractographic Effect of Glassy Organic Networks

D. T. TURNER

Dental Research Center and Department of Operative Dentistry, University of North Carolina, Chapel Hill, NC 27514

An unusual fractographic effect has been observed in phenol-formaldehyde polymers. This consists of a regular array of tracks and features running in the direction of crack propagation. Similar effects have been observed in other highly crosslinked organic networks viz. polyesters, epoxy resins, and polydimethacrylates. Effects which may be related have been observed in some thermoplastics, such as polymethyl methacrylate and a polycarbonate, and appear to be enhanced when fracture is caused by cyclic loading. The fractographic effect can be modeled by Preston's mechanism of intersecting crack propagation but, additionally, needs to invoke localized plastic deformation. In networks prepared by polymerization of ethylene glycol dimethacrylate, both the "track-feature" effect and flexural strength can be increased by inclusion of as little as 1% polymethyl methacrylate which, it is supposed, serves to increase localized plastic deformation.

Fractography, the study of the morphology of surfaces formed by fracture, can provide information about microstructure and crack propagation. This can contribute towards an understanding of the relationship between the structure and strength of materials. The earliest studies in this field dealt with metals and ceramics, but in recent years considerable attention has been given to organic polymers (1-6). Initially, the emphasis was on thermoplastic polymers because of insight about molecular structure which can be deduced from solution properties. Another advantage of working with thermoplastics is that they can be shaped conveniently into massive and intricate specimens, suitable for more sophisticated evaluation of properties such as fracture energy. In contrast, relatively little is known about the structure of highly crosslinked networks and, in many cases, specimen preparation is

difficult. Despite these difficulties, an increasing effort is
being made on highly crosslinked polymers because of their
superior form stability when exposed to adverse environmental
conditions, such as heat, radiation, and contact with fluids.
     The objective of the present review is to draw attention to an
unusual fractographic effect of glassy organic networks which, in
a first approach, can be explained by adoption of a simple
mechanism of crack intersections suggested previously to account
for the brittle fracture of inorganic (silicate) glasses. The
effect is described as unusual, in the case of organic networks,
on account of striking regularities of the features and also
because of the need to invoke localized plastic deformation in
order to account for departures from the distinctive morphology to
be expected for ideal brittle fracture. The occurrence of
localized plastic deformation indicates a relief from extreme
brittle fracture and may be used as a guide in formulating
stronger highly crosslinked networks.

Fractography of Brittle Materials

Descriptions of the fractography of brittle materials may be
confusing because of the difficulty of naming distinctive effects
among a whole spectrum of morphological patterns. One
simplification can be made by concentrating on just one type of
material and the most appropriate choice would seem to be
inorganic (silicate glass) networks (7-9). Another simplification
is to envisage an idealized course of events as when a crack,
initiated from a notch by an applied tensile stress, accelerates
in generating the fracture surface. At first the release of
elastic strain energy just suffices to cleave a smooth even
surface termed the "mirror" region. Eventually, the increasing
amount of energy released is manifested in a rougher surface which
appears like a "mist." This is succeeded, in turn, by a much
rougher surface described as a "hackle" region. Finally, the
available energy may be sufficient to eject needle-like splinters
termed "shards." Actual fracture surfaces are quite diverse in
appearance and the regions are by no means so discrete and
well-defined as represented in Figure 1. The hackle region is
especially complex and includes a variety of features, running in
the direction of crack propagation, including ones which have been
designated as "river markings" and "stries." The stries remain
attached to the surface and have characteristic cross-sections,
which were sketched by de Fréminville from early but acute
experimental observations (7). These sketches will not be
reproduced here and instead reference will be made to a similar,
but idealized, cross-section which will be indicated later.

Phenol-Formaldehydes

Because of their practical importance and relatively early
development, by Baekeland, a considerable amount of work has been
done on condensation products of phenol and formaldehyde and,
also, on other related highly crosslinked glassy polymers. A 1957
study of a cast resole, given a prolonged high temperature cure,
included examination of fracture surfaces by electron microscopy.
One micrograph was shown in which "long, thin strips of plastic
were separated by cleavage from the mass." There was also a
limited region which included an array of lines which were spaced
fairly regularly (10). No comment was made on the orientation and
origin of the lines and, as far as is known, the observation was
not pursued in the scientific literature.
    In 1971, a study was made of a polymer similar to the one
mentioned above, exceptional care being taken to prepare well
annealed specimens. A notch of controlled geometry was introduced
into massive specimens by means of a metallic foil. After
breaking in tension, the fracture surfaces appeared to resemble
ones previously reported for silicate glasses. Five regions were
distinguished (Figure 2). The first, under the foil, is dull and
featureless (region 1). It is followed by a jumbled transition
(region 2) which preceeds a relatively short mirror (region 4).
The final much more extensive region 5 includes grosser surface
features, such as shard depressions (11).
    A striking difference from reports on silicate glasses was
revealed when regions 4 and 5 were examined at higher
magnification. Extended parallel arrays of lines were seen
running in the direction of crack propagation. At still higher
magnification, "features" could be observed to be lying on
"tracks." In some cases, the features were only partially
attached to the tracks with either the ends or a middle section
detached (Figure 3). In other cases, the features were either
missing completely or else disposed irregularly across the tracks
(11).
    Although a most striking aspect of the tracks is their
linearity over considerable distances, there were some notable
exceptions. In particular, it was observed that the tracks could
curve sharply in the vicinity of some shard depressions. This may
be seen by examination of part of a shard depression which was
generated by a principle crack running from right to left in
Figure 4. Both above and below the shard depression, tracks and
features are aligned in the direction of propagation of the
principle crack front. In contrast, within the depression itself,
the tracks curve in until they are disposed almost perpendicularly
to their original direction. It is supposed that this particular
depression was formed by a process in which, locally, the crack
front had changed direction so as to form a shard by a transverse
peeling, from the bottom to the top in Figure 4, around the shard
axis (12).
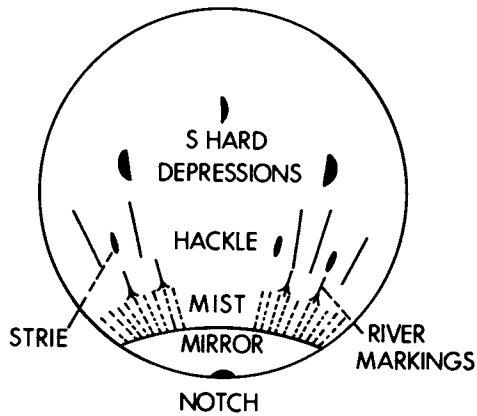
Figure 1. Schematic representation of regions of increasing roughness on the fracture surface of a silicate glass rod.
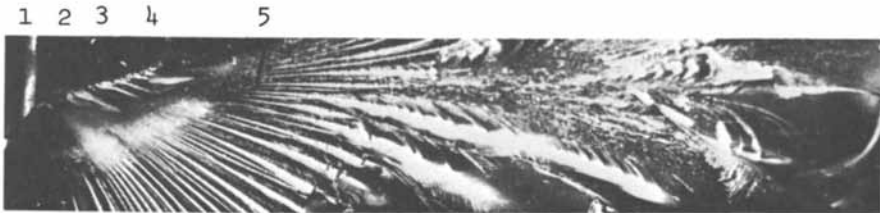
Figure 2. Fracture surface of a phenol-formaldehyde polymer (X2). Reproduced with permission from Ref. 11 Copyright 1971, John Wiley & Sons, Inc.
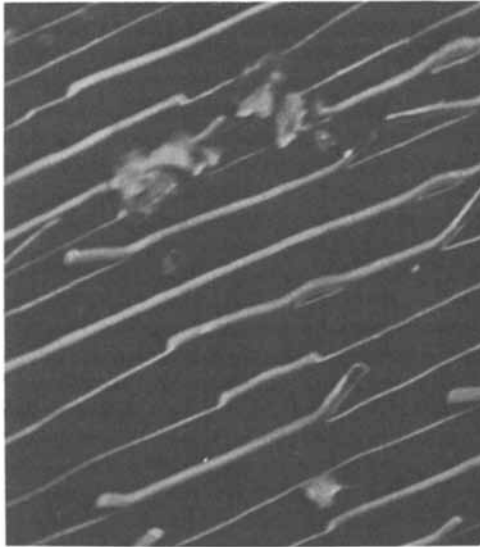
Figure 3. Scanning electron micrograph showing tracks and features on the fracture surface of a phenol-formaldehyde polymer (X4650). Reproduced with permission from Ref. 12 Copyright 1972, John Wiley & Sons, Inc.
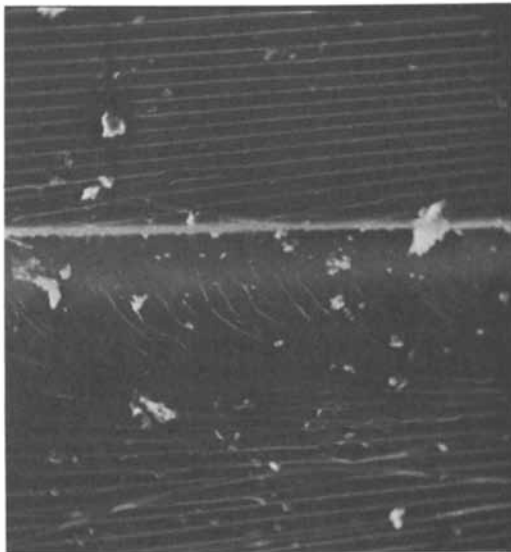
Figure 4. Scanning electron micrograph showing curvature of tracks into a shard depression. Reproduced with permission from Ref. 12 Copyright 1972, John Wiley & Sons, Inc.

In an extension of the work described above, the influence of
ambient temperature on both fracture morphology and fracture
energy was investigated. At 120°C the "track-feature" effect
could still be seen, along with interference colors, but was less
pronounced than at room temperature. At 175°C, and above,
interference colors were not seen; neither was there any
indication of localized plastic deformation. As the temperature
was raised, the fracture energy approached a low value, such as
could be calculated for an ideally brittle network. The decrease
was particularly marked at temperatures ≥ 175°C. A glass
transition was detected near 150°C and it was suggested that above
this temperature the work of plastic deformation became negligible
(13).

Some Other Glassy Networks

The fracture of highly crosslinked polymers has been reviewed, up
to 1976 (14), from a broad point of view but here attention will
be confined to fractographic observations which may be related to
the "track-feature" effect. The main criterion for inclusion is
that lines on fracture surfaces were observed, which run in the
direction of crack propagation.
      Cast crosslinked polyesters were studied mainly from the point
of view of factors which influence fracture toughness and the rate
of crack propagation. Massive specimens with a central notch were
pulled in tension. In one experiment, crack propagation was begun
under cyclic loading, at a frequency of 0.17 Hz. Cyclic loading
was then stopped and fracture completed under a static load. The
part of the fracture surface generated by cyclic loading exhibited
an array of parallel features, described as "furrows," running in
the direction of crack propagation. The remainder of the surface,
generated by the final static load, was much smoother and did not
exhibit furrows (15).
      In studies similar to those described above, the fracture
surfaces "showed small mirror and mist regions giving way to
hackle and crack branching."..."Long narrow features, 'river
lines,' were usually seen running from the initiation point
through the mirror and merging into the structure of the mist
regions. Extended filaments can be seen along the tracks." It
was noted that "Similar observations have recently been made on a
brittle phenol-formaldehyde thermoset resin." It was concluded
that "The fracture surface morphology of the polyester resin is
very similar to that of glass but there are signs of limited
plastic deformation. This includes curved filaments of material,
often seen attached to tracks on the surface" (16).
      A number of studies have been made of epoxy resins and, again,
major emphasis has been on the relationship between the mode of
crack propagation and toughness (17-21). Slip-stick crack
propagation was observed which, in some ways, has features similar
to observations made on many linear polymers. More pertinent were

observations made after crack arrest in double cantilever beam
specimens: "Large amounts of plastic flow are indicated by a
considerable surface roughness. The initiation marks (steps or
ridges) are visible to the naked eye." This region was confined
to a relatively small length of several hundred μm and was
succeeded by a surface which was mirror-smooth to the naked eye
(19). Examination of micrographs of the ridges shows that, from
the present viewpoint, some of them might be described as tracks
with features partially detached.
    Work on epoxy resins, crosslinked by polyamines, culminated in
a detailed study of the morphology of surfaces formed by fracture
of double cantilever beam specimens. It was noted that "Of
particular interest are detached fibers 1 or 2 μm in diameter
which are visible over a wide range of the diffuse region.
Microscopy suggests that the fibers have irregular surfaces and
appear to be formed by brittle cleavage from the ridges of the
fracture surface. In some cases, they become reattached further
along the surface." The conclusions section began with the
following paragraph:
    "Slow, stable, or subcritical crack extension is associated
with the formation of a furrowed surface. This type of behavior
is promoted by slow testing rates and the presence of a
plasticizer in the resin. Comparison with other work suggests
that this may be a common mode of fracture in epoxy resins,
including fully cured systems, and possibly in highly crosslinked
polymers in general" (21). This statement was made from an
informed knowledge of prior work on phenol-formaldehydes and
polyesters.

Methacrylate Networks

Methacrylate networks have been of special interest in
fractographic studies because they would seem to afford a
methodical way of proceeding from knowledge of an extensively
studied linear polymer, polymethyl methacrylate (PMMA), to
networks with increasing amounts of crosslinking e.g. made by
copolymerization of ethylene glycol dimethacrylate (EGDM) with
methyl methacrylate. Beginning with PMMA itself, it seems likely
that most investigators who have examined its fracture surface
under the microscope by reflected light will have noticed gleaming
little protrusions from the surface. It is one of those common
observations which momentarily excites attention but then fades
away in the mind because it does not fit into any verbalized
pattern of knowledge. Now, because the present point of view does
focus on such a pattern, it becomes of interest to re-examine such
observations. A typical micrograph of a fracture surface of a
specimen of PMMA, of M_v = 140,000, is shown with the direction of
crack propagation indicated by the arrowhead in the top right hand
corner (Figure 5). Part of the boundaries of one of the ribs has
been indicated by circles joined by irregular lines (22). Also,
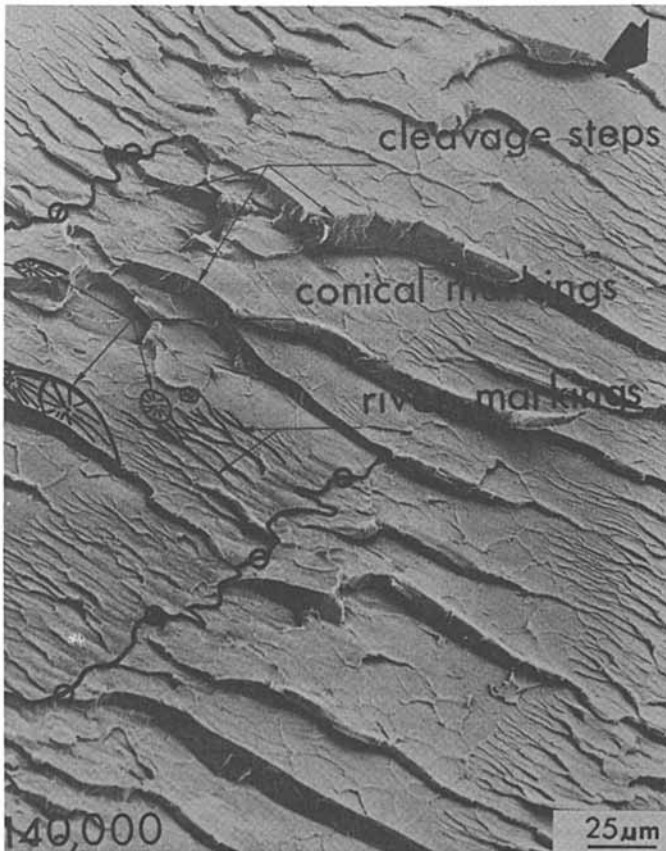
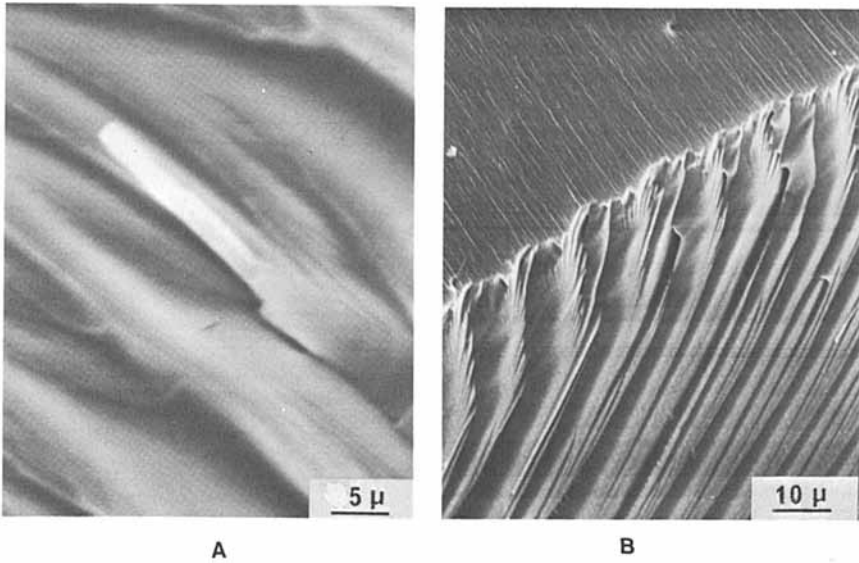Figure 5. Scanning electron micrograph of a fracture
surface of PMMA. Reproduced with permission from Ref. 22
Copyright 1977, Butterworth & Co. (Publishers, Ltd.).

some well-known fractographic features have been emphasized for
convenience of recognition. An example of a protrusion is to be
seen just below the words "river markings." This might be
regarded as an incipient case of a feature protruding from a
track. Taking into account the whole array of river markings
suggests how a roughly parallel set of incipient tracks and
features might be formed. However, in the case of a linear
polymer the length of such markings is limited to the short
distance between ribs and hidden in a multiplicity of other
morphological details.

Under conditions in which rib markings were prevented, by the
slow crack growth accompanying cyclic loading, it was possible to
generate extremely long torn out fibers which remained attached to
river patterns. A micrograph and a sketch were presented to
emphasize this discovery. It was stated that "In the river
pattern of the PMMA fracture ribbon-like fibres of material have
been observed torn out from the river patterns after having been
produced by a similar mechanism. The fibres remained attached at
one end producing a hairy appearance (23).

As an aside to the polymethacrylates discussed in this
section, mention must be included of earlier and much more
striking results obtained with a polycarbonate. The fracture
surfaces reported were more akin to ones characteristic of a quite
brittle polymer, in contrast to results for other linear polymers.
A grain structure was observed which appears closely similar to
that discussed in the present work. Its formation was attributed
to a mechanism of crack intersection in river pattern areas.
"Such fibrils also were observed on the final fracture area of
polycarbonate specimens broken in fatigue tests."..."It is
worthwhile to note that these fibrils were never observed on
static fracture surfaces of polycarbonate and that their formation
must be supported by the forgoing cyclic loads, probably by
changing material properties" (24). Thus, in both PMMA and in a
polycarbonate, there is evidence that the formation of long tracks
and features is favored by crack propagation under cyclic loading.
As mentioned above, this may be due to elimination of rib spacings
which curtail the growth of river markings.

Studies of crosslinking of methacrylate polymers were mainly
concerned with the influence of crosslinking on fracture energy
and strength. In addition, incidental observations were made of
changes in fracture surface morphology. In all cases, it was
reported that as the concentration of crosslinks was increased,
the bright surface colors, a characteristic of linear PMMA of high
molecular weight, decreased in intensity and eventually
disappeared (25). In slow cleavage tests, no difference in
morphology was noted between linear and crosslinked specimens; in
all cases, the fracture surfaces were mirror smooth (26). Also,
at higher rates of extension, at 0.1 cm/min in a conventional
tensile test, the usual surface morphology (ribs, parabolic
markings, etc.) were observed in both linear and crosslinked

specimens (27). Although no effect of crosslinking, other than on
the disappearance of colors, was detected in the above
investigations, it should be emphasized that crosslinking levels
were limited to copolymers made with up to only 10 mole-% EGDM.

Early attempts to prepare more highly crosslinked methacrylate
networks provided only polymeric fragments because of the combined
effects of contraction during polymerization and the brittleness
of the products (28-30, 25). The first opportunity to test a
highly crosslinked methacrylate polymer came as a result of the
fortuitous polymerization of a bottle of EGDM to give a massive
uncracked specimen (31). A saw cut was made in a portion of this
specimen and a fracture surface generated by driving in a wedge.
A sketch of the fracture surface indicates mist and hackle regions
along with the smooth, undulating ribs often observed in very
brittle materials (Figure 6A). Optical micrographs illustrate the
formation of closely spaced lines running in the direction of
crack propagation, except where they curve into some of the shards
(Figures 6B-C). In an extension of this work, a method of
polymerization was devised which allowed preparation of small
specimens, suitable for three point bending tests, covering the
complete range of comonomer compositions from 0 to 100 mole-%
dimethacrylate. The presence of "track-feature" morphology was
confirmed for fracture specimens which contained above 50 mole-%
EGDM or triethylene glycol dimethacrylate. Scanning electron
micrographs also revealed some further details about tracks and
features. Figure 7A is interpreted as showing a transition in
cross-section of a feature which remains partially locked into the
surface zone and which, for the rest, protrudes above the surface.
Figure 7B shows an edge view of a fracture surface which is
interpreted as the beginning of an array of tracks; these are
disposed at an angle of about 60° to the vertical, in the lower
part of the figure (32).

Mechanism of Formation of Stries

Cross-sections of stries were sketched by de Fréminville in 1914
but the mechanism of their formation was not explained
satisfactorily until Preston's analysis of 1931 (7, 33). Preston
considered the upward propagation of a crack through a block of
glass. Imagine that the crack has traversed only part of the way
and is to be seen advancing from a top view (Figure 8A). Up to
this time, the crack has propagated with a continuous front which
is perpendicular to the principle tensile stress, oriented as
indicated by the arrowheads. More generally, it is a basic
hypothesis that cracks will always propagate at right angles to
the principle tensile stress just ahead of the crack tip. Suppose
now that the crack tip cleaves into a region in which the
principle tensile stress is inclined at an angle to its former
direction, as indicated by the arrowheads in Figure 8B. By
hypothesis, further crack propagation must be at right angles to
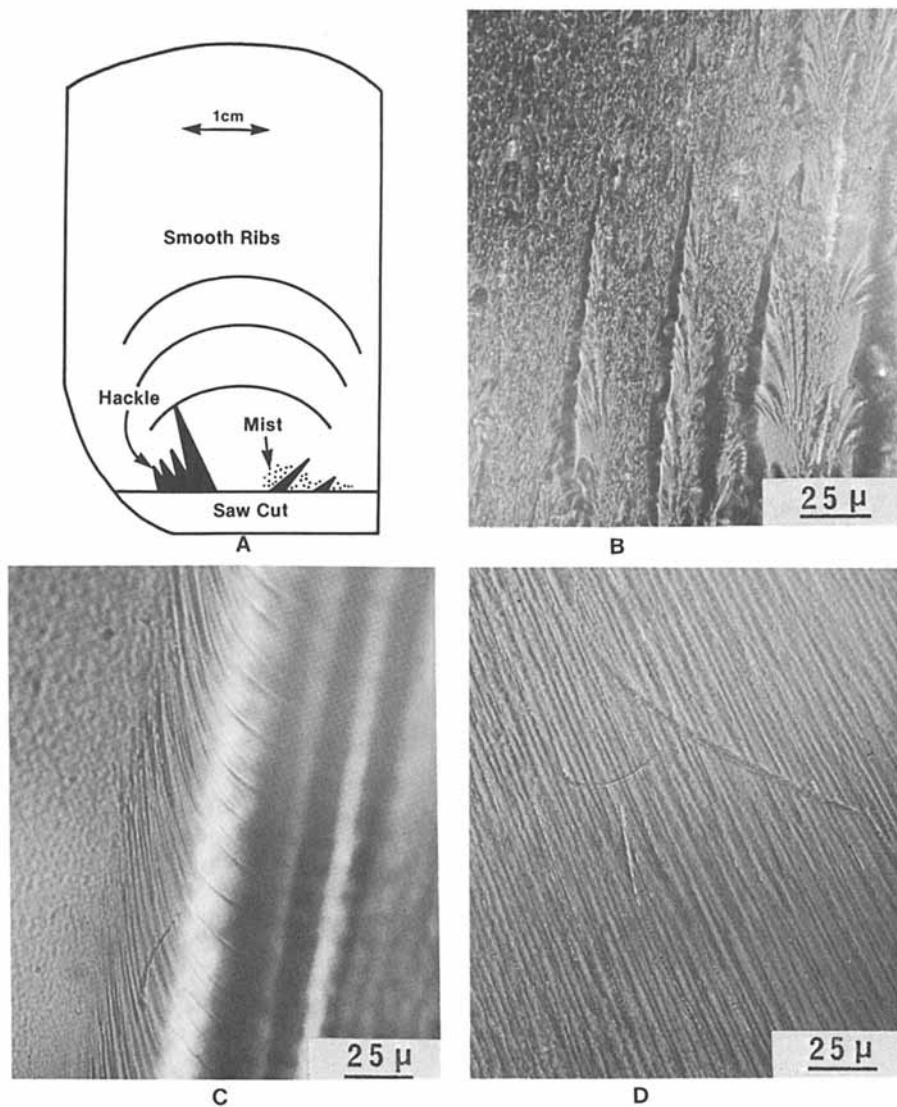
Figure 6. Sketch and details of a fracture surface of poly(EGDM). Reproduced with permission from Ref. 31 Copyright 1982, John Wiley & Sons, Inc.

Figure 7. Scanning electron micrograph of details of a
fracture surface of poly(EGDM). Reproduced with
permission from Ref. 33 Copyright 1982, Chapman & Hall,
Ltd.
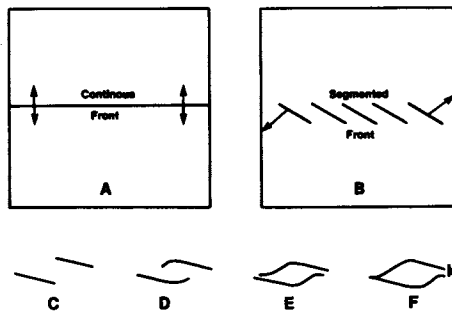
Figure 8. Development of the strie cross-section
characteristic of brittle fracture. Reproduced with
permission from Ref. 31 Copyright 1982, John Wiley & Sons,
Inc.

this new stress field, but obviously the whole continuous crack
front cannot immediately swing round. Instead, by way of
compromise, it splits up into an array of microcracks each of
which is appropriately oriented (Figure 8B). In this new
configuration, the upward progress of the discontinuous array of
microcracks is momentarily arrested. In order for upward progress
to proceed, the microcracks must first join together to form a
continuous front. Preston discussed how this occurs in some
detail but in a first approach it will suffice to indicate the
joining of a single pair of microcracks, as in Figures 8C to E.
It will be seen that the ends of the microcracks swing towards
each other and eventually join at one site. As a result of
renewed propagation of the modified crack front, the fracture
morphology would consist of a linear array of "stries" attached to
one fragment of the block, or the other, by small unbroken
connections (at k, as in Figure 8F). Thus, Preston's mechanism
can account for a linear array of stries with a characteristic
cross-section, such as is shown in Figure 8F (31). With a less
symmetrical change in the stress field ahead of the crack tip, it
can also account for less regular patterns, including isolated
stries.

    Preston's mechanism was adopted to explain the "feature-track"
effect observed in the fractography of glassy organic networks
(32). However, a major difference is that the cross-section of
the features departs widely from predictions for an ideal brittle
material, and such as were reported in de Fréminville's work on
inorganic silicate networks (7). Instead, the features generally
approximate to a circular cross-section. A possible
rationalization is that the shape of a strie may be modified by
considerable, though localized, plastic deformation. Such a
transition is evidenced as when a strie appears to have a
cross-section similar to that predicted for brittle fracture so
long as it remains locked into the surface zone. Yet, when part
of the same strie protrudes from the surface, it tends towards a
cylindrical shape (Figure 7A). If the above considerations are
correct, then it would be appropriate to redesignate "features" as
"stries modified by localized plastic deformation." However, for
the sake of caution, the more non-commital designation will be
retained.

    The formation of an individual strie was emphasized in Figure
8. It may also be helpful to visualize the formation of a set of
stries, as in Figure 9 (34). The way in which a continuous
modified crack front (Figure 9B) might be formed has been
discussed already. Now imagine, further, that the two surfaces
are separated by a (shaded) gap (Figure 9C). In this
representation of one extreme case, all the stries are shown to be
on one of the fracture surfaces. The other surface shows an array
of tracks alone. Its appearance may be compared with the
experimental observation of an edge view of a fracture surface,
shown in Figure 7B. Of course, the experimental observation is

less regular than would be predicted from the idealized sequence
of events leading up to Figure 8C. Nevertheless, it can still be
recognized as a side view of a case in which all the tracks have
been denuded of features.
    The lower portion of Figure 9 indicates how grosser stries
might be formed from a different disposition of microcracks.
    An obscure aspect of the concept of localized plastic
deformation is just how it might lead to a drastic departure from
a cross-section characteristic of brittle fracture towards that of
a circle (Figure 9D). If the features are regarded as solid
fibers, then it might be argued that the change in form is just a
case of a transient fluid tending towards a surface of minimum
area before setting. On the other hand, there is good evidence,
in the case of phenol-formaldehydes, that occasional features
consist of curled-up films. Such observations led to the
suggestion that features are formed by a curling mechanism (11).
This view is now regarded as less general than the likelihood that
most features are solid fibers.

Localized Plastic Deformation and Strength

It is widely recognized that localized plastic deformation may be
desirable in order to reduce brittleness. For example, there is
very little plastic deformation in very brittle inorganic glasses,
such as silicates (35). For this reason, evidence for localized
plastic deformation has been carefully sought in organic glasses.
In thermoplastic polymers, of sufficiently high molecular weight
(22), there is usually extensive evidence of plastic deformation
which can be related to crazing (6). In highly crosslinked
networks, crazing does not occur and evidence of localized plastic
deformation is deduced from departures from the fracture
morphology of silicate glasses. For example, there may be fibrous
features on the fracture surface which are curved or which taper
in a way which seems unlikely for a brittle material. The present
criterion for localized plastic deformation, though still
qualitative, seems to be better defined i.e. that the stries
should have a cross-section which departs considerably from
Preston's prediction for an ideally brittle material, towards a
circular cross-section.
    It is difficult to conceive of a mode of localized plastic
deformation in a material with a high density of uniformly
distributed crosslinks. Rather, such a material should have
extremely brittle properties approaching those of diamond.
Therefore, following Houwink (36-38), it has long been considered
that phenol-formaldehyde networks actually have a particulate
microstructure which is inconsistent with uniform crosslinking.
In fact, gross microgel clusters are commonly observed, as in
Figures 3 and 5. More discriminating studies at higher
magnification revealed much smaller particles of ca 80 nm (10).
Observations of the above kind have been rationalized by reference

to Houwink's suggestion of highly crosslinked particles embedded
in a matrix of a much less highly crosslinked material. It is
this matrix which makes possible localized plastic deformation.
    Recently, considerable attention has been given to the
characterization of the particulate microstructure of highly
crosslinked polymers with an eye to correlation with mechanical
strength. In the case of epoxy resins, it was reported that
localized plastic deformation and strain energy release rate were
correlated with particle size in the range 15-45 nm (19). It has
been recognized that this quantitative approach to
structure/property relations is important, although doubt has been
expressed about the validity of this particular correlation (20).
    The present approach towards reducing brittle fracture is only
the general one of seeking conditions which increase localized
plastic deformation. The main criterion is the extent of the
"track-feature" effect on fracture sufaces. This is only a
qualitative approach but, nevertheless, it does allow a convenient
examination of small specimens which can be broken by bending.
This allows a rapid screening of materials prepared in various
ways. Those materials which generate fracture surfaces with
"track-feature" regions can then be tested for strength. Results
of this approach can be illustrated for networks prepared by
polymerization of EGDM. First, polymerization conditions were
found which gave the strongest specimens, with a flexural strength
of 66 ± 15 MPa. Then the polymerization was repeated with PMMA
(M_v = 3.2 x 10^5) predissolved in the EGDM monomer. Strength was
increased by about 40% by as little as 1% PMMA (39). Specimens
with 1% PMMA were transparent and exhibited a more marked
"track-feature" morphology than did controls without PMMA. These
results (Figure 10) were rationalized by supposing that, during
the polymerization, the PMMA was segregated to the surface of
growing microgel particles. This resulted in a more discrete
particulate microstructure. This inhomogeneity in the
distribution of crosslinks favored localized plastic deformation
and hence an increase in strength (34).
    In order to get the results mentioned above (Figure 10), the
PMMA must be of high molecular weight. Presumably this is
necessary in order to benefit from a contribution to strength from
entanglements. In the case of PMMA above, an entangled network is
just formed for specimens with a number average molecular weight
in the range 10,000-20,000 (40).

Concluding Remarks

An important question about any effect is the range of its
occurrence. It will be recalled that it was suggested that the
"track-feature" effect may be general to highly crosslinked
polymers on the basis of results known for phenol-formaldehydes,
polyesters, and epoxy resins (21). Subsequently, this suggestion
was given further weight when the effect was found in
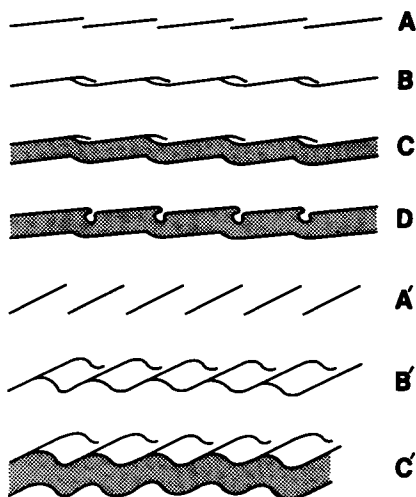
Figure 9. Mechanism for the formation of stries and
linear features. Reproduced with permission from Ref. 34
Copyright 1982, Society of Plastics Engineers.

WEIGHT PERCENTAGE OF PMMA IN MIXTURE
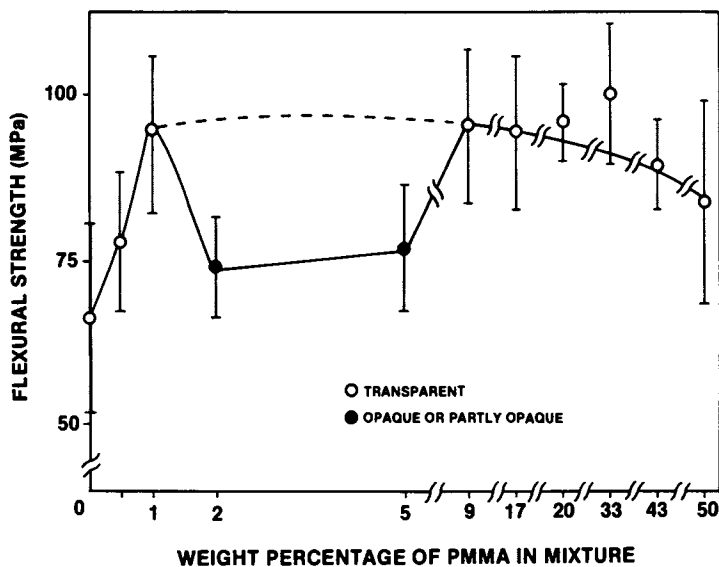
Figure 10. Dependence of flexural strength on amount of
PMMA incorporated in poly(EGDM) networks. Reproduced with
permission from Ref. 39 Copyright 1983, Chapman & Hall,
Ltd.

polymethacrylate networks. Furthermore, an incipient effect,
which may be related, was pointed out in the case of PMMA. This
incipient effect was enhanced when fracture was caused by cyclic
loading and was most true to pattern in results for another linear
polymer, a polycarbonate. It seems that the effect is favored in
linear polymers when the test conditions preclude the gross
changes in fracture surface morphology which accompany rib
formation. In summary, there are indications that the
"track-feature" effect can be detected in many organic glasses,
provided they are of sufficiently high molecular weight.
    A further question which should be considered is whether the
"track-feature" effect is limited to organic glasses or whether,
with an informed eye, it can be detected also in inorganic
networks. Preston did suggest that regular arrays of columns of
basalt, up to four feet thick and thirty feet high, which are to
be seen in various geological formations (41) can be explained by
his mechanism (33). On a still grander scale, there is the
possibility that recently discovered features on the sea-floor, up
to 15 km in cross-section (42), might be attributed to a similar
cause (43).
    On a more modest, and a more pertinent, scale, it seems
worthwhile to look more closely into literature on the fracture of
silicate glasses. In some of the earliest work de Fréminville did
refer to a phenomenon termed "cheminement parallèl" which may
imply a regular array similar to tracks and features.
Unfortunately, because of low magnification, it is difficult to
judge whether this really is the case. In an authoritative work
of 1936, Smekal discussed the fracture morphology of brittle
substances in some detail but does not give examples of parallel
arrays, apart from one curious exception observed when silicate
glass rods were fractured at high temperatures approaching the
softening point. He described these arrays as occurring on an
"Oberfläche," whereas he usually referred to a fracture surface as
a "Zerreissfläche" (44). Therefore, his description, as well as
that of the original author Mengelkoch (45), seems to imply that
the arrays were on the walls of the rod rather than on the
fracture surface itself. If this reading is correct, then
another, but equally striking, phenomenon would be involved. In
any event, this work deserves re-examination because the fracture
of inorganic glasses at high temperatures is of special interest
for comparison with data obtained on organic glasses at room
temperature. It would also be of interest to study the
fractography of recently developed glasses of high strength to
find whether they exhibit evidence of localized plastic
deformation.
    Judging from the range of occurrence of an effect first
observed in phenol-formaldehyde networks has led eventually to
comparison with extreme cases which, pattern-wise, seem to be
related only remotely. The most closely related patterns were
observed in four chemical types of organic networks and, next, in

a linear polycarbonate fractured by cyclic loading. The justification for consideration of other more extreme cases is the view that they are all related by Preston's mechanism. A more informed view will be possible with further focused documentation of these diverse fractographic observations.

Acknowledgments

Literature Cited

1. Zandman, F. "Études de la Deformation et de la Rupture des Matières Plastiques"; Publications Scientifiques et Techniques du Ministère de l'Air: Paris, 1954; No. 291.
2. Wolock, I.; Kies, A.J.; Newman, S.B. "Fracture Phenomena in Polymers" in "Fracture"; Averbach, B.L.; Felbeck, D.K.; Hahn, G.T.; Thomas, D.A.; Eds.; Technology Press and Wiley: New York, 1959.
3. Berry, J.P. in "Fracture Processes in Polymeric Solids"; Rosen, B., Ed.; Interscience Publishers: New York, 1964; Chap. II.
4. Newman, S.B. Polymer Eng. and Sci. 1965, 59.
5. Andrews, E.H. "Fracture in Polymers"; Elsevier: New York, 1968; Chap. 6.
6. Kambour, R.P. J. Polym. Sci., Macromol. Rev. 1973, 7, 1.
7. de Fréminville, C. Rev. Metal 1914, 11, 971.
8. Preston, F.W. J. Soc. Glass Technol. 1929, 13, 3.
9. Smekal, A. Ergebn. exact. Naturwiss. 1936, 15, 106.
10. Spurr, R.A.; Erath, E.H.; Myers, H. Ind. Eng. Chem. 1957, 49, 1838.
11. Nelson, B.E.; Turner, D.T. J. Polym. Sci. B 1971, 9, 677.
12. Nelson, B.E.; Turner, D.T. J. Polym. Sci. A-2 1972, 10, 2461.
13. Nelson, B.E.; Turner, D.T. J. Polym. Sci. (Phys. Ed.) 1973, 11, 1949.
14. Pritchard, G.; Rhoades, G.V. Mater. Sci. Eng. 1976, 26, 1.
15. Owen, M.J.; Rose, R.G. J. Phys. D: Appl. Phys. 1973, 6, 42.
16. Christiansen, A.; Shortall, J.B. J. Mater. Sci. 1976, 11, 1113.
17. Phillips. D.C.; Scott, J.M.; Jones, M. J. Mater. Sci. 1978, 13, 311.
18. Yamini, S.; Young, R.J. J. Mater. Sci., 1979, 14, 1609.
19. Mijović, J.; Koutsky, J.A. Polymer 1979, 20, 1095.
20. Yamini, S.; Young, R.J. J. Mater. Sci. 1980, 15, 1831.
21. Cherry, B.W.; Thomson, K.W. J. Mater. Sci. 1981, 16, 1925.
22. Kusy, R.P.; Turner, D.T. Polymer 1977, 18, 391.
23. Johnson, F.A.; Radon, J.C. Materialprüf 1970, 12, 307.
24. Jacoby, G.H. ASTA STP 1969, No. 453, 147.
25. Berry, J.P. J. Polym. Sci. A 1963, 1, 993.

26. Broutman, L.J.; McGarry, F.J. J. Appl. Polym. Sci. 1965, 9, 585.
27. Lee, H.B.; Turner, D.T. Polym. Eng. and Sci. 1979, 19, 95.
28. Losaek, S.; Fox, T.G. J. Amer. Chem. Soc. 1953, 75, 3544.
29. Losaek, S. J. Polym. Sci. 1955, 15, 391.
30. Fox, T.G.; Loshaek, S. J. Polym. Sci. 1955, 15, 371.
31. Atsuta, M.; Turner, D.T. J. Polym. Sci. (Phys. Ed.) 1982, 20, 1609.
32. Atsuta, M.; Turner, D.T. J. Mater. Sci. Letters 1982, 1, 167.
33. Preston, F.W. J. Amer. Cer. Soc. 1931, 14, 419.
34. Atsuta, M.; Turner, D.T. Polym. Eng. and Sci. 1982, 22, 1199.
35. Marsh, D.M. Proc. Roy Soc. (London) 1964, A282, 33.
36. Houwink, R. Trans. Faraday Soc. 1936, 32, 131.
37. Houwink, R. J. Soc. Chem. Ind. 1936, 55, 247.
38. Houwink, R. "Elasticity, Plasticity, and Structure of Matter"; 2nd Ed., Dover: New York, 1958.
39. Atsuta, M.; Turner, D.T. J. Mater. Sci. 1983, 18, 1675.
40. Turner, D.T. Polymer 1982, 23, 626.
41. Iddings, J.P. Amer. J. Sci. 1886, 31, 321.
42. Macdonald, K.C.; Fox, P.J. Nature 1983, 302, 55.
43. Taylor, D.F.; Turner, D.T. "Overlapping Spreading Centers on the Sea-floor and the Morphology of Brittle Fracture"; unpublished work.
44. Smekal, A. see ref. 9; Fig. 32.
45. Mengelkoch, K. Z. Physik 1935, 97, 46.

Peroxide Cross-linked Natural Rubber and *cis*-Polybutadiene

Characterization by High-Resolution Solid-State Carbon-13 NMR

DWIGHT J. PATTERSON and JACK L. KOENIG

Department of Macromolecular Science, Case Western Reserve University,
Cleveland, OH 44106

Changes in the structure of natural rubber and cis-
polybutadiene have been observed using solid state
carbon-13 NMR. Cis-trans isomerization has been
shown to occur in the natural rubber by rearrangement
of the allylic free radical. At least four different
methyl groups have been detected in the cross-linking
of natural rubber by dicumyl peroxide, which indicates
that the simple combination of allylic free radical is
an oversimplification of the curing process. Quater-
nary aliphatic carbons have been detected which suggest
double bond migration. Polybutadiene showed only
methine and methylene carbons in the cross-linked net-
work with a small amount of methyl end groups. The
increase in the line width of the highly cross-linked
elastomers has been shown to be due in part to the
static dipolar interaction between carbons and protons
and chemical shift dispersions. The formation of trans
double bonds has been observed in the infrared spectra
of cis-polybutadiene. Weak broad bands around 1320 cm^{-1}
observed in the difference spectrum of cured rubbers
may be due to carbon–carbon cross-links. From the
structural interpretation of spectra obtained from
solid state carbon-13 NMR and Fourier transform infra-
red spectroscopy, models are proposed for the cross-
linked networks of natural rubber and cis-1, 4-
polybutadiene formed by peroxide vulcanization.

The range of end use applications of elastomeric materials is ex-
tended by their ability to be cross-linked. It is well known that
the chemical microstructure of rubber influences its physical
properties and the reaction mechanism of the curing process.
The use of dicumyl peroxide as a curative for natural rubber
and cis-polybutadiene produces a network that contains

only carbon-carbon cross-links (1). The thermal homolytic scis-
sion of the peroxide leads to the formation of cumyloxy radicals
that abstract allylic hydrogens from the elastomer. The polyiso-
prenyl or polybutadienyl radical, once formed, are expected to
undergo combination exclusively.

The resulting cross-linked network can be characterized by
studying the chemical and physical property changes that have
occurred in the elastomers. The physical properties of vulcan-
izates that are usually evaluated are: (a) modulus, (b) ultimate
tensile properties, (c) swelling ratio, (d) glass-transition
temperature (Tg), (e) dynamic mechanical properties and (f) creep
(2). An estimate of the effective degree of cross-linking of the
vulcanizate can be calculated from the measured physical proper-
ties and the appropriate empirical equations. Even though these
techniques have been developed to a high degree of sophistication,
they do not provide an absolute means of characterizing the net-
work structure of a vulcanizate.

Various spectroscopic methods such as UV, IR, X-ray, and
Raman, which are direct methods for chemical characterization,
have been employed with limited success (3-7).

The development of high resolution solid state carbon-13 NMR
has provided a means for studying solid intractable polymeric sys-
tems. (The term "solid state NMR" evolves from the rigidity of
the ·sample under investigation. That is, samples with reduced
molecular mobility, for which removal or averaging of various
nuclear spin interaction is impossible, in contrast to liquid
samples, which have substantial molecular mobility such that the
nuclear spin interactions can be averaged or removed by micro-
Brownian molecular motion.) Combining the techniques of dipolar
decoupling, DD, (8), cross-polarization, C-P, (9), and magic-
angle sample spinning, (MASS) (10), a high resolution carbon-13
solid state spectrum of the rigid cross-linked network is obtain-
able. Other pulse sequences such as gated high power decoupling
(GHPD) and the normal FT (NFT) NMR pulse sequences can be
employed to examine the high mobility regions (liquid-like) of the
cross-linked network. Therefore, one is able to spectroscopically
isolate and study the various structures present in the rubber
vulcanizate. We will present results of Fourier transform infra-
red spectroscopy and solid state carbon-13 NMR spectroscopy that
show a multiplicity of resultant structures indicating that the
mechanism of cross-linking is more complex than simple abstrac-
tion of allylic hydrogens followed by combination of the polymeric
free radical.

Carbon-13 NMR Pulse Sequence

Because the cross-linking of elastomers by peroxides is a
random process, regions will be formed that differ in chemical
environment and segmental mobility. Since the process of cross-
linking will increase the rigidity of the network junctions, the
use of a single pulse sequence may only probe one of the possible
amorphous morphologies. The cross-link junction points will take
longer to relax to equilibrium after being perturbed by an RF
pulse than the linear segments of the same molecular chains. The
difference in relaxation times will be exploited by use of dif-
ferent solid state pulse sequences in the analysis of cross-
linked networks.

Diagrams of the pulse sequences used in this study are shown
in Figures 1, and 2. In Figure 1, the normal FT (NFT) pulse
sequence is utilized to observe molecular environments that have
liquid-like segmental mobilities. Here a 90° carbon pulse is
applied, the free induction decay (FID) under conditions of low
power continuous proton decoupling is observed. In the gated
high power decoupling (GHPD) pulse sequence, a 90° carbon pulse
is applied and the FID is observed under the condition of high
power proton decoupling. In the GHPD pulse sequence the high
power proton RF pulse is required in systems where the carbons and
protons are strongly coupled dipolarly, but have sufficient mobil-
ity to give narrow liquid-like resonance lines without the cross-
polarization sensitivity enhancement step.

The cross-polarization pulse sequence in Figure 2 is employed
for systems that are rigid and a strong dipolar interaction exists
between carbon and protons. Because rigid systems possess longer
T_1^C relaxation times than mobile systems, the repetition between
carbon pulses ($\sim 5T_1^C$'s) would be adversely long, (for polyethylene,
$T_1^C \sim 1000$ seconds) (11). Because the carbons and protons are
strongly coupled and proton T_1^H 's are on the order of milliseconds
the proton reservoir can be engaged to provide the carbon-13 reso-
nance with a much shorter delay between pulses ($\sim 5T_1^H$'s). The
cross-polarization (CP) pulse sequence consists of applying a 90°
proton pulse, followed by phase shifting of the proton pulse by
90°. Upon phase shifting of the proton pulse a carbon 90° pulse
is applied simultaneously for a specific time in order to spin-
lock the proton and carbon spin system (Hartmann–Hahn condition)
(9). This process builds up the carbon magnetization. After the
duration of the spin-locking time the carbon FID is observed
under high power proton decoupling (DD). The cross-polarization
with protonated carbon suppression (CP-PCS) pulse sequence is
essentially the same as the CP pulse sequence except for the τ
delay, where the high power proton RF is turned off. The CP-PCS
pulse sequence allows one to differentiate between protons that

NORMAL FT PULSE SEQUENCE
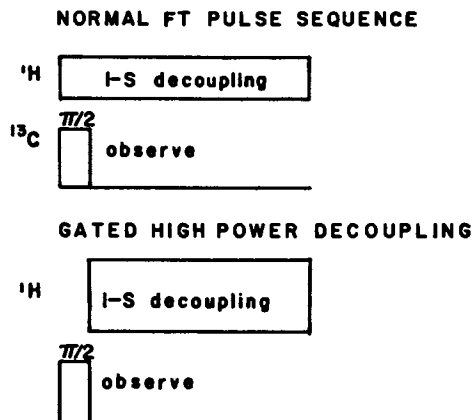
Figure 1. Multiple pulse sequences showing normal FT pulse and gated high power decoupling pulse to observe the very mobile components.

CROSS POLARIZATION PULSE SEQUENCE
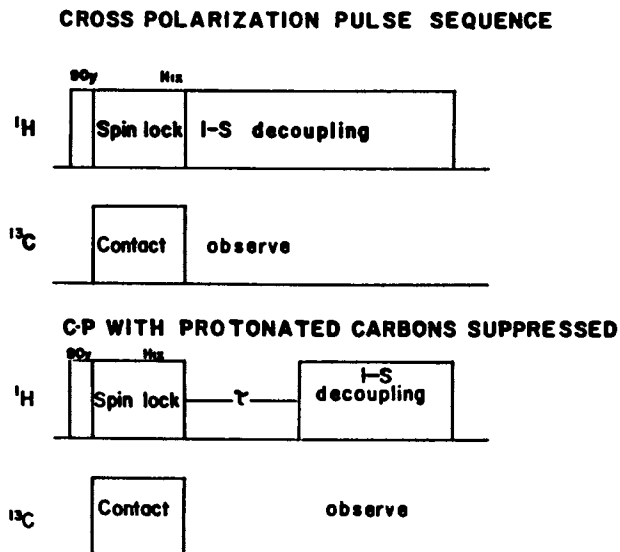
Figure 2. Multiple pulse sequences showing cross-polarization pulse and cross-polarization with protonated carbons suppressed. Used to observe the rigid components.

have attached protons and non-protonated carbons. The carbon di-
polar relaxation rate, T_{1DD}^{-1}, is the governing mechanism which
allows differentiation between carbon types and can be expressed
as

$$T_{1DD}^{-1} = N_H \gamma_H^2 \gamma_C^2 (h/2\pi) \tau_C r_{CH}^{-6} \qquad (1)$$

where N_H is the number of directly bonded protons, γ_C and γ_H are
the magnetogyric ratios of the carbons and protons, and r_{CH} the
internuclear vector between the carbons and the protons and τ_C is
the correlation time (measure of how rapidly the molecule under-
goes reorientation) (12,13). It can be seen that carbons with
directly bonded protons will relax faster than carbons without
protons and the r_{CH}^{-6} dependence will rule out enhancement of the
relaxation rate by intermolecular effects. By turning off the
proton decoupling RF (^{1}H), the carbons with directly bonded pro-
tons will relax faster and one is left with the resonances of the
non-protonated carbons. The drawback to this pulse sequence is
that in order to be efficient, the dipolar coupling must be quite
strong. Methyl groups undergo rapid rotation reducing the carbon-
proton dipolar coupling (14) and hence are not completely elimi-
nated in this CP-PCS pulse sequence. Because of the different
chemical shift range of the methyl groups, they are not hard to
identify in relation to the quaternary carbons.

Fourier Transform Infrared Analysis of the Curing Process

The use of solid state NMR for analysis of rubber vulcanizates
is relatively new, and therefore the NMR results have been
calibrated against another technique, Fourier transform infrared
spectroscopy (FTIR).

Infrared spectroscopy of peroxide cured rubbers has revealed
only minimal spectroscopic information on the new cross-linked
structure. What has been observed is the decrease in the inten-
sities of the C-H out-of-plane bending modes of the olefin
double bond which absorb at 837 cm^{-1} for the natural rubber and
at 740 cm^{-1} for cis-1,4-polybutadiene. While these bands reflect
losses in the amount of unsaturation in the final material, when
compared to the starting material, no evidence of the network
carbon-carbon single bond absorption bands has been reported.
This is mainly due to the fact that in the infrared the carbon-
carbon stretching mode has very weak infrared intensities. In
some cases, the C-C stretching modes are optically inactive.

In spite of the relative weakness of the cross-link bands,
the course of the peroxide curing process can be followed to
extract kinetic data. Examining Figure 3, where the infrared
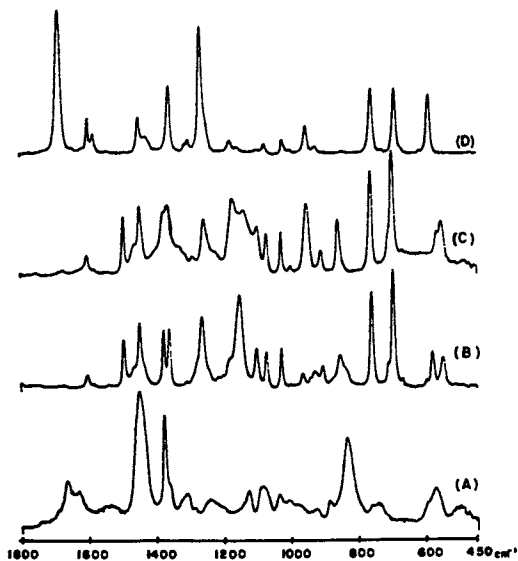spectra of (A) natural rubber, (B) dicumyl peroxide, (C) dicumyl

alcohol and (D) acetophenone in the 1800 cm^{-1} to 450 cm^{-1} region are presented, cause for skepticism arises because of the large number of overlapping absorption peaks that are present because of the degradation products (C and D) of dicumyl peroxide.

For reliable data, the concentration of the components of the mixture must be determined. Measuring peak intensities and then relating these values to the amount of each component present is practically impossible by standard analytical techniques for this system. In order to do quantitative analysis, first, frequencies must be found that are unique to each component and, second, intermolecular interactions must be at a minimum. Re-examining Figure 3, reveals that only the carbonyl stretching mode at 1685 cm^{-1} may be free of overlap. The difficulty presented by these systems (natural rubber-peroxide and polybutadiene-peroxide) provides a test of the sensitivity of the FTIR spectrometer.

Data processing techniques can be used in this complex analysis to improve the sensitivity. The least-squares curve-fitting criterion developed for polymeric systems by Koenig et al. (15) is such a technique. The method fits spectra of the pure components to the spectra of the mixture of these components and calculates the fractional amounts of each component. In essence, the method determines extinction values for the pure compounds over the region specified and fits this data to the spectra of the mixture, assuming the absorptions of each component is additive in the mixture. This has been demonstrated to work very well for polymeric systems even in situations where molecular interactions occur (16).

EXPERIMENTAL

A sample of high cis-polybutadiene (CB221) (cis content > 98%) was obtained from the B. F. Goodrich Research Center. Prior to use, a polybutadiene-benzene solution (thiophene free) was filtered through a glass fritted filter and reprecipitated with a 50/50 mixture of acetone-methanol. The samples were placed in a dark vacuum oven at 50°C for 2 hours to remove any entrapped benzene. The samples were placed under a nitrogen atmosphere in glass screw top vials and stored in a chemical refrigerator until used. A natural rubber sample was obtained from the Inland Division of General Motors Company and has the technical classification SMR-5. Portions of the natural rubber were placed in a Soxhlet extractor with a 50/50 mixture of reagent grade acetone and ethanol. The system was brought to reflux under a nitrogen atmosphere and maintained for 24 hours. The solvent was removed and the product stored in a desiccator, painted black to keep out light.

Three grams of rubber samples with varying amounts of dicumyl peroxide needed to make up samples containing 0.0, 0.5, 1.0, 2.0, 5.0, 7.0, 10.0, 15.0, 20.0, 25.0 and 30.0 phr of dicumyl peroxide were placed in one pint amber bottles and dissolved in benzene. Only the first five sample weights were used for the polybutadiene mixtures. The samples were periodically shaken to insure complete dissolution and mixing of the components. After a week, the bottles were uncapped, placed in a hood where the benzene was evaporated at room temperature (1 week). Efforts to minimize the amount of exposure to UV light were taken.

Once dried, the samples were cured at 150°C for 2 hours and 138 MPa of pressure in a template that gave a final thickness of 25 µm. After curing, the samples were extracted with acetone for 48 hours to remove any low molecular weight degradation products, dried and stored in the painted desiccator. Dicumyl peroxide was obtained from the Hercules Chemical Company and reprecipitated from an ethanol solution. The acetophenone and dicumyl alcohol were purchased from the Aldrich Chemical Company and used as received.

Instrument Analysis

The rubber samples were examined by FTIR for microstructural changes on curing, and solid state carbon-13 FT-NMR for identification of the cross-link types and microstructural changes of the polymeric chain.

Fourier Transform Infrared Spectroscopy Analysis (FTIR). A mixture of rubber and dicumyl peroxide were made up in the ratio 65/35 weight percent and dissolved in benzene to make a 2% solution. Films were cast from the solution and sandwiched between two KBr salt plates, whose edges were wound with Teflon (Dupont trademark) tape to minimize oxidation during heating. These samples were used for isothermal curing studies. The spectra of the curing films were obtained on a Digilab Model FTS-14 Fourier transform spectrometer. The resolution of the spectra was 2 wavenumbers (2 cm^{-1}). The spectra of dicumyl peroxide, acetophenone, and dicumyl alcohol were obtained as liquids pressed between two KBr salt plates.

Fourier Transform Carbon-13 Solid State NMR. The C-13 spectra were recorded on a Nicolet Technology NT-150 spectrometer operating at 37.7 MHz and equipped with a cross-polarization accessory. Radio-frequency amplifiers delivered ∿ 450 watts at 150 MHz and ∿ 800 watts at 37.7 MHz were adjusted to satisfy the Hartmann-Hahn condition at roughly 72 KHz (9). All spectra obtained by the CP-MASS and CP-PCS used spin-lock cross-polarization. The contact time was 1 msec and the delay between pulse sequence repetitions was 2 sec. unless otherwise noted. The spectrometer used quadrature detection.

The NMR coil is a 5-turn, double tuned, 11-mm free standing coil of 16-gauge copper buss wire, supported by a hollow poly-tetrafluoroethylene O-ring of 22-mm i.d.

The hot pressed cured rubber samples were cut into disks 4 mm in diameter and packed into hollow Beams-Andrews rotors (17, 18), which were machined from polyoxymethylene and spun at speeds between 3.3 and 3.8 KHz. The magic-angle was set to 54.7 ± 0.1 by maximizing the intensity of the carbonyl peak of glycine. The polyoxymethylene rotor served as the reference its resonance is 89.1 ppm down field from that of tetramethylsilane (TMS) in the CP-MASS experiment (19) and 90 ppm in the normal FT experiment. All FID's were zero-filled to a total of 8192 data points for convenience in interpolation in the Fourier transformed spectrum. In the CP-MASS experiment, 10,000 transients were accumulated while 15,000 were needed in the CP-PCS experiment, 2000 and 1000 were sufficient in the GHPD and NFT experiments, respectively. The spin temperature alternation was used to reduce systematic noise sources as discussed by Stejskal and Schaefer for solids (20) in the experiments employing cross-polarization.

RESULTS AND DISCUSSION

The carbon-13 NMR spectra of cross-linked natural rubber are shown in Figures 4, 5, and 6. The spectra were obtained with the normal FT (NFT) NMR pulse sequence and magic-angle sample spin-ning (MASS). In Figure 4, the aliphatic region is shown along with the amounts of initial dicumyl peroxide present in each sample. As the level of peroxide increases (increase in cross-link density), the intensity of the γ-methylene, δ-methylene and ϵ-methyl carbon resonances decrease. These resonances are prim-arily due to the cis structure. In addition to loss of intensity the peak widths at half-height increase as the cross-link density increases. These effects on the carbon resonances arise from the decrease in the segmental motional freedom of the carbon backbone and the consequent decrease in spin-spin relaxation times, which are inversely proportional to the line width at half height, $\Delta v(T_2 = 1/\pi\Delta v)$ (21). At higher cross-link density, Figure 6, line broadening due to dipolar interactions dominate the cross-link network. Spectral information is lost because the scalar decoupling employed is not sufficient to remove the dipolar interaction (spectra I and J) (22). The spectral evidence indi-cates that cis-trans isomerization occurs in the main chain back-bone. The two carbon resonances designated γ(T) 41.5 ppm and ϵ(T) 17.3 ppm in Figure 4 and the high field shoulder at 125.6 ppm in the olefin region of Figure 5, occur at equivalent posi-tions in the trans isomer, see Figure 7. Because of the three sets of allylic hydrogens next to the double bond, six possible

Figure 3. Comparison of the infrared spectra of (A) natural rubber, (B) dicumyl peroxide, (C) dicumyl alcohol and (D) aceto-phenone in the 1800 cm^{-1} to 450 cm^{-1} region.
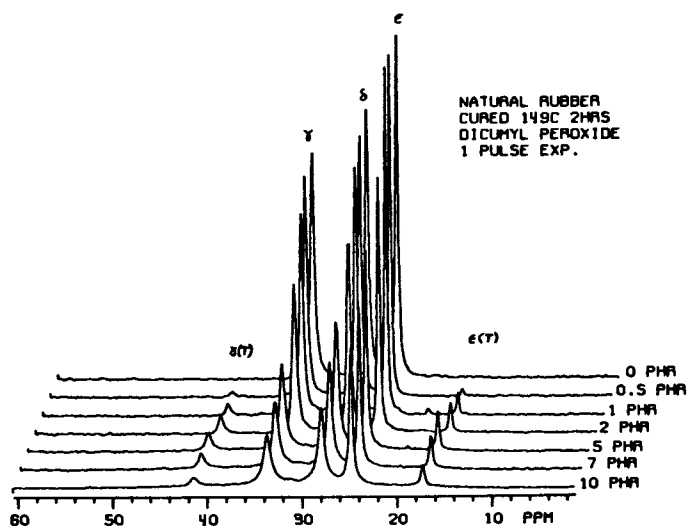
Figure 4. Aliphatic region of natural rubber cross-linked with dicumyl peroxide. Spectra were taken under normal FT conditions. The loading of peroxide is indicated at the high field side of the spectra.

NATURAL RUBBER
CURED 149C 2HRS
DICUMYL PEROXIDE
1 PULSE EXP.
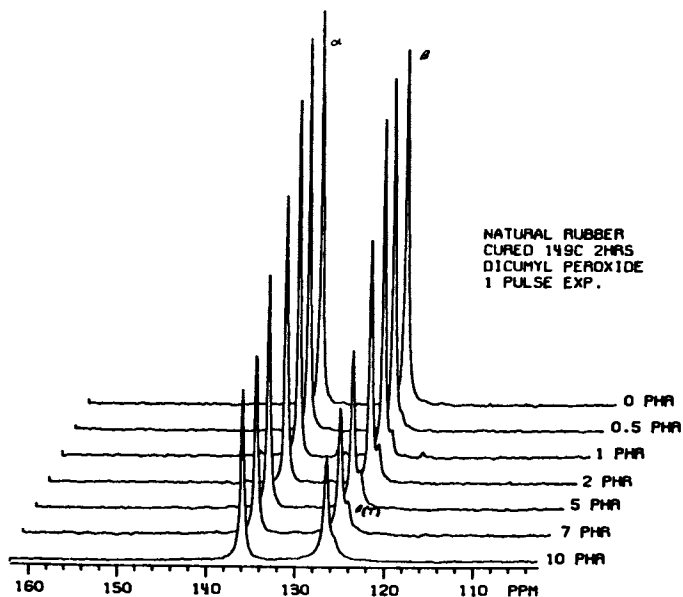
Figure 5.   Olefinic region of natural rubber cross-linked with
dicumyl peroxide. Spectra conditions, same as Figure 4.

NATURAL RUBBER
CURED 149C 2HRS
DICUMYL PEROXIDE
1 PULSE EXP.
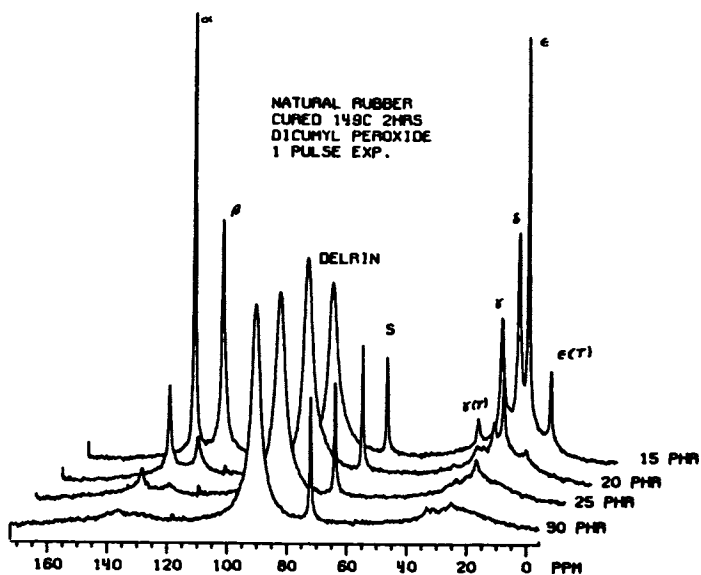
Figure 6. Superposed spectra of natural rubber cured with
dicumyl peroxide. Amount of peroxide indicated at the high field
side of the spectra.

isomeric free radical structures are possible (see Figure 8). Of the pathways shown in Figure 8, only A and B will lead to a new structure with the double bond being trans. Another possible path to the trans structure is through A with reforming of the double bond in its original position, i.e.,
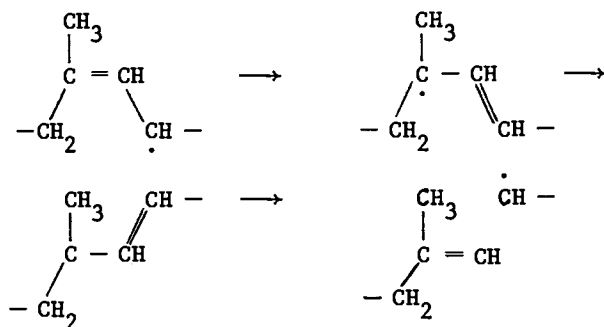
Although it is not possible to differentiate the mechanism responsible for the trans structure, earlier researchers (23) believed path B to be very minor. Table I lists the normally observed, solid state NMR, carbon resonances for natural rubber and polybutadiene

Table I

Solid State Carbon-13 Chemical Shifts of Elastomers

Polybutadiene

Saturated Carbon Region (ppm)	Olefinic Carbon Region (ppm)
26.5 $-VCC-CH_2$	129.8 $-CCC-HC=$
28.9 $-CCC-CH_2$	115.8 $-VVV-=CH$
34.1 $-CCV,TTT-CH_2$	143.6 $-VVV-=CH$
35.7 $-CVC-CH$	130.5 $-TTT-HC=$
45.0 $-CVC-CH$	

Polyisoprene

17.3 $-trans-CH_3$	148.0 $-vinyl -C=$
20.0 $-3,4$ vinyl$-CH_3$	135.9 $-cic,trans -C=$
24.7 $-cis -CH_2$	126.5 $-cis -CH=$
27.8 $-cis,trans -CH_2$	125.6 $-trans =CH-$
33.7 $-cis -CH_2$	112.9 $-vinyl =CH$
41.5 $-trans -CH_2$	
46.2 $-3,4$ vinyl$-CH$	
49.2 $-3,4$ vinyl $-CH$	

CCC, VCC etc. triad notation
T=trans, C=cis, V=vinyl
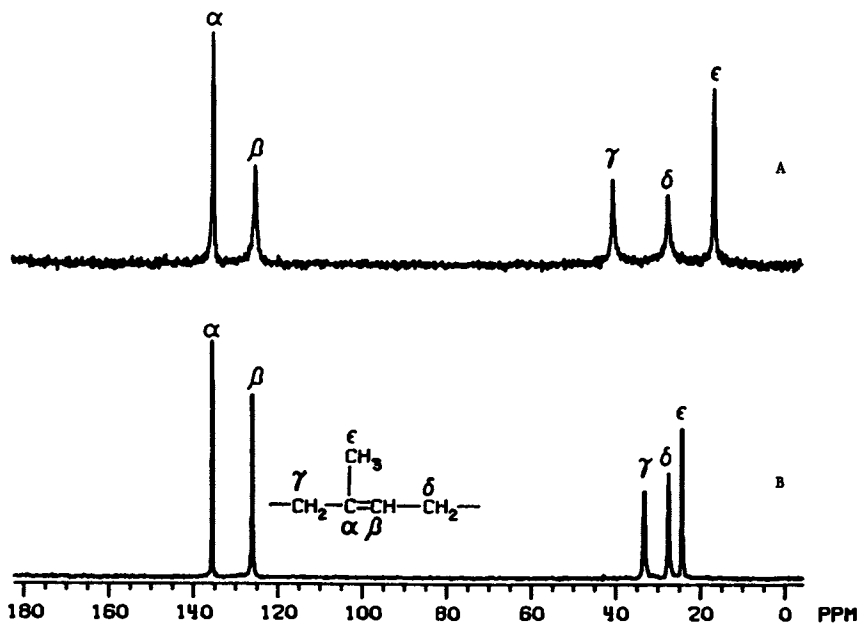
Figure 7. Comparison of cis and trans natural rubber in a NFT experiment. (A) trans natural rubber, and (B) cis natural rubber: 3.4 KHz spinning, 11 watts decoupling and at the magic-angle 54.7°.
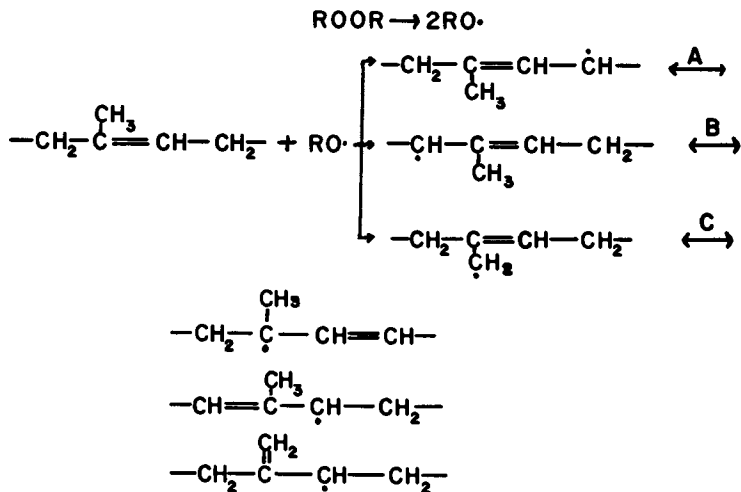
Figure 8. The six possible isomeric structures of the polyisoprenyl free radical.

Another possibility for the formation of the trans structure is
the oxidation of the specimens during the curing process. The
polyoxymethylene rotor used in this work resonate at 89.1 ppm
and interfere with the observation of peroxide groups ∿ 89 ppm.
But no -O-CH - resonances were observed in the 70-60 ppm region,
suggesting that oxidation is at a minimum, certainly less than
the amount of trans isomer formed.

In examining the NFT NMR spectra of cis-polybutadiene cross-
linked with dicumyl peroxide, Figure 9, the same trends of
decrease in intensities and line broadening are observable. In
spectra B and C, the up field shoulder in the olefinic region is
due to a benzene reference. The two peaks in the center of the
spectra are due to the rotor.

Employing the GHPD NMR experiment, regions of high mobility
are enhanced over regions with reduced molecular mobility. In
Figure 10, superposed spectra of cis-polybutadiene cured with
5 phr peroxide are shown. Spectra A and B differ in the delay
time between pulses. Spectrum A was taken with a 2 sec delay and
spectrum B with a 20 sec delay. With the addition of high power
decoupling, network resonance can be seen in the region between
55 to 33 ppm. In spectrum A, resonances centered at 44 ppm and
35 ppm can be observed by increasing the delay to 20 sec. In
spectra B, the rigid network is enhanced at the expense of atten-
uation of the methylene group at 29 ppm. The increase in the
signal of the network resonances with longer delay times indi-
cates that the T_{1c}'s of the cross-linked network are longer than
the T_{1c}'s of the uncross-linked chain.

Figure 11 shows superposed spectra of cis-polybutadiene
obtained by CP-MASS. With the increase in cross-link density,
the network resonance structures increase. The increase in the
resonances with cross-link density is due to the higher effic-
iency in the cross-polarization process. As the cross-link
density increases, the mobility of the chain backbone decreases.
With the increased rigidity, the internuclear vectors describing
the carbon-hydrogen distances become static. Because of this
static nature, the cross-polarization, which depends on the di-
polar coupling between protons and carbons, can occur with higher
efficiency than in a system where the internuclear vector is
continuously changing (24-26).

The examination of cross-linked natural rubber by the
CP/MASS experiment yields the spectra shown in Figures 12 and 13.
In addition to the resonances observed in the NFT experiment
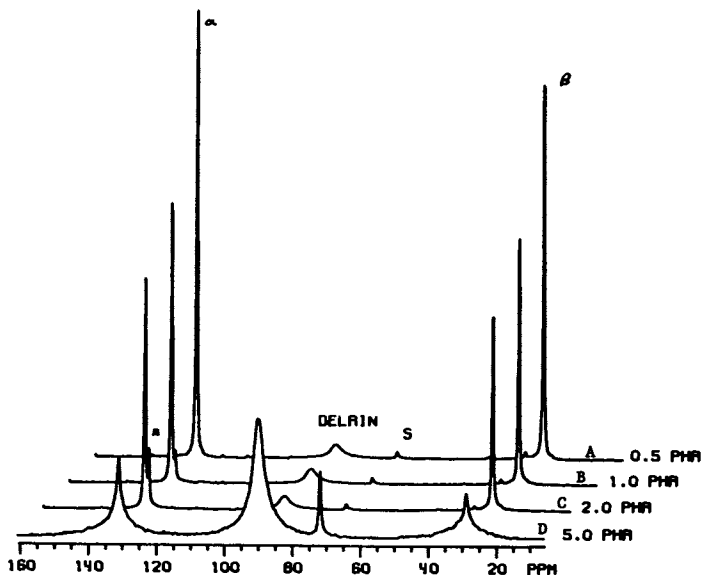
Figure 9. Superposed spectra of cured cis-polybutadiene with
varying amounts of dicumyl peroxide. All spectra were taken
under NFT conditions with magic angle sample spinning (MASS).
Samples were cured at 149 °C for 2 hrs in a hot press. Sample (A)
contained 0.5 phr ROOR, sample (B) 1.0 phr ROOR, sample (C)
2.0 phr and sample (D) 5.0 phr ROOR. The shoulders to the high
field side of spectra B and C are due to benzene.
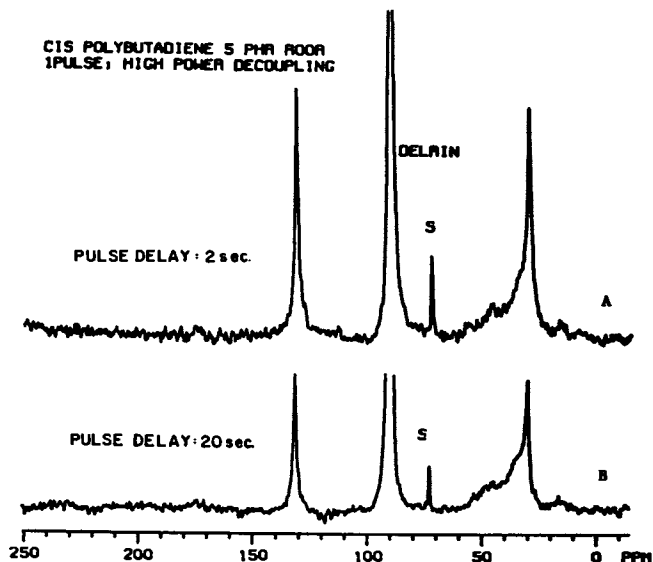
Figure 10. Spectral enhancement of rigid network. Spectra (A)
obtained from the gated high power decoupling pulse sequence
with a delay between repetitive pulses of 2 sec. Spectrum (B)
obtained with same pulse sequence except the delay between
pulsing increased to 20 sec.
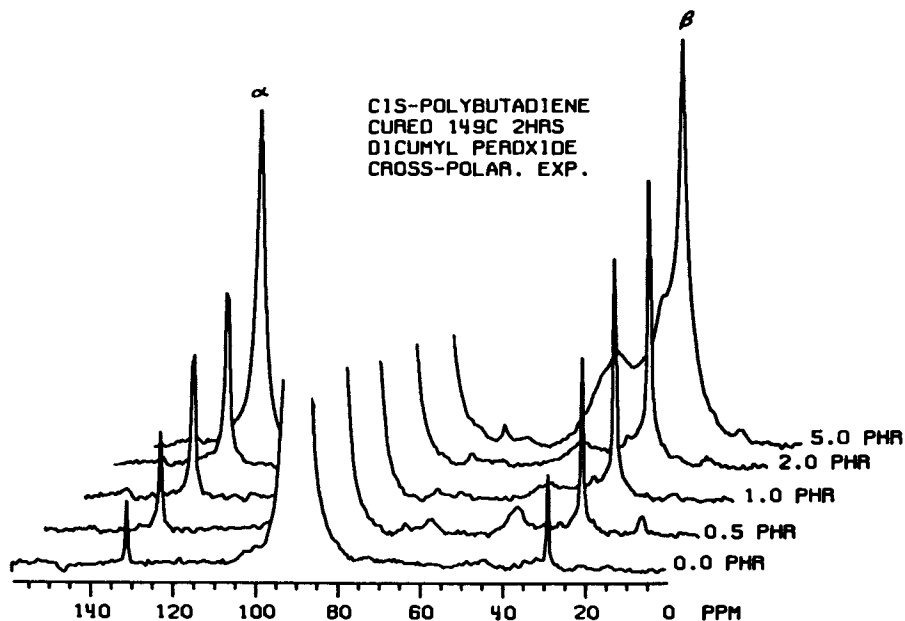
Figure 11. Cis-polybutadiene cured with various amount of dicumyl peroxide. Spectra obtained under CP-MASS experiment. The amount of peroxide needed to obtain spectra given at the high field side of spectra.
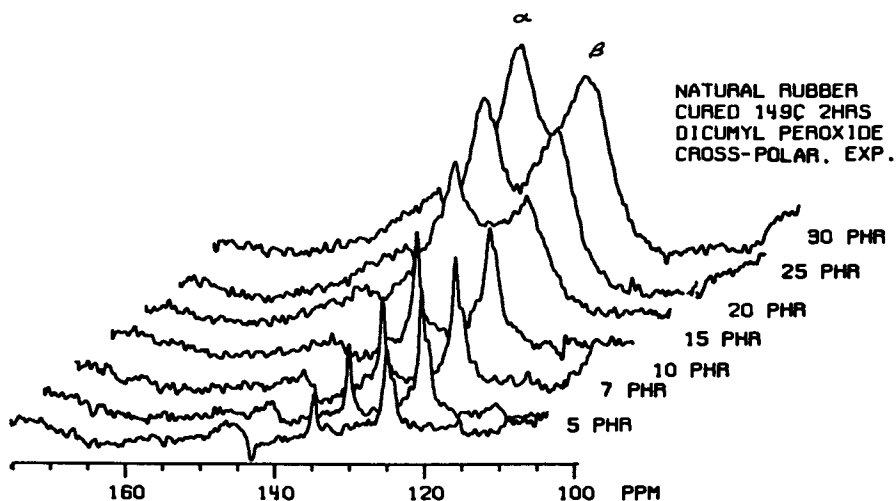
Figure 12. CP-MASS spectra of natural rubber cured with dicumyl peroxide. Olefinic region shown only. The amount of peroxide indicated on the high field side of spectra. The arrow indicates an artifact of the carrier. Greek letters represent identical carbons as in Figure 7.

that depict cis and trans structures, resonances at 45.0 ppm, 37.5 ppm, 30.6 ppm, 21.4 ppm and 14.9 ppm are observed in the CP-MASS experiment. In addition to the new resonances, the efficiency of the cross-polarization experiment is seen to increase at 20 phr peroxide. Some of the resonance broadening may be due to chemical shift dispersions which are not averaged out due to incomplete motional averaging of the C-13 resonances and bulk magnetic susceptibility differences due to cross-linking. The resonance at 45 ppm is due to quaternary aliphatic carbons. This has been substantiated by employing the CP-PCS experiment, see Figure 14 and 15. Figure 14 is a comparison of spectra obtained by the normal CP-MASS (A) experiment and CP-PCS (B) experiment. By employing the 100 μsec. delay between the contact pulse and acquisition, without proton decoupling, the carbon nuclei can interact with the local dipolar fields of their neighboring protons. With the decoupler off during the τ delay, nuclei dephase as they experience different dipolar fields due to the geometrical dependence of the dipolar interaction. Because of the r^{-3} dependence of the dipolar interaction, carbon nuclei, with attached protons retain less of their initial intensity than carbons without attached protons (12,27,28). Because methyl groups can undergo rapid rotation, the carbon-proton dipolar coupling is reduced and hence the resonance for methyl groups remains. Figure 15 shows spectra of natural rubber, with varying cross-link densities obtained by the CP-PCS pulse sequence. At 15 phr peroxide, the mobility of the chains is rapid enough to diminish the carbon-proton dipolar coupling, so as not to dephase in the 100 μsec. delay. As the cross-link density increases, the methylene resonances are lost and the quaternary resonances remain (see arrow). In addition, the olefinic quaternary carbon remains, with loss of the resonance of the methine olefin carbon. The spectra indicate that at peroxide levels greater than 20 phr ROOR the molecular motion of various carbons, when coupled to protons relax faster than 100 sec. At peroxide levels less than 20 phr ROOR, the motion is sufficiently long as not to relax in 100 μsec.

In trying to increase the resolution of the CP-MASS spectra of the highly cross-linked rubber networks, the samples were swollen in benzene to equilibrium. The gel was then packed into the rotor and spectra accumulated as if the sample was a dry solid. Figure 16 shows the spectra of natural rubber cross-linked with 25 phr peroxide, obtained from the CP-MASS experiment (A) and from the GHPD experiment (B). By swelling the rigid network, increased segmental motion is imparted to the sample and hence a narrowing of the resonance lines. Swelling also decreases the carbon-proton dipolar interaction. In spectra A and B, the resonance peaks due to cis and trans isomers are recognizable as in the samples with low cross-link densities. The subtraction of B from A leaves a broad resonance from 10 to 50 ppm. This
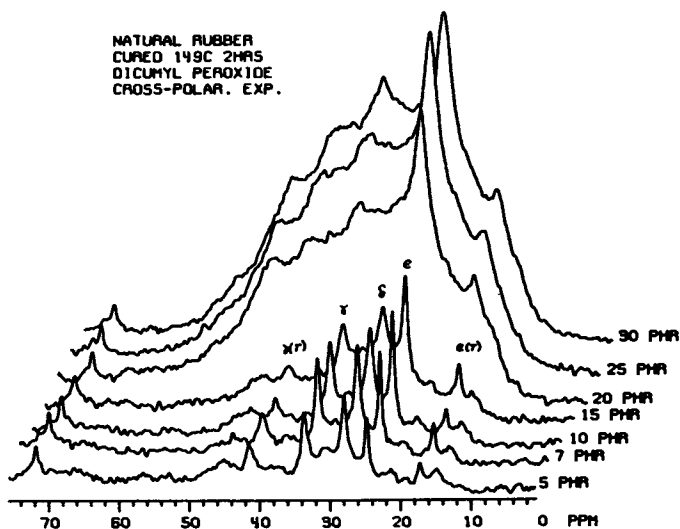
Figure 13. CP-MASS spectra of the aliphatic region of natural rubber cured with dicumyl peroxide. The amount of peroxide is indicated to the high field side of the spectra.
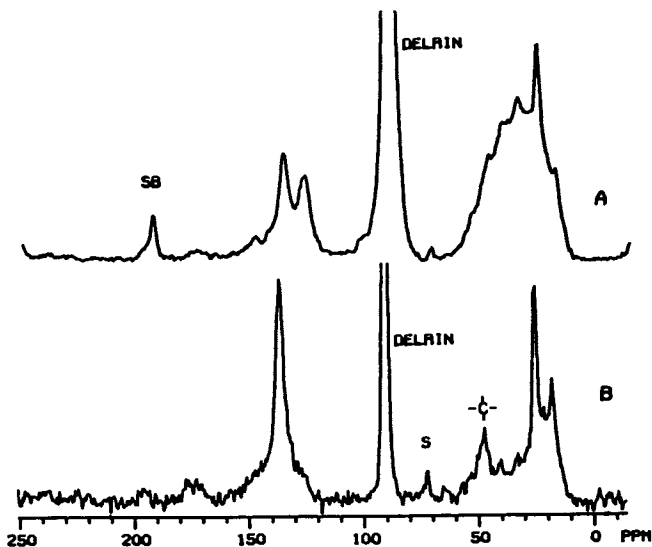
Figure 14. Natural rubber cured with 30 phr dicumyl peroxide. Spectrum (A) obtained under CP-MASS. Spectrum (B) obtained with the CP-MASS experiment with a delay between acquisition of 100 μsec, the quartenary carbons are distinguishable at 135 ppm and 45 ppm.

NATURAL RUBBER

PROTONATED CARBON SUPPERS.

DELAY 100 USEC
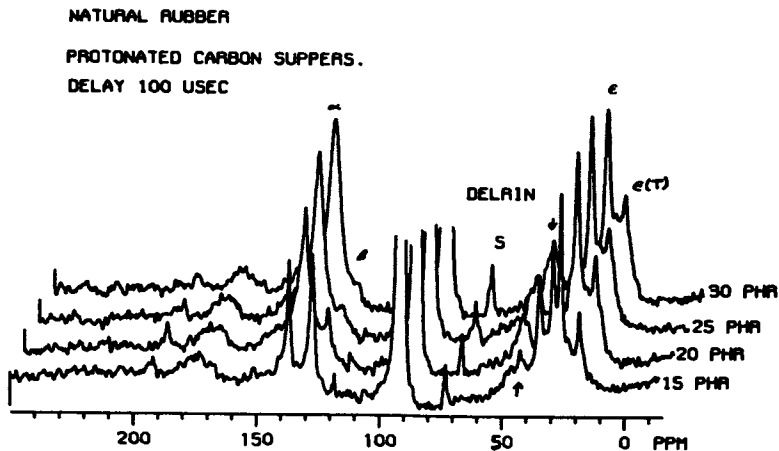
Figure 15. Superimposed spectra of cross-linked natural rubber obtained with the CP-PCS experiment.
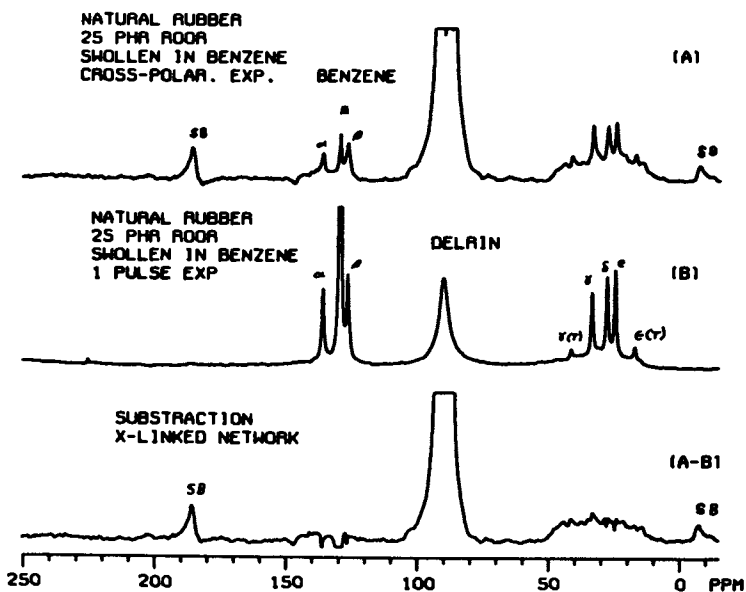
Figure 16. Spectra of natural rubber cross-linked with 25 phr ROOR. Spectrum (A) swollen in benzene to equilibrium swelling. Spectrum obtained under conditions of NFT experiment. Spectrum (B) same sample as (A), obtained under CP-MASS. The asterisk marks resonance of benzene solvent. Spectrum (C) the difference between (A-B).

difference spectrum is due to the chemical shift dispersion of
natural rubber produced by cross-linking and made up of multiple
chemical structures. Figures 17 and 18 are the spectra of poly-
butadiene obtained after swelling in benzene. Spectrum B, in
Figure 17 (CP-MASS exp.) depicts the decrease in the static
dipolar interaction by the decrease in the intensity of the
resonances. The chemical shift dispersion remains, indicating a
greater distribution of different types of cross-links in the
network structure. In Figure 18, the NFT experiment generates a
high resolution spectrum of cross-linked polybutadiene that is
similar to the uncross-linked elastomer. The small resonance at
34 ppm is probably due to trans and cis methylenes. No evidence
of trans structure is observed in the olefinic region; this is
probably due to the fact that the cis and trans resonances differ
by only 0.5 ppm and the resolution of these spectra are 1 ppm.
There is (to be discussed later) evidence of trans polybutadiene
structure as detected by FTIR.

    After observing the complex solid state C-13 NMR spectra of
cross-linked natural rubber and cis-polybutadiene, the additivity
relationships (29-31) were used in connection with model struc-
tures obtained from the possible chemical pathways to form the
network models. Figure 19 depicts the possible network formed in
dicumyl peroxide cured cis-polybutadiene. Figures 20 and 21 com-
pare the model cross-linked structures and the calculated spectra
using the additivity relationships. The calculated spectra are
to be used as a guide in interpreting the observed spectra. It
can be seen that the calculated resonances fall in the ranges
observed in the actual cross-linked spectra. Although impossible
to assign definitely an observed resonance to the structural
model used for the calculations, it is highly suggestive that the
model may give rise to the observed resonances. Certain struc-
tures can be ruled out as being improbable when no resonance
appears in the expected region. After studying the possible
structures, a network picture of cross-linked polybutadiene was
deduced and is depicted in Figure 19. The methine resonance is
expected to occur at 33 ppm. The main feature of this model net-
work is the loss of unsaturation due to attack of the polybut-
adienyl radical at the α -methylene group and the carbon-carbon
double bond.

    A model network for dicumyl peroxide cross-linked natural
rubber is proposed in Figure 22. The T represents trans double
bonds formed by the rearrangement of the allylic free radicals.
By examining Figure 8, twenty-one isomeric structures can be
generated by simple combination of the radical forms. Elimina-
tion of the vinylene radical in path C leads to 15 possible
structural networks. The pathway leading to the formation of
vinylene groups was dismissed because no evidence of its expected
resonances was observed. While there is NMR data showing the
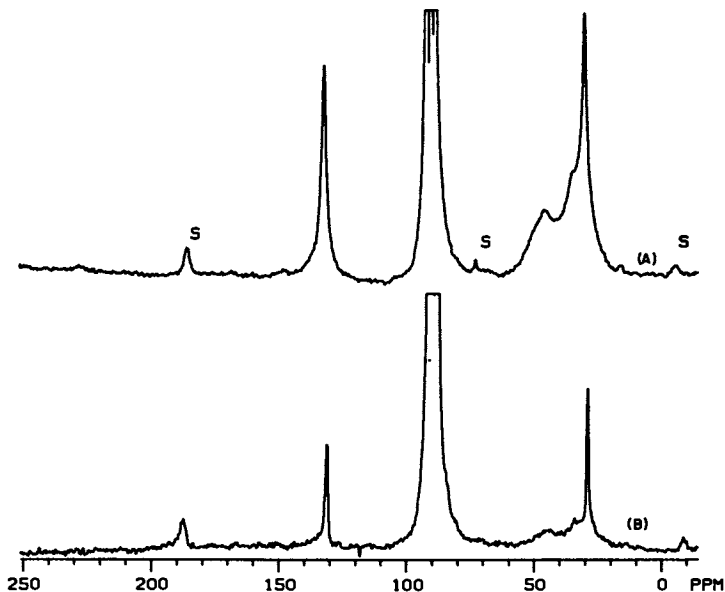
Figure 17. Cross-polarization magic angle sample spinning of
cis-polybutadiene with 5phr ROOR. Spectrum (A) cross-linked
polybutadiene obtained in dry state. Spectrum (B) same as (A)
except swollen in benzene to equilibrium swelling, S artifact
of rotor.
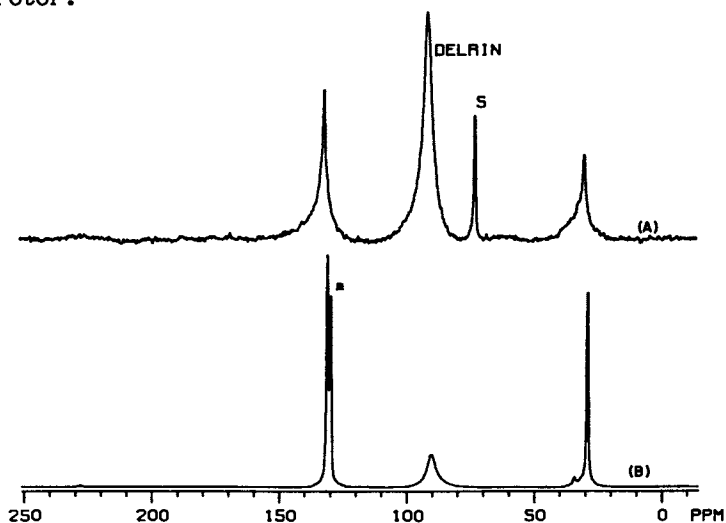
Figure 18. Normal FT spectrum of cis-polybutadiene cross-linked
with 5 phr ROOR. Spectrum (A) cross-linked polybutadiene in dry
state. Spectrum (B) same as A except swollen in benzene to
equilibrium swelling. S artifact of rotor, High field olefinic
peak due to benzene.
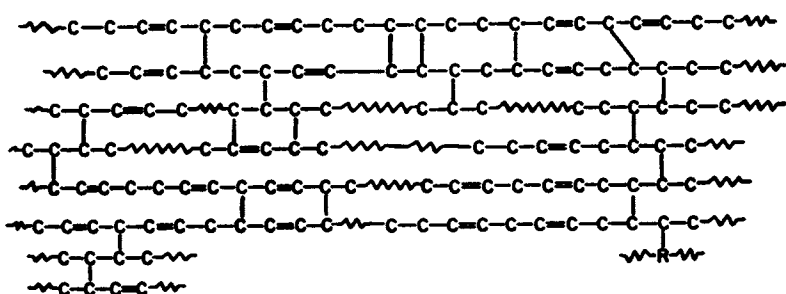
Figure 19. Proposed cross-linked structure of cis-polybutadiene vulcanized with dicumyl peroxide.
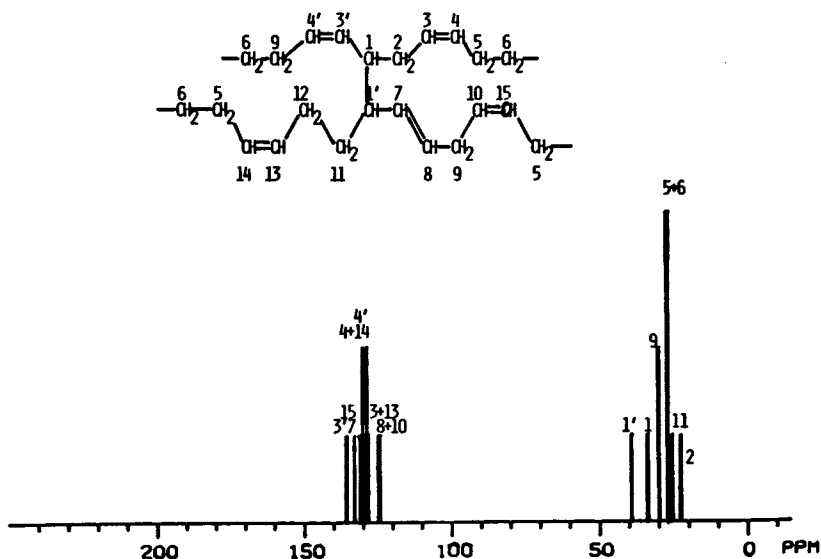
Figure 20. Schematic drawing of the combination of two poly-butadiene chains. The lower stick drawing is of the calculated spectrum, using the additivity relationship.
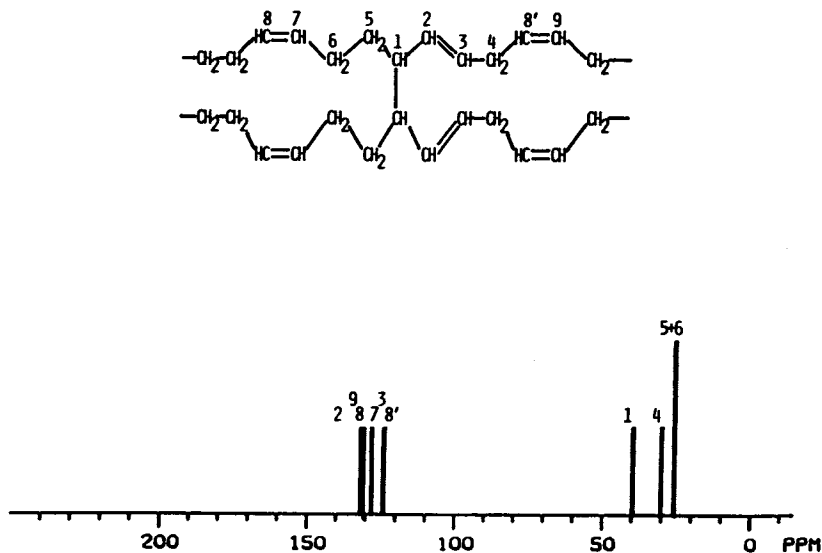
Figure 21. Schematic drawing of the combination of two cis poly-butadiene chains. The lower stick drawing is of the calculated spectrum, using the additivity relationships.
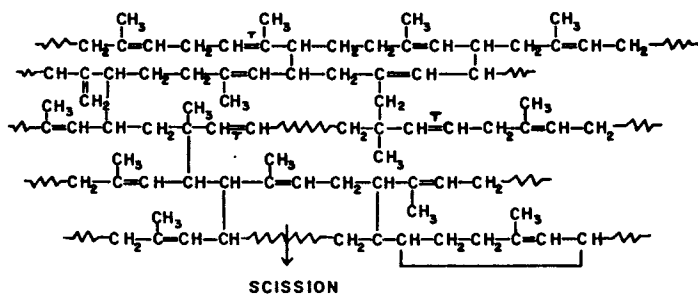
Figure 22. Proposed cross-linked structure of natural rubber vulcanized with dicumyl peroxide.

formation of trans-structures, the FTIR data is not indicative of the presence of such structures.

FTIR data is presented in Figure 23 for polybutadiene cured with peroxide. There are at least two features in the polybutadiene spectra that are worth noting: first, the olefinic out-of-plane bending mode occurring at 740 cm^{-1} decreases with time of cure and secondly, the appearance of the band at 965 cm^{-1}, which is probably due to the formation of trans double bonds. This is substantiated in Figure 24, that has been obtained by least squares analysis of a cured polybutadiene sample. The least squares analysis was performed between 2000 cm^{-1} to 780 cm^{-1}. Shown is the difference spectrum of the observed and calculated spectra. The band at 965 cm^{-1}, observed in the difference spectrum, is not in any of the spectra of the starting compounds or the degradation compounds of the curing process. In order to further characterize the infrared data, least squares analysis was performed on all the cured polybutadiene samples and natural rubber samples. Table II lists the weight percent of each component in the curing polybutadiene sample; also listed is the relative change in the amount of the cis double bond, which was calculated using the 780 cm^{-1} to 450 cm^{-1} region.

Table II

Relative Concentration in Curing Polybutadiene

Sample	Time of cure (min)	wt.% PB	wt.% peroxide	wt.% alcohol	wt.% ketone	std. error	%Δ C=C
PBF1	2.0	62.6	32.4	4.2	0.8	0.5	
PBF2	10.0	59.3	26.2	11.7	2.7	1.0	13.8
PBF3	17.3	57.4	20.0	17.0	5.6	2.0	26.0
PBF4	25.7	57.7	14.9	19.3	8.2	2.0	33.8
PBF5	33.6	57.6	11.3	20.9	10.1	2.1	35.0
PBF6	41.6	57.6	8.7	22.1	11.6	2.0	37.3
PBF7	49.6	57.6	6.9	22.9	12.6	3.0	38.8
PBF8	57.7	57.5	5.2	23.8	13.5	2.0	40.3
PBF9	65.5	57.6	3.9	24.3	14.2	2.2	41.4
PBF10	73.5	57.3	2.8	24.8	15.0	2.5	43.0
PBF11	81.5	57.1	1.9	25.2	15.4	2.5	43.5
PBF12	89.6	57.4	1.2	25.5	15.9	2.5	44.4
PBF13	98.0	57.5	0.6	25.8	16.1	2.5	44.9
PBF14	105.9	57.5	0.4	26.1	16.4	2.7	45.6
PBF15	114.0	56.8	---	26.0	16.3	2.7	46.5
PBF16	122.0	56.8	---	26.0	16.3	2.7	46.0

The values given are only relative values because one complicating mechanism in the polybutadiene mixture is an interaction

Band (cm^{-1})	Resulting from
1691	C=O stretching of acetophenone
1171	C=O stretching of dicumyl alcohol
965	out-of-plane bending mode of trans-olefinic group
740	same as 965, except cis-isomer
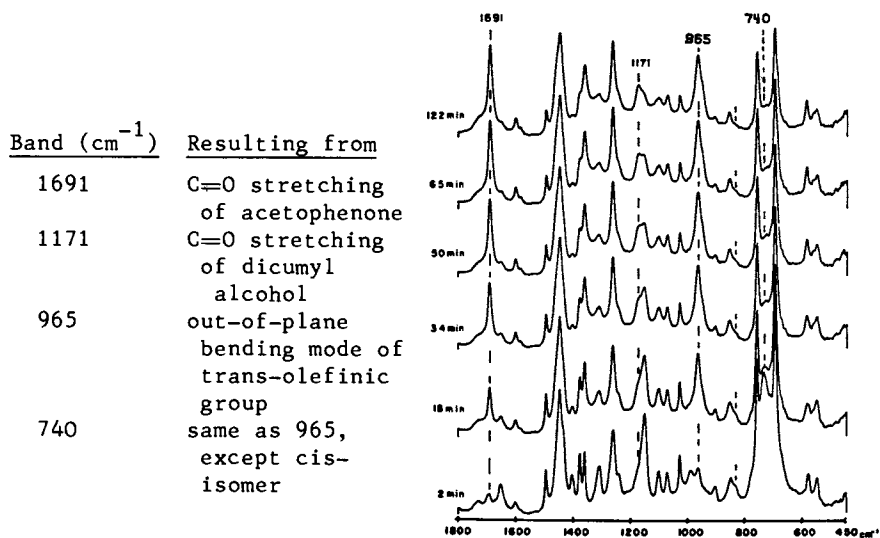
Figure 23. Superposed infrared spectra of curing cis-polybutadiene with 35 phr dicumyl peroxide vs. time.
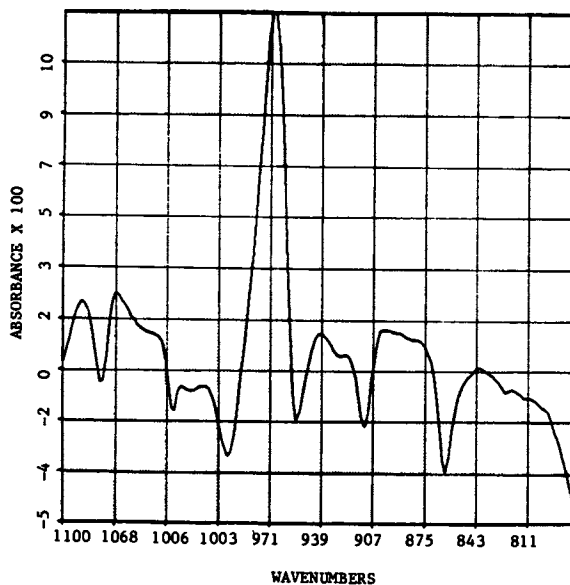
Figure 24. The difference spectrum of a cured polybutadiene sample, showing the 965 cm absorption band of the trans isomer. The difference spectrum was obtained by substraction of the components determined by least squares from the said mixture.

between polybutadiene and dicumyl peroxide (see Figure 25) where the known amount of dicumyl peroxide has been spectrally subtracted from the mixture. It is apparent that residual absorption of the 740 cm^{-1} band remains while the 1662 cm^{-1} band has been eliminated. Similar complex formation has been reported by Koenig and Pecsok for polybutadiene and aromatic antioxidants (16).

In Figure 26, the spectra of cured cis-polybutadiene are displayed with the subtraction of the degradation products of the curing process. Spectrum A is of the mixture, spectrum B is minus the unreacted rubber, spectrum C is minus the dicumyl peroxide, spectrum D is minus dicumyl alcohol and spectrum E is minus the last component, acetophenone. Spectrum E in Figure 26 is of the cross-linked network (positive bands), except for the out-of-plane bending modes of the aromatic ring. Except for the strong bands at 965 cm^{-1} in the polybutadiene spectrum, no other major bands are present that would be due to the carbon-carbon cross-links, but our current feelings are that this broad absorption is assignable to the cross-link structure.
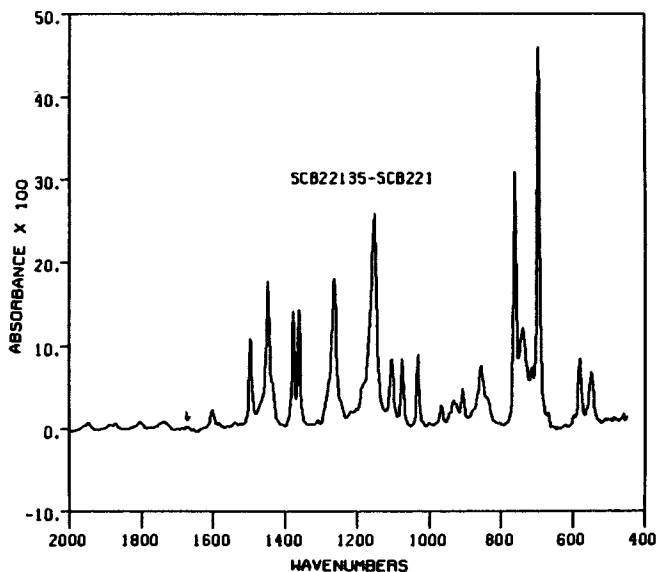
Figure 25. A spectrum showing the enhanced intensity of the 740 cm band of cis-polybutadiene. The percent of calculated polybutadiene and dicumyl peroxide. The 1662 cm^{-1} band has been removed but the 740 cm band remains.
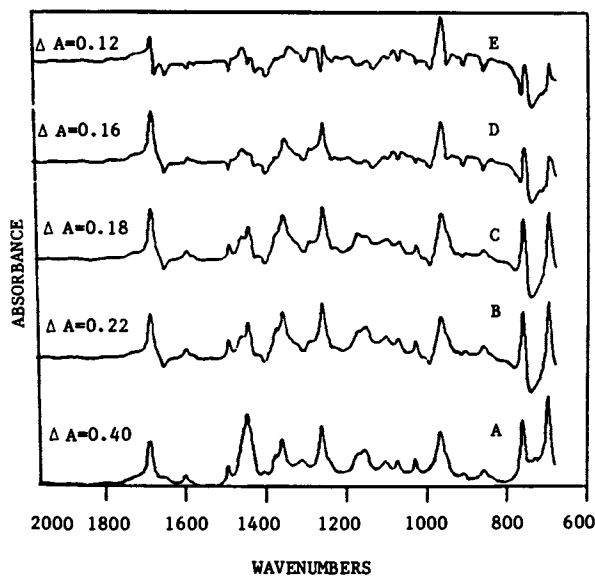
Figure 26. Superposed spectra of cured cis-polybutadiene minus its components. Spectrum A, polybutadiene and the products of the degrading dicumyl peroxide. Spectrum B, cured spectrum minus uncured polybutadiene; spectrum C, B minus dicumyl peroxide; spectrum D, C minus dicumyl alcohol; and spectrum E, D minus acetophenone. The amount of each component determined by least squares analysis.

LITERATURE CITED

1. M. M. Coleman, J. R. Shelton, and J. L. Koenig, Ind. Eng. Chem., Prod. Res. & Dev., 13, 155 (1974).
2. L. E. Nielson, J. Macro. Sci., Rev. in Macro. Chem. 4, 69 (1970).
3. D. W. Hake and C. E. Kendall, Rubber Chem. & Tech., 37, 709 (1964).
4. K. Fujimato and K. Wataya, Rubber Chem. & Tech., 43, 860 (1970).
5. R. D. Stiehler and J. H. Wakelin, Rubber Chem. & Tech., 21, 325 (1948).
6. J. L. Koenig, J. R. Shelton, M. M. Coleman and P. H. Starmer, Rubber Chem. & Tech., 44, 71 (1971).
7. F. J. Linning and J. E. Stewart, J. Res. Natl. Bur. Std., 60, 2816 (1958).
8. F. Block, Phys. Rev., 11, 841 (1958).
9. S. R. Hartmann and E. L. Hahn, Phys. Rev., 128, 2042 (1962).
10. J. R. Lyerla, "High Resolution Carbon-13 NMR Studies of Bulk Polymers", in Contemporary Topics in Polymer Science, M. Shen, Ed., 3, Plenum Press, 1979.
11. W. L. Earl and D. L. VanderHart, Macromol., 12, 762 (1979).
12. G. L. Nelson and G. C. Levy, "Carbon-13 Nuclear Magnetic Resonance", John Wiley & Sons, Inc., N.Y., 1980.
13. R. J. Abraham and P. Loftus, "Proton and Carbon-13 NMR Spectroscopy: An Integrated Approach", Heyden, Pennsylvania (1979).
14. S. J. Opella and M. H. Fry, J. Amer. Chem. Soc., 101 5854 (1979).
15. M. K. Antoon, J. H. Koenig and J. L. Koenig, Appl. Spect., 31, 518 (1977).
16. J. R. Shelton, R. L. Pecsok and J. L. Koenig, ACS Symp. Series, 95, R. K. Eby, Ed., 75 (1979).
17. E. R. Andrew, Prog. Nucl. Magn. Reson. Spect., 8, 1 (1971).
18. J. W. Beams, Rev. Sci. Instrum., 1, 667 (1930).
19. W. L. Earl and D. L. VanderHart, J. Magn. Reson., 44, 35 (1982).
20. E. O. Stejskal and J. Schaefer, J. Magn. Reson., 18, 560 (1975).
21. J. Schaefer, Macrol., 4, 110 (1971).
22. F. A. Bovey, Pure and Appl. Chem., 54, 559 (1982).
23. C. G. Moore and W. F. Watson, J. Polym. Sci., 19, 237 (1956).
24. M. Mehring, "NMR Basic Principles and Progress", E. Fluck and R. Kosfeld, Eds., 11, 153, Springer-Verlag Publ., 1979.

25. J. Schaefer and E. O. Stejskal, "High Resolution C-13 NMR
     of Solid Polymers", in Topics in Carbon-13 NMR Spectroscopy,
     G. Levy, Ed., 3, 283, John Wiley & Sons Publ., 1979.
26. D. L. VanderHart, J. Chem. Phys., 64, 830 (1976).
27. P. D. Murphy, B. C. Gerstein, V. L. Weinberg and T. F. Yen,
     Analy. Chem., 522 (1982).
28. M. J. Sullivan and G. E. Maciel, Analy. Chem., 54, 1606
     (1982).
29. D. Grant and E. Paul, J. Amer. Chem. Soc., 86, 2984 (1964).
30. J. B. Strothers, "Carbon-13 NMR Spectroscopy", Academic
     Press, N.Y. (1972).
31. L. Lindemann and J. Adams, Analy. Chem., 43, 1245 (1971).

Carbon-13 Magic Angle NMR Spectroscopic Studies of an Epoxy Resin Network

A. CHOLLI, W. M. RITCHEY, and JACK L. KOENIG

Department of Macromolecular Science, Case Western Reserve University, Cleveland, OH 44106

Cross-polarization (CP) and high power proton decoupling with magic-angle spinning (MAS) were used to obtain high resolution C-13 NMR spectra (3.5 T) for cured epoxy polymers. The diglycidyl ether of bis-phenol A (DGEBA) was cured with dimethylbenzylamine (BDMA) and spectra were obtained at various cure times. During the reaction the decrease of resonance or intensity due to the epoxy ring and increase in the oxymethylene carbons was noticed. C-13 NMR data were used to analyze the network structure. The plot of increase in the oxymethylene carbons versus the decrease in the epoxide ring follows a non-ideal curve and the transition at the extent of reaction 0.57 may suggest the gelation point. If this point is the gelation point, the effective functionality of the system is 2.6.

The chemical analysis of the structure of crosslinked polymer networks is complex in nature and various approaches have been given in an effort to understand these systems (1-8). The usual chemical or physical methods are limited because of the insolubility and infusibility of the system. However, recently CP/MASS (cross-polarization magic-angle sample spinning) has made it possible to obtain a high resolution NMR spectrum of these insoluble solid polymers (9,10).

We report here the application of the solid state carbon-13 NMR with cross-polarization (CP), high power proton decoupling, and magic-angle sample spinning (MAS) to study the curing of epoxy resins. On the basis of our preliminary studies, we show here the application of solid state carbon-13 NMR spectroscopic data to determine some of the important parameters such as the gelation point and effective functionality of the epoxy monomers.

EXPERIMENTAL

The diglycidyl ether of bisphenol A (DGEBA) was obtained from the Shell Company (EPON 828) and was cured with 2% dimethyl-benzylamine (BDMA, Eastman Kodak Company). Samples were thoroughly mixed prior to curing and were cured at 125°C and 160°C for various lengths of time.

The carbon-13 NMR spectra were obtained at 37.7 MHz with a Nicolet Technology NT-150 spectrometer equipped with a cross-polarization accessory. Radio frequency amplifiers delivering ca. 550 W at 150 MHz and ca. 1000 W at 37.7 MHz were adjusted to satisfy the Hartman-Hahn condition at roughly 80 KHz. The cross-polarization (CP/MASS) spectra were recorded with a single contact per polarization period at a 1.0 ms contact time and the delay between the pulse sequence repetition was 2.0 s. Magic-angle of 54.7 degrees was set by maximizing the intensity of the carbonyl peak of glycine. Typical speeds of the rotor were 3.8 KHz. The samples were machined to (7) a rod shape which fits in the sample chamber of the Delrin rotor of the Andrew type. 6000 transients were collected to obtain good S/N spectra. The resonance of the Delrin (89 ppm downfield from the tetramethyl silane) was used as a reference. Spin temperature alteration was used to eliminate various artifacts (11). The static field was not locked during accumulations.

RESULTS AND DISCUSSION

Some of the solid state carbon-13 NMR spectra of cured epoxy polymers are shown in Figure 1. The resonance peaks are assigned with the aid of the carbon resonance assignments of the monomers (12), prepolymers and polymers. The resonance peak at 33.6 ppm (from TMS) is assigned to the methyl carbons. The quaternary carbons are assigned to the resonance peak at 43.4 ppm. This resonance peak is asymmetrical in Figure 1a indicating the presence of more than one component. The methylene carbon resonance of the epoxide ring occurs at 44.3 ppm. This resonance peak makes the peak at 43.4 ppm (quaternary carbons) assymetrical on the lower field side (Figure 1a). The methine carbon resonance of the epoxide ring appears at 50.2 ppm. The methylene carbon resonance of the epoxide ring appears at 44.3 ppm. The resonance peak of the methylene carbon attached to the oxygen appears at 71.3 ppm. The downfield resonances are assigned to the aromatic carbons. The resonance peaks at 115.9, and 129.0 ppm are assigned to the protonated carbons, whereas the peaks at 145.9, and 159.4 ppm are due to nonprotonated carbons.

The spectral changes upon curing can be seen in Figure 1. The decrease in the intensity of the resonance peak of the epoxide ring carbons is noticed as the curing takes place. The
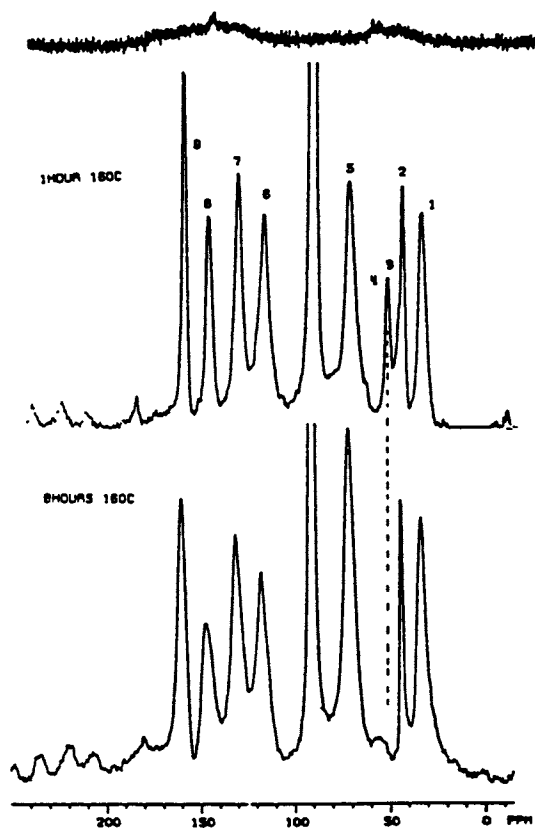
Figure 1. Solid state C-13 NMR spectra (obtained at 37.7 MHz)
of the cured epoxy resins with BDMA, after 1 hour curing, after
8 hours of curing. At top is the spectrum of the 1-hour cured
sample under solution spectrometer conditions.

decrease in the intensities of the methine carbons (resonance
peak at 44.3 ppm) can be seen in Figure 1b. There is an increase
in the intensity of the methylene carbons attached to the oxygen
atom. These intensity changes in the solid state spectra of
cured epoxy resins are plotted in Figure 2. These data are plot-
ted for two different curing temperatures; 125 and 160°.

    In Figure 3, we have plotted the increase in the oxymeth-
ylene carbon intensities versus the decrease in the epoxide carbon
intensities. Under ideal conditions, the conversion of one epox-
ide group should yield an additional one oxymethylene unit. This
ideal situation of conversion leads to a straight line with a
slope of one as a function of conversion. But the experimental
data do not follow the ideal straight line but instead yield the
curve as shown in Figure 3. The deviation from ideality decreases
as the extent of reaction proceeds and follows ideal behavior
after the extent of reaction reaches 0.57.

    The behavior of the experimental curve in Figure 3 can be
analyzed in two possible ways: a) on the basis of chemical
reactions during curing and b) the physical state of the system
as a function of curing.

    One interpretation of the curve in Figure 3 is that during
the early stages of curing, the epoxide units react to form
products in addition to the new oxymethylene units. The reaction
of epoxy with water, alcohol or HX may consume epoxy groups with-
out the formation of oxymethylene units (13). Another source of
these side reactions may be the presence of impurities. The main
crosslinking reaction may compete with the reaction of the impur-
ities until they are consumed. However, the NMR spectra do not
reflect the resonance of these new products. Although it is
certain the by-products exist, they must be less than 2-3% and
therefore would not account for the very substantial deviation
from ideal behavior.

    Another possible explanation of the deviation from ideal
behavior is a change in the physical state of the system induced
during curing. The number of crosslinks increases as the curing
process proceeds. These crosslinks make the system more rigid.
As a result the molecular motion is also restricted. The changes
of molecular motion at different stages of curing may have an
affect on the efficiency of the cross-polarization between the
protons and carbons. The reduction of molecular motion may
effect the transfer of polarization between protons and carbons.
These effects would be manifested in the cross-relaxation time
constants (9,14). Thus, at the early stages of curing, the effi-
ciency of the cross-polarization of the oxymethylene carbons may
be lower as compared to the final stage of curing. Our prelimi-
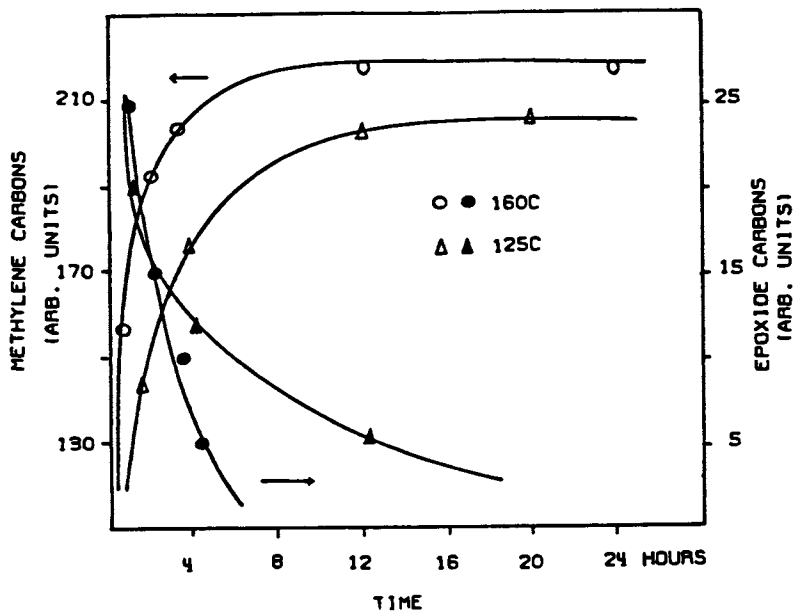
Figure 2. Plot of peak intensities of methylene, epoxide carbon intensities against time.
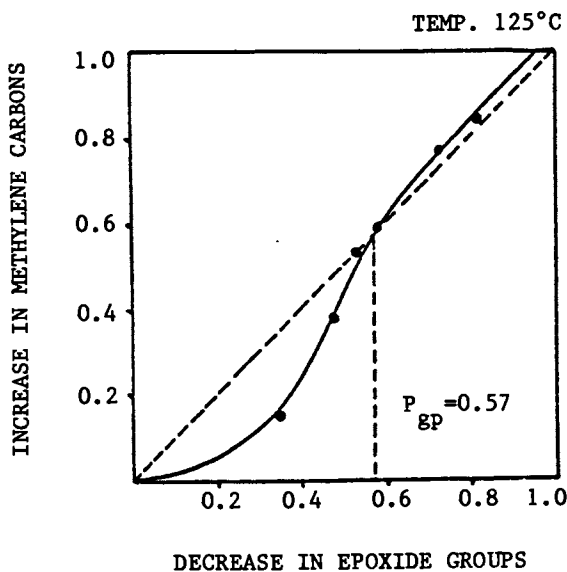
Figure 3. Plot of increase in methylene resonance against the decrease in the epoxide group.

nary studies indicate both views seem to be appropriate under reasonable assumptions.

Another interesting feature of the experimental curve in Figure 3 is that there is a smooth transition at the extent of reaction 0.57. After this transition, data follows the ideal straight line. The transition point at this extent of reaction may indicate the gelation point. Dusek and coworkers (8) have treated the curing of epoxy resins with amine curing agents statistically with the aid of theory of cascade processes, with reasonable assumptions. This statistical theory provides the changes in the structural parameters with conversion. The indication of gelation point (at extent of reaction 0.57) from NMR data (Figure 3), allows the determination of the functionality of the epoxide which is determined to be 2.6.

In summary, we have shown here the usefulness of solid state carbon-13 NMR spectroscopy to characterize an epoxy resin network. Curing of epoxy resins can be followed using carbon-13 NMR spectroscopy. This technique is useful for characterization of insoluble polymers. Our data anlaysis enable us to find the important parameters required in the network analysis such as the gelation point.

Literature Cited

1. H. Lee and K. Neville, Handbook of Epoxy Resins, McGraw-Hill Book Co., N.Y., 1967, ch. 6.
2. D. W. Brazier and N. V. Schwartz, Thermomechanics Acta, 39, 7 (1980).
3. L. Bateman, The Chemistry and Physics of Rubber Like Substances, Maclaren, London, 1963, ch. 15.
4. L. D. Loan, in Chemical Transformation of Polymers, R. Rado, Ed., Butterworth Sci. Publ., 1971.
5. E. F. Cluff, E. K. Gladding and R. Parisser, J. Polym. Sci., 45, 344 (1960).
6. K. E. Polmanteer and J. D. Helmer, Rubber Chem. & Tech., 38, 123 (1965).
7. K. Dusek, J. Polym. Sci., 37C, 83 (1973).
8. K. Dusek, B. Sedlacacek, C. G. Overberger, H. F. Mark and T. G. Fox, Eds., Crosslinking and Networks, John Wiley & Sons, Inc., N. Y., 1975.

9. A. N. Garroway, W. B. Moniz, H. A. Resing, in C-13 NMR in Polymer Science, Ed., R. Pasika, ACS Symp. Series, 103, 67-87 (1979).

10. A. N. Garroway, W. M. Ritchey and W. B. Moniz, Macromol. 15, 1051 (1982).

11. E. O. Stejskal and J. Schaefer, J. Magn. Reson., 18, 560 (1975).

12. C. F. Poranski, Jr., W. B. Moniz, D. L. Birkle, J. T. Kopfle, and S. A. Sojka, NRL Report 8092, Naval Res. Lab., Washington DC (1977).

13. J. R. Shelton, Private communications.

14. J. R. Lyerla, in Methods of Experimental Physics, 16A, Academic Press, N.Y., 1980, pp. 241-369.

NMR Kinetic Analysis of Polyethylene–Peroxide Cross-linking Reactions

V. D. MCGINNISS and J. R. NIXON

Battelle, Columbus Laboratories, Columbus, OH 43201

In this study it was observed that peroxide induced
crosslinking reactions caused major changes in NMR
line shapes of polyethylene materials. It is possi-
ble that this observed variation in NMR line shape
is a measure of kinetic polymer structural changes
although morphological changes are also possible
under the experimental conditions used in this study.
Competition reactions among peroxide, polyethylene
and antioxidant were also observed by NMR analysis.

Three-dimensional networks of polyethylene are manufactured
through peroxide-initiated covalent bonding between preformed
linear molecules. These peroxide-thermal-decomposition reactions
lead to free radical intermediates which abstract hydrogen atoms
from the polyethylene backbone to produce long chain polymer
radicals. Combinations of these chain polymer radicals lead to
a crosslinked network. (1) (Figure 1)
     The area of commercial interest in this study is the manu-
facture and use of crosslinked polyethylene as a dielectric
material in high voltage wire and cable applications. A typical
cable configuration is shown in Figure 2. (2)
     One of the concerns in commercial wire and cable application
of crosslinked polyethylene technologies is the type and amounts
of peroxide decomposition products (Figures 3 and 4) and their
relationship to the polymer's dielectric strength performance
capabilities. Peroxide decomposition products such as acetophen-
one have been shown to increase the breakdown voltage limits of
chemically crosslinked polyethylene materials (Figure 5). (3)
     Another concern is the competitive interaction among poly-
ethylene, peroxide, air and a required oxidative stabilizer
additive necessary for the extrusion manufacture of crosslinked
polyethylene cables. (4)

〜〜〜〜〜**POLYETHYLENE**〜〜〜〜〜〜

ROOR or ROOH

| ΔT

[Free Radicals (R·)]

R·

〜〜〜 CH 〜〜〜 ⟶ 〜〜 CH 〜〜
+
RH

(Peroxide Decomposition Products)

**Crosslinked
Polyethylene**
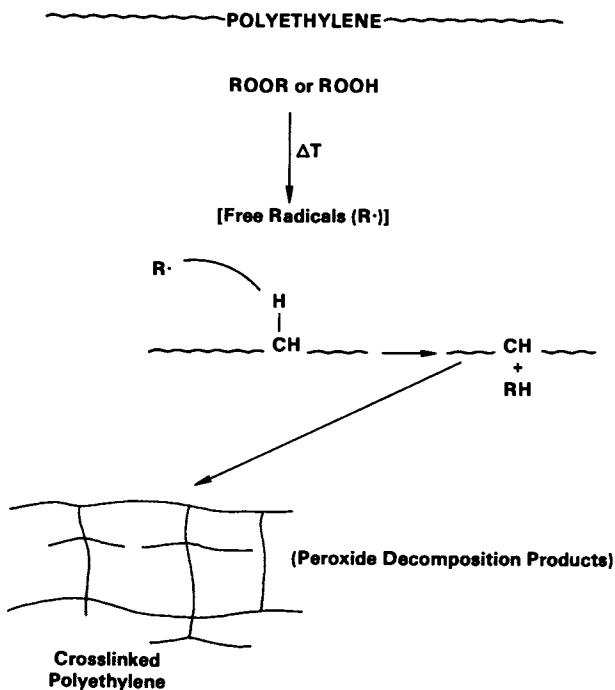
Figure 1.   Chemical Crosslinking of Polyethylene.

**Return
(Copper Braid)**

**Outer Screen
(Graphite ~ 6 mil)**

**Conductor
(Copper) AWG = 9
(100 mil)**

**Dielectric
(1009 mil)**

**Inner Shield
(12 mil)**

**Conductor
Coating
(17 mil)**
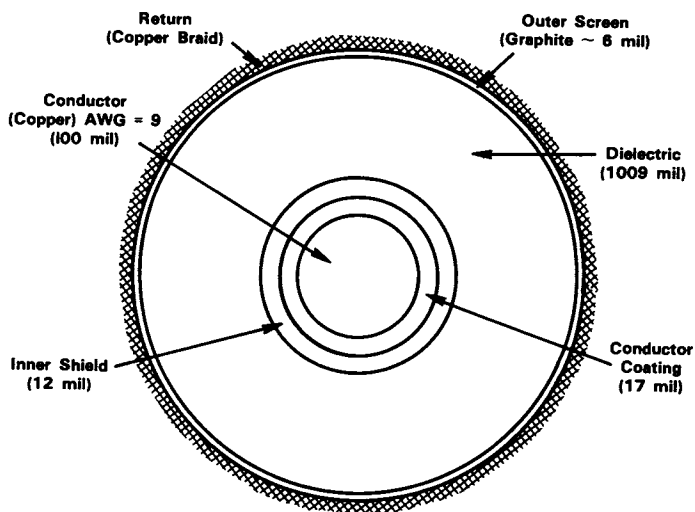
Figure 2.   Cross Section of Model Cable Configuration.
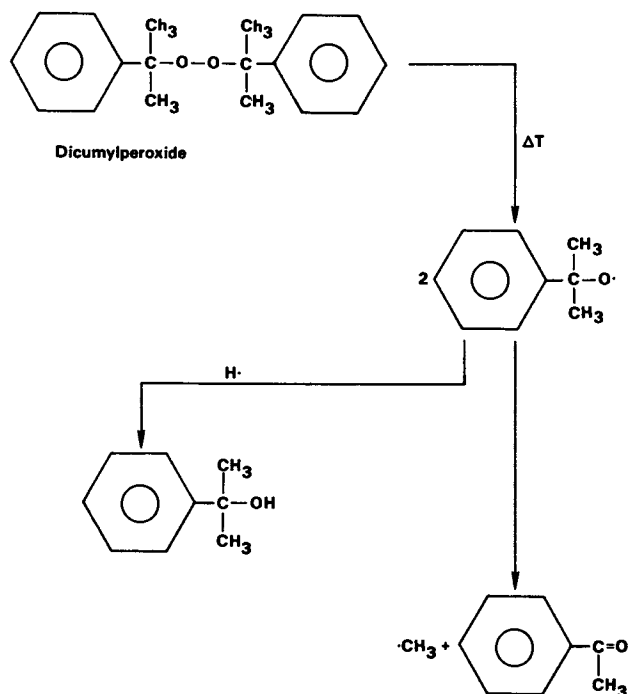
Figure 3.   Thermal Decomposition of Dicumylperoxide.
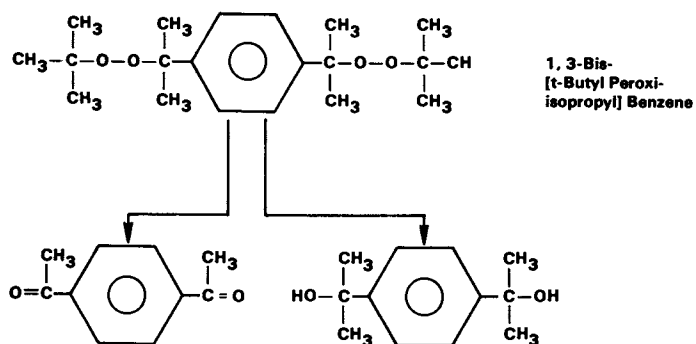
Figure 4.   Thermal Decomposition of 1,3-Bis[t-Butyl Peroxiisopropyl]Benzene.

Polyethylene (PE) + peroxides (ROOR) $\xrightarrow{\text{Heat}}$
polyethylene radical intermediates [PE·] +   (1)
peroxide radical intermediates [R·]

[R·] $\xrightarrow{\hspace{1cm}}$ products   (2)

n [PE·] $\xrightarrow{\text{combination}}$ crosslinked polyethylene   (3)

$\left.\begin{array}{l} \text{[R·]} + O_2 \\ \text{[PE·]} + O_2 \end{array}\right\}$ $\xrightarrow{\text{termination}}$ $\begin{array}{l} ROO· \\ PEOO· \end{array}$ (4)

[R·] + antioxidant additive (AA)
stabilizer radicals[AA·] + products   (5)

[PE·] + AA $\xrightarrow{\hspace{1cm}}$ products + PE + [AA·]   (6)

[AA·] + PE $\xrightarrow{\hspace{1cm}}$ [PE·] + AA   (7)

[AA·] + [PE·] $\xrightarrow{\hspace{1cm}}$ products   (8)
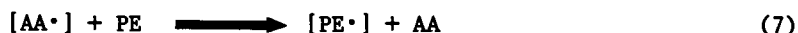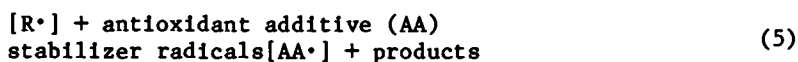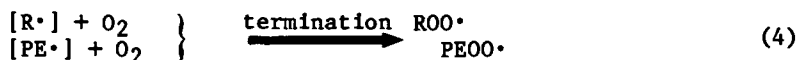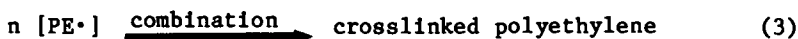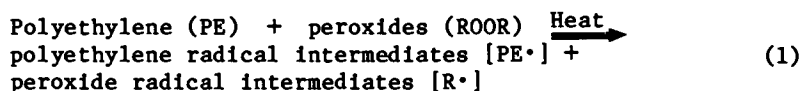
It was of interest in this study to develop a simple
analytical technique which would allow one to easily examine
the complex effects of peroxide-polyethylene interactions in
the presence of a phenolic antioxidant stabilizer additive.
The analytical method used to monitor reaction progress was NMR
spectroscopy. This technique can be used to rapidly measure
changes in polyethylene peak height absorptions during a com-
plex chemical reaction process. (5)

Numerous variables affect the line width observed in
nuclear magnetic resonance (NMR) experiments. (6,7,8) Among
the more important is the inherent viscosity of the sample
under observation. (9) The effect of viscosity on the line
width of a particular absorption largely results from both its
influence on the efficiency of magnetic field averaging
achieved by spinning of the sample, and its effect on the spin
lattice relaxation time of the nuclei under observation. Since
it is well established that the crosslinking of linear poly-
ethylene results in substantial changes in the viscosity of the
polymer, we sought to determine the potential of using the
analysis of changing NMR line shapes or relative peak heights
as a technique for investigating antioxidant:peroxide inter-
actions in crosslinking polyethylene systems.

Experimental

The experiments described herein were performed on a Varian
CFT-20 spectrometer equipped with a variable temperature ac-
cessory using pulsed Fourier Transform (PFT) techniques.
Virgin polyethylene (AC-617A, 0.91 density, Allied Chemical)
and mixtures of polyethylene with additives were observed as

neat samples at 140 ± 1 C. The polymer melt was contained
within a 2-mm ID capillary tube which was symmetrically posi-
tioned within a 5-mm OD tube. The larger tube contained 1,4--
dibromobenzene-d4 which served as the deuterium source for the
internal lock of the CFT-20. A small amount of undeuterated
dibromobenzene was also added to the larger tube to act as an
external proton standard for evaluation of the lineshape
changes occurring in the polyethylene. (Figure 6) A nitrogen en-
vironment was maintained over all samples in these experiments.

Results

The NMR samples were prepared by adding the polyethylene powder
(100-125 mg) to a capillary tube which then was immediately
inserted into the 5-mm tube containing the preheated (140C)
di-bromobenzene solution. This assembly was placed into the
spectrometer probe and data acquisition then was initiated.
(25 acquisitions, 1.023 second acquisition time, 90° tip
angle). Virgin polyethylene containing no additives was first
examined to determine the inherent stability of the polymer.
Peak height was the experimental variable most easily deter-
mined. The peak height of the methylene absorbance of poly-
ethylene was observed to be essentially constant (± 4%) for
about the first 100 minutes of observation. However, after 140
minutes, the peak height had decreased 40%. This decrease in
peak height is attributed to changes in viscosity of the poly-
mer due to autoxidation. Further experiments were limited to
observation times of less than 100 minutes to avoid complica-
tions due to this phenomenon.
    Three dry blends of the polyethylene powder were prepared
containing 1) 2 wt % stabilizer (4,4'-methylenbis(2,6-di--
tert-butylphenol) (Ethyl Corporation), 2) 4 wt % peroxide
(di-isopropyl cumyl peroxide), and 3) 2 wt % stabilizer plus 4
wt % peroxide. The NMR line height changes observed with these
blends are shown in Table I and Figures 7 through 10.
    Polyethylene containing only stabilizer showed essentially
no change over the period of observation. (Figure 7) This
behavior contrasts dramatically with that observed for poly-
ethylene with added peroxide (Figures 8 and 9) which shows
large and rapid changes in peak height. These changes grad-
ually diminish in magnitude and cease to occur after about 45
minutes.
    The polyethylene containing both stabilizer and peroxide
showed changes in line height intermediate to those observed
above (Figures 9 and 10). The changes in line shape seemed to
occur as rapidly as they do with the polymer containing per-
oxide only but were much smaller and stopped more quickly.
    The observation of the mediation of the peroxide effect by
the antioxidant is an interesting one. These data indicate
that the cross-linking reaction is initially affected by the

Table I. Normalized Peak Heights Relative to Final "Constant" Peak Height for Polyethylene Blends.

Stabilizer Only		Peroxide Only		Stabilizer and Peroxide	
Time (min)	Rel. Pk. Ht.	Time (min)	Rel. Pk. Ht.	Time (min)	Rel. Pk. Ht.
5	1.02	2	3.37	4	1.37
10	1.01	6	2.09	7	1.43
26	0.99	10	5.02	10	1.20
34	1.02	14	4.67	14	0.87
44	1.00	17	3.28	17	0.87
		19	3.35	21	0.98
		23	3.09	24	1.15
		27	2.70	31	0.96
		32	1.60	35	0.98
		35	2.59	40	0.93
		38	2.35	46	1.06
		42	1.52	55	0.96
		48	1.00	61	1.00
		51	1.02		
		54	1.09		
		63	1.00		
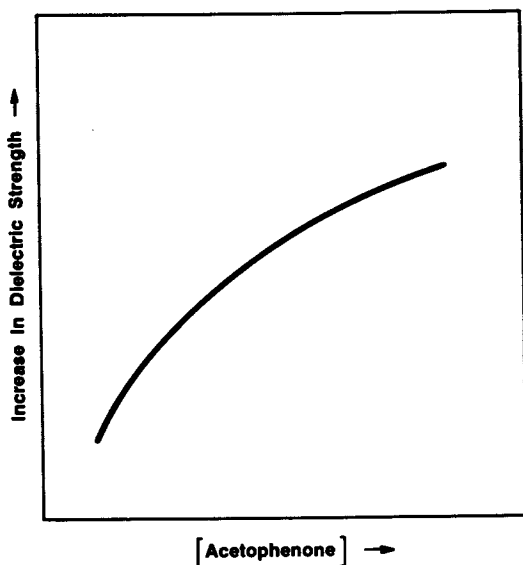
Figure 5. Generalized Voltage Breakdown Curve for Polyethylene Containing High Concentrations of Liquid Peroxide Decomposition Products (acetophenone).
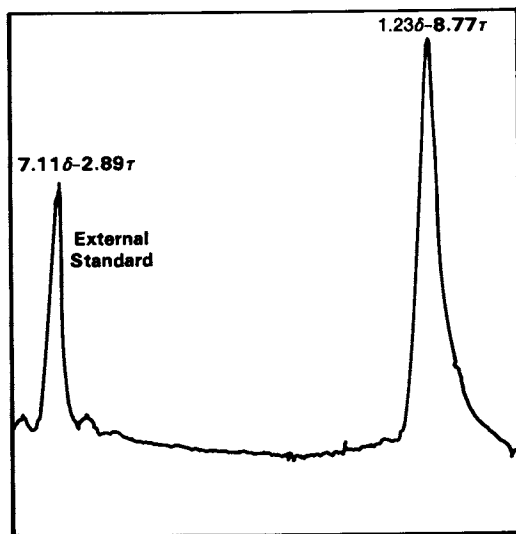
Figure 6. NMR Spectra of a Polyethylene Melt Sample.
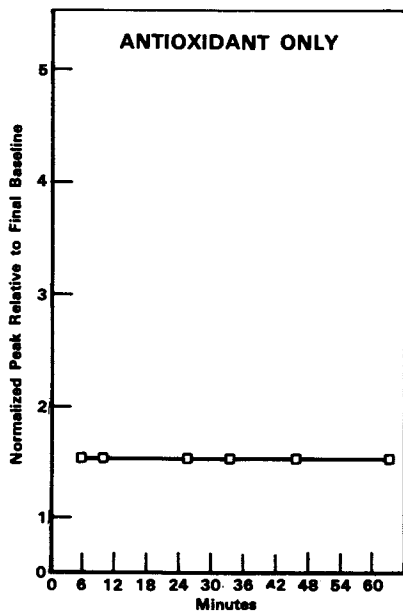
Figure 7. Change in NMR Peak Height of a Polyethylene and Antioxidant Sample.
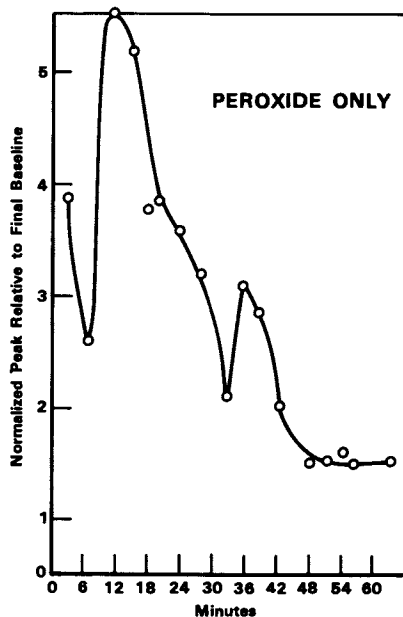
Figure 8. Change in NMR Peak Height of a Polyethylene and Peroxide Sample.

PEROXIDE PLUS AA
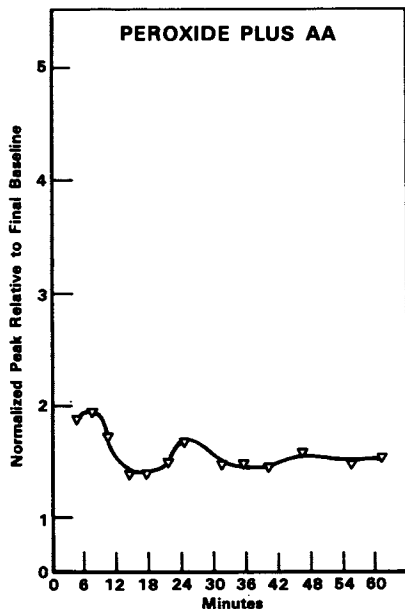
Figure 9. Changes in NMR Peak Height of a Polyethylene, Peroxide and Antioxidant (AA) Sample.
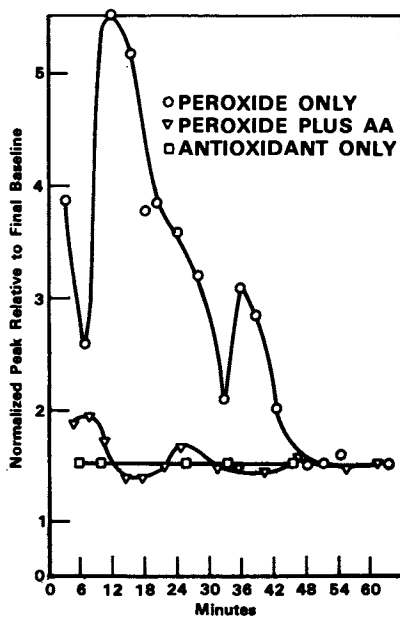
Figure 10. Composite Representation for Changes in NMR Peak Height of Polyethylene Materials in Combination with Peroxides and Antioxidant (AA).

antioxidant which itself probably is consumed to a significant extent. (10)

The NMR spectrum of linear polyethylene in the melt is not described by a single Lorentzian line shape. Several re-searchers (11,12,13) have attributed the deviation of the ex-perimental spectrum of molten polyethylene from the single Lorentzian as being evidence for the presence of special structures, e.g., ordered bundles of molecular chains. A later reference (14) reports that although the polyethylene melt [spectra] can be decomposed to produce two Lorentzian curves, the decomposition has no physical meaning although a distribu-tion of the correlation times might relate to mechanical or dielectric relaxation phenomena. (15,16)

In the present study rapid changes in polyethylene NMR spectral line shape, peak heights or area with time at constant temperature were observed under typical peroxide crosslinking reaction conditions. These changes in NMR line shape over relatively short peroxide reaction time periods could be caused by several factors. One explanation might be a plasticization effect on the polymer caused by melting and dissolution of the peroxide molecules. Plasticization would lead to changes in viscosity and other polymer physical properties with a result-ant averaging out of the NMR signal. If this were simple plasticization, however, other low molecular weight solids, e.g., antioxidants, would be expected to cause similar phenom-ena. This type of kinetic change in NMR line shape, however, was not observed with other low melting or low molecular weight additives unless they contained reactive peroxide function-ality.

The data strongly suggest that crosslinking reactions are the major contributor to changes of NMR line shapes under these experimental conditions. This appears to be consistent with the finding that crosslinking reactions of peroxide poly-ethylene at 140 C are known to occur and produce three dimen-sional networks at approximately the same rate (3-minute re-action time) as observed in the current study. (17)

In this preliminary study it is shown that the major effects of interest occur within 6 to 30 minute reaction times. The spectra taken at longer reaction times may not be fully relaxed and changes in peak heights or peak areas in the 30-50 minute time period may not be accurately represented. The spectra taken within 6 to 30 minute time intervals are very reproducable and can be confidently utilized to observe initial complex inter-action processes among various formulation components in cross-linked polyethylene systems. In Figure 10, after 6 minutes of reaction time, there is a loss observed in peak height (peroxide only) and this is consistent with network formation causing an increase in viscosity of the polyethylene system. Subsequently, increases in peak height would correspond to a decrease in vis-cosity and these processes are observed at the initial phase of

the reaction [dry powder (t=0 min)→melt (t=6 min)] and after 30 minutes [similar increases in peak heights were observed after 18 and 40 minutes for the peroxide plus antioxidant (Figure 11)]. These later increases in peak heights could correspond with some sort of degradation of the network (oxygen may be present to some degree in these systems) but it is also possible that complete melt mixing of the powder sample or uniform heat transfer does not occur except at the later reaction time periods. The ability to maintain uniform heat transfer of a reactive melt polymer system is difficult even in an extruder, and is part of the reason why there is sometimes a gradient or inhomogeneity in cross-link density observed in production run XLPE cable insulations.

Other factors that are important to this process are the amount of gel (crosslinked polymer) formed, the effect of peroxide concentration on the reaction rate and the temperature at which the reaction is carried out. An example of the relationship among cure temperature (150–180 C), gel content (100% – % extractables) and a solvent swelling ratio (xylene or toluene) for polyethylene containing 2% dicumyl peroxide is shown in Figure 11.

The relationship between gel content of crosslinked polyethylene and peroxide concentration (cure time of 3 minutes at 170C) is shown in Figure 12.
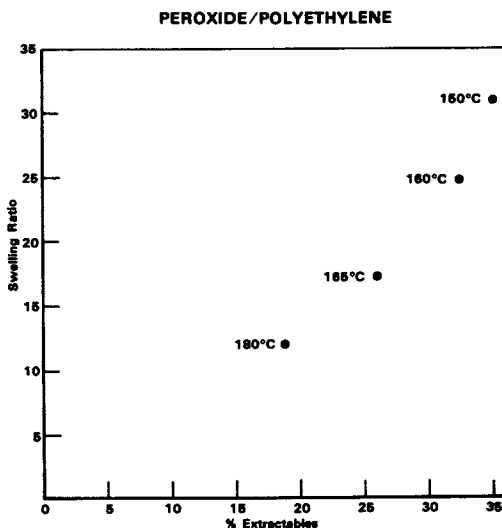
Figure 11.   Relationship Between Swelling Ratio and % Soluble Extractables for Polyethylene/Peroxide Mixtures Cured Under Various Temperature Conditions and a Constant Reaction Time of 3 Minutes.
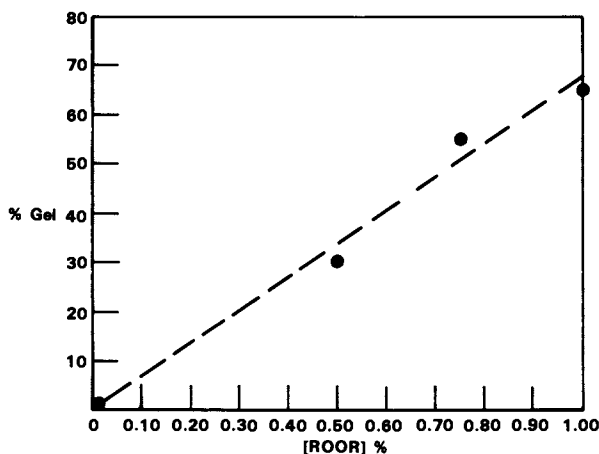
Figure 12.   Relationship Between % Gel Formation and
Peroxide Concentration [ROOR] in the Crosslinking of
Polyethylene Materials.

A simple kinetic reaction scheme for the interaction of
peroxides with polyethylene can be described as follows:

$$ROOR \xrightarrow{\Delta T} R \cdot \qquad (9)$$

$$R \cdot \xrightarrow{K_1} Products \qquad (10)$$

$$PE + R \cdot \xrightarrow{K_2} PE \cdot + RH \qquad (11)$$

$$PE \cdot + PE \cdot \xrightarrow{K_3} XLPE \text{ (Gel)} \qquad (12)$$

$$PE \cdot + RH \xrightarrow{K_4} PE \text{ (Sol)} + R \cdot \qquad (13)$$
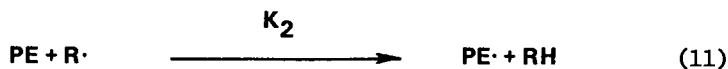
$$\frac{d[PE \cdot]}{dt} = K_2[PE][R \cdot] - 2K_3[PE \cdot]^2 - K_4[PE \cdot][RH] \qquad (14)$$

$$\frac{d[PE \cdot]}{dt} \cong K_2[PE][R \cdot] - 2K_3[PE \cdot]^2 \qquad (15)$$

$$\frac{d[R \cdot]}{dt} \cong [ROOR] - K_1[R \cdot] - K_2[PE][R \cdot] \qquad (16)$$

$$\frac{d[R \cdot]}{dt} \cong [ROOR] - (K_1 + K_2[PE])[R \cdot] \qquad (17)$$

$$-\frac{d[R\cdot]}{dt} \cong 0 \tag{18}$$

$$[R\cdot] = \frac{[ROOR]}{(K_1 + K_2[PE])} \tag{19}$$

$$\frac{d[PE\cdot]}{dt} \cong \frac{K[PE][ROOR]}{K_1 + K_2[PE]} - 2K_3[PE\cdot]^2 \tag{20}$$

$$\frac{d[PE\cdot]}{dt} \cong 0 \tag{21}$$

$$[PE\cdot] = \left\{ \frac{1}{2K_3}\left(\frac{K_2[PE][ROOR]}{K_1 + K_2[PE]} \right) \right\}^{1/2} \tag{22}$$

$$\frac{d(Gel)}{dt} = K_3[PE\cdot]^2 - [PE\cdot][RH]K_4 \tag{23}$$

$$\frac{d(Gel)}{dt} \cong K_3[PE\cdot]^2 \tag{24}$$

$$\text{Rate of Formation} = \frac{1}{2}\left(\frac{K_2[PE][ROOR]}{K_1 + K_2[PE]} \right) \tag{25}$$

From these equations one can show that the rate of gel or crosslink formation (assume measured gel = crosslink formation) (Equation 25) exhibits a first order dependence on peroxide concentration [ROOR] which is consistent with the experimental data presented in Figure 12.

A similar reaction scheme can be derived for the interaction of peroxide (ROOR) and antioxidant (AA) materials with polyethylene under thermal crosslinking conditions.

$$ROOR \xrightarrow{\Delta T} R\cdot \tag{26}$$

$$R\cdot \xrightarrow{K_1} Products \tag{27}$$

$$R\cdot + AA \xrightarrow{K_2} Products + AA\cdot \tag{28}$$

$$PE + R\cdot \xrightarrow{K_3} PE\cdot + RH \tag{29}$$

$$PE\cdot + PE\cdot \xrightarrow{K_4} XLPE\ (Gel) \tag{30}$$

$$PE\cdot + RH \xrightarrow{K_5} PE\ (Sol) + R\cdot \tag{31}$$

$$PE\cdot + AA \xrightarrow{K_6} PE\ (SOL) + AA\cdot \tag{32}$$

$$AA\cdot + R\cdot \longrightarrow Products \tag{33}$$

$$AA\cdot + PE\cdot \longrightarrow Products \tag{34}$$

$$AA\cdot + AA\cdot \longrightarrow Products \tag{35}$$

$$AA\cdot + RH \longrightarrow AAH + R\cdot \tag{36}$$

$$ROOR \xrightarrow{\Delta T} R\cdot \tag{37}$$

$$R\cdot + AA \xrightarrow{K_2} Products \tag{38}$$

$$PE + R\cdot \xrightarrow{K_3} PE\cdot + RH \tag{39}$$

$$PE\cdot + PE\cdot \xrightarrow{K} XLPE\ (Gel) \tag{40}$$
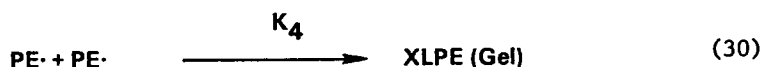
Rate of Gel Formation $\cong f\ [ROOR]$ **and** $f\ [AA]$ $\tag{41}$

$$\frac{d[R\cdot]}{dt} = [ROOR] - K_2[R\cdot]\ [AA] - K_3[PE]\ [R\cdot] \tag{42}$$

$$\frac{d[R\cdot]}{dt} = 0 \tag{43}$$

$$[R\cdot] = \frac{[ROOR]}{K[AA] + K_3[PE]} \tag{44}$$

$$\frac{d[PE\cdot]}{dt} \equiv K_3[PE][R\cdot] - 2K_4[PE\cdot]^2 \tag{45}$$

$$\frac{d[PE\cdot]}{dt} \cong K_3[PE]\left\{\frac{[ROOR]}{K_2[AA] + K_3[PE]}\right\} - 2K_4[PE\cdot]^2 \tag{46}$$

$$\frac{d[PE\cdot]}{dt} \cong 0 \tag{47}$$

$$[PE\cdot] = \left\{\frac{1}{2K_4}\left(\frac{K_3[PE][ROOR]}{K2[AA] + K3[PE]}\right)\right\}^{1/2} \tag{48}$$

Under ideal conditions the rate of gel formation is a function of $[PE\cdot]^2$ or

$$\text{Rate of Gel Formation} \cong f\left\{\frac{[ROOR]}{[AA]}\right\} \tag{49}$$

This idealized reaction scheme (Equations 26 through 48) has not been verified experimentally but is used as an illustration of the kind of methodology required to understand multiple interactions of components in complex systems.

In conclusion this work demonstrates the usefulness of NMR analysis methodologies for observing complex kinetic interactions of components associated with crosslinking reactions of polyethylene materials.

Literature Cited

1. "Petrothene Polyolefins", U.S.I. Chemicals Processing Guide, 1971, 4th ed.
2. McGinniss, V. D., Mangaraj, D. and Gaines, G., IEEE, Annual Report, Conference on Electrical Insulation and Dielectric Phenomena, 1981, p. 450.
3. Wagner, H., Wartusch, J., IEEE Trans. Electrical Insulation, Vol. El-12, No. 6, 1977, p. 395.
4. K. D. Kiss et al., "Durability of Macromolecular Materials", R. K. Eby, Editor, ACS Symposium Series 95, 1979, p. 433.
5. Farrar, T. C., Analytical Chemistry, Vol. 42, No. 4, 1970, p. 109A.
6. Shimizu, H. and Gujiwara, S., _J. Chem. Phys., 34,_ 1961, p. 1501.
7. Kaplan, J. I., and Meiboom, S., _Phys. Rev., 106,_ 1957, p. 106.

8. Meiboom, S., Luz, Z., and Gill, D., <u>J. Chem. Phys., 27,</u>
    1957, p. 1411.
9. Mitchell, R. W., and Eisner, M., <u>J. Chem. Phys., 33,</u> 1960,
    p. 33.
10. Pospisil, J., "Advances in Polymer Science", <u>36,</u> 1980,
    p. 70.
11. Wilson, C. W. and Pake, G. E., <u>J. Polym. Sci., 10,</u> 1953,
    p. 503.
12. Eichhoff, U. and Zachmann, H. G., <u>Ber. Bunsenges. Phys.</u>
    <u>Chem., 74,</u> 1970, p. 919.
13. Zachmann, H. G. "2nd International Symposium on Polymer
    Characterization", F. A. Sliemers and K. A. Boni, editors,
    J. Polym. Sci., Polymer Symposia 43, 1973, p. 111.
14. Horii, F., Kitamoru, R., and Suzuki, T., <u>J. Polym. Sci.,</u>
    <u>Polymer Letters, 15,</u> (2), 1977. p. 65.
15. Olf, H. G. and Peterlin, A., <u>J. Polym. Sci., A-2(8),</u> 1970,
    p. 7771.
16. Mathew, J., Shen, M., and Schatzki, T. F., <u>J. Macro-</u>
    <u>molecular Science, Physics, B13(3),</u> 1977, p. 349.
17. Carlson, B. C., <u>Rubber World, 142,</u> 1960, p. 91.

Degradation Chemistry of Primary Cross-links in High-Solids Enamel Finishes

Solar-Assisted Hydrolysis

ALAN D. ENGLISH and HARRY J. SPINELLI

E. I. du Pont de Nemours and Company, Wilmington, DE 19898

Diffuse reflectance infrared spectroscopy and solid state ^{13}C NMR spectroscopy have been used to study the crosslinking and degradation chemistry of a melamine formaldehyde cured acrylic copolymer coating. The bulk composition of the cured unweathered coating has been semi-quantitatively analyzed by solid state ^{13}C NMR spectroscopy, and a depth profile of weathering chemistry has been obtained using diffuse reflectance infrared spectroscopy. These data allow us to identify the extent of crosslinking, the molecular composition after curing, and to obtain mechanistic insight into degradation chemistry taking place under realistic exposure conditions. The insight obtained infers methods in inhibiting degradation.

The crosslinking and degradation chemistry of melamine formaldehyde acrylic copolymer coatings has been a field of renewed interest recently.(1-4) The intractability of these highly crosslinked systems makes them difficult to study with conventional physical techniques. We illustrate here that modern physical methods can give substantially more information as to both the reaction and degradation chemistry of highly crosslinked systems.

We have used diffuse reflectance infrared spectroscopy and solid state ^{13}C NMR spectroscopy to study the crosslinking and degradation chemistry of a melamine formaldehyde cured acrylic copolymer coating. The bulk composition of the cured unweathered coating has been semi-quantitatively analyzed by solid state ^{13}C NMR spectroscopy, and a depth profile of weathering chemistry has been obtained using diffuse reflectance infrared spectroscopy. These data allow us to identify the extent of crosslinking, the molecular composition after curing, and to obtain mechanistic

insight into degradation chemistry taking place under realistic
exposure conditions.   The insight obtained infers methods of
inhibiting degradation.

Experimental Section

Coating Preparation.   Coatings were prepared by mixing the
acrylic resin with RESIMENE X-747 (nominally hexamethoxy-
methylmelamine) at a 70/30 weight ratio in methyl ethyl ketone
and adding 0.30% p-toluenesulfonic acid (PTSA) as a catalyst.
The pigmentation (4% of binder) in the coating contained aluminum
flake, titanium dioxide, carbon black, phthalocyanine blue, fumed
silica, and MONASTRAL Red pigment.   The coatings were baked for
30 minutes at 120°C.   The cured thicknesses were 50 ± 5 microns.
     Coatings were exposed in Florida on a black box rack for a
total of 24 months.   The panels faced south and were inclined at
an elevation of 5° above horizontal.   After exposure, the panels
were washed with a mild soap solution, rinsed, and dried before
being analyzed.

Coating Depth Profiling.   Depth profiling of coatings that had
been applied to steel panels was accomplished by abraiding the
panel with 600-A TUFBAK Durite T44 cloth (14 μ silicon carbide
particle size) in a water medium.   After a short period of
abrasion (ca. 30 seconds), the material removed was collected,
filtered, and dried in a vacuum oven at 55-65°C for 24-48 hours
to remove residual water.   This procedure was repeated 10-30
times on each panel until the primer was barely visible.   The
material collected in each sample was then cryogenically milled
and dried in a vacuum oven at 55-56°C for 24-48 hours.   This
procedure produces particle sizes prior to cryomilling of 1μ
size which then agglomerate upon drying.   The cryomilling
procedure is necessary to produce infrared spectra that are
particle size independent.

Infrared.   All infrared spectra were obtained with a Nicolet 7199
FT-IR spectrometer operating in a diffuse reflectance configur-
ation.   The design of the diffuse reflectance bench was similar
to that of Fuller and Griffiths ($\underline{5}$). Two hundred fifty-six inter-
ferograms were averaged, apodized with a polynomial function
F_3,($\underline{6}$) and transformed to give two cm^{-1} resolution spectra.

NMR.   NMR spectra were recorded on a Bruker CXP300 NMR
spectrometer.   Solid state ^{13}C NMR spectra were obtained using
cross polarization, dipolar decoupling, and spin temperature
alternation techniques ($\underline{7}$) using a radio frequency field strength
H_1 = 64KHz with a cross polarization time of 5 msec to minimize
intensity distortion in spin counting due to varying strength of
carbon-proton dipolar interactions among individual carbon
nuclei. Samples were contained in rotors of the Beams($\underline{8}$)-
Andrew($\underline{9}$) geometry fabricated from perdeuterated poly(methyl-

methacrylate).   Sample spinning speeds were chosen to minimize spinning side band overlap and a 5.0KHz spinning rate appeared to be optimum at this field strength and rotor size.

Results

Recent investigations into curing chemistry of intractable polymer systems have demonstrated that solid state ^{13}C NMR spectra may be used to examine curing chemistry in thermally polymerized polyimides (10) and expressed hope(11) that these techniques may be used in conjunction with infrared spectroscopy to give further mechanistic insight.   We have used both solid state ^{13}C NMR and diffuse reflectance infrared spectroscopies to characterize the curing and degradation chemistry of melamine formaldehyde crosslinked acrylic copoylmer coatings.

NMR.   Solid State ^{13}C NMR spectra are of particular use in characterizing and curing chemistry of this system because non-carbonaceous pigments and other fillers used in the formulation of these coatings are transparent.   Extraction of quantitative chemical compositions from cross polarization magic angle spinning ^{13}C NMR spectra is complicated by spin polarization dynamics and the distribution of significant signal intensity into spinning sidebands for many of the magnetically distinct cabon nuclei at the magnetic field strength and spinning speeds we employ.   The question of the relationship between spin polarization dynamics and spectral populations has been dealt with previously(12-14); in this case where proton spin diffusion is able to produce a homogeneous spin bath that is characterized by a singly exponential $T_1(H)$, we have used long cross polarization times (5msec) and large spin locking fields (γH_1 = 64KHz) to obtain representative spectral populations even for those carbon nuclei with small static proton-carbon dipolar interaction.
      Figure 1 illustrates a ^{13}C NMR solid state NMR spectrum of an unpigmented melamine formaldehyde acrylic copolymer coating prepared from MMA/BA/S/HEA and crosslinked with RESIMENE X-747 (see above).   Chemical shifts and spectral assignments are given in Table I.   This spectrum illustrates that all carbon nuclei which are distinct on the most elementary level (not comparable to solution NMR) may be assigned in the spectrum.   In Table I we have also tabulated integrated intensities measured from this spectrum which have been corrected for estimated spinning sideband contributions and additionally intensities calculated from the known initial composition of the film assuming complete primary crosslinking and no side reactions (see below).   The experimental and calculated results are in reasonable qualitative agreement and support the infrared spectroscopic results (see below) that the primary crosslinking goes to completion under the cure conditions used and the extent of competing side reactions is minimal.
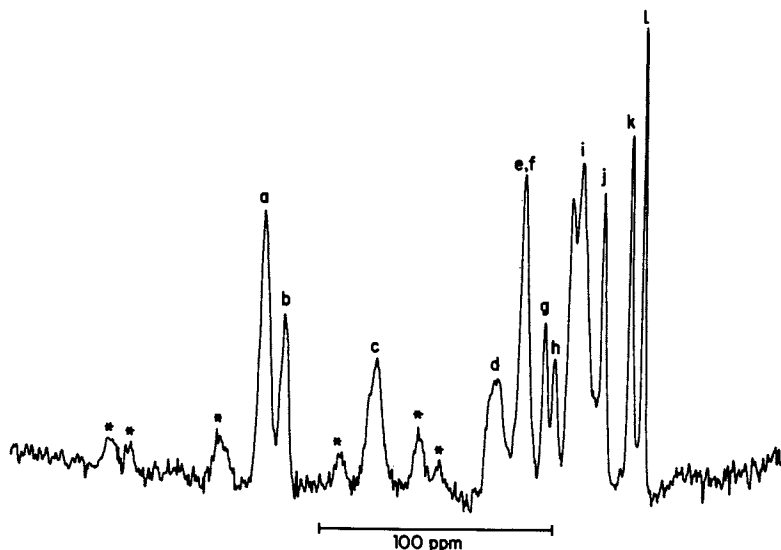
Figure 1.   Solid state ^{13}C NMR spectrum of a melamine formaldehyde crosslinked acrylic copolymer coating. The static magnetic field is 7.0 T and the spinning rage is 5.0KHz   Chemical shifts and assignments are given in Table I and features marked with an asterisk are resolved spinning side bands.

Table I.   Composition of MMA/BA/S/HEA Crosslinked with RESIMENE X-747

	Structure	δ^1	Concentration Experimental	Calculated
a	Acrylic carboxyl	175.2	2.6	2.3
b	Triazine ring	166.5	1.7	1.1
c	Styrene aromatic	127.8	3.3	2.8
d	NCH$_2$O	76.6	1.5	2.1
e,f	OCH$_2$CH$_2$O + OCH$_2$ (NBA)	64.5	2.3	2.7
g	NCH$_2$OCH$_3$	55.5	.8	1.3
h	-OCH$_3$ (MMA)	51.6	.6	.5
i	Acrylic Backbone	44.4, 40.4	3.9	5.5
j	CH$_2$ (NBA)	31.1	1.1	1
k	αCH$_3$ (MMA) + CH$_2$ (NBA)	19.3	1.1	1.5
l	CH$_3$ (NBA)	13.9	1	1

1) δ in ppm from TMs; referenced to glycine at = 176.1

We have also obtained solid state ^{13}C NMR spectra of a few selected pigmented coatings and these results are similar to those found for the unpigmented system. At this time the NMR results are of use only to corroborate the infrared results.

Infrared.   Diffuse reflectance infrared spectroscopy has been used to characterize both the curing and degradation chemistry of melamine formaldehyde crosslinked acrylic copolymer coatings. This technique is useful for not only clear coats, but most appropriately for coatings that contain pigment, aluminum flake, and other fillers that are by their very nature intended to be efficient scatterers and thus cannot usually be examined with transmission infrared techniques.   Figure 2 illustrates both a conventional transmission and a diffuse reflectance infrared spectrum of a clear coating (MMA/BA/S/HEA and RESIMENE X-747). The infrared bands of interests may be integrated and the relative integrals of the bands in each spectrum are with +3% of each other when peak absorbance values of less than 2.0 and peak Kubelka–Munk values less than 20 are used.   The regions of the infrared spectrum of interest are 816cm^{-1} (melamine triazine ring deformation),   913 and   870cm^{-1} (methoxymethyl deformation), 3570cm^{-1} (ROH stretch),   3350cm^{-1} (N-H stretch).   Resolution of any methylol contribution to the infrared spectrum requires deconvolution of the observed band shape using the unreacted polymer as a model for the OH band and the unreacted melamine, which contains   0.6 amine per triazine ring, as a model for the NH band.   In all cases, the ratio of the integrated intensity of the band of interest to the integrated intensity of the melamine triazine ring deformation has been used to measure normalized intensity.   The melamine concentration, as measured from the intensity of the triazine ring deformation mode, is independent of depth in all samples with random fluctuation of +10% for a given formulation; additionally, depth profiling of unexposed clear film demonstrates that the extent and type of cure is independent of depth.   As reference compounds 2-chloro-4,6-bis-(propyl-amino)-s-triazine and RESIMENE X-747 (see Experimental Section) have been used as primary standards for >N-H and >NCH$_2$OCH$_3$ respectively.

Infrared analysis of both clear and pigmented coatings prepared as described in the Experimental Section show complete consumption of all hydroxy functionality on the acrylic copolymer within +2% when cured at 120°C for 30 minutes.   Additionally there is no detectable generation of free amine and the loss of methoxymethyl functionality on the melamine is equivalent on a molar basis to consumption of hydroxyl on the acrylic copolymer within the accuracy (+5%) of the measurement of methoxymethyl functionality.   These observations are in agreement with previous work   (2-16)   that   demethylation (reaction   2,   Figure   3) deformylation   (reaction   3),   and   melamine   self-condensation (reaction 4),   do not occur to a significant extent and that transetherification (reaction 1) goes essentially to completion
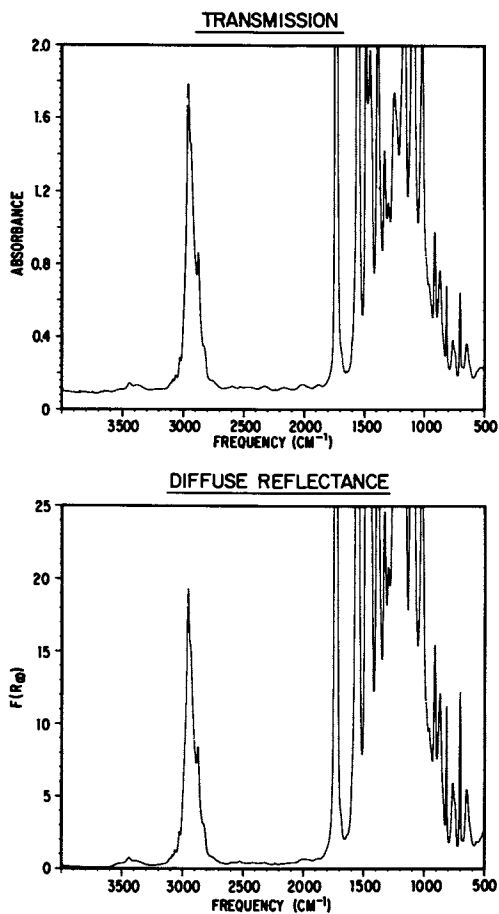
Figure 2.   Transmission and diffuse reflectance infrared spectra of a clear melamine formaldehyde crosslinked acrylic copolymer coating.
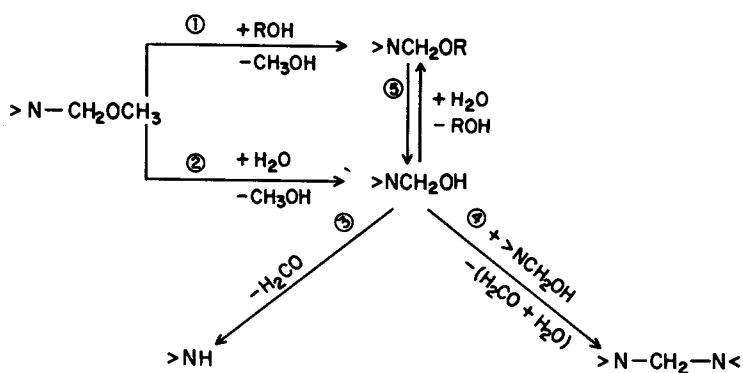
Figure 3.   Elementary crosslinking and hydrolytic degradation reactions involved in melamine formaldehyde ($>NCH_2OCH_3$) crosslinking reactions with hydroxy functionalized acrylic copolymers (ROH).

under these curing conditions with a fully methylated melamine. Figure 3 outlines the most elementary scheme of melamine formaldehyde crosslinking and hydrolytic degradation reactions that must be considered. These results for the bulk curing of the coatings indicate that only reaction (1) is of significance during the curing step with the conditions we have used and thus the initial chemical state of the coating to be exposed is known.

Pigmented coatings that had been exposed in Florida for 2 years were depth profiled, via the abrasion procedure described in the Experimental Section. One part of the coating was exposed to sunlight and the second part was protected from sunlight but exposed to all other elements. Seventeen and twelve samples were collected for the exposed and covered portions of the coating respectively and analyzed by diffuse reflectance infrared analysis for ROH, $>$NH, $>$NCH$_2$OCH$_3$, and melamine concentration as a function of depth. There was no alcohol functionality detectable in any of the samples. The remainder of the data obtained from the sample exposed to sunlight are shown in Figure 4 and illustrate the following: i) $>$NH concentration is highest at the surface and decreases monotonically as the depth of the sample increases, approaching the value (rhs graph) calculated from the starting material with the knowledge that only reaction (1) is significant and goes to completion.; ii) $>$NCH$_2$OCH$_3$ concentration is near zero at the surface and becomes nonzero near the middle of the film and once again approaches the value (rhs graph) calculated from the starting material and known reaction chemistry; iii) X is essentially independent of depth and is very close to that calculated (rhs graph) from the starting material and known reaction chemistry except at the surface where it is 30% smaller.

$$X \text{ equals } (6 - [>NH] - [>NCH_2OCH_3])$$

and is a measure of the sum of primary crosslinks (reaction 1) and melamine self condensation (reaction 4) (see Discussion). As noted, each graph in Figure 4 indicates the amount of each species that is expected to be present in the absence of weathering based upon our observations of the curing chemistry of each film. It is clear that there has been significant production of $>$NH, loss of $>$NCH$_2$OCH$_3$ and X is invariant to weathering except at the surface to a depth of 5–10μ. This observation is not at variance with the traditional method of characterizing film degradation: gloss loss. The gloss of this coating decreased from 60 to 30 during the 2 years of Florida weathering.

Data for the covered (protected from sunlight) coating are shown in Figure 5 and illustrate that the degradation chemistry is much different than in the presence of sunlight (Figure 4). Figure 5 illustrates that weathering in the absence of sunlight may be characterized by: i) $>$NH concentration is independent of depth and is essentially the same as that seen in an unweathered
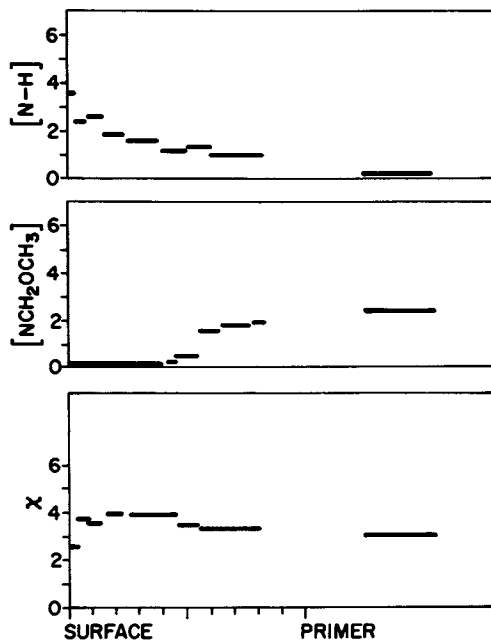
Figure 4. Depth profile of free amine, methoxy methyl, and primary crosslink density of a 50 μ thick blue pigmented melamine formaldehyde crosslinked acrylic copolymer coating that was exposed for two years in Florida. Bars on rhs of graph indicate concentrations expected in the absence of degradation.
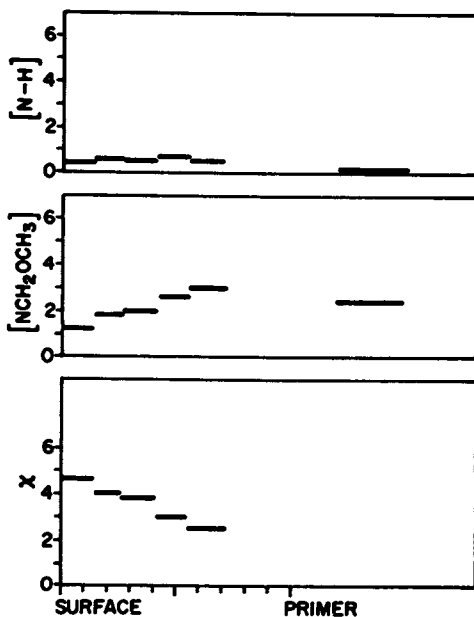
Figure 5. Depth profile of free amine, methoxy methyl, and primary crosslink density of a 50 μ thick blue pigmented melamine formaldehyde crosslinked acrylic copolymer coating that was exposed for two years in Florida but protected from sunlight. Bars on rhs graph indicate concentrations expected in the absence of degradation.

coating; ii) $>NCH_2OCH_3$ concentration is lower near the surface than at the middle of the coating and approaches the concentration of an unweathered coating near the primer; iii)   X is largest near the surface, decreases monotonically with depth, and is much larger near the surface ($\sim$4.8) than is observed in an unweathered coating (X $\sim$ 3.4).

Discussion

The structure and degradation chemistry of melamine formaldehyde crosslinked acrylic copolymer coatings that we have discussed is limited only to considerations of reactions at or near the primary crosslink site involving the melamine with the acrylic copolymer hydroxyl site or with another melamine. There exists copious evidence in the literature that physical appearance degradation occurs in pure acrylic coatings and similar degradative pathways involving only acrylic backbone degadation are expected to exist in the system we have examined as well. Nevertheless, we have chosen to confine ourselves to an examination of the reactions and degradation chemistry at the primary crosslinking site because this is the major difference between the two systems.

Figure 3 illustsrates that the number of species that must be identified and followed in the most simplistic examination of primary crosslink chemistry followed is six ($>NCH_2OCH_3$, $>NCH_2OR$, $>NCH_2OH$, $>NH$, $>NCH_2N$, melamine) if we wish to completely characterize even this elementary scheme.   We can reduce this number with the following conditions:

i)   Reaction 3 has been shown (4) to be facile in fully alkylated systems and we do not observe methylol groups in the infrared spectra.

ii)   The relative concentrations of $>NCH_2OCH_3$, $>NH$, ROH, and melamine can be measured quantitatively by infrared methods.

iii)   The consumption of ROH during cure is assumed to be accomplished by only reaction (1).

With these conditions it is possible to measure $>NH$ and $>NCH_2OCH_3$ relative to melamine concentration and also to calculate from mass balance a crosslink parameter (X) which is the sum of $>NCH_2OR$ and $>N-CH_2-N<$ (or other condensed species) relative to melamine.   The calculated value (X) may then be compared to the expected concentration of NCH_2OR obtained from ROH consumption to evaluate the likelihood of any condensation products (reaction 4).   An examination of Figure 4 shows that the value of X obtained throughtout the coating except at the very surface is quite close to that calculated from ROH consumption. Additionally, we find no infrared spectroscopic evidence for the presence of $>NCH_2N<$ (15) or free ROH at any point in the coating profile.   These observations when taken as a whole lead to the

following description of the primary crosslink reaction and
degradation chemistry that takes place in the <u>presence of</u>
<u>sunlight</u>:

1.   The primary crosslinking reaction (reaction (1)) goes
     to completion and no other reaction takes place to a
     significant extent when the cure is 30 minutes at 120°C.
2.   Degradation under realistic exposure conditions is
     facilitated near the surface with all degradation
     below the surface 2-5μ layer in the coating that
     remains after exposure attributable to reactions (2)
     and (3).
3.   Primary crosslink degradation is observed only at the
     very surface where X is decreased by ∿30% and there
     is no evidence for either ROH or $>NCH_2OH$ in this
     layer.
4.   There is no evidence for any significant amount of
     melamine - melamine self condensation at any time
     during cure or exposure.

     The degradation chemistry in the <u>absence of sunlight</u> is
quite different than is observed in the presence of sunlight:

1.   Loss of unreacted $>NCH_2OCH_3$ is observed, but not to the
     extent observed in the presence of sunlight, and the
     concomittant production of $>NH$ expected via reactions
     (2) and (3) is not observed.
2.   The crosslink concentration is much higher at the
     surface than is found in the unexposed coatings and
     decreases with depth.

     This description of both dark and light degradation
chemistry enables us to propose a pathway of primary crosslink
degradation in this system.

1.   The initially hydrophobic surface of the coating is
     oxidized photolyticaly which increases the concentration
     and/or mobility of water and increases the mobility of the
     residual acid.
2.   Acid catalyzed hydrolysis of $>NCH_2OCH_3$ to form free amine is
     favored due to production of volatile products which may
     escape to the atmosphere.
3.   Acid catalyzed hydrolysis of primary crosslinks is rever-
     sible and therefore unobserved except where the hydrolysis
     products undergo further reaction to prevent back reaction.
     At the very surface of the coating, where there is insuf-
     ficient pigment to provide an effective solar screen, ROH
     and $>NCH_2OH$ in reaction (5) are consumed presumably by
     photo-oxidation and reaction (3), respectively.
4.   Further melamine crosslinking, reaction (4), does not occur
     to a significant extent in the presence of sunlight or is
     unstable.

5.   Unreacted melamine can form additional stable crosslinks
     when sunlight is absent.

The proposed pathway requires the presence of light, residual
acid, and atmospheric water to promote degradation. This implies
that removal of any of these three components should retard
degradation. This pathway also suggests that accelerated
weathering studies which employ a might higher light flux for a
shorter period of time may well give an unrepresentatively large
amount of primary crosslink degradation due to photo-oxidation of
transient ROH produced in reaction (5).

Literature Cited

1.   Bauer, D. R.; Dickie, R. A. J. Polym. Sci. Polym. Phys.
     Ed. 1980, 18, 1997.
2.   Bauer, D. R.; Dickie, R. A. J. Polym. Sci. Polym. Phys.
     Ed. 1980, 18, 2015.
3.   Blank, W. J. J. Coat. Tech., 1979, 51, 656, 61.
4.   Bauer, D. R. J. Appl. Polym. Sci., 1982, 27, 3651.
5.   Fuller, M. P.; Griffiths, P. R. Anal. Chem., 1978, 50,
     1906.
6.   Norton, R. H.; Beer, R. J. J. Opt. Soc. Am., 1976, 66,
     259.
7.   Stejskal, E. O.; Schaefer, J. J. Magn. Reson., 1975,
     18, 560.
8.   Beams, J. W. Rev. Sci. Instrum., 1930, 26, 747.
9.   Andrew, E. R. Progr. NMR. Spectrosc., 1972, 8.
10. Wang, A. C.; Garroway, A. N.; Ritchey, W. M. Macromole-
     cules, 1981, 14, 832.
11. Meyers, G. E. J. Appl. Polym. Sci., 1981, 26, 747.
12. Pines, A.; Gibby, M. G.; Waugh, J. S. J. Chem. Phys.,
     1973, 59, 569.
13. Demco, D. E.; Tegenfeldt, J.; Waugh, J. S. Phys. Rev.
     B, 1975, 11, 4133.
14. Mehring, M. NMR Basic Princ. Prog., 1975, 11, 112.
15. Reference 4 claims the identification of an infrared
     band at 1360cm^{-1} that is thought to be characteristic
     of >NCH$_2$N<. We do not observe any spectroscopic changes in
     this region as a function of weathering of depth.
16. Lazzara, M. G. Preprints Organic Coatings and Applied
     Polymer Science Proceedings, 1982, 47, 528.

IR Spectroscopic Studies of Degradation in Cross-linked Networks

Photoenhanced Hydrolysis of Acrylic–Melamine Coatings

D. R. BAUER and L. M. BRIGGS

Ford Motor Company, Dearborn, MI 48121

Infrared spectroscopy has been used to follow
changes in the chemical crosslink structure of
acrylic/melamine coatings during weathering as a
function of ultraviolet light intensity, humidity,
and coating composition. It has been found that
crosslinks between the acrylic polymer and the
melamine crosslinker hydrolyze rapidly during
exposure. The hydrolysis rate increases both with
increasing humidity and light intensity. The
hydrolysis rate is also a function of coating
composition, being greatest for coatings composed
of low molecular weight, low T_g acrylic polymers.
The enhancement of hydrolysis by ultraviolet light
has been attributed to the fact that melamine
molecules have a weak absorbance in the near
ultraviolet (300 nm). The excited state has been
found to be more easily protonated than the ground
state (by a factor of over 1000 for
hexamethoxymethylmelamine). Since the first step
in hydrolysis is protonation, hydrolysis should be
more rapid in the excited state than in the ground
state.

Thermoset coatings consist of materials which during cure form a
crosslinked network that is in large part responsible for the
physical properties of the coating. As a coating weathers the
crosslinked network may change. Infrared spectroscopy has been
found to be a valuable tool for monitoring crosslinking in
acrylic copolymer melamine formaldehyde crosslinked coatings
(1-9). Melamine crosslinkers take part in two main crosslinking
reactions (Table I) (5,10). Melamine alkoxy groups react with
hydroxy groups on the polymer to form acrylic–melamine
crosslinks. Melamine methylol groups condense to form

melamine-melamine crosslinks. The relative contributions of these reactions and their rates depend primarily on the structure of the melamine crosslinker. Coatings containing fully alkylated melamines require strong acids to cure and under normal conditions crosslink solely by reaction 1. Those containing partially alkylated melamines undergo both reactions 1 and 2 and can be catalyzed by weak acids. Extents of reaction in these systems have been measured by following the disappearance of acrylic hydroxy, melamine methylol, and melamine methoxy groups (5).

TABLE I.   CROSSLINKING AND HYDROLYSIS REACTIONS.

1. $N-CH_2-O-CH_3$ + ROH $\longrightarrow$ $N-CH_2-O-R$ + CH_3OH

2. $N-CH_2-OH$ + $N-CH_2-OH$ $\longrightarrow$ $N-CH_2-N$ +$CH_2=O$ + H_2O

3. $N-CH_2-O-R$ + H_2O $\longrightarrow$ $N-CH_2-OH$ + ROH

4. $N-CH_2-O-CH_3$ + H_2O $\longrightarrow$ $N-CH_2-OH$ + CH_3OH

5. $N-CH_2OH$ $\longrightarrow$ $N-H$ + $CH_2=O$
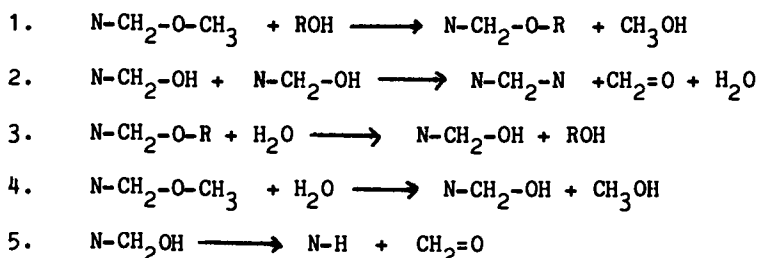
Since the reactions are reversible and involve hydroxy groups, crosslinking in melamine containing coatings can be sensitive to hydrolysis. Hydrolysis of melamine crosslinkers has been studied in solution (11) and in cured acrylic/melamine coatings subjected to condensing and non-condensing humidity (12). It was found (12) that both acrylic-melamine bonds and unreacted melamine methoxy groups can hydrolyze to yield hydroxy groups and melamine methylol groups (reactions 3 and 4). The rate of hydrolysis depends on the following variables: temperature (the activation energy for hydrolysis is 22 kcal/mole), the level of acid in the coating (hydrolysis is acid catalyzed), the concentration of water in the coating (which in turn is a function of the degree of crosslinking of the coating, the molecular weight of the polymer and the glass transition temperature of the polymer), and the structure of the melamine crosslinker (under weak acid conditions, partially alkylated melamines hydrolyze some 30 times faster than fully alkylated melamines). The melamine methylol group produced on hydrolysis can either self condense to form a melamine-melamine crosslink (reaction 2) or deformylate to yield an amine (reaction 5). For

coatings crosslinked with partially alkylated melamines, both reactions 2 and 5 were observed. Since reaction 2 forms crosslinks, it can compensate for acrylic melamine bond hydrolysis. Even though network chemistry may be drastically altered by hydrolysis, the crosslink density and overall physical properties may not be greatly affected (12). In particular, well cured coatings do not generally lose gloss or show other signs of weathering when they are subjected only to condensing humidity. For coatings crosslinked with fully alkylated melamines, no significant melamine-melamine bond formation was observed on hydrolysis though for most conditions studied the amount of hydrolysis was small.

These experiments were performed in the absence of light. It is generally believed that photooxidation is the primary source of weathering in these coatings (13), though it has been noted that coatings lose physical properties more rapidly when weathered in humid conditions than dry conditions (14). Recent ESR studies (15) have demonstrated that photooxidation rates in acrylic/melamine coatings increase with increasing humidity. It was also reported (15) that the rate of disappearance of methoxy groups (reaction 2) at constant humidity increased with increasing ultraviolet light intensity. It was speculated that the rate of hydrolysis was enhanced by ultraviolet light and that the oxidation of formaldehyde released as a by-product of the hydrolysis contributed to the increased rate of photooxidation observed under humid conditions (15). It has also been reported that hydrolysis of acrylic/melamine coatings occurs during natural exposure (16).

It is the purpose of this paper to further characterize the changes in crosslink structure that occur on weathering. In particular, a detailed study of the dependence of the rate of methoxy disappearance on humidity and light intensity is presented which verifies the photoenhancement of hydrolysis. The effect of changes in the composition of the acrylic/melamine coating and the effect of common photostabilizers on the rate of photohydrolysis has been determined. Finally, possible mechanisms for photoenhanced hydrolysis are discussed.

Experimental

Coating Formulation. The acrylic copolymers used in this study were prepared by conventional free radical polymerization. The monomer compositions, molecular weights and glass transition temperatures are given in Table II. Coatings A-G were comprised of acrylic polymers A-G and a partially alkylated melamine (Mel-D of Ref. 7). Coating G' was comprised of acrylic polymer G and hexamethoxymethylmelamine. The ratio of polymer to crosslinker

was 70:30 in all cases. Coatings were cured by baking at 130 C
for 20 minutes (0.1% p-toluene sulfonic acid was used to catalyze
the cure of coating G').

TABLE II.   ACRYLIC COPOLYMER COMPOSITION

Polymer	A	B	C	D	E	F	G
Mn	1700	6400	3900	3600	4500	2500	2700
T_g	-27	9	-26	18	-9	-11	-13
%STY	0	25	0	25	15	25	25
%BMA	68	43	68	0	0	43	23
%BA	0	0	0	0	53	0	0
%MMA	0	0	0	43	0	0	0
%EHA	0	0	0	0	0	0	20

STY = Styrene
BMA = Butylmethacrylate
BA = Butylacrylate
MMA = Methylmethacrylate
EHA = Ethylhexylacrylate
All copolymers contain 30% by weight hydroxyethylacrylate and 2%
by weight acrylic acid.

Weathering. Samples were exposed to constant ultraviolet (UV)
light in a modified weatherometer which allowed the independent
control of air temperature and humidity.   Air temperature was
maintained at 60 ± 1 C.   The humidity was controlled by
controlling the temperature of the water in the bottom of the
weatherometer and rapidly circulating air in the weatherometer to
establish equilibrium.   Weathering was studied at humidities with
the following dew points: 50 ± 1 C (UV:50), 25 C ± 1 C (UV:25),
and -40 ± 5 C (UV:-40).   The UV:-40 exposure condition was
achieved by removing the water from the bottom of the
weatherometer and rapidly circulating dry air in the
weatherometer.   Standard FS-20 sunlamps were used. The peak
wavelength was 300nm. Light intensity was varied with neutral
density filters (intensity = 1 denotes use of no filter, 0.5
denotes use of a 50% transmission filter, 0.1 denotes use of a
10% transmission filter). The UV light intensity without filters
was around 1 mw/cm^2.

Infrared Measurements. Thin (10 micron) coatings were cast on
KRS-5 plates and cured.   Infrared spectra were obtained in
transmission using a Nicolet Fourier transform IR.

Results and Discussion

The changes in network structure that occur on hydrolysis in the dark were clearly elucidated in the infrared (12). The reappearance of acrylic hydroxy functionality was used to measure the hydrolysis rate of acrylic-melamine bonds. For coatings containing partially alkylated melamines, prolonged hydrolysis resulted in the rupture of virtually all of the original acrylic melamine bonds. The disappearance of methoxy was used to follow the hydrolysis of unreacted methoxy groups. For fully alkylated melamines, the rate of hydrolysis of unreacted methoxy groups was identical to that of acrylic melamine bonds. For partially alkylated melamines, the rate of hydrolysis of unreacted methoxy groups was slower than that for acrylic-melamine bonds and the rate of hydrolysis decreased with increasing hydrolysis. This can be explained by the fact that different methoxy groups on partially alkylated melamines have different reactivities. More reactive methoxy groups will both crosslink and hydrolyze more rapidly leading to the observation that acrylic melamine bonds hydrolyze more rapidly than unreacted methoxy groups. The most reactive groups hydrolyze first and as hydrolysis proceeds, the rate of hydrolysis slows as less reactive groups begin to hydrolyze. The increase of a relatively weak band at 1350 cm^{-1} was used to monitor semi-quantitatively the formation of melamine- melamine crosslinks. This band was only observed in coatings crosslinked with partially alkylated melamines.

The spectral changes that occur on photodegradation are more complex than those for hydrolysis in the dark (Figure 1). In addition to hydrolysis-like changes (appearance of hydroxy groups, disappearance of methoxy groups and appearance of melamine-melamine crosslinks) there are changes in other parts of the spectrum. In particular, there are significant changes in the carbonyl part of the spectrum with the appearance of two new bands at 1770 cm^{-1} and 1710 cm^{-1}. Similar changes have been observed in the photooxidation of polybutylacrylate (17). The band at 1710 cm^{-1} is most likely due to carboxylic acid formation; the band at 1770 cm^{-1} was ascribed to lactone formation (17) but may also be in part due to peracid or perester formation. The increase in intensity of these bands can be used as a qualitative measure of the rate of photooxidation.

Although the changes in the IR spectrum due to hydrolysis are readily apparent in the spectrum of coatings degraded under UV:50 conditions, other photodegradation processes can make quantitative measurements of hydrolysis difficult. For example, various photooxidation reactions lead to the formation of hydroxy groups. These hydroxy groups make it impossible to quantify the amount of acrylic hydroxy groups which are generated on

hydrolysis. The rate of disappearance of methoxy functionality can be measured relatively easily. There are two possible mechanisms which lead to a decrease in the methoxy band during weathering: hydrolysis and abstraction of methoxy hydrogens by free radicals produced photochemically. By measuring the rate of disappearance of methoxy as a function of light intensity and humidity, it is possible to separate these two mechanisms. The disappearance of methoxy for Coating G is shown as a function of humidity in Figure 2 and as a function of UV light intensity in Figure 3. In all cases except dark hydrolysis (discussed above) the disappearance of methoxy functionality obeys simple first order kinetics. The rate constants for Coating G and Coating G' are given in Table III as a function of humidity and light intensity.

TABLE III. RATES OF METHOXY LOSS ($\times 10^3$ $^{-1}$).

		COATING G		COATING G'
INTENSITY	UV:-40	UV:25	UV:50	UV:50
1.0	1.2	1.9	3.8	3.3
0.5	0.8	1.1	2.3	1.7
0.1	0.35	0.55	1.15	0.4
0.0	---	0.15	0.6	0.03

Hydrolysis should not occur during UV:-40 exposure and the rate of disappearance of methoxy during this exposure should give a good measure of hydrogen abstraction rates. The methoxy group was found to disappear under UV-DRY conditions at a rate proportional roughly to the square root of the intensity. No formation of melamine-melamine bonds was observed during UV:-40 exposure indicating that the disappearance of methoxy did not lead to the formation of methylol groups which could subsequently crosslink. Both of these findings are consistent with the loss of methoxy being due to photochemically produced radicals abstracting a hydrogen from the methoxy group (hydrogens alpha to ethers are easily abstractable).

The rate of disappearance of methoxy groups during humid exposure was much greater than that for the dry exposure. It was greater than the sum of the UV-DRY rate and the dark hydrolysis rate indicating a photoenhancement of the hydrolysis. To a good approximation the rate constant for the disappearance of methoxy can be given by the following expression:

$$K_{meth} = K_{hyd} \times HUM \times (I + D) + K_{abs} \times I^{1/2} \qquad (1)$$
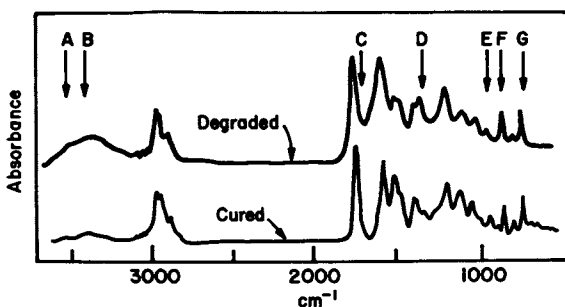
Figure 1.   Infrared spectra of cured and degraded (230 hours, UV:50) samples of Coating G. Peaks of interest include: A, Acrylic hydroxy; B, Melamine methylol; C, 1710 cm^{-1};   D, Melamine-melamine crosslink;   E, Melamine methoxy; F, Melamine triazine ring; G, Styrene.
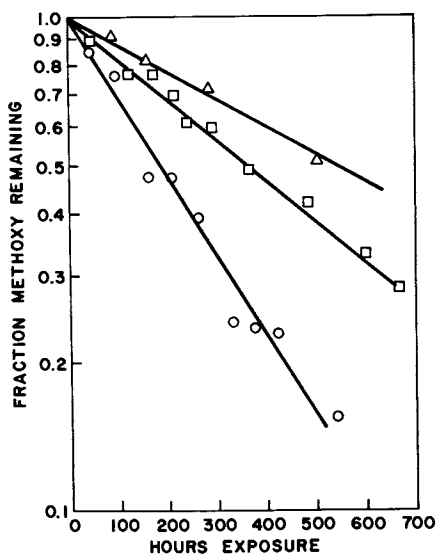
Figure 2.   Fraction of methoxy remaining versus hours exposure for coating G under UV:50 (O), UV:25 (▢), and UV:-40 (△) exposure conditions. Light intensity = 1.
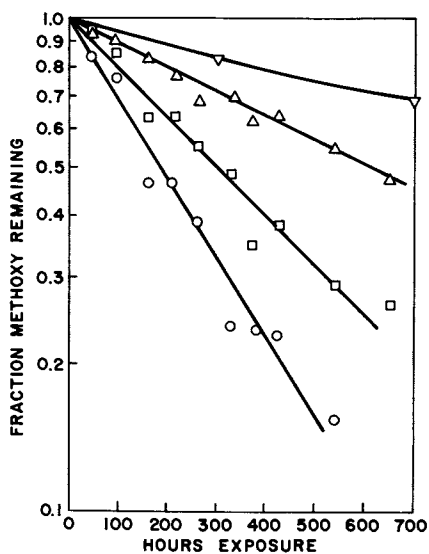
Figure 3.   Fraction of methoxy remaining versus hours exposure for coating G under UV:50 exposure conditions. Light intensity = 1.0 (O), 0.5 (▢), 0.1 (△), and 0.0 (▽).

where K_{hyd} and K_{abs} are rate constants, HUM is the humidity, and I is the light intensity. The product K_{hyd} x HUM x D gives a measure of the dark hydrolysis rate while the product K_{hyd} x HUM x I gives a measure of the photoenhanced hydrolysis rate. For Coating G, comparison of the rates of methoxy loss under UV:-40 and UV:50 exposures and the observation significant formation of melamine–melamine bonds during UV:50 exposure suggests that most of the loss of methoxy group is due to hydrolysis and that acrylic–melamine bond hydrolysis is also photoenhanced. The relative increase in hydrolysis with light intensity was much greater for the fully alkylated melamine than for the partially alkylated melamine primarily due to the very slow rate of dark hydrolysis for the fully alkylated melamine. In fact, values of K_{hyd} are very similiar in Coating G and Coating G' implying that for photoenhanced hydrolysis, all methoxy groups (and by inference all acrylic–melamine bonds) are equally reactive. This is consistent with the observation of simple first order kinetics for photoenhanced hydrolysis of Coating G. It should be noted that the band associated with melamine–melamine crosslinks was not observed for Coating G' exposed to UV:50 conditions. Either the methylol groups do not react as efficiently for the fully alkylated melamine or the band associated with melamine–melamine bond formation is specific to partially alkylated melamines.

The rate constants for the disappearance of methoxy groups for Coatings A-G during exposure to UV:50 and full light are summarized in Table IV. The rate constants increase with decreasing glass transition temperature and molecular weight of the acrylic copolymer. Since the concentration of water in the coating should increase with decreasing glass transition temperature and effective crosslink density, the behavior of these rate constants is consistent with hydrolysis being the primary mechanism for methoxy disappearance (note: it has been previously shown in Ref. 7 that lowering the acrylic copolymer molecular weight results in a decrease in effective crosslink density). In all cases, a substantial increase in the band associated with melamine–melamine self condensation was observed also implying that in these coatings under this exposure the primary mechanism for loss of methoxy is hydrolysis. In Ref. 15 it was suggested that hydrolysis influences the rate of photooxidation through the oxidation of formaldehyde, a hydrolysis by-product. To test this hypothesis, photooxidation rates (as monitored by the increase in absorbance at 1710 cm^{-1}) were measured under standard QUV exposure conditions for two samples of coating G one of which had been hydrolyzed extensively in the dark to reduce the number of hydrolyzable groups. It was found that the rate of photooxidation was slower for the prehydrolyzed sample consistent with the above hypothesis. It is also interesting to note that qualitatively, the rates of

photooxidation of Coatings A-G roughly correlate with the rates
of methoxy loss. Further work to determine the exact
relationship between hydrolysis and photooxidation is in
progress.

TABLE IV. RATES OF METHOXY LOSS $(\times 10^3 \text{ hr}^{-1})$

COATING	K_{meth}
A	3.9
B	1.5
C	3.2
D	1.2
E	2.5
F	3.0
G	3.8

Exposure conditions: UV:50, light intensity = 1

     There are at least two possible explanations for the
increase in the apparent rate of hydrolysis with light intensity.
One possibility is that photooxidation produces carboxylic acids
which catalyze the hydrolysis. Another is that melamines excited
by UV light hydrolyze more rapidly than ground state melamines.
To test these possibilities, the rate of disappearance of methoxy
was followed for solutions of hexamethoxymethylmelamine in water
buffered to pH 7 and in methanol for both light and dark
exposure. The results are shown in Figure 4. The observed
hydrolysis behavior in the dark is similiar to that observed by
Berge et al (11), and from comparisons of the rates in the two
experiments an activation energy of 21 ± 2 kcal/mole can be
determined in excellent agreement with the activation energy
previously determined for hydrolysis in coatings (12). The rate
of methoxy loss in the presence of light was some 6 times faster
than the dark hydrolysis rate. Since the pH was constant, this
can not be attributed to carboxylic acid formation. Since the
rate was zero in the methanol solutions, it can not be attributed
to hydrogen abstraction or some other photochemical process. The
degree of enhancement by UV light was smaller in the solution
experiments than in the coatings in part due to the fact that the
light intensity was lower in the solution experiments.

     For hydrolysis to be enhanced by the absorption of UV light,
the excited state must be sufficiently long lived for hydrolysis
to occur and the rate of hydrolysis in the excited state must be
faster than that in the ground state. A weak absorption in the

region ~300nm has been previously reported for melamine resins and assigned to a singlet to triplet transition (18). The absorption spectra of both the protonated and the non-protonated forms of hexamethoxymethylmelamine are shown in Figure 5. Similiar spectra of the partially alkylated melamine are shown in Figure 6. It is clear that the absorption peak ~300nm shifts to higher wavelength on protonation. One possible explanation for this shift is that the excited state of the melamine is more easily protonated than the ground state. If this effect is responsible for all of the shift, the shifts in pKa of the excited state relative to the ground state are calculated to be +3.2 and +1.6 ($\pm$0.5) for hexamethoxymethylmelamine and the partially alkylated melamine respectively. In both cases the excited state is much more easily protonated. Since the first step in hydrolysis involves protonation, it can be inferred that hydrolysis may indeed be faster in the excited state. The larger enhancement observed in Coating G' relative to Coating G is consistent with the larger shift in pKa observed for the fully alkylated melamine. Adding the pKa shift to measured values of the pKa of ground state melamines (19) indicates that the pKa in the excited state is virtually identical for both melamines (4.5-5.0). This result is consistent with the fact that similiar values of K_{hyd} were observed for Coatings G and G'.

Finally, the effect on the rate of loss of methoxy functionality under UV:50 exposure of the addition of typical photostabilizers is shown in Figure 7. The benzotriazole (CGL-900 from Ciba-Giegy) is a UV absorber and reduces the rate of photohydrolysis by reducing the light intensity. Surprisingly, it was found that when bis(2,2,6,6-tetramethylpiperidinyl-4) sebacate (a hindered amine light stabilizer - CGL-770, Ciba-Giegy) was added to coating G at a level of 2%, the rate of photoenhanced hydrolysis was reduced by a factor of 2. The mechanism for this effect is not known, though at least two explanations are possible. One is that the amine neutralizes the acid that catalyzes the hydrolysis. Another is related to the fact that nitroxides, produced on oxidation of the amine, are known triplet quenchers (20). If the nitroxide quenches the excited state of the melamine, the rate of photoenhanced hydrolysis would be reduced. It is interesting to note that the rate of methoxy loss is decreased more by using a combination of UV absorber and hindered amine than by using either stabilizer alone.

<u>Conclusion</u>

Infrared spectroscopy can be used to monitor changes in the chemical structure of acrylic/melamine coatings during photodegradation. The principal changes in the crosslink
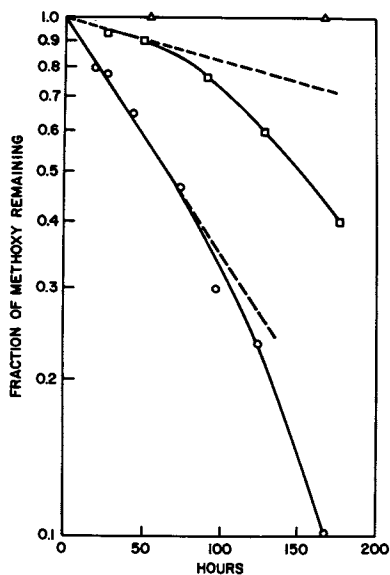
Figure 4.   Fraction   of   methoxy   remaining   versus   hours
exposure for hexamethoxymethylmelamine in water at pH 7 for
UV light exposure (O) and dark exposure (▢)   at   55 C.
Also   shown   in hexamethoxymethylmelamine in methanol under
similiar exposures (△).
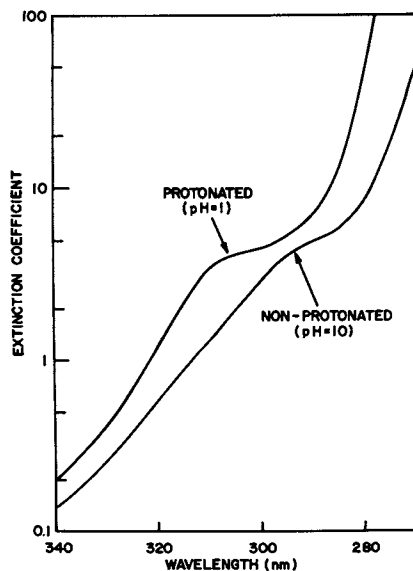
Figure 5.   Absorbance of   hexamethoxymethylmelamine   versus
wavelength for protonated and nonprotonated melamine.
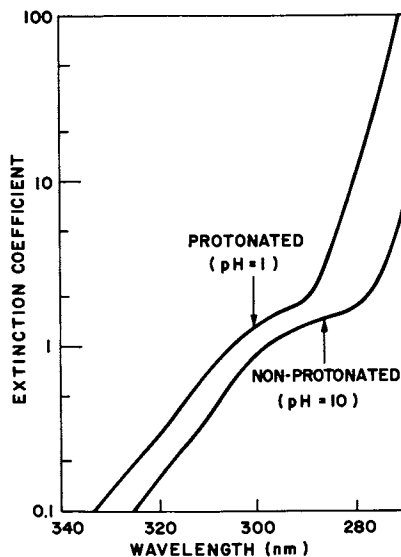
Figure 6. Absorbance of Mel-D versus wavelength for protonated and nonprotonated melamine.
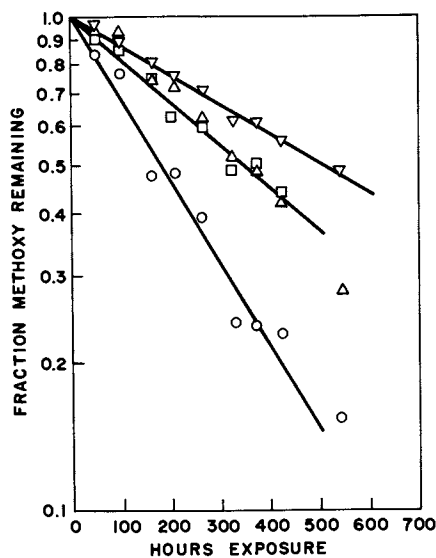
Figure 7. Fraction of methoxy remaining versus hours exposure for Coating G under UV:50 exposure conditions (light intensity = 1). No stabilizer (⊙), 2% Benzotriazole UV absorber (⧠), 2% Hindered Amine Light Stabilizer (△), 1% Benzotraizole and 1% Hindered Amine (▽).

structure are the hydrolysis of acrylic-melamine crosslinks and the subsequent formation of melamine-melamine crosslinks. The rate of hydrolysis during exposure depends on both the humidity and the ultraviolet light intensity as well as the coating composition. The enhancement by ultraviolet light has been attributed to a singlet-triplet transition by the melamine molecule.

Literature Cited

1. R. Saxon and F. C. Lestienne, J. Appl. Polym. Sci., **8**, 475 (1964).
2. K. H. Hornung and U. Biethan, Farbe und Lacke, **76**, 461 (1970).
3. U. Biethan, K. H. Hornung, and G. Peitscher, Chem. Zeitung, **96**, 208 (1972).
4. J. Dorffel and U. Biethan, Farbe und Lacke, **82**, 1017 (1976).
5. D. R. Bauer and R. A. Dickie, J. Polym. Sci., Polym. Phys., **18**, 1997 (1980).
6. D. R. Bauer and R. A. Dickie, J. Polym. Sci., Polym. Phys., **18**, 2015 (1980).
7. D. R. Bauer and G. F. Budde, Ind. Eng. Chem. Prod. Res. Dev., **20**, 674 (1981).
8. D. R. Bauer and R. A. Dickie, J. Coat. Techno., **54**, (685) 57 (1982).
9. D. R. Bauer and G. F. Budde, J. Appl. Polym. Sci., **28**, 253 (1983).
10. W. J. Blank, J. Coat. Tech., **51**, (656) 61 (1979).
11. A. Berge, B. Kvaeven, and J. Ugelstad, Euro. Poly. J., **6**, 981 (1970).
12. D. R. Bauer, J. Appl. Polym. Sci., **27**, 3651 (1982).
13. J. L. Scott, J. Coat. Tech., **49**, 37 (1977).
14. F. A. Kinmonth Jr. and J. E. Norton, J. Coat. Techno., **49**, 37 (1977).
15. J. L. Gerlock, H. Van Oene, and D. R. Bauer, Euro. Poly. J., **19**, 11 (1983).
16. A. D. English and H. J. Spinelli, Previous Paper.
17. H. R. Dickenson, C. E. Rogers, and R. Simha, Polymer Preprints, **23**, 217 (1982).
18. G. W. Costa, R. C. Hirt, and D. J. Smalley, J. Chem. Phys., **18**, 434 (1950).
19. J. K. Dixon, N. T. Woodberry, and G. W. Costa, J. Am. Chem. Soc., **69**, 599 (1947).
20. A. S. Tatikolov and A. V. Kuz'min, Dokl. Akad. Nauk. SSSR., **223**, 403 (1975).

Electron Spin Resonance (ESR) of Photodegradation in Polymer Networks

Photoinitiation Rate Measurement by Nitroxide Termination

JOHN L. GERLOCK, DAVID R. BAUER, and L. M. BRIGGS

Ford Motor Company, Dearborn, MI 48121

Free radical photoinitiation rates have been measured for a variety of melamine crosslinked acrylic resins using a radical scavenging technique. The technique involves photolyzing the crosslinked resin in the presence of a known amount of a persistent nitroxide. Free radicals produced during photolysis of the crosslinked resin are scavenged by the nitroxide. Extrapolation of the rate of nitroxide decay during photolysis to zero nitroxide concentration corrects for the contribution from nitroxide photochemistry and yields the photoinitiation rate of free radicals in the crosslinked resin. Photoinitiation rates can be measured in ~ 1 hour of exposure time. For the series of acrylic melamine resins studied, the photoinitiation rates correlate well with the rates of gloss loss of fully formulated coatings as determined in conventional QUV exposure conditions (over 200 hours of exposure). Both photoinitiation rates and gloss loss rates increase with decreasing acrylic copolymer molecular weight and glass transition temperature.

Evaluation of photodegradation in crosslinked polymeric coatings generally involves measurements of changes in physical properties such as gloss. Outdoor exposure, the most reliable method currently available for determining coating durability, suffers from the fact that long exposure times (2-5 years) may be required to differentiate between good and very good coatings. Accelerated tests shorten the exposure time by employing harsher exposure conditions (e.g., higher than ambient light intensity, humidity, and/or temperature) (1,2). Successful use of such an accelerated test requires at the very minimum, that all of the

important degradation reactions are accelerated to the same
extent. Without an understanding of the mechanisms and rates of
the various chemical degradation processes that occur on
photolysis it is impossible to know whether or not this criterion
is met, and accelerated test results on new paint systems are
often viewed with skepticism. Although a great deal of
information is availiable from experiments on polymers in
solution (3), much less is known about photodegradation of
crosslinked polymers. Most of the photodegradation processes
that occur in organic coatings are thought to be free radical in
nature (3). In the preceeding paper (4), a photoenhanced
hydrolytic degradation of acrylic melamine coatings was
described. Although hydrolysis is not directly a free radical
process, evidence suggests that hydrolysis contributes to coating
photooxidation through formaldehyde, a hydrolysis byproduct and
free radical precursor (5). This study also suggested that there
is a direct connection between the rate of free radical chemistry
in coatings and the rate of loss of physical properties (5).
Degradation by free radicals involves initiation, propagation,
and termination reactions. In this paper, we describe a
technique for measuring the photoinitiation rates of free
radicals in crosslinked polymers under controlled exposure
conditions. The photoinitiation rates are compared with gloss
loss rates of pigmented coatings determined under similiar
exposure conditions.

ESR and Free Radical Quantification

Electron Spin Resonance (ESR) is one of the most sensitive
techniques available for detecting the formation of free radicals
and it has been used to study a variety of free radical processes
in polymers including degradation (6). Free radicals produced
during photolysis of coatings are generally unstable and the
steady state concentration of these radicals is usually very
small under ambient exposure conditions. This makes it very
difficult to directly quantify the rate of free radical formation
in coatings. Transient radicals can often be converted to longer
lived radicals by the method of spin trapping (7). In this
method, a nitrone is added to the material. Photoinduced
oxidants (Y·) react with the nitrone to form ESR observable
nitroxides.

$$\begin{array}{c} R \\ \diagdown \\ R \diagup \end{array} C = \overset{+}{N} - R'' \quad + \quad Y\cdot \quad \longrightarrow \quad \begin{array}{c} R \\ \diagdown \\ R \diagup \end{array} Y - C - \overset{O\cdot}{N} - R''$$
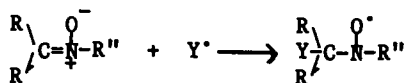
Both phenyl t-butyl nitrone (PBN) and 4-pyridinyl t-butyl nitrone (4-PyBN) were evaluated for use in coatings, however, in no case were nitroxides observed on photolysis.

It has been shown that hindered amine light stabilizers of the 2,2,6,6-piperidine type are rapidly oxidized to nitroxides by polymer photoinduced oxidants (Figure 1) (5, 8-12). These oxidants can also react with the nitroxides that are formed to yield diamagnetic substituted hydroxyl amines (Figure 1) (13-17). Thus, although it is possible to quantify the amount of nitroxide formed by this reaction, it is difficult to quantify the amount of free radical chemistry because the amount of nitroxide seen is a complex function of reactions involving formation and decay of the nitroxide. The nitroxide kinetics can be simplified if the coating is doped with a persistent nitroxide radical rather than a hindered amine. The nitroxide radical scavenges free radicals produced on photolysis and in principal it is possible to measure the rate of formation of free radicals by measuring the rate of disappearance of nitroxide. Nitroxide decay kinetics are complicated by the fact that the nitroxides themselves undergo photochemistry (18-20). Nitroxides can absorb light, and excited nitroxides can abstract a hydrogen to form a hydroxyl amine and a radical on the polymer. In addition both hydroxyl amines and substituted hydroxyl amines (NOY) can be recycled back to nitroxide by certain photochemical oxidants (21). It has been shown that the rate of free radical formation in polymers can be determined by measuring the rate of nitroxide decay on photolysis in the initial stages of decay (to eliminate the importance of the recycling reactions) and extrapolating these decay rates to zero nitroxide concentration (to eliminate the contribution from nitroxide photochemistry) (22). This technique is basically equivalent to the inhibitor method for measuring free radical initiation as described by Emanuel and is subject to the limitations described (23). There exist several techniques which can be used to measure the free radical initiation rate in solution (23). An advantage of this technique is that it can be used to measure the free radical initiation rate in fully crosslinked polymers. In this paper, the nitroxide doping technique is used to determine the photoinitiation rates in a series of acrylic melamine coatings.

Experimental

Materials. The acrylic melamine coatings used in this study are described in the preceeding paper (4). Formulations used in the gloss loss measurements contained 23% by weight of TiO_2. The synthesis of the nitroxide dopant used in these studies[2] (1) has been previously described (24).

$$CH_3\ (CH_2)_{16}\ CH_2 - NH\overset{\overset{\displaystyle O}{\|}}{C}NH - \underset{}{\text{(ring)}} N - O^{\bullet}$$

I
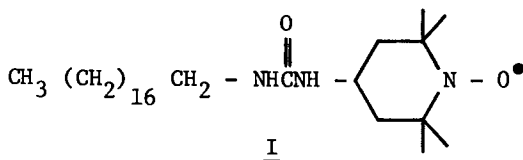
This nitroxide has been found to be sufficiently nonvolatile to be substantially retained in the film after cure (80-100%). Samples for the nitroxide doping experiments were unpigmented. Coating formulations were doped with known amounts of nitroxide (in the range 1 - 10 x 10^{-6} moles/gram), cast on precision cut quartz slides, cured for 20 minutes at 130 C, and then weighed. The nitroxide concentration before exposure was determined by ESR as described below.

ESR Measurements of Nitroxide Concentration. The methods used to quantify the nitroxide concentration in these coating films has been described in detail (24) and are only briefly summarized here. All ESR measurements were obtained using an Bruker-IBM ER 200 D spectrometer equipped with an Aspect 2000 data system and a variable temperature controller. Reliable quantification requires among other things that the samples be reproducibly positioned in the resonance cavity of the spectrometer (25). For these experiments, an all quartz sample holder was designed to allow the rapid positioning of the sample plates in the resonance cavity. Using this sample holder, samples could be repeatedly removed and inserted into the cavity with less than $\pm$ 1% variation in signal intensity. Nitroxide concentrations were determined by measuring the first derivative of the nitroxide absorption (Figure 2), correcting the signal for a weak underlying signal from the quartz sample holder, and then double integrating the signal. The relationships between signal area and nitroxide concentration and sample weight were determined by measuring the signal area for a series of samples of known concentration of Nitroxide I. It was found (24) that the spectrometer sensitivity was a weak function of coating thickness so that the signal area was not simply proportional to coating weight at constant nitroxide concentration. A correction factor for the dependence of the spectrometer sensitivity on film weight was determined (24) and a plot of corrected signal area versus nitroxide concentration is shown in Figure 3. Signal area is linear in nitroxide concentration over this range and absolute nitroxide concentrations can be determined to better than $\pm$ 5%.

Exposure Conditions. For the gloss loss measurements, samples were placed in a conventional QUV weatherometer. The exposure conditions consisted of repeated cycles of 4 hours exposure to ultraviolet light at 60 C followed by 4 hours exposure to
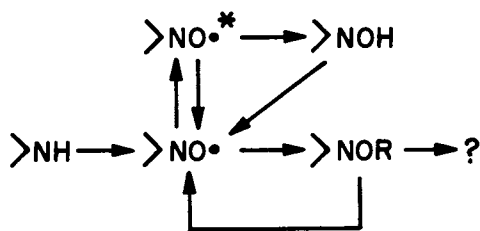
Figure 1. Hindered amine and nitroxide dopant chemistry.
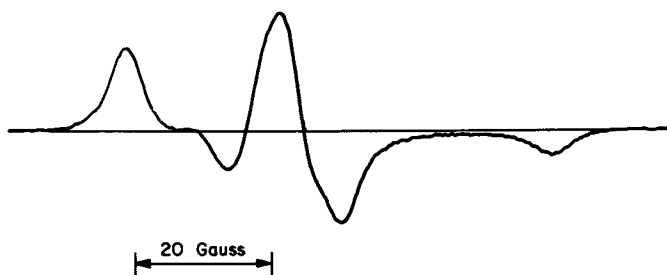
Figure 2. Nitroxide first derivative signal.

condensing humidity at 50 C. Glosses were measured using a Hunterlab D48D glossmeter at 20°.

The nitroxide doped acrylic melamine films were photolyzed in a modified Atlas UV2 ultraviolet screening device. As shown in Figure 4, the device was modified to allow simultaneous and independent control of the air and water temperatures in the device. Air temperature was maintained at 60 C while the water temperature was maintained at 25 C. A fan was added to insure uniform air temperatures and to equilibrate the water in the vapor phase with the water in the bottom of the chamber (to control the dew point). Because of the position of the samples in the device, the light intensity at the sample was some 2 - 3 times lower for the nitroxide doping experiments than for the gloss loss measurements. Since FS fluorescent bulbs were used in both experiments, the wavelength distribution was identical. Samples were repeatedly exposed to the ultraviolet light, removed from the weathering chamber and the nitroxide concentration determined. Since the exposure times were quite short (as short as one minute between measurements), and since the nitroxide kinetics have been found to be sensitive both to temperature and humidity, (5) it was necessary to equilibrate the samples to the temperature and humidity in the chamber before exposure to the ultraviolet light. This was done by inserting the samples into a chamber which though shielded from the light was open to the atmosphere of the chamber. Samples were equilibrated for at least 5 minutes. No nitroxide decay was observed during the equilibration and equilibration times longer than 5 minutes were found to be unnecessary.

Kinetics of Nitroxide Decay

The kinetic behavior of nitroxides in a photolabile medium under exposure to light has been described (22). The derivation is a modification of an analysis by Buchachenko for photolysis of nitroxide in a photoinert medium (18). As described by Equations 1 - 6, nitroxide decay proceed by two distinct pathways involving nitroxide photochemistry and polymer photochemistry. Nitroxide photochemistry (Equations 1 - 3) involves absorption of light by nitroxide followed by hydrogen abstraction from the medium to produce hydroxyl amines and polymer radicals. These polymer radicals as well as the polymer radicals produced by polymer photochemistry (Equations 4 - 6) are scavenged by nitroxide.

$$\backslash\!\!\!/NO^{\bullet} \;\; + \;\; h\nu \;\; \underset{k_{-1}}{\overset{k_1}{\rightleftharpoons}} \;\; \backslash\!\!\!/NO^{*} \qquad\qquad (1)$$
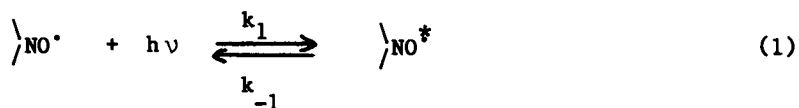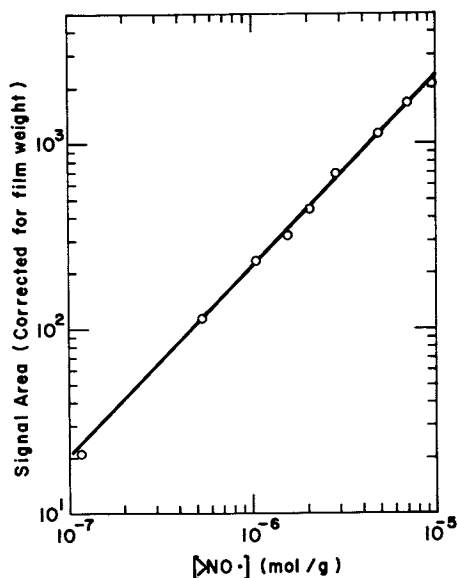
Figure 3. Nitroxide signal area (corrected for coating film weight) versus nitroxide concentration. The slope of the log-log plot is 1.03+.04 and the correlation coefficient is 0.998.
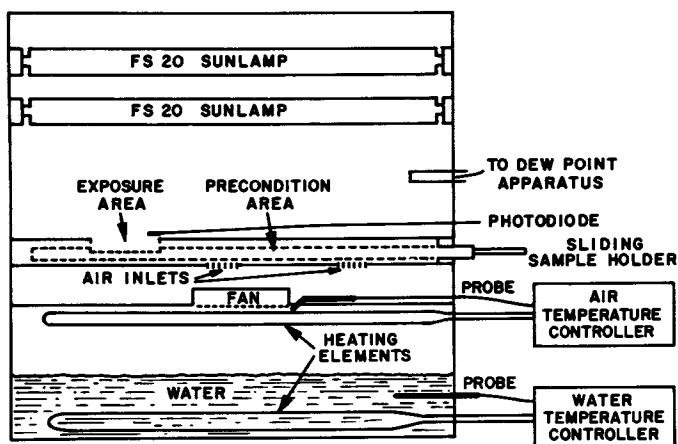
Figure 4. Weathering chamber for nitroxide decay experiments. Samples are placed in the preconditioning area to reach equilibrium with the chamber atmosphere. They are then slid into the exposure area. Air temperature, water temperature, light intensity, and dew point can be continuously monitored during the experiment.

$$\text{\textbackslash}NO^* \quad + \quad YH \quad \xrightarrow{\text{\hspace k_2}} \quad \text{\textbackslash}NOH \quad + \quad Y^{\cdot} \tag{2}$$

$$Y^{\cdot} \quad + \quad \text{\textbackslash}NO^{\cdot} \quad \xrightarrow{\text{\hspace k_3}} \quad \text{\textbackslash}NOY \tag{3}$$

$$A \quad + \quad h\nu \underset{k_{-4}}{\overset{k_4}{\rightleftharpoons}} \quad A^* \tag{4}$$

$$A^* \quad \xrightarrow{\text{\hspace k_5}} \quad 2X^{\cdot} \tag{5}$$

$$X^{\cdot} \quad + \quad \text{\textbackslash}NO^{\cdot} \quad \xrightarrow{\text{\hspace k_6}} \quad \text{\textbackslash}NOX \tag{6}$$
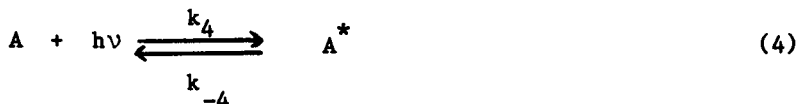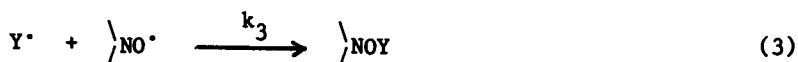
Eqs. 1-6 can be solved for the rate of nitroxide loss assuming steady state kinetics in $\text{\textbackslash}NO^*$, $Y^{\cdot}$, A^*, and $X^{\cdot}$,

$$\frac{d[NO^{\cdot}]}{dt} = -2k_1 I \left(\frac{\varepsilon}{1+\varepsilon}\right) [NO^{\cdot}] - 2k_4 I \left(\frac{1}{1+\varepsilon'}\right) [A] \tag{7}$$

where $\varepsilon = k_2[YH]/k_{-1}$, $\varepsilon' = k_{-4}/k_5$, and I is the intensity of the light. The rate $2k_4 I \left(\frac{1}{1+\varepsilon'}\right) [A]$ is just the rate of photoinitiation of $X^{\cdot}$ radicals. An identical equation results even if the radical does not react directly with nitroxide as long as it is rapidly converted to a radical species which does react with nitroxide before it undergoes either termination or chain branching. Although it is possible to integrate Eq. 7 and fit experimental decay curves to determine the rates, it should be noted that in the derivation of Eq. 7, reactions which convert substituted hydroxyl amines formed in reactions 3 and 6 back to nitroxides have been ignored. These reactions occur (Figure 1) and affect the shape of the decay curves at extended exposure times. It is possible to determine the rates by measuring the initial rate of nitroxide decay as a function of the initial nitroxide concentration. The initial rate of nitroxide loss can be written as,

$$\left(\frac{d[NO^{\cdot}]}{dt}\right)_o = - C[NO^{\cdot}]_o - D[A]_o \tag{8}$$

where C and D are defined by Eq. 7. Eq. 8 has been tested by measuring nitroxide decay kinetics in media containing known amounts of photolabile species. It was found that over the nitroxide concentration range 1 - 10 x 10^{-6} moles/g, the rate of initial nitroxide loss was linear with initial nitroxide concentration and that the intercept, D, was proportional to the concentration of photolabile species (22). Thus, the measured slope is a measure of the ease of hydrogen atom abstraction by nitroxide while the intercept is a measure of the rate of photoinitiation of radicals in the coating. Below concentrations of 1 x 10^{-6} moles/g, the nitroxide level is insufficient to prevent chain branching and deviations from linearity are observed (22).

Results

Gloss Loss. Plots of gloss versus exposure time for the six acrylic melamine coatings are shown in Figures 5 and 6. Over the first 100 - 500 hours (depending on the coating) the loss of gloss seems to obey simple first order kinetics. From the slope of the gloss loss curves, a rate of gloss loss can be determined for the six coatings. These data are tabulated in Table I. The rates of gloss loss vary by over a factor of three. The general trends of the gloss loss data for the acrylic melamine coatings are consistent with data previously reported, namely, that the rate of gloss loss is greatest for coatings based on low molecular weight (26) and low glass transition temperature (27) acrylic copolymers.

TABLE I. COATING DEGRADATION DATA

		COATING			
	A	B	C	D	E	F
Gloss Loss Rate x 10^3 hr^{-1}	5.1	1.4	3.0	2.1	2.8	3.6
Photoinitiation Rate x 10^8 mole/g-min	7.3	0.6	2.0	1.0	1.3	5.1
Slope x 10^3 min^{-1}	4.2	0.7	1.8	1.7	2.4	6.6

Nitroxide Decay Kinetics. Plots of nitroxide decay versus time are shown in Figure 7 for different nitroxide concentrations. Plots of nitroxide decay versus time are shown in Figure 8 for two different coatings at similiar initial nitroxide concentrations. Equation 7 predicts that the nitroxide decay is the sum of a first order term (in nitroxide) and a zeroth order
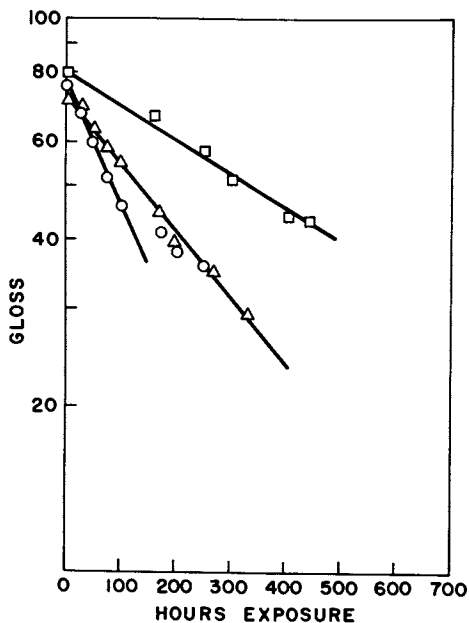
Figure 5. Gloss versus hours of QUV[R] exposure for Coatings
A, O ; B, □ ; and C, △ . The compositions of the
coatings are given in the preceeding paper (4).
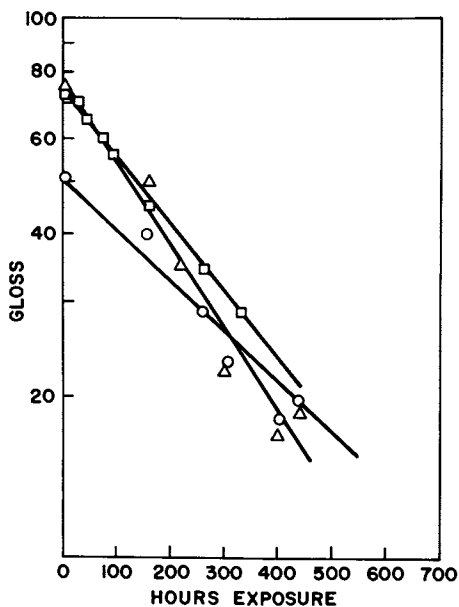
Figure 6. Gloss versus hours of QUV exposure for Coatings
D, O ; E, □ ; and F, △ . The compositions of the
coatings are given in the preceeding paper (4).

term. As can be seen from Figures 7 and 8, the nitroxide decay is pseudo zeroth order (i.e., linear with time) over the first 10 - 20% of the decay. The slope of the initial decay curve is the initial rate of nitroxide loss and was determined by a least squares fit of the initial data. The decay rate was reproducible to $\pm 10\%$. As shown in Figure 8, after the first 20% or so of the decay the rate of nitroxide decay slows considerably. At long decay times, the curves failed to fit Eq. 7 implying that recyling reactions are important at long times.

As discussed above, it is necessary to extrapolate the nitroxide loss kinetics to zero nitroxide concentration in order to determine the photoinitiation rate of the coating. Shown in Figure 9 is a plot of initial nitroxide decay rate versus initial nitroxide concentration for the six coatings studied. Over the nitroxide concentration range studied, the decay rate was found to be linear in nitroxide concentration for all six coatings. The slopes and intercepts are given in Table I for the six coatings. The slope is a measure of the ease of hydrogen abstraction by excited nitroxide in the coating while the intercept is the rate of formation of free radicals by the coating under these exposure conditions. The rate of photoinitiation of free radicals can be determined to $\pm 20\%$ by this technique. For the coatings studied here, the photoinitiation rate varied by over a factor of 10. Photoinitiation rates were highest for coatings based on low molecular weight, low T_g acrylic copolymers. A direct correlation between photoinitiation rate and gloss loss rate was observed in these coatings. As shown in Figure 10, the rate of gloss loss is roughly proportional to the square root of the photoinitiation rate. This behavior is consistent with the degradation being a free radical process with bimolecular termination (23). The slopes of the lines in Figure 9 also varied by almost a factor of 10. According to Eq. 9, changes in slope must reflect changes in the rate of hydrogen abstraction $(k_2[YH])$ or changes in the rate of decay of excited nitroxide (k_{-1}). The data in Table I suggest that the slope increases with decreasing acrylic copolymer molecular weight. Whether this is due to a higher abstraction rate or a longer excited state lifetime is not known at present.

Discussion

The direct correlation observed in this study between gloss loss rates and photoinitiation rates suggests that the nitroxide doping technique could provide a rapid test for the evaluation of coating durability. Measurements of nitroxide decay kinetics to determine coating photoinitiation rates can be made at near ambient exposure conditions in a few days (compared to years for
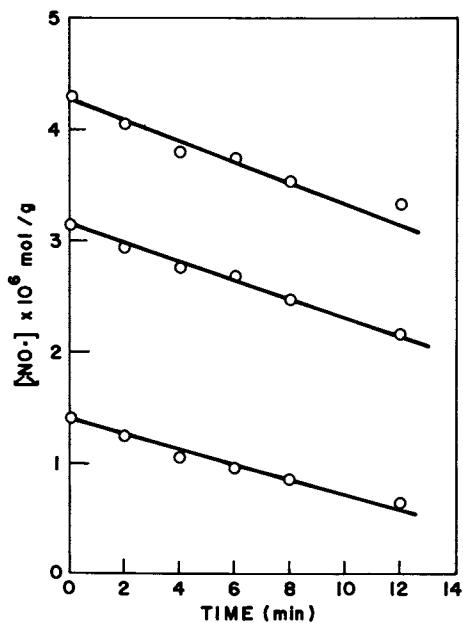
Figure 7. [Nitroxide] versus time for Coating A at three different levels of Nitroxide I.
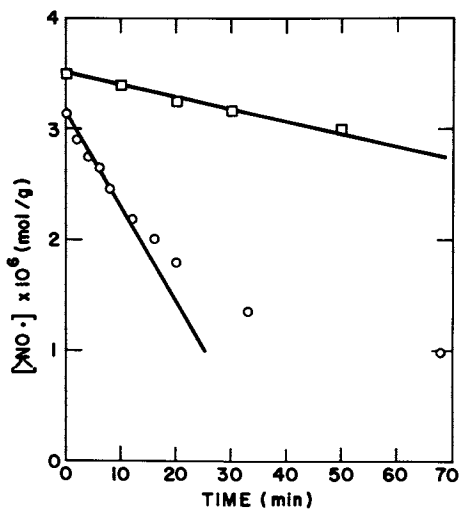
Figure 8. [Nitroxide] versus time for Coating A, ⬤ and Coating B, ◻ at similiar levels of Nitroxide I
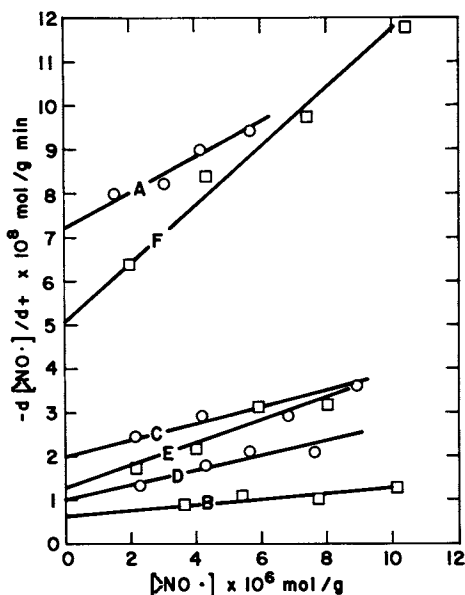
Figure 9.   Initial rate of nitroxide loss versus initial nitroxide concentration for the six coatings. The slope is a measure of the ease of hydrogen abstraction by excited state nitroxide while the intercept is the rate of free radical photoinitiation in the coating.
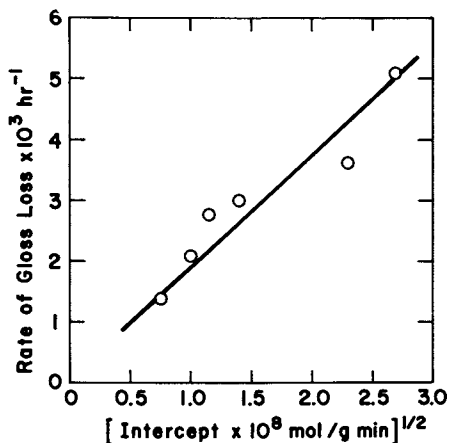
Figure 10. Rate of gloss loss versus the square root of the coating photoinitiation rate determined from the nitroxide doping experiments for the acrylic melamine coatings.

the gloss loss measurements) (5). The use of free radical formation rate data to predict long term durability in a series of coatings requires that the basic degradation chemistry be the same (with only the rates being different) and that a given amount of chemical degradation results in a given amount of loss of physical properties. These criteria are apparently met for the series of acrylic melamine coatings studied. Measurements of the photoinitiation rate as a function of exposure conditions should also prove useful for defining acceptable accelerated weathering conditions and for quantifying the acceleration factor in coating systems where the degradation chemistry and the relationship between degradation chemistry and loss of physical properties are different. For example, by measuring the photoinitiation rates for different coatings under both near ambient and accelerated exposure conditions it can be determined whether or not the acceleration factor is the same for the different coatings. If it is, the results of gloss loss tests at the accelerated conditions can be used with some confidence to predict service life.

These measurements may also provide a better understanding of the mechanisms or the different photodegradation processes and may provide a means to assess the importance of the different processes to the overall durability of a coating. For example, measurements currently in progress of the dependence of the photoinitiation rate on humidity should help quantify the role of hydrolysis in the overall photodegradation process and may help confirm whether or not formaldehyde is responsible for the increase of photooxidation rate with increasing humidity. Further experiments are also in progress to determine the reason for the strong dependence of the photoinitiation rate and slope on the acrylic copolymer molecular weight in acrylic melamine coatings. An understanding of the role of molecular weight in photoinitiation may lead to the design of more durable high solids coatings.

Conclusion

A nitroxide doping technique has been developed which makes it possible to measure the rate of photoinitiation in a crosslinked organic coating. A direct correlation has been found between this photoinitiation rate and rates of gloss loss under similiar exposure conditions for a series of acrylic melamine coatings. Since the photoinitiation rates can be measured rapidly (a few hours or so), the nitroxide doping technique may provide a rapid test for coating durability. It may also be useful for determining appropriate conditions for accelerated tests. Work is in progress to determine the dependence of photoinitiation rates on exposure conditions for a variety of coating systems to further evaluate the utility of this approach.

Literature Cited

1. J. L. Scott, J. Coat. Techno., 49, 27 (1977).
2. G. W. Grossman, J. Coat. Techno., 49, 45 (1977).
3. V. Ya. Shlyapintokh and V. B. Ivanov, "Developments in Polymer Stability - 5", G. Scott, Ed., Applied Science, London, pp 41-70 (1982).
4. D. R. Bauer and L. M. Briggs, preceeding paper.
5. J. L. Gerlock H. Van Oene and D. R. Bauer, Eur. Polym. J., 19, 11 (1983).
6. B. Ranby and J. F. Rabek, "ESR Spectroscopy in Polymer Research" Springer-Verlag, Berlin 1977.
7. E. G. Janzen, Accts. Chem. Res., 4, 31 (1971).
8. K. B. Chakraborty and G. Scott, Chem. Ind., 237 (1978).
9. D. J. Carlsson, D. W. Grattan, T. Suprunchuk, and D. M. Wiles, J. Appl. Polym. Sci., 22, 2217 (1978).
10. D. W. Grattan, A. H. Reddoch, D. J. Carlsson, and D. M. Wiles, J. Polym. Sci., Polym. Lett., 16, 143 (1978).
11. G. Scott, Pure and Appl. Chem., 52, 365 (1980).
12. D. J. Carlsson, K. H. Chan, and J. Durmis, and D. M. Wiles, J. Polym. Sci., Polym. Chem., 20, 575 (1982).
13. E. G. Rozantsev, "Free Nitroxyl Radicals", p 120, Plenum Press, New York (1970).
14. J. T. Brownlie and K. U. Ingold, Can. J. Chem., 45, 2427 (1967).
15. B. Felder, R. Schumacher and F. Sitek, Helv. Chim. Acta, 63, 132 (1980).
16. S. Nigam, K. D. Asmus and R. L. Wilson, J. Chem. Soc., Faraday I, 2324 (1976).
17. R. L. Wilson, Trans. Faraday Soc., 67, 3008 (1971).
18. A. I. Bogatyreva and A. L. Buchachenko., Kinetics and Catalysis, 12, 1226 (1971).
19. J. F. W. Keana, R. Dinerstein and F. Baitis, J. Org. Chem., 36, 209 (1971).
20. J. F. W. Keana and F. Baitis, Tetrahedron Lett., 365 (1968).
21. D. J. Carlsson, D. W. Grattan, and D. M. Wiles, Org. Coat. Plast. Chem., 39, 628 (1981).
22. J. L. Gerlock and D. R. Bauer, submitted to J. Polym. Sci.
23. N. M. Emanuel, E. T. Denisov and Z. K. Maizus, "Liquid-Phase Oxidation of Hydrocarbons," p 50, Plenum Press, New York (1967).
24. J. L. Gerlock, J. Anal. Chem., 55, 1520 (1983).

25. J. E. Wertz and J. R. Bolton, "Electron Spin Resonance:
     Elementary Theory and Practical Applications", McGraw Hill,
     New York, 1972 (pp. 464-464).
26. H. J. Spinelli, Org. Coat. and Appl. Polym. Sci.
     Proc., 47, 529 (1982).
27. A. N. Theodore and M. S. Chattha, Org. Coat. and Appl.
     Polym. Sci. Proc., 47, 610 (1982).

Highly Cross-linked CR-39 Polycarbonate and Its Degradation by High-Energy Radiation

J. L. CERCENA, J. GROEGER, A. A. MEHTA, R. PROTTAS, J. F. JOHNSON[1], and S. J. HUANG[1]

Institute of Materials Science, University of Connecticut, Storrs, CT 06268

Highly crosslinked CR-39 polycarbonate samples were prepared from carefully purified monomer. The degradation of these polycarbonates by high energy radiation was studied. Results indicated CR-39 polycarbonate to be suitable material for dosimetry application.

Highly radiation sensitive polymers have been used as resists for production of microelectronic circuitry and as detectors for identification of tracks of energetic nuclear particles. Diethylene glycol bis(allyl carbonate), CR-39, can be polymerized with peroxide initiators into optically clear highly crosslinked polymer films. These films undergo high energy radiation induced scission of the carbon main chains, Fig. 1. Base etching of the irradiated films results in detectable tracks of the energetic nuclear particles. (1-7) The possibility of using these films as dosimeters for high energy radiation has been explored. CR-39 polymer is one of the most sensitive polymers presently available for this purpose, Fig. 1. Among the difficulties encountered in using the presently available CR-39 polymers for dosimetry are the impurities present in the commercially available monomer samples, the poor reproducibility of the polymerization process, and the lack of understanding of the structure of the highly crosslinked polymer samples. The purposes of our present study were to: 1) purify the monomer; 2) develop a reproducible polymerization process; 3) establish methods for the characterization of the highly crosslinked polymer samples; 4) study the effects of high energy radiation on the polymer and develop a sensitive method for counting the tracks of radiation.

[1]To whom correspondence should be directed.

Figure 1. CR-39 Polymer

Experimental

Purification of CR-39 Monomer. Samples of CR-39 monomer which were dissolved in chloroform were purified by passing the solution through a column containing activated charcoal, aluminum oxide, or silica. The treated monomer in chloroform was then analyzed by Gas Chromatography/Mass Spectrometry (GCMS).

To avoid the large solvent peak due to chloroform a second set of samples were passed through columns without solvent. The samples were run through activated charcoal, aluminum oxide or silica columns and also through sequential combinations of these columns (see Table I).

Preparation of CR-39 Polymer. Benzoyl peroxide was dissolved in CR-39 monomer at room temperature in an argon atmosphere. Once dissolved, the solutions were poured into glass casting plates and placed in an 80°C oven in an argon atmosphere. The samples were removed from the oven after 24 hrs.

Irradiation of Polymers. Polymer samples were exposed to recoil protons with 1.06 MeV energy at Battelle Pacific Northwest Laboratories.

Characterization of Polymers. Swelling experiments were carried out by placing small cut out sections of the crosslinked polymer in tetrahydrofuran for a period of 24 hours. After which time the weight of the polymer was measured. This wet weight was then substracted from the dry weight (the weight of the polymer after extraction and sufficient drying) to obtain the percent swelling of the polymer. Percentage of extractables tests consisted of measuring the weight of the polymer both before and after the 24 hour extraction in tetrahydrofuran. The difference in weight yields the percentage of extractables.

Counting of High Energy Radiation Tracks. A computerized image analyzer, the Cambridge Instrument model 900, was used to count the radiation tracks of the irradiated polycarbonate samples. The measurements include track size (diameter), track density in each field of view, roundness, sample area in each field, and total area of the sample. Samples of polycarbonates examined included those prepared in our laboratory and neutron irradiated samples provided by Dr. G. Tarlé of University of California at Berkeley.

Results and Discussion

Commercially available CR-39 monomer samples contain various impurities. The nature and the amounts of these troublesome impurities cause difficulty in producing polycarbonate dosimeters of uniform quality. Therefore, obtaining a high purity CR-39 monomer sample was of utmost importance in solving the problem of

reproducibility in the preparation of CR-39 polymer samples. CR-39 samples from various sources were examined by GC and GC-mass spectrometry. The two major impurities were found to be allyl diethylene glycol monocarbonate and water. Methods to remove these from commercial samples were explored. Washing with aqueous HCl did not remove the impurities. Distillation over calcium hydride at reduced pressure did remove moisture but not the hydroxy terminated allyl diethylene glycol monocarbonate. Column chromatography using aluminum oxide, silica gel, and activated carbon was found to be an effective method for the removal of impurities from commercial CR-39 monomer samples. Table I.

Table I. Purification of CR-39 Monomer Samples

Treatment	Polysciences	PPG	Sola Optical	Allymer
None	+++	+++	++	+++
Aq. HCl				+++
Distillation over CaH_2	+++	+++	++	+++
Al_2O_3	+	++	trace	trace
SiO_2	+	trace	trace	trace
Carbon	+	trace	trace	trace

Note: +++ - high impurity 0.1-1%
         ++ - moderate
          + - light
      trace - less than 10 ppm

CR-39 monomer is generally thermally polymerized with diisopropyl percarbonate as initiator into crosslinked polymer samples with allyl side chains. The presence of allyl side chains can result in several undesirable properties in terms of the use of CR-39 polymer in dosimetry. Allyl groups are sensitive to oxidation by air. Surface oxidation of polymer films can be expected and indeed has been observed by Tarlé. (4) This will shorten the shelf life of the dosimeter. Allyl groups might also undergo polymerization caused by radiation. The stress due to volume shrinkage during such polymerization could cause cracking of the polymer film, a secondary degradation process that is undesirable. Diisopropyl percarbonate is an extremely thermally sensitive initiator. Purification of the initiator is impractical. This has contributed to the difficulty in obtaining reproducibility in the polymerization of CR-39 monomer. The fast rate of thermal decomposition of diisopropyl percarbonate also results in quick gel formation during the CR-39 polymerization. This prevents the

complete reaction of the allyl groups and results in low cross-linking density of the final polymer. We chose to use the more stable benzoyl peroxide and long reaction time to achieve maximum reaction of the allyl groups in order to prepare reproducible highly crosslinked samples. Our best result was obtained carrying out the polymerization at 80°C under argon with 2% benzoyl peroxide as initiator. Increase in the amount of peroxide caused fast gelation which resulted in incomplete reaction of the allyl groups - polymer samples of lesser crosslinking were obtained.

The degree of crosslinking was examined by swelling in THF and measuring the amount of extractable materials in the polymer samples. Representative results are listed in Table II. The GPC analysis, Fig. 2 and Table III showed that although the samples have similar structures the highly crosslinked Sample I-2 showed the least extent of swelling and also the least amount of extractables. Better reproducibility was also obtained with lower initiator concentration in the polymerization mixture and longer reaction time.

The highly crosslinked CR-39 polycarbonate samples were irradiated with recoil protons at Battelle Memorial Institute, Pacific Northwest Laboratories. Although the amount of radiation-caused degradation resulted in similar increases in the amount of extractable fraction, the increases of % swelling were quite different. The highly crosslinked sample I-2-A showed no increase of % swelling while the less crosslinked sample I-5-A showed an increase of 15.6% swelling. The six fold increase in the amount of extractable materials and the negligible change of swelling after irradiation with recoil protons make I-2 the most suitable for dosimetry application.

The Cambridge Instruments Quantimet 900 Image Analyzer was used to analyze the radiation tracks on exposed CR-39 polymer. This system features a computer controlled stage and focus system. Automatic focus was selected for the microscope. These accessories allow the system to automatically scan samples for features of interest over an average area of 8cm x 10cm, while keeping the

Table II. Effects of Radiation on CR-39 Polymers

Sample	% BPO in Polymerization[a]	% Extractable	% Swelling
I-2	2	1	4.6
I-2-A[b]	2	7	4.7
I-5	5	15	30.2
I-5-A[b]	5	22	45.8

a. At 80°C, 24 hrs.
b. After irradiation with proton.

Table III.   G.P.C. Peaks Present in CR-39 Polymer Samples

Sample	% Extractable	Peaks
I-2	1	3,4
I-2-A[a]	7	2,3,4
I-5	15	1,3,4
I-5-A[a]	22	1,2,3,4

a.   After irradiation with proton.

desired feature in focus. Results on the analysis of a CR-39
polymer sample irradiated with neutrons are reported here. The
8cm x 8cm sample was irradiated and etched by Dr. G. Taulé of the
University of California at Berkeley. The measurements made on
this sample include track size (diameter), track density in each
field of view, roundness, sample area in each field, and total
area of the sample. The roundness measurement is made for appli-
cation as a feature acceptance criterion; the tracks for normal
incidence are almost perfectly round and it is therefore easy to
reject anomalous features using this parameter. This is shown by
SEM picture of the sample, Fig. 3. Fig. 4 and 5 show the distri-
bution of tracks sizes and the track density as a function of
field number.

     The results from this sample show that the distribution of
track sizes is certainly non-Gaussian. It has very definite upper
and lower bounds. The resolution of the instrument for this
analysis was approximately 1 micron. The distribution of track
density shows a reasonably uniform distribution of track density
versus location. The sample was scanned in sequential fields and
the center of the plot corresponds to the center of the sample.
It appears that the dosage rate on this sample is not completely
homogeneous but the variations are random. The analysis of 4200
fields to cover the entire sample used for this report took
approximately 4.0 hours of machine time. The time spent on each
field was about 3-4 seconds and varied as a function of the number
of detected features per field.

Conclusions

     We have shown that commercial CR-39 monomer samples can be
purified by column chromatography. Polymerization with benzoyl
peroxide as initiator gives highly crosslinked polycarbonate
samples suitable for use as high energy radiation dosimeters. A
method has been developed to characterize the polymer and to
count radiation tracts with a computer controlled Quantimet image
analyzer.

REFRACTIVE INDEX

RESPONSE

(1)

(2)

(3)

(4)

15   FLOW TIME (min.)   23

FLOW RATE: 1 ml/min
CHART SPEED: 2 cm/min
SOLVENT: Unstab. THF
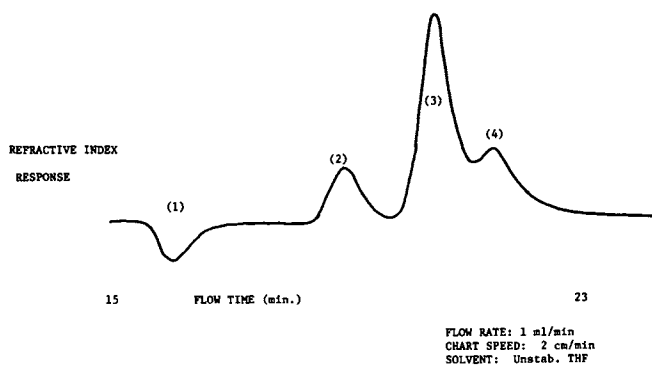
Figure 2. Gel Permeation Chromatograph of CR-39 Polymer

Figure 3. SEM picture of neutron irradiated and etched CR-39 polymer.

```
       LIMITS           COUNT
Size-microns
20.00 -  21.00     0.   :
21.00 -  22.00    77.   :*******************
22.00 -  23.00    81.   :*********************
23.00 -  24.00    73.   :******************
24.00 -  25.00     9.   :**
25.00 -  26.00    35.   :*********
26.00 -  27.00    80.   :********************
27.00 -  28.00     0.   :
28.00 -  29.00    58.   :**************
29.00 -  30.00   101.   :*************************
30.00 -  31.00    64.   :****************
31.00 -  32.00     0.   :
32.00 -  33.00    75.   :******************
33.00 -  34.00    80.   :********************
34.00 -  35.00     0.   :
35.00 -  36.00    66.   :****************
36.00 -  37.00    59.   :**************
37.00 -  38.00    71.   :*****************
38.00 -  39.00     0.   :
39.00 -  40.00    70.   :*****************
40.00 -  41.00    73.   :******************
41.00 -  42.00     0.   :
42.00 -  43.00    49.   :************
43.00 -  44.00    76.   :*******************
44.00 -  45.00    89.   :**********************
45.00 -  46.00     0.   :
46.00 -  47.00    78.   :*******************
47.00 -  48.00   110.   :***************************
48.00 -  49.00     0.   :
49.00 -  50.00   142.   :***********************************
50.00 -  51.00    20.   :*****
51.00 -  52.00     8.   :**
52.00 -  53.00     0.   :*
53.00 -  54.00     0.   :*
54.00 -  55.00     5.   :*
55.00 -  56.00     0.   :
56.00 -  57.00     7.   :*
57.00 -  58.00     2.   :
58.00 -  59.00     0.   :
59.00 -  60.00     0.   :
60.00 -  61.00     2.   :
61.00 -  62.00     0.   :
62.00 -  63.00     0.   :
63.00 -  64.00     0.   :
64.00 -  65.00     0.   :
65.00 -  66.00     0.   :
66.00 -  67.00     0.   :
67.00 -  68.00     0.   :
68.00 -  69.00     1.   :
69.00 -  70.00     0.   :
70.00 -  71.00     0.   :
71.00 -  72.00     3.   :
72.00 -  73.00     0.   :
73.00 -  74.00     1.   :
74.00 -  75.00     5.   :
75.00 -  76.00     1.   :
76.00 -  77.00     0.   :
77.00 -  78.00     0.   :
78.00 -  79.00     0.   :
79.00 -  80.00     0.   :
                        Number →
```

Figure 4.   Neutron track size distribution of CR-39 polymer analyzed by Quantimet Image Analyzer.

```
      LIMITS              T:E:S
   0.00 -     70.00   109.915300   :*******************************
  70.00 -    140.00    76.?*518C   :*********************
 140.00 -    210.00    42.273090   :***********
 210.00 -    280.00    74.686010   :*********************
 280.00 -    350.00    8C.322690   :***********************
 350.00 -    420.00    69.049320   :******************
 420.00 -    490.00    38.047590   :**********
 490.00 -    560.00    69.049320   :******************
 560.00 -    630.00    84.550200   :************************
 630.00 -    700.00    50.730110   :*************
 700.00 -    770.00    88.777720   :*************************
 770.00 -    840.00    40.865920   :***********
 840.00 -    910.00    69.049320   :******************
 910.00 -    980.00    63.412650   :*****************
 980.00 -   1050.00    70.458490   :******************
1050.00 -   1120.00    59.185130   :***************
1120.00 -   1190.00    69.049310   :******************
1190.00 -   1260.00    71.867650   :******************
1260.00 -   1330.00    57.775950   :***************
1330.00 -   1400.00    38.047590   :**********
1400.00 -   1470.00   128.234500   :***********************************
1470.00 -   1540.00    38.047590   :**********
1540.00 -   1610.00    59.185129   :***************
1610.00 -   1680.00    67.640150   :*****************
1680.00 -   1750.00    46.502590   :***********
1750.00 -   1820.00    91.596050   :************************
1820.00 -   1890.00    94.414400   :*************************
1890.00 -   1960.00    63.412640   :*****************
1960.00 -   2030.00    40.594290   :****************
2030.00 -   2100.00    63.412645   :*****************
2100.00 -   2170.00    77.504340   :********************
2170.00 -   2240.00    87.368550   :***********************
2240.00 -   2310.00    80.322690   :**********************
2310.00 -   2380.00    49.320940   :*************
2380.00 -   2450.00    62.003460   :****************
2450.00 -   2520.00    76.095170   :********************
2520.00 -   2590.00    83.141040   :**********************
2590.00 -   2660.00    78.913510   :*********************
2660.00 -   2730.00    94.414400   :*************************
2730.00 -   2800.00    57.775960   :***************
2800.00 -   2870.00    70.458480   :******************
2870.00 -   2940.00    50.730100   :*************
2940.00 -   3010.00    49.320940   :*************
3010.00 -   3080.00   104.278500   :****************************
3080.00 -   3150.00    56.366770   :**************
3150.00 -   3220.00    32.410910   :********
3220.00 -   3290.00    46.502590   :***********
3290.00 -   3360.00    49.320940   :*************
3360.00 -   3430.00    36.638410   :*********
3430.00 -   3500.00    47.911770   :************
3500.00 -   3570.00    49.320940   :*************
3570.00 -   3640.00    55.348460   :**************
3640.00 -   3710.00    55.730110   :**************
3710.00 -   3780.00    50.730110   :*************
3780.00 -   3850.00    85.322680   :***********************
3850.00 -   3920.00    53.548450   :**************
3920.00 -   3990.00    47.911750   :************
3990.00 -   4060.00    56.730100   :**************
4060.00 -   4130.00    52.139270   :**************
4130.00 -   4200.00    43.684260   :***********
```

Track Density →

Figure 5. Neutron track density of CR-39 polymer analyzed by Quantimet Image Analyzer.

Acknowledgments

Literature Cited

1. Sullivan, D. O.; Price, P. B.; Kinoshita, K.; Wilson, C. G. J. Ekctrochem. Soc. 1982, 811–813.
2. Tarlé, G.; Allen, S. P.; Price, P. B. Nature 1981, 293, 556.
3. Price, P. B. Phil. Mag. 1982, 45(2), 331–346.
4. Tarlé, G., Ninth DOE Workshop on Personnel Neutron Dosimetry, Pacific Northwest Laboratory, PNL-SA-10714, 1982, pp. 74–84.
5. Huang, S. J.; Johnson, J. J. ibid, 1982, pp. 85–91.
6. Faermann, S.; Eisen, Y.; Schlesinger, T.; Ovadia, E. ibid, 1982, pp. 92–102.
7. Griffith, R. V.; McMahon, T. A. ibid, 1982, pp. 103–119.

Author Index

Bauer, D. R., 271,285
Briggs, L. M., 271,285
Burchard, Walther, 55
Cercena, J. L., 301
Cholli, A., 233
Chung, Shirley Y., 91
Curro, J. G., 47
Eichinger, B. E., 21
English, Alan D., 257
Fedors, Robert F., 91
Fernandez, A. M., 71
Gerlock, John L., 285
Groeger, J., 301
Hertzberg, R. W., 109
Hong, Su-Don, 91
Huang, S. J., 301
Johnson, J. F., 301
Kajiwara, Kanji, 55
Kelley, F. N., 165
Koenig, Jack L., 205,233
Kong, Eric S. W., 125
Landin, D. T., 33

LeMay, J. D., 165
Leung, Yu-Kwan, 21
Macosko, C. W., 33
Manson, J. A., 109
Mark, J. E., 47
McGinniss, V. D., 241
Mehta, A. A., 301
Michel, J. C., 109
Neilson, George, 91
Nixon, J. R., 241
Patterson, Dwight J., 205
Prottas, R., 301
Qureshi, Shahid, 109
Ritchey, W. M., 233
Sperling, L. H., 71,109
Spinelli, Harry J., 257
Stanford, J. L., 1
Stepto, R. F. T., 1
Still, R. H., 1
Swetlin, B. J., 165
Turner, D. T., 185
Wignall, G. D., 71

Subject Index

A

Acetophenone
  IR spectra, 209-10,213f
  in polyethylene, voltage breakdown
    curve, 241,243f
Acrylic coatings
  cured with melanine, IR studies of
    hydrolysis, 271-83
  cured with melanine
    formaldehyde, 258
  cross-linking and degradation
    chemistry, 267-69
  hydroxy functional
    groups, 261,262f
  IR, 261-67
  NMR, 259-61
Acrylonitrile-butadiene epoxy
  resin, 91-107
Activation energy of fiberite
  epoxy, 141-43
Aerospace epoxy resins
  curing process, 127-29
  density, 129,143
  differential scanning
    calorimetry, 138-42

Aerospace epoxy resins--Continued
  dynamic mechanical analysis, 134-38
  hardness, 129,143
  moisture sorption
    kinetics, 129-30,150-57
  NMR, 130, 157-61
  stress-strain analysis, 131-34
  thermal mechanical
    analysis, 129, 143-50
Aggregation networks, polyethylene and
  styrene-divinyl benzene
  polymers, 74-87
Aging of fiberite epoxy, 131-62
Alcohol concentration in curing
  polybutadiene, 227t
Aliphatic region of polyisoprene
  cross-linked with dicumyl
  peroxide, 212,213f,217,221f
Amine and nitroxide dopant
  chemistry, 289f
Amine light stabilizer, melamine-
  acrylic copolymer
  degradation, 281-83
Amine-cured epoxy networks
  cross-link density, 166-67,177-81
  structure characterization, 172-73

313

Author Index

Bauer, D. R., 271,285
Briggs, L. M., 271,285
Burchard, Walther, 55
Cercena, J. L., 301
Cholli, A., 233
Chung, Shirley Y., 91
Curro, J. G., 47
Eichinger, B. E., 21
English, Alan D., 257
Fedors, Robert F., 91
Fernandez, A. M., 71
Gerlock, John L., 285
Groeger, J., 301
Hertzberg, R. W., 109
Hong, Su-Don, 91
Huang, S. J., 301
Johnson, J. F., 301
Kajiwara, Kanji, 55
Kelley, F. N., 165
Koenig, Jack L., 205,233
Kong, Eric S. W., 125
Landin, D. T., 33

LeMay, J. D., 165
Leung, Yu-Kwan, 21
Macosko, C. W., 33
Manson, J. A., 109
Mark, J. E., 47
McGinniss, V. D., 241
Mehta, A. A., 301
Michel, J. C., 109
Neilson, George, 91
Nixon, J. R., 241
Patterson, Dwight J., 205
Prottas, R., 301
Qureshi, Shahid, 109
Ritchey, W. M., 233
Sperling, L. H., 71,109
Spinelli, Harry J., 257
Stanford, J. L., 1
Stepto, R. F. T., 1
Still, R. H., 1
Swetlin, B. J., 165
Turner, D. T., 185
Wignall, G. D., 71

Subject Index

A

Acetophenone
  IR spectra, 209-10,213f
  in polyethylene, voltage breakdown
      curve, 241,243f
Acrylic coatings
  cured with melanine, IR studies of
      hydrolysis, 271-83
  cured with melanine
      formaldehyde, 258
    cross-linking and degradation
        chemistry, 267-69
    hydroxy functional
        groups, 261,262f
    IR, 261-67
    NMR, 259-61
Acrylonitrile-butadiene epoxy
    resin, 91-107
Activation energy of fiberite
    epoxy, 141-43
Aerospace epoxy resins
  curing process, 127-29
  density, 129,143
  differential scanning
      calorimetry, 138-42

Aerospace epoxy resins--Continued
  dynamic mechanical analysis, 134-38
  hardness, 129,143
  moisture sorption
      kinetics, 129-30,150-57
  NMR, 130, 157-61
  stress-strain analysis, 131-34
  thermal mechanical
      analysis, 129, 143-50
Aggregation networks, polyethylene and
    styrene-divinyl benzene
    polymers, 74-87
Aging of fiberite epoxy, 131-62
Alcohol concentration in curing
    polybutadiene, 227t
Aliphatic region of polyisoprene
    cross-linked with dicumyl
    peroxide, 212,213f,217,221f
Amine and nitroxide dopant
    chemistry, 289f
Amine light stabilizer, melamine-
    acrylic copolymer
    degradation, 281-83
Amine-cured epoxy networks
    cross-link density, 166-67,177-81
    structure characterization, 172-73

313

U

UV degradation, melamine-cured acrylic
    copolymer
    coating, 267-68,271-83,285-98

V

Vinyl copolymerization, cyclization
    and branching theory, 33-45
Viscoelastic response, epoxies with
    epoxidized natural oils, 114-23
Viscosity of vinyl and divinyl
    copolymers, 37,41,43f
Voltage breakdown curve for
    polyethylene with peroxide
    decomposition products, 241,243f
Volume recovery of aerospace epoxy
    resins
  density, 129,143
  differential scanning
      calorimetry, 138-42
  dynamic mechanical analysis, 134-38
  hardness, 129,143
  moisture sorption
      kinetics, 129-30,150-57
  NMR, 130, 157-61

Volume recovery of aerospace epoxy
    resins--Continued
  stress-strain analysis, 131-34
  thermal mechanical
      analysis, 129, 143-50

W

Weight average degree of
    polymerization, equation, 57-58
Weight average of longest linear chain
    through a branched molecule, 37-39
Weight average radii of gyration
    corrected for molecular size
    mismatch. 83-84
Wire applications for
    polyethylene, 241,242f

X

X-ray scattering, small-angle, of
    butadiene-acrylonitrile epoxy
    resin, 104-7

Y

Young's moduli of stoichiometric
    amine-cured epoxy
    networks, 177,179f